Recent history of natural hazards in Chile

Imprints of earthquakes and volcanic events in lacustrine and marine sediments

Recente geschiedenis van natuurlijke risico's in Chili

Sporen van aardbevingen en vulkanische activiteit in lacustriene en mariene sedimenten

Maarten Van Daele

2012

Dissertation submitted for the degree

of Doctor of Science: Geology

Supervisor: Prof. Dr. Marc De Batist

Research funded by FWO - Vlaanderen

Members of the reading committee:

Prof. Dr. M. Pino (Universidad Austral de Chile, Valdivia, Chile)
Prof. Dr. D. Ariztegui (University of Geneva, Switzerland)
Prof. Dr. N. Davies (Ghent University, Belgium)

Members of the examination committee:

Prof. Dr. J. Verniers (Ghent University, Belgium): chair
Prof. Dr. M. De Batist (Ghent University, Belgium): supervisor, secretary
Prof. Dr. M. Pino (Universidad Austral de Chile, Valdivia, Chile)
Prof. Dr. D. Ariztegui (University of Geneva, Switzerland)
Prof. Dr. A. Hubert-Ferrari (Université de Liège, Belgium)
Prof. Dr. D. Verschuren (Ghent University, Belgium)
Prof. Dr. N. Davies (Ghent University, Belgium)
Prof. Dr. D. Van Rooij (Ghent University, Belgium)

Cover illustration: picture of Llaima Volcano erupting on January 1, 2008, taken from the shores of Lake Villarrica (K. Heirman).

Maarten Van Daele carried out the research with financial support of the Research Foundation – Flanders (FWO – Vlaanderen).

This research project was conducted at the Renard Centre of Marine Geology, Ghent University (Ghent, Belgium)

To refer to this thesis: Van Daele, M., 2011. Recent history of natural hazards in Chile: Imprints of earthquakes and volcanic events in lacustrine and marine sediments. PhD thesis, Ghent University, Ghent, Belgium.

Table of contents

List of figures

List of tables

List of abbreviations

AC	Andean Cordillera
AD	Anno Domini (Since birth of Jesus)
asl	above sea level
BP	before present (before AD 1950)
bsf	below sea floor
bsl	below sea level
BSS	basal shear surface
c	coarse
CR	Coastal Range
CT	computed tomography
CTD	conductivity, temperature, depth sensor
CVRZ	Concepción-Valparaíso rupture zone
ED	event deposit
EDS	energy dispersive spectrometer
e.g.	exempli gratia (*for example*)
EQ	earthquake
ERC	earthquake recording capability
etc	etcetera
f	fine
FeL	Fe-rich lamina
ID	Intermediate Depression
i.e.	id est (*that is*)
kV	kilo Volt
LAH	lahar
LOI	Loss on ignition
LT	lacustrine turbidite
m	meter or medium
max.	maximum
MMI	Modified Mercalli Intensity
MS	magnetic susceptibility
ms	milliseconds
MSK	Medvedev–Sponheuer–Karník (Macroseismic Intensity)
MTD	mass-transport deposit
M_w	moment magnitude
nA	nano Ampère
Rep.	reported
RV	Research Vessel
SD	standard deviation
SEM	scanning electron microscope
SI	Seismic Intensity (= Macroseismic Intensity)
SL	stratigraphic level
TEF	tephra
TWT	two-way travel time

UGent	Ghent University
v c	very coarse
v f	very fine
VRZ	Valdivia rupture zone
VY	varve year
XRD	X-ray diffraction
XRF	X-ray fluorescence
yr	year
3D	three-dimensional

Acknowledgements - dankwoord

Eerst en vooral wil ik graag mijn promotor, Marc De Batist, bedanken voor mij de mogelijkheid te geven dit fascinerende onderzoek te verrichten. Tist, bedankt voor al de tijd (gedurende de week en in het weekend) die je in mijn doctoraat en mijn vorming tot wetenschapper geïnvesteerd hebt, en voor alle kansen die je me gedurende mijn doctoraat gegeven hebt!

Jasper en Katrien, ook zonder jullie had dit doctoraat er nu niet gelegen! In het bijzonder bedankt om mij te introduceren in Chili en er onvergetelijke momenten met mij te delen (zie o.a. de cover-afbeelding van dit doctoraat). Bedankt om altijd klaar te staan als ik nog maar eens langskwam met een nieuwe figuur of een nieuw idee om op jullie los te laten, en uiteraard ook voor de wetenschappelijke en minder wetenschappelijke discussies (met al dan niet een pisco sour in de hand)!

I also want to thank Willem, Sébastien, Philipp for great times in Chile, and letting me also disturb you during your work over and over again…

Koen, merci voor alle hulp, op en naast het water! Wim, het was geweldig dat je erbij was in Aysén, bedankt voor alle hulp!

Anita, Javiera, Tuco, Mario y Alto del Carmen, gracias para llevar un poco de Chile a Bélgica!

I also want to thank all other RCMG colleagues, for football breaks, puntje 3 and much more: Andres, Arne, David, Dries, Els, Hans, Huy, Isabelle, Jean-Pierre, Jeffrey, Jeroen, Lies, Lieven, Marc, Matthias, Michael, Mieke, Peter, Rindert, Sonia, Stan, Thomas, Tine and Vera.

Thanks to all (job ,BSc and MSc) students: Camille, Hendrik-Jan, Korneel, Lindsey, Maikel, Myriam, Thomas, Steven and Zoë.

I also want to thank all other colleagues regularly crossing my path in the S8: Danielle, Dimitri, Dirk, Ingrid, Jan, Jan, Jan, Jacques, Johan, Kenneth, Koen, Kurt, Marijn, Neil, Patrick, Peter, Stijn, Stephen, Thomas, Tim, Veerle, Wesley etc.

Thanks to everyone who in some way contributed to getting samples analyzed, data processed, etc: Philippe De Smet, Jan Vandenbulcke, Sabine Schmidt, Nathalie Fagel, Achim Brauer, Christian Wolff, Jens Greinert, Rieneke Gilles, Rik Tjallingii, Dierk Hebbeln, Vera Lukies, Veerle Cnudde, Jan Dewanckele, Jan Mortier, Peter Van den haute, Jan Jurcika, David García, Aurélia Hubert-Ferrari, Karen Fontijn, Adrian Gilli…

Thank you for the great limnostages in Kastanienbaum: Jeroen, Leen, Flavio and Michi 3, and all other people of the Swiss lake group: KellyAnn, Mona, Anna, Michi 2, etc.

Richard, Yoeri and Koen, thank you for the nice and informative week in Mondsee.

Mario y Roberto, sin vuestro hospitalidad habría sido imposible hacer todo este trabajo en Chile, gracias! Robert, gracias para estar presente a qualquier hora! Jorge y todo la tripulación del Don Este, gracias para la inolvidable semana en los fiordos! Alejandro, gracias para “el terrible” y cualquier tipo de soporte durante todas estas semanas, meses… No me puedo imaginar trabajo de terreno en Chile sin tí, eres realmente increíble!

También quiero dar la gracias a varios organizaciones/empresas chilenos para darnos permisos para hacer nuestro trabajo de terreno: Fundación Huilo Huilo, Aguas Andinas, CONAF y SHOA.

Thanks to everyone who joined our Chilean Lake Team on the field: Steve, Manuel, Paulina, Rolf, Marcelo, Rodrigo, Zakaria, Eddy, Olaf, Martin, Julie, Nicole, Nathalie and Josephine!

Gracias a todos que trabajeron conmigo en (los datos de) Venezuela: Bill, Franck, Aurélien, Jesús, Cristian y la tripulación del Guaiqueri II!

Los dueños de todos los hospedajes y discoteques, Donde la Negra, Elizabeth, Suzy & Rolando, Melissa, Jorge, Tonca, Valentina, todos los huevones y muchos más, gracias para hacer mis tiempos in Chile tan increíble! En particular quiero decir gracias a Christian, Margarita, María Paz and Conchi para la ayuda y el soporte en los tiempos más difíciles, nunca olvidaré lo que hicísteis este día!

Merci aan al mijn klasgenoten voor de geweldige jaren die mijn doctoraat voorafgingen: Kathleen, Charissa, Tom, Dirk, Frederik, David, Fun, Maite enz.

Bart, Charissa, Cindy en al wie er nog over de vloer kwam, bedankt voor de leuke jaren in de Musschestraat!

Carmen, Colin, Marquitos and Matt, thanks for the legendary reunions!

Bregt, Fre, Gertje, Joost, Thomas en nog vele anderen, merci voor leuke spelavonden, feestjes, etentjes, babbels...

Samuel, Alicia, Lauren, Joris, Lieven, Ellen, Mario, mama en papa, bedankt om er altijd te zijn, in goede en slechte tijden. Steven, je zal voor altijd een plaats hebben in ons hart!

Inka, thanks for everything, you’re the best!

I sincerely apologize to everyone I forgot.

Summary

In the past decade, a series of major endogenic, natural catastrophic events caused hundreds of thousands of casualties, as well as a tremendous amount of structural and economic damage. Megathrust earthquakes at subduction zones (i.e. interplate earthquakes) resulted in damage and fatalities over areas of hundreds of kilometers, and, moreover, triggered ocean-crossing tsunamis that in turn caused devastation on several continents. Smaller, but shallow, earthquakes were locally even more destructive than most of the megathrust events. Also, volcanic eruptions disrupted air travel in several parts of the world. Along subduction zones, these three types of potentially catastrophic events occur in the same area and are genetically linked. The subduction process does not only directly produce the megathrust earthquakes, but can also influence the stress regime within the overriding (continental) plate, resulting in continental faults potentially causing local but shallow earthquakes. Moreover, the subduction process induces volcanism in the overriding plate.

Assessing the past behavior of faults or volcanoes can lead us towards understanding their current behavior and hazard. Hence, there is a need to study the recurrence and magnitudes of past events. However, in many regions of the world, such as South-Central Chile (the study area of this thesis), historical records are not long enough and barely cover one or two cycles of some of these events. Therefore, prehistoric events should be studied. Sedimentary sequences in lakes and fjords can be used to reconstruct both past earthquakes and volcanic events. Earthquakes can trigger mass-transport deposits, in-situ deformation and several types of turbidites, which can, for example, be used to estimate local seismic intensities. Volcanic events can cause fallout ash layers, but also lahars and ashes that are deposited in the catchment can eventually leave traces in lakes or fjords. Moreover, continuous inter-event sedimentation supports preservation and allows achieving good, reliable age models.

To be able to correctly interpret these event deposits, it is crucial to study the sedimentary impact of recent catastrophic events, and thereby “calibrate” the method. In this thesis, the event deposits of several recent, well-described natural events are studied: i) sedimentary event deposits related to volcanic activity of Villarrica Volcano in the last 100 years (Chapter 3); ii) the sedimentary imprint of the 1960 M_w 9.5 Valdivia and 2010 M_w 8.8 Maule Chilean megathrust earthquakes in 19 lakes (Chapter 4); and iii) the impact of the 2007 M_w 6.2 Aysén earthquake and related onshore landslides in Aysén fjord (chapters 5 and 6).

Following a general introduction in Chapter 1, an overview of the methods that are used in this study is presented in Chapter 2.

In Chapter 3, a multi-lake and multi-proxy analytical approach is used to obtain reliable and high-resolution records of past natural catastrophes from c. 600-year-old annually-laminated (varved) lake-sediment sequences extracted from three lakes, Villarrica, Calafquén and Riñihue, in the volcanically and seismically active Chilean Lake District. Using a combination of µXRF scanning, microfacies analysis, grain-size analysis, color analysis and magnetic susceptibility, four different types of event deposits (lacustrine turbidites, tephra-fall layers, runoff cryptotephras, lahar deposits) are detected and characterized, and the eruption record for the nearby volcanoes (i.e. Villarrica, El Mocho) is revised. This eruption record is unprecedented in its continuity and temporal resolution. Time series analysis shows 112 eruptions with a Volcanic Explosivity Index (VEI) ≥ 2 from Villarrica

Volcano in the last c. 600 years. Mocho-Choshuenco Volcano has been significantly less active since 1900 compared to preceding centuries. Also deposits of eruptions from the more remote Carrán-Los Venados Volcanic Complex, Quetrupillán and Lanín or Huanquihue volcanoes are identified in the studied lake sediments. The last VEI ≥ 2 eruption of Villarrica Volcano occurred in 1991. The probability of the occurrence of future eruptions from Villarrica Volcano is estimated, and it is statistically demonstrated that the probability of a 21-year repose period (anno 2012) without eruptions is ≤ 1.9 %. This new perspective on the recurrence interval of eruptions and historical lahar activity will help improve volcanic hazard assessments for this rapidly expanding tourist region.

In Chapter 4, short sediment cores, sometimes combined with high-resolution reflection seismics, are used to study the sedimentary impact of the 1960 M_w 9.5 Valdivia and the 2010 M_w 8.8 Maule earthquakes in 19 lakes in South-Central Chile (from north to south: Negra, Lo Encañado, Aculeo, Vichuquén, Laja, Lanalhue, Butaco, Villarrica, Calafquén, Pullinque, Pellaifa, Panguipulli, Neltume, Riñihue, Ranco, Maihue, Puyehue, Rupanco and Llanquihue). By using image-analysis, magnetic susceptibility and grain-size analysis, five types of event deposits (seismites) are identified and are attributed to one of the abovementioned megathrust earthquakes: i) mass-transport deposits (MTDs), ii) in-situ deformation, iii) lacustrine turbidites with a similar composition as the background sediments (LT1s), iv) lacustrine turbidites with a different composition as the background sediments (more terrestrial; LT2s), and v) homogenites. These seismites are compared to local seismic intensities, eyewitness reports, post-earthquake observations, vegetation and geomorphology of the catchment. Homogenites consistently represent lake seiches and LT2s can be a result of local near-shore mass wasting, delta collapse or onshore landslides surging into the lake (direct imprint), but also of debris or mud flows entering the lake, or of fluvial reworking of landslide debris in the catchment (indirect imprint). LT1s are the most reliable seismites, since they can have almost no other triggers then earthquake shaking. Moreover, they most sensitively record different seismic intensities, which is reflected in a different thickness and distribution in a certain lake. For the other seismites, the lake sub-basins only have a minimum intensity threshold. In general, the minimum encountered seismic-intensity threshold for most seismites is VI, but it can differ between the lakes and/or sub-basins. Finally, coastal lakes on the border between the Valdivia and Concepción-Valparaíso rupture zones (i.e. lakes Lanalhue and Butaco), where seismic shaking is frequent, appear to record lake-level rise due to the coastal tilting rather than the seismic shaking itself.

In Chapter 5, widespread basin-plain deformation that is caused by the 2007 M_w 6.2 earthquake in Aysén fjord is studied. This earthquake caused many onshore landslides which, in turn, triggered several destructive tsunamis in the fjord. Both superficial and buried deformed basin-plain deposits are mapped using multibeam bathymetry and seismic-reflection (sparker) profiling. The seismic signature of the sub-bottom is ground-truthed with short sediment cores on key locations. Deformed basin-plain deposits induced by the 2007 earthquake can be subdivided into frontally emergent and confined deformed basin-plain deposits, with a deep and shallow basal shear surface. All deformed basin-plain deposits with a deep basal shear surface are induced by the weight and impact of a slope-adjacent mass-flow wedge. The frontally emergent –most mobile– basin-plain deformation is triggered by mass flows originating from onshore landslides (i.e. debris flows, rock slides and avalanches) propagating into the fjord. This basin-plain deformation results in vertical seafloor offsets of up to 20 m and might be even more important for tsunami generation than the impact on the sea surface of the onshore landslides themselves. In the depressions created by the basin-plain deformation, megaturbidites occur, while more distally, sandy density-flow deposits cover the

seafloor. The data also indicates that these density flows propagate slower than the basin-plain deformation. Based on correlations with the two main eruptions of the Hudson Volcano, it is hypothesized that during the Holocene three to four similar events have struck the fjord. Due to the constant structural characteristics of the Liquiñe-Ofqui Fault Zone in the northern Patagonian fjordland and historical seismic swarms in this area, it is concluded that similar hazards should be taken into account for most of the fjords in this region. Finally, there are indications that both the prehistoric events and the 2007 fluid-driven seismic swarm may have been accompanied by fluid flow from tectonic structures below the fjord to the seafloor.

In Chapter 6, the density-flow deposits that are recognized in the previous chapter are studied in more detail. Twenty two short sediment cores taken in the inner Aysén fjord help to better understand the sedimentary-facies successions and intercalation of the density-flow deposits. By combining grain-size analysis with X-ray computed tomography (CT) scanning, it is possible to demonstrate that the encountered facies correspond to classical divisions of density-flow deposits and turbidites. The deposits consist of a succession of several sub-deposits with different paleoflow directions and can be interpreted as amalgamated density-flow deposits. Orientations of i) folds, ii) imbricated mud clasts, iii) back- and foresets of climbing ripples and iv) asymmetric convolute lamination, are used to determine relative paleoflow directions at the location of the cores. By assigning the basal flow of the amalgamated density-flow deposits to the closest principal mass-flow, the absolute flow directions of the sub-deposits is determined, which, in combination with multibeam basin-floor morphology, allows reconstruction of the 2007 density-flow successions in Aysén fjord. Furthermore, alternating flow directions observed in some of the cores provide evidence for a seiche induced by the density flows. Traction carpets, in which rip-up mud clasts correspond to the floating, coarsest grains, occur at the base of the density-flow deposits. The main conclusion is that X-ray CT scans provide crucial information for reconstructing paleoflows and can be a useful tool in marine and lacustrine sedimentology and paleoseismology. Multidirectional, amalgamated density-flow deposits and turbidites are an indication for simultaneous triggering of density flows and can therefore in most cases be attributed to earthquakes, ruling out other triggers, such as e.g. floods.

In conclusion, this PhD dissertation shows that lake and fjord sediments are excellent recorders of natural events. The most frequently encountered type of deposits linked to catastrophic events are density-flow deposits (which include turbidites). It was possible to differentiate between mass-wasting generated turbidites triggered directly by earthquakes and turbidites triggered by onshore debris or mud flows, lahars (for the first time described in lakes), or floods reaching the lake shore. Amalgamated density-flow deposits were used to prove simultaneous triggering (and hence, earthquake triggering) of mass-wasting events. Another breakthrough is the recognition of deposits related to volcanic events that are not fallout, but have been transported from the catchment. Therefore, independent of wind directions during an eruption, even fine fallout ashes in the catchment can reach the lakes through runoff and leave a permanent sedimentary imprint. Finally, it can be concluded that the deposits in all the study areas match very well with reports, seismic intensities etc., and can therefore be used to reconstruct similar events in the past, in a semi-quantitative way.

Samenvatting

In het voorbije decennium hebben verscheidene endogene natuurrampen vele slachtoffers gemaakt en zowel structurele als economische schade veroorzaakt. Subductie-aardbevingen (dit zijn interplaat-aardbevingen in subductiezones) eisten een hoge dodentol en hebben enorme schade berokkend over gebieden van honderden kilometers lang. Bovendien veroorzaakten deze aardbevingen ook tsunamis die de oceanen overkruisten en zo op verschillende continenten schade aanrichtten. Een andere soort, minder zware, maar ondiepe aardbevingen waren op lokale schaal zelfs destructiever dan de subductie-aardbevingen. Ook vulkanische erupties eisten hun tol door het vliegverkeer in grote delen van de wereld lam te leggen, maar ook soms door hele dorpen te vernietigen. Aan subductiezones komen deze drie soorten catastrofale natuurfenomenen samen voor en zijn deze zelfs genetisch gekoppeld. Het subductieproces veroorzaakt niet alleen rechtstreeks de subductieaardbevingen, maar kan ook het spanningsregime binnen de overrijdende (continentale) plaat beïnvloeden en zo kunnen continentale breuken ontstaan die meer lokale, maar ondiepe aardbevingen kunnen veroorzaken. Bovendien brengt het subductieproces ook vulkanisme teweeg in de overrijdende plaat.

Het in kaart brengen van de activiteit van breuken en vulkanen in het verleden kan ons helpen om hun huidige en toekomstige activiteit en risico's beter in te schatten. Daarom is het belangrijk om de sterkte en frequentie van deze fenomenen in het verleden te bestuderen. In verschillende delen van de wereld, zoals in Zuid-Centraal Chili (het studiegebied van deze thesis), gaan de historische gegevens echter niet ver genoeg terug in de tijd en omvatten die slecht één à twee cycli van deze natuurlijke fenomenen. Als gevolg daarvan is het onontbeerlijk om ook de prehistorische aardbevingen en vulkaanuitbarstingen te bestuderen. Sedimentaire sequenties in meren en fjorden zijn zeer geschikt om de geschiedenis van deze fenomenen te reconstrueren. Aardbevingen kunnen afglijdingen, in-situ vervormingen en verschillende soorten van turbidieten veroorzaken, en die afzettingen kunnen dan later gebruikt worden om bijvoorbeeld de seismische intensiteit (dit is de intensiteit van lokale grondbewegingen) in te schatten. Vulkanische activiteit kan niet alleen zorgen voor neervallende as op een het wateroppervlak, maar kan ook lahars (vulkanische modderstromen) of neervallende as veroorzaken in het drainagebekken van een meer of fjord, hetgeen uiteindelijk ook sporen kan nalaten in het sedimentaire bekken. Bovendien wordt preservatie van de afzettingen en het bekomen van een goed ouderdomsmodel in de hand gewerkt door de continue sedimentatie tussen deze natuurfenomenen door.

Om deze afzettigen correct te kunnen interpreteren is het echter noodzakelijk om de sedimentaire impact van recente natuurrampen te bestuderen en zo de methode te "kalibreren". In deze doctoraatsthesis worden de afzettingen van verschillende recente, goed beschreven natuurrampen onderzocht: i) de afzettingen veroorzaakt door vulkanische activiteit van de Villarrica vulkaan gedurende de laatste eeuw (Hoofdstuk 3); ii) de sedimentaire afdruk van de 1960 M_w 9.5 Valdivia en 2010 M_w 8.8 Maule aardbevingen in 19 chileense meren (Hoofdstuk 4); en iii) de impact van de 2007 M_w 6.2 Aysén aardbeving en de hierdoor veroorzaakte afglijdingen in de Aysén fjord (hoofdstukken 5 en 6).

Na het geven van een algemene inleiding in Hoofdstuk 1, wordt er in Hoofdstuk 2 een overzicht gegeven van de methodes die gebruikt worden in deze studie.

In Hoofdstuk 3 worden jaarlijks gelamineerde sedimenten van drie meren (Villarrica, Calafquén en Riñihue) onderzocht met behulp van verschillende analytische methodes met als bedoeling een betrouwbare, hoge resolutie inventaris te maken van natuurrampen die het seismisch en vulkanisch actieve Merendistrict in Chili gedurende de laatste 600 jaar geteisterd hebben. Met behulp van een combinatie van µXRF-scans, microfacies-analyse, korrelgrootte-analyse, kleurenanalyse en magnetische susceptibiliteit, worden vier types van afzettingen herkend en gekarakteriseerd (lacustriene turbidieten, tefra lagen, ingespoelde cryptotefra-laminaties en laharafzettingen) en wordt de eruptiegeschiedenis van de Villarrica en Mocho vulkanen herbekeken. De continuïteit en resolutie van de gereconstrueerde eruptiegeschiedenis van de Villarrica vulkaan is ongezien, met gedurende de laatste 600 jaar, 112 erupties met een vulkanische explosiviteitsindex (VEI) ≥ 2. Bovendien worden voor het eerst lahars gereconstrueerd aan de hand van meersedimenten. De Mocho vulkaan is in vergelijking met de voorgaande eeuwen, duidelijk minder actief sinds het begin van de 20ste eeuw. Ook afzettingen van erupties van verderaf gelegen vulkanen zoals het Carrán-Los Venados vulkanisch complex, de Quetrupillán en Lanín of Huanquihue vulkanen, worden teruggevonden in de bestudeerde meersedimenten. De laatste VEI ≥ 2 eruptie van de Villarrica vulkaan dateert van 1991 en door het berekenen van de kans op het voorkomen van toekomstige erupties wordt bepaald dat de kans op een periode van 21 jaar zonder erupties (anno 2012) kleiner is dan 1.9 %. Deze nieuwe informatie betreffende de frequentie van vulkanische erupties en lahars in het verleden zal helpen om de risico's verbonden aan vulkanische activiteit beter in te schatten in deze snel groeiende toeristische regio.

In Hoofdstuk 4 worden korte sedimentkernen (lokaal in combinatie met hoge-resolutie reflectie-seismische profielen) bestudeerd om de sedimentaire impact van de 1960 M_w 9.5 Valdivia en de 2010 M_w 8.8 Maule aardbevingen op 19 meren in Zuid-Centraal Chile (van noord naar zuid: Negra, Lo Encañado, Aculeo, Vichuquén, Laja, Lanalhue, Butaco, Villarrica, Calafquén, Pullinque, Pellaifa, Panguipulli, Neltume, Riñihue, Ranco, Maihue, Puyehue, Rupanco en Llanquihue) te achterhalen. Met behulp van foto-analyse, magnetisch susceptibiliteit en korrelgrootte-analyses worden 5 soorten afzettingen aan deze aardbevingen toegeschreven (seismieten): i) afglijdingen, ii) in-situ vervormingen, iii) lacustriene turbidieten met een gelijkaardige samenstelling als de achtergrondsedimenten (LT1s), iv) lacustriene turbidieten met een verschillende samenstelling als de achtergrondsedimenten (meer terrigeen; LT2s), en v) homogenieten. Deze seismieten worden vervolgens vergeleken met de lokale seismische intensiteit, historische rapporten, getuige-waarnemingen, observaties van de effecten na de aardbeving, vegetatie en geomorfologie van het drainagebekken. Zo worden homogenieten steeds gevormd na een seiche op het meer en kunnen LT2s afgezet worden als gevolg van kustnabije afglijdingen, afglijdingen in deltas of grondverschuivingen die rechtstreeks in het meer terechtkomen (directe afdruk), maar ook door modderstromen die de meerkust bereiken of door fluviatiele herwerking van grondverschuivingen in het drainagebekken (indirecte afdruk). LT1s zijn de meest betrouwbare seismieten, aangezien zij bijna enkel door een aardbeving veroorzaakt kunnen worden. Bovendien zijn dit ook de seismieten die verschillende seismische intensiteiten op de meest gevoelige wijze vastleggen door middel van een verschillende dikte en distributie in de meren, terwijl de aanwezigheid van de andere seismieten slechts een minimale drempelintensiteit weergeeft. Over het algemeen is de minimum seismische intensiteit waarbij seismieten veroorzaakt worden VI, maar dit kan verschillen van meer tot meer en/of van sub-bekken tot sub-bekken. Sedimenten van kustmeren ter hoogte van waar de tijdens de 1960 en 2010 aardbevingen geactiveerde breukzones overlappen (de meren Lanalhue en Butaco),

registreren de stijging van de meerspiegel als gevolg van co-seismische kanteling in plaats van de seismische grondbewegingen.

In Hoofdstuk 5 wordt wijdverspreide vervorming van de bekkenvloer bestudeerd, die veroorzaakt werd door de 2007 M_w 6.2 aardbeving in de Aysén fjord. Deze aardbeving veroorzaakte verschillende grondverschuivingen en -lawines, die op hun beurt leidden tot verschillende destructieve tsunamis in de fjord. Zowel oppervlakkige als begraven vervorming van de bekkenvloer werd uitgekarteerd met behulp van multibeam bathymetrie en reflectieseismische profielen (sparker). De seismische signatuur van de fjordsedimenten wordt op cruciale locaties geverifieerd met behulp van korte sedimentkernen. De vervormingen van de bekkenvloer, die geïnduceerd werden door de 2007-aardbeving, wordt opgesplitst in afzettingen die frontaal begrensd of frontaal opduikend zijn, en die een diep of ondiep basaal schuifoppervlak hebben. De vervormde bekkenvloer met een diep basaal schuifoppervlak werd steeds veroorzaakt door de impact en het gewicht van massastroomafzettingen. De frontaal opduikende, meest mobiele, vervorming werd steeds teweeg gebracht door massastromen die ontstonden wanneer grondverschuivingen en -lawines in de fjord terecht kwamen. De vervorming van de bekkenvloer brengt verticale diepteverschillen in de zeebodem van meer dan 20 m teweeg en kan bijgevolg belangrijker zijn bij de vorming van tsunamis dan de grondverschuivingen zelf. In de depressies die ontstonden door de vervorming van de bekkenvloer, komen megaturbidieten voor. Op meer distale locaties bedekken afzettingen van densiteitstromen de zeevloer. Deze densiteitstromen bewegen zich trager voort dan de vervorming van de bekkenvloer, wat aangetoond wordt doordat de laatste soms ingesneden zijn door de densiteitstromen. Op basis van correlaties van afzettingen met de twee belangrijkste gekende erupties van de Hudson vulkaan, wordt verondersteld dat er zich gedurende het Holoceen drie tot vier gelijkaardige natuurfenomenen voordeden. In het licht van de structurele uniformiteit van de Liquiñe-Ofqui breukzone (verantwoordelijk voor de aardbeving in 2007) in het noordelijk patagonisch fjordgebied, en van de recente seismische zwermen in dat gebied, wordt besloten dat er gelijkaardige risico's als in de Aysén fjord gelden voor de hele regio. Ten slotte zijn er ook indicaties dat zowel de seismische zwerm in 2007, als gelijkaardige prehistorische gebeurtenissen, gepaard gingen met (hydrothermale) vloeistofstromen langsheen tektonische structuren onder de fjord.

In Hoofdstuk 6 worden de afzettingen van de densiteitstromen, die geïdentificeerd werden in Hoofdstuk 5, in meer detail bestudeerd. Om de successies van verschillende sedimentaire facies in de afzettingen en de intercalatie van verschillende densiteitstromen beter te begrijpen, worden 22 korte sedimentkernen in de Aysén fjord onderzocht. Door korrelgrootte-analyses te combineren met computertomografie (CT) wordt aangetoond dat de aangetroffen facies overeen komen met klassieke onderverdelingen van densiteitstromen en turbidieten. De afzettingen zijn opgebouwd uit een successie van deelafzettingen met verschillende paleostroomrichtingen en kunnen geïnterpreteerd worden als samengestelde densiteitstromen. Om de relatieve paleostroomrichtingen ter hoogte van de kernen te bepalen, worden de oriëntaties van de volgende structuren gebruikt: i) plooien, ii) imbricatie van siltklasten, iii) afzettingen op de loef- en lijzijde van klimmende ribbels, en iv) asymmetrische convolute laminatie. Door de basale stroomrichting van de samengestelde densiteitstroomafzetting toe te wijzen aan de dichtstbijzijnde massastroom, worden de absolute paleostroomrichtingen bepaald. In combinatie met de morfologie van de zeebodem (bepaald met multibeam bathymetrie) worden vervolgens de 2007-densiteitstromen in de Aysén fjord gereconstrueerd. Wisselende stroomrichtingen tonen ook een seiche-effect aan dat waarschijnlijk veroorzaakt werd door de densiteitstromen. Aan de basis van de

densiteitstroomafzettingen komen tractielagen voor waarin de siltklasten de drijvende, grootste korrels voorstellen. Computertomografie levert cruciale informatie voor het reconstrueren van paleostroomrichtingen en kan een handige methode zijn in mariene en lacustriene sedimentologie en paleoseismologie. Multidirectionele, samengestelde densiteitstroomafzettingen en turbidieten vormen een indicatie voor het gelijktijdig ontstaan van de densiteitstromen en kunnen daarvoor meestal toegeschreven worden aan aardbevingen.

Deze doctoraatsthesis toont aan de sedimenten van meren en fjorden zeer geschikt zijn om catastrofale natuurfenomenen vast te leggen. De meest voorkomende afzettingen die gekoppeld werden aan deze fenomenen zij densiteitstroomafzettingen (waartoe ook turbidieten behoren). Het was mogelijk om turbidieten die rechtstreeks door aardbevingen veroorzaakt werden te onderscheiden van turbidieten die afkomstig zijn modderstromen, lahars (die voor het eerst beschreven werden in meren) of fluviatiele herwerking van grondverschuivingen. Samengestelde densiteitstroomafzettingen kunnen worden gebruikt om het gelijktijdig ontstaan van de verschillende densiteitstromen aan te tonen, en daardoor ook dat een aardbeving hen veroorzaakte. Een ander belangrijk resultaat is het herkennen van vulkanische afzettingen die niet rechtstreeks neervallen op het meer, maar vanuit het drainagebekken naar het meer getransporteerd werden. Onafhankelijk van de windrichting tijdens de uitbarsting kan daardoor fijne as die in het drainagebekken neerviel later in het meer ingespoeld worden en daar een permanente afzetting achterlaten. Er kan besloten worden dat in alle studiegebieden de sedimentaire afzettingen in overeenstemming zijn met historische rapporten, seismische intensiteiten etc., en dat ze bijgevolg gebruikt kunnen worden om gelijkaardige natuurfenomenen in het verleden op een quasi kwantitatieve wijze te reconstrueren.

“Los cerros se juntaron”

“The hills united”

A Mapuche woman living at the foot of Cerro Añiques (southeast of Lake Pellaifa) talking about landslides triggered by the 1960 earthquake, coming from both sides of the valley and filling the valley floor with landslide deposits.

Chapter 1

Introduction

1.1 Recent catastrophic natural events

Throughout Earth's history, endogenic, natural events, such as earthquakes and volcanic eruptions, have been continuously active in shaping and reshaping the surface of this dynamic planet. However, with the continuously increasing population, urbanization and human development, the aftermath of such natural events becomes ever more dramatic. In the past decade, a series of major catastrophic events caused hundreds of thousands of casualties, as well as a tremendous amount of structural and economical damage. Many major and great earthquakes have made the news headlines worldwide. Some of the most mind-captivating and broadcasted were the giant megathrust earthquakes at subduction zones (i.e. interplate earthquakes) such as the 2004* M_w 9.1 Sumatra-Andaman (Indonesia) earthquake and tsunami, the 2010 M_w 8.8 Maule (Chile) earthquake and tsunami and the 2011 M_w 9.0 Tohoku-Oki (Japan) earthquake and tsunami (USGS, 2012). These three devastating earthquakes (all in the top 6 of strongest instrumentally recorded earthquakes) directly resulted in damage and fatalities over areas of hundreds of kilometers and additionally, triggered ocean-crossing tsunamis causing devastation on several continents. These mega-events, however, are not the only catastrophic earthquakes that grabbed the media's attention for days or even weeks. Local, but shallow, earthquakes such as the 2003 M_w 6.6 Bam (Iran; depth: 10 km), the 2010 M_w 7.0 Haïti (depth: 13 km) and the 2010 M_w 7.1 Christchurch (New Zealand; depth: 10 km) earthquakes (USGS, 2012) were locally even more destructive than most of the megathrust events. Apart from earthquakes, also volcanic eruptions have caused a lot of human suffering and economic damage in the past years. The eruption of the Eyjafjallajökull (Iceland) in April 2010 resulted in major disruption of air travel across Europe. Similarly, the eruptions of the Chilean Chaitén Volcano in 2008 and the Puyehue-Cordón Caulle Volcanic Complex in 2011 led to disrupted air travel in mainly Argentina, but also as far as Australia and New Zealand. Next to the eruption itself, several catastrophic events can be triggered by volcanic activity. The lahars (i.e. volcanic mud flows) following the Chaitén eruption, for example, first flooded the town of Chaitén to finally nearly completely destroy it (Siebert and Simkin, 2012-).

Along subduction zones, these three types of potentially catastrophic events (i.e. megathrust earthquakes, shallow crustal earthquakes and volcanic eruptions) occur in the same area and are genetically linked. The subduction process does not only directly produce the megathrust earthquakes, but can also influence the stress regime within the continental (overriding) plate, resulting in the (re)activation of continental faults and potentially causing local but shallow earthquakes. Moreover, the subduction process induces volcanism in the overriding plate. On a shorter time scale, the separate events can even influence one another. For example, in South-Central Chile, the Puyehue-Cordón Caulle volcanic complex started an eruption only 2 days after the M_w 9.5 1960 Great Chilean earthquake (the largest earthquake on record; Wright and Mella, 1963; USGS, 2012), and it has been suggested that also the eruption in 2011 was facilitated by the 2010 Maule earthquake (Costa et al., 2011). Also, the 2007 M_w 6.2 Aysén earthquake was a tectonic earthquake and a major event in a fluid-driven seismic swarm lasting several months (Legrand et al., 2011).

* All dates in this dissertation will be given in AD.

1.2 The necessity of geological records

The magnitude, frequency and regularity of these natural events depend on many factors such as the rate of stress build-up at the plate interface, segmentation and roughness of the plate interface of the rupture for earthquakes. For volcanic eruptions, the pressure build-up in the magma chamber, the composition of the magma and the type of conduit system are important. Assessing the past behavior of faults or volcanoes can lead us towards understanding their current and future behavior and the hazard they represent. Hence, there is a strong need to study the recurrence pattern and magnitudes of past events.

In many regions of the world, such as South-Central Chile (the study area of this thesis; Fig. 1.1), however, historical records are not long enough and barely cover one or two cycles of some of these events. The first Spanish colonists, led by Pedro de Valdivia, only started settling in Chile in 1540. The town of Villarrica (the main town in the study area of Chapter 3) was founded just 120 years ago, in 1882 (Petit-Breuilh, 2004). Puerto Aysén, one of the main ports in the Chilean fjordland and the only town in the study area of chapters 5 and 6, was founded as late as 1928, less than a century ago. These examples show that there is a need to study prehistoric events, which is only possible with geological records. Most of the traditional paleoseismological methods, such as trenching, can only be applied in those cases where there is a surface rupture (e.g., Audemard, 2005), while onshore landslide studies are subjected to preservation and dating problems (e.g., Jibson, 1996). Alternative methods are turbidite stratigraphy in submarine channels (e.g., Goldfinger et al., 2012) or the use of onshore tsunami deposits (e.g., Cisternas et al., 2005). Tephrostratigraphic studies typically combine several outcrops around the studied volcanoes (e.g., Stern, 2008). However, all these methods face some problems. Ocean sites are distal and cannot record the impact of the events on society. Also, low sedimentation rates complicate high-resolution dating of prehistoric deposits. With onshore studies of outcrops and trenches, preservation issues arise due to erosion, and dating is mostly based on soils above or below the deposit, which can only provide minimum and maximum ages. Lakes and fjords can offer solutions for many of these issues. Lakes and fjords are located close to, or, in, inhabited regions and can record the onshore impact of the earthquake shaking. Moreover, their records can be used to estimate local seismic intensities (e.g., Monecke et al., 2004). Also, in these environments, background sedimentation between events is a continuous process and therefore a better age model can be established, with potential annual resolution; additionally, the deposits are well preserved. Hence, lakes and fjords combine the advantages of onshore and marine studies, and potentially record both earthquakes and volcanic events, which allows comparison between the timing and possible links between events.

However, to be able to correctly interpret the geological archive of these sedimentary basins, it is crucial to learn how to *read* it. This PhD study is therefore particularly inspired by *Principles of Geology*, the famous book by Charles Lyell in which the central argument is that *"the present is the key to the past"*, meaning that we should study the deposits of processes occurring today to understand the deposits of processes that occurred in the past (Lyell, 1830). Hence, by studying the impact of recent catastrophic events, we are able to reconstruct similar events in the past. Evidently, many studies have been dedicated to this idea, however, as discussed in the following paragraphs, there was and still is some work left.

1.3 Research questions

An eruption record of a volcano can be established by tephrostratigraphic studies in the area near the volcano. However, classic tephrostratigraphic studies, such as the ones presented for southern Patagonia by Stern (2008), are, as a result of the terrestrial preservation constraints, typically limited to relatively large-scale eruptions with regionally widespread tephra-fall deposits, ignimbrites and/or voluminous lava flows. Establishing a well-dated record of relatively small-scale, but locally possibly significant eruption events remains a major challenge. Between single events, erosion and soil formation can alter terrestrial deposits, while lahars often re-use the same pathways during subsequent events, eroding older deposits (Naranjo and Moreno, 2004). In Chapter 3 we show how lake sediments can offer a solution for some of these problems. Volcanic ash layers and lahar deposits are often deposited in the catchment, but not always directly into the lake. Independent of the wind direction during the eruption, these deposits can be washed into the lake during the subsequent rainfall events; hence, the lake sediments have the potential to contain a record of all eruptions that affected the lake's catchment.

Lakes have also been proven to be excellent recorders of past earthquakes in Alpine lakes (e.g., Schnellmann et al., 2002; Beck, 2009; Strasser et al., accepted). Lacustrine mass-transport deposits (MTDs), turbidites, liquefaction structures and in-situ deformation were used to reconstruct past earthquakes. For some Swiss lakes, these deposits were linked to historically reported seismic intensities (Monecke et al., 2004), and subsequently used to estimate paleo-epicenters of these earthquakes (Strasser et al., 2006). In Chilean and Argentinian lakes, turbidites and MTDs have been used to reconstruct past earthquakes (Moernaut et al., 2007; Bertrand et al., 2008). In New Zealand, Howarth et al. (2012) also observed post-seismic turbidites originating from the fluvial remobilization of landslide debris in the catchment. However, not all lakes record earthquakes in the same way. Apart from the seismic intensities, the climate, vegetation, morphology of the catchment, the bathymetry of the lake and its tectonic setting will also influence the earthquake recording capability (ERC) of a lake or location in the lake. In Chapter 4, we compare the sedimentary imprint of the iconic 1960 Great Chilean earthquake and the recent 2010 Maule earthquake in 19 lakes in different settings to assess the importance of these issues. However, MTDs and turbidites (or in a broader sense density-flow deposits; Mulder and Alexander, 2001) can also occur spontaneously (Girardclos et al., 2007), and a key challenge is to prove a seismic trigger for these deposits in order to be able to attribute them with certainty to seismic activity. This issue is a central theme in this dissertation and is addressed in all research chapters. The main criterion that is used to deduce earthquake triggering of turbidites in submarine channels, is the simultaneous triggering of several turbidity flows in different channels, forming amalgamated turbidites at their confluence (Goldfinger et al. 2012). Mainly in Chapter 6, but also in Chapter 4, we use the same principle in fjords and lakes. In lacustrine paleoseismology, the differentiation between seismically and flood-triggered turbidites is an ever-returning problem (Beck, 2009). Moreover, mud flows, which can be triggered both by floods and earthquakes, can also result in the deposition of a turbidite. Lahars, on the other hand, represent a specific type of mud flow triggered by volcanic activity. These matters will be explained in greater detail in chapters 3 and 4.

Also other onshore events can potentially leave traces in the sedimentary record of lakes or fjords. During the 1960 earthquake, onshore landslides surged directly into several lakes, causing lake tsunamis and seiches (Weishet, 1963; Wright and Mella, 1963). In 2007, an M_w 6.2 shallow (<9 km)

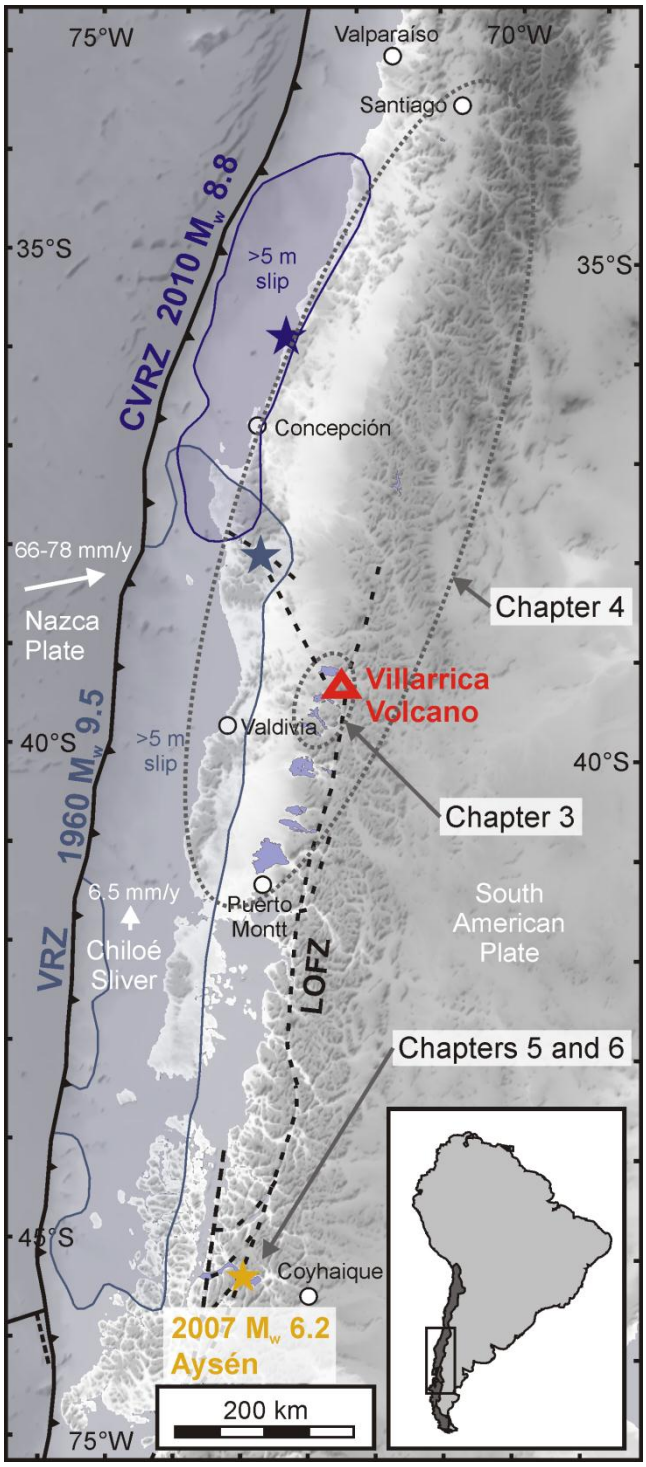

Fig. 1.1 *Overview of the study areas in South-Central Chile, with indication of different tectonic plates, the subduction zone, intercontinental fault zones and studied earthquakes. In Chapter 3, the historical eruption record of Villarrica Volcano (red) and other nearby volcanoes is improved by studying event deposits in three lakes at the latitude of Valdivia. In Chapter 4, the sedimentary imprint of the 1960 Great Chilean (gray-blue) and 2010 Maule (purple) earthquakes is studied in 19 lakes between Santiago in the north and Puerto Montt in the south. In chapters 5 and 6, the impact of the 2007 Aysén earthquake on Aysén fjord (yellow) is studied in high detail. Relative motion of the Nazca Plate (DeMets et al., 1994; Angermann et al., 1999) and the Chiloé Sliver from (Wang et al., 2004), and coseismic slip area (>5 m) for the 1960 and 2010 events (Moreno et al., 2009; 2012) are indicated. CVRZ: Concepción-Valparaíso Rupture Zone; VRZ: Valdivia Rupture Zone; LOFZ: Liquiñe-Ofqui Fault Zone (dashed line); LF: Lanalhue Fault (dashed line).*

earthquake occurred below Aysén fjord, and triggered many subaerial landslides, some of which propagated into the fjord and caused several destructive tsunamis or impact waves (Sepúlveda and Serey, 2009). The scars of the 2007 landslides are still clear at first view when sailing through the fjord today (or when looking at the fjord from Google Earth). However, the temperate rainy climate of this region in Chile causes the vegetation to grow and evolve rapidly, and in a full-grown forest will have covered the landslide scars in only a few decades from now. Consequently, it is hard to find the scars or deposits of similar prehistoric events, let alone to date them. The sedimentary imprint that these landslides leave in lakes and fjords can thus be used to detect older, similar events. In chapters 4, 5 and 6 the offshore deposits of these onshore events are characterized.

1.4 Dissertation outline

In this PhD study, the sedimentary deposits of well-documented, natural, catastrophic events are fingerprinted in lakes and in a fjord. After giving a general introduction in Chapter 1, the methods that are used in this study are presented in Chapter 2. Chapters 3 and 4 of this dissertation focus on imprints of historic megathrust earthquakes and volcanic activity on lacustrine sediments in South-Central Chile. In chapters 5 and 6 of this dissertation a specific case study of the 2007 event in Aysén fjord is discussed. Chapter 7 is the final chapter of this dissertation and provides the main conclusions and an outlook.

In Chapter 2, the methods that have been used in the different research papers are described in more detail.

In Chapter 3, the different imprints that a volcanic eruption can have in lake sediments are characterized based on an excellent correlation of historical records with a varved sedimentary record. Micro-X-ray fluorescence (µXRF) mapping is used in combination with more standard sedimentological methods to characterize the different event deposits. Four different types of event deposit (lacustrine turbidites, tephra-fall layers, runoff cryptotephras and lahar deposits) are detected and characterized; and the eruption record of the nearby volcanoes (i.e. Villarrica, El Mocho; Fig. 1.1) is revised, which is unprecedented in its continuity and temporal resolution. Chapter 3 is a modified version of a manuscript submitted for publication in "*GSA Bulletin*" (Van Daele et al., submitted b).

In Chapter 4, mainly short sediment cores are studied to compare the sedimentary imprint of the 1960 Great Chilean and the 2010 Maule earthquakes in a total of 19 lakes in different settings (Fig. 1.1), with the reports of phenomena that occurred around the lakes at the time of the earthquakes, the type of lake, its setting and the local seismic intensity. Five types of seismites which are encountered in the studied lakes are defined and a catalog of lake characteristics and their potential to record certain earthquakes is provided. All the lakes on the rupture zone with a high potential of recording earthquake shaking, did indeed record that earthquake. The only exceptions are coastal lakes that lie on the edge of the two rupture zones and record co-seismic uplift rather than seismic shaking. A modified version of Chapter 4 will be submitted for publication in "*Sedimentology*".

In Chapter 5, the imprint in the Aysén fjord sedimentary infill of the onshore landslides that were triggered by the 2007 Aysén earthquake (Fig. 1.1) is characterized by multibeam bathymetry and seismic-reflection profiling. The weight and impact of the mass-flows originating from the onshore landslides induced basin-wide basin-plain deformation. Based on the reflection seismics, it is concluded that three to four similar events have struck the fjord during the Holocene. Chapter 5 is a modified version of a manuscript submitted for publication in "*Marine Geology*" (Van Daele et al., accepted).

In Chapter 6, grain-size analysis and X-ray computed tomography (CT) scanning are combined in order to unravel the amalgamated density-flow deposits originating from the 2007 mass flows discussed in Chapter 5 (Fig 1.1). Orientations of sedimentary structures are used to determine paleoflow directions and thereby source areas (landslides) are successfully attributed to individual sub-deposits. The main conclusion is that X-ray CT-scans provide crucial information for reconstructing paleoflows and can therefore be a very powerful new tool in marine and lacustrine

sedimentology and paleoseismology. Chapter 6 is a modified version of a manuscript submitted for publication in "*Sedimentology*" (Van Daele et al., submitted a).

In Chapter 7, the general conclusions of this dissertation are presented and suggestions for future work are proposed.

References

Angermann, D., Klotz, J. and Reigber, C. (1999) Space-geodetic estimation of the nazca-south america euler vector. *Earth and Planetary Science Letters*, **171,** 329-334.

Audemard, F.A. (2005) Paleoseismology in Venezuela: Objectives, methods, applications, limitations and perspectives. *Tectonophysics*, **408**, 29-61.

Beck, C. (2009) "Late Quaternary lacustrine paleo-seismic archives in north-western Alps: Examples of earthquake-origin assessment of sedimentary disturbances". *Earth-Science Reviews*, **96**, 327-344.

Bertrand, S., Charlet, F., Chapron, E., Fagel, N. and De Batist, M. (2008) Reconstruction of the Holocene seismotectonic activity of the Southern Andes from seismites recorded in Lago Icalma, Chile, 39°S. *Palaeogeography, Palaeoclimatology, Palaeoecology*, **259**, 301-322.

Chapron, E., Ariztegui, D., Mulsow, S., Villarosa, G., Pino, M., Outes, V., Juvignié, E. and Crivelli, E. (2006) Impact of the 1960 major subduction earthquake in Northern Patagonia (Chile, Argentina). Quaternary International, **158**, 58-71.

Cisternas, M., Atwater, B.F., Torrejon, F., Sawai, Y., Machuca, G., Lagos, M., Eipert, A., Youlton, C., Salgado, I., Kamataki, T., Shishikura, M., Rajendran, C.P., Malik, J.K., Rizal, Y. and Husni, M. (2005) Predecessors of the giant 1960 Chile earthquake. Nature, 437, 404-407.

Costa, F., Lara, L.E. and Singer, B.S. 2011. Possible tectonic control on the origin and pre-eruptive conditions of the Cordon Caulle (Chile) 1921, 1960, and 2011 silicic eruptions. In: 2011 Fall Meeting, AGU, San Francisco, California.

DeMets, C., Gordon, R.G., Argus, D.F. and Stein, S. (1994) Effect of recent revisions to the geomagnetic reversal time scale on estimates of current plate motions. *Geophysical Research Letters*, **21,** 2191-2194.

Girardclos, S., Schmidt, O.T., Sturm, M., Ariztegui, D., Pugin, A. and Anselmetti, F.S. (2007) The 1996 AD delta collapse and large turbidite in Lake Brienz. *Marine Geology*, **241**, 137-154.

Goldfinger, C., Nelson, C.H., Morey, A.E., Johnson, J.E., Patton, J.R., Karabanov, E., Gutiérrez-Pastor, J., Eriksson, A.T., Gràcia, E., Dunhill, G., Enkin, R.J., Dallimore, A. and Vallier, T. (2012) Turbidite event history—Methods and implications for Holocene paleoseismicity of the Cascadia subduction zone. U.S. Geological Survey Professional Paper 1661–F170.

Howarth, J.D., Fitzsimons, S.J., Norris, R.J. and Jacobsen, G.E. (2012) Lake sediments record cycles of sediment flux driven by large earthquakes on the Alpine fault, New Zealand. Geology.

Jibson, R.W. (1996) Use of landslides for paleoseismic analysis. *Engineering Geology*, **43**, 291-323.

Legrand, D., Barrientos, S., Bataille, K., Cembrano, J. and Pavez, A. (2011) The fluid-driven tectonic swarm of Aysen Fjord, Chile (2007) associated with two earthquakes (Mw=6.1 and Mw=6.2) within the Liquiñe-Ofqui Fault Zone. Continental Shelf Research, **31**, 154-161.

Lyell, C. (1830) Principles of Geology, being an attempt to explain the former changes of the Earth's surface, by reference to causes now in operation, **1**. The Geological Society of London, London, 512 pp.

Monecke, K., Anselmetti, F.S., Becker, A., Sturm, M. and Giardini, D. (2004) The record of historic earthquakes in lake sediments of Central Switzerland. Tectonophysics, **394**, 21-40.

Moreno, M.S., Bolte, J., Klotz, J. and Melnick, D. (2009) Impact of megathrust geometry on inversion of coseismic slip from geodetic data: Application to the 1960 Chile earthquake. *Geophysical Research Letters*, **36**, 5.

Moreno, M., Melnick, D., Rosenau, M., Baez, J., Klotz, J., Oncken, O., Tassara, A., Chen, J., Bataille, K., Bevis, M., Socquet, A., Bolte, J., Vigny, C., Brooks, B., Ryder, I., Grund, V., Smalley, B., Carrizo, D., Bartsch, M. and Hase, H. (2012) Toward understanding tectonic control on the Mw 8.8 2010 Maule Chile earthquake. *Earth and Planetary Science Letters*, **321-322,** 152-165.

Mulder, T. and Alexander, J. (2001) The physical character of subaqueous sedimentary density flows and their deposits. *Sedimentology*, **48**, 269-299.

Naranjo, J.A. and Moreno, H. (2004) Laharic debris-flows from Villarrica Volcano. In: Villarrica Volcano (39.5°S), Southern Andes, Chile (Eds L.E. Lara and J. Clavero), **61**, pp. 28-38. Servicio Nacional de Geología y Minería.

Petit-Breuilh, M.E. (2004) La Historia Eruptiva De Los Volcanes Hispanoamericanos (Siglos XVI Al XX): El Modelo Chileno. Casa de los Volcanes. Servicio de publicaciones exmo. cabildo insular de Lanzarote, 435 pp.

Siebert, L. and Simkin, T. (2012-) Volcanoes of the World: an Illustrated Catalog of Holocene Volcanoes and their Eruptions. Smithsonian Institution, Global Volcanism Program Digital Information Series, GVP-3 (http://www.volcano.si.edu/world/).

Schnellmann, M., Anselmetti, F.S., Giardini, D., McKenzie, J.A. and Ward, S.N. (2002) Prehistoric earthquake history revealed by lacustrine slump deposits. *Geology*, **30**, 1131-1134.

Sepulveda, S.A. and Serey, A. (2009) Tsunamigenic, earthquake-triggered rock slope failures during the April 21, 2007 Aisen earthquake, southern Chile (45.5 degrees S). *Andean Geology*, **36**, 131-136.

Stern, C. (2008) Holocene tephrochronology record of large explosive eruptions in the southernmost Patagonian Andes. *Bulletin of Volcanology*, **70**, 435-454.

Strasser, M., Anselmetti, F.S., Fah, D., Giardini, D. and Schnellmann, M. (2006) Magnitudes and source areas of large prehistoric northern Alpine earthquakes revealed by slope failures in lakes. *Geology*, **34**, 1005-1008.

Strasser, M., Monecke, K., Schnellmann, M. and Anselmetti, F.S. (Accepted) Lake sediments as natural seismographs: A compiled record of Late Quaternary earthquakes in Central Switzerland and

its implication for Alpine deformation. *Sedimentology*.

USGS (Unites States Geological Survey) (2012) *Earthquake Hazards Program – Significant earthquake archive,* (http://earthquake.usgs.gov/earthquakes/world/events/1960_05_22.php, last consulted in November 2012).

Van Daele, M., Cnudde, V., Duyck, P., Pino, M., Urrutia, R. and De Batist, M. (submitted a) Multidirectional, amalgamated density-flow deposits revealed by X-ray computed tomography (CT) *Sedimentology*.

Van Daele, M., Moernaut, J., Silversmit, G., Schmidt, S., Fontijn, K., Heirman, K., Vandoorne, W., De Clercq, M., Van Acker, J., Wolff, C., Pino, M., Urrutia, R., Roberts, S.J., Vincze, L. and De Batist, M. (submitted b) Multi-proxy analysis of annually laminated sediments from three neighboring lakes in South-Central Chile : a continuous record of regional volcanic activity for the past 600 years. *Bulletin of the Geological Society of America*.

Van Daele, M., Versteeg, W., Pino, M., Urrutia, R. and De Batist, M. (accepted) Widespread deformation of basin-plain sediments in Aysén fjord (Chile) due to impact by earthquake-triggered, onshore-generated landslides. *Marine Geology*.

Wang, K., Hu, Y., Bevis, M., Kendrick, E., Smalley, R. and Lauria, E. (2007) Crustal motion in the zone of the 1960 Chile earthquake: Detangling earthquake-cycle deformation and forearc-sliver translation. *Geochemistry Geophysics Geosystems*, **8,** 14.

Watt, S.F.L., Pyle, D.M., Naranjo, J.A., Rosqvist, G., Mella, M., Mather, T.A. and Moreno, H. (2011) Holocene tephrochronology of the Hualaihue region (Andean southern volcanic zone, ~42° S), southern Chile. *Quaternary International*, **246**, 324-343.

Weishet, W. (1963) Further observations of geologic and geomorphic changes resulting from the catastrophic earthquake of May 1960, in Chile. *Bulletin of the Seismological Society of America*, **53**, 1237-1257.

Wright, C. and Mella, A. (1963) Modifications to the soil pattern of South-Central Chile resulting from seismic and associated phenomenona during the period May to August 1960. *Bulletin of the Seismological Society of America*, **53**, 1367-1402.

“Hay una zona donde este lago no tiene fondo”

“There is an area where this lake doesn’t have a bottom”

Local inhabitant of Frutillar (Lake LLanquihue), recalling that when the SHOA (Servicio Hidrográfico y Oceanográfico de la Armada de Chile) was making the lake bathymetry, from a certain area in the lake, the sounder didn’t receive an echo, indicating the lake doesn’t have a bottom there.

The legend of the lake without bottom is common for many lakes.

Chapter 2

Methodology

Although each research chapter (chapters 3-6) has its own separate method section, this chapter provides more detailed information on some of the methods used throughout this PhD thesis.

2.1 Multibeam bathymetry

Multibeam echosounders are powerful tools used to establish a detailed bathymetry relatively quickly. A multibeam system can measure the depth of the sea- or lake floor along a band perpendicular to the cruising direction. This is achieved by transmitting a fan of multiple acoustic pulses from a transducer and measuring the arrival time of the acoustic pulses (reflected from the sea- or lake floor) in specific directions. If the motion of the vessel is tracked and the sound velocity is known throughout the water column, the two-way-travel time of a returning beam can be used to determine the water depth at a certain location.

To map the bathymetry in Aysén fjord (chapters 5 and 6), an ELAC SeaBeam 1050 multibeam sonar was used. The two 50 kHz transducer arrays were installed on a pole at the bow of *RV Don Este*, and operated with 120° swath, transmitting and receiving 108 beams of 3° by 3° beam angle. In order to correct for roll, pitch and heave, an IXSEA Octans motion sensor was installed right above the transducers; to minimize errors, positioning was done using a SIMRAD GPS. The sound-velocity profile was made using the pressure, temperature and salinity data from an IDROMAR IP039D CTD. Continuous CTD measurements at the surface were made with a Valeport CTD.

The data was first cleaned with HDPedit and tide information was added in HDPpost. From the ASCII XYZ data a PFM was created in the IVS 3D DMagic software to perform final data cleaning using the IVS 3D Fledermaus™ software. The cleaned data was subsequently gridded by the IVS 3D AvGrid software at different resolutions ranging from 4 m for the shallow areas to 20 m for the deeper areas. Depth-dependent grids were then merged in the Global Mapper software and finally regridded at 4 m resolution by the IVS 3D AvGrid software. Interpretation of the data was performed using the IVS 3D Fledermaus™ software.

2.2 High-resolution seismic profiling

Seismic-reflection profiling is used to obtain a cross section of the sedimentary infill of a basin in which structures and sedimentary units are visualized. A seismic source emits an acoustic pulse that will be partly reflected when propagating into a medium with different acoustic impedance (i.e. the acoustic velocity multiplied by the density of the medium; Mitchum et al., 1977). A receiver will detect the reflected pulse and the two-way-travel time of the pulse is used to plot the data and determine the depth of a reflector (i.e. the interface that reflects the acoustic pulse). Generally, the first strong reflector is the sea or lake floor, followed by more reflectors within the sedimentary infill. The vertical resolution of the reflection seismic data depends on the wavelength of the seismic signal and corresponds to a quarter of the latter. The horizontal resolution can be calculated by dividing the survey speed by the shot rate.

In this study, two types of reflection-seismic systems are used: a high-resolution CENTIPEDE sparker (developed at RCMG) and a very-high resolution GEOPULSE subbottom profiler (pinger). The high-resolution multi-electrode CENTIPEDE sparker source (operated at 300-400 J, mean frequency: 1.3 kHz, vertical resolution: 37-75 cm) is used in combination with a high-resolution single-channel streamer (10 hydrophones and a grouplength of 2.7 m) as a receiver. The GEOPULSE transducer

(both source and receiver; frequency: 3.5 kHz; vertical resolution: 10-20 cm) is mounted on an inflatable cataraft. Data was acquired at an average survey speed of 3-4 knots. On the lakes (chapters 3 and 4), both systems were towed by the *Huala II*, a small (6 m long) research vessel from the Universidad Austral de Chile (Valdivia). In Aysén fjord (chapters 5 and 6), the sparker and streamer were towed by the *RV Don Este*. Seismic and GPS (SIMRAD) data were digitally recorded and converted to SEG-Y format with the IXSEA™ Delph Seismic Acquisition system. Interpretation of the data was done using The Kingdom Suite™ software.

2.3 Core acquisition

Short gravity cores of the upper sedimentary infill (including the sediment-water interface) of the lakes and fjord are the base of most of the research presented in this dissertation. Gravity cores were taken by controlled fall from the zodiac *Percilia* (EULA, Universidad de Concepción) or the research vessel *Huala II* (Universidad Austral de Chile) in the lakes (chapters 3 and 4), and from the *RV Don Este* in Aysén fjord (chapters 5 and 6). To facilitate coring operations from the zodiac, a winch system was developed and installed centrally, perpendicular to the long axis of the zodiac (design by A. Peña). The cores were taken with a UWITEC gravity core system (BAS and Limnology Unit, Ghent University) or with a *Swiss* corer (Universidad Austral de Chile, Valdivia) holding transparent liner tubes with a diameter of 60 mm. The weight on these systems is concentrated at the top of the liner tube. To achieve vertical fall and penetration in the sediments, an additional, cylindrical weight was hung freely around the lower part of the tube (*El Terrible*, design by A. Peña, EULA). The maximum length of the retrieved cores is around 130 cm.

2.4 Core analysis

All sedimentological analyses were done on short sediment cores that, after acquisition and packing, were shipped to Belgium. Cores were opened in the core-opening lab at Ghent University (Hydrogeology Unit), cleaned, described and photographed. For some cores, this was followed by more analyses described in this section.

2.4.1 Image acquisition

To make pictures with homogenous illumination, an adjustable photo set-up was designed during this PhD. This comprised a 120 x 50 x 60 cm box with powdered glass walls in the long direction, black wooden walls with 25 x 12 cm openings (to slide the core through) on each end, and a roof of which the height can be adjusted (>60 cm) with a cylindrical opening in the center (above which the camera is installed; diameter: 15 cm). On each side, two 1.5 m long, white-light emitting fluorescent tubes were installed behind the powdered glass, resulting in scattered white light inside the set-up. The gap between the upper side of the walls and the roof was closed with black opaque fabric. This set-up results in >99% homogenous illumination in the central 20 cm (along axis) of the set-up. The height of the roof was adjusted (60 + 30 cm) in order to image about 30 cm of core using the highest zoom of the used camera lens. Pictures were taken at 15 cm intervals with fixed diaphragm and exposure time, and the central 15 cm of the pictures were stitched using the Corel PHOTO-PAINT software.

2.4.2 Image analysis

Color of the composite core pictures was analyzed in the L*a*b* color space along a band of approximately 1 mm wide using the Strati-Signal Software (Ndiaye, 2007). L* stands for lightness and ranges from 0 (black) to 100 (white). Both a*- and b*-values range from negative (green and blue, respectively) to positive (red and yellow, respectively) (Nederbragt and Thurow, 2004).

Histogram equalization was applied on the original pictures using the Corel PHOTO-PAINT software. When applying this processing method, the histogram of each color channel (Red, Green and Blue) is re-distributed over each entire spectrum, thereby equally distributing the histogram over the respective spectrum. This processing method produces unnatural colors, but is very effective in optimizing the contrast within the image. Composite core pictures in this thesis that are referred to as being processed, are processed using this method.

2.4.3 Impregnation

Some cores were impregnated to subsequently prepare thin sections. Cores VILLSC01, CAGC02bis and RINGC03 were impregnated at RCMG (Ghent University), while RINGC04 was impregnated at GFZ Potsdam, following a slightly different protocol (Wolff et al., 2011). At GFZ Potsdam, 26-cm-long, 34-mm-wide and 10-mm-thick U-channels were taken. From these U-channels 3 subsamples (100 x 17 x 10 mm) with a 20 mm overlap were extracted and shock frozen with liquid nitrogen followed by freeze-drying for 48 hours and impregnation with Araldite resin. At RCMG, a new protocol combining the methods of GFZ Potsdam and of Boës and Fagel (2005) was used. A 28 mm wide and 11-mm-thick U-channel spanning the entire core length was taken. The sediment in the U-channel was cut in 100-mm-long sediment slabs with an overlap of 10 mm. Each sample was shock frozen with liquid nitrogen, followed by freeze-drying for 48 hours and slow (approximately 6 hours) impregnation under low vacuum with a mixture of TRA resin, MEKP (catalyst) and cobalt octoate (accelerator), diluted with acetone. One thin section was made for microscopic analysis from the impregnated sediment, while the remainder of the sediment block was polished.

Thin sections and sediment blocks were used for lamination counting, microfacies analysis and µXRF scanning. Lamination-thickness measurements were performed on both the thin sections and on the sediment blocks.

2.4.4 High-resolution magnetic-susceptibility (MS)

The magnetic susceptibility (MS) is the degree to which a material can be magnetized in response to an external magnetic field. Changes in MS are due to variations in the concentration and/or the composition of the magnetic minerals and their grain size (e.g., Zolitschka et al., 2001). Along-core MS was measured with a Bartington MSE2 surface sensor (Royal Observatory of Belgium and Department of Soil Management, UGent) on split-core surfaces. The along-core resolution of this sensor is 3.5 mm, and the step size during the measurements was 2.5 mm, causing a 1 mm overlap between successive measurements.

2.4.5 Grain-size analysis

Grain-size measurements were performed with a Malvern Mastersizer 2000 (Marine Biology Research group, UGent), theoretically detecting a size range from 0.02 to 2000 µm. To reach the

optimal laser obscuration of 10-20 %, samples had a variable volume and sampling intervals ranged from 1 to 5 mm. Fresh-sediment samples were measured during 15 s after 60 s of 10 % sonification. This was the strongest sonification that could be used without changing the grain-size mode. A longer and/or intenser sonification resulted in a shift of the mode towards lower values, indicating that diatom frustules started to shatter. Grain-size distribution parameters were calculated according to Folk and Ward (1957) using the GRADISTAT software (Blott and Pye, 2001). Grain-size distribution maps were gridded using the Golden Software Surfer software.

2.4.6 Loss-on-ignition (LOI)

Organic-matter (OM) content was determined by loss-on-ignition (LOI) at 550°C in a muffle furnace (4 hours) after drying during 24 hours at 105°C (Heiri et al., 2001). As the sample weight can influence the results, always approximately 1 gram of dried sediment was used.

2.4.7 X-ray diffraction (XRD)

X-ray diffraction (XRD) is a method that is commonly used to determine the (crystalline) mineral content of a sample. The method is based on Bragg's law, which relates the wavelength of electromagnetic radiation to the diffraction angle and the lattice spacing in a crystalline sample. After freeze-drying and manually crushing bulk samples, bulk mineralogy was determined by N. Fagel using a Bruker D8-Advance diffractometer with CuKα radiations (Université de Liège). XRD was performed on selected samples to get a better idea of the general mineralogy of the sediments.

2.4.8 Scanning electron microscope (SEM), energy dispersive spectrometer (EDS) and electron microprobe

A scanning electron microscope (SEM) creates an image of a sample by sending a focused electron beam on the sample. The interaction of this beam with the sample results in the reflection and emission of electrons and the emission of electromagnetic radiation, which are all detected by the SEM. Moreover, X-ray signals are emitted by the sample and these can be measured by the energy dispersive spectrometer (EDS). The energy of these X-rays is dependent on the atomic structure of the specimen and therefore EDS can be used to obtain the elemental composition of materials. The functioning of an electron microprobe is based on the same principle, but includes apart from an EDS, also wavelength dispersive spectrometers (WDS), which measure the wavelength of the emitted X-rays, and are more precise.

To characterize and image the composition of specific laminae, freeze-dried bulk samples were mounted on a JEOL aluminum stub with self-adhesive surface and subsequently coated with gold. Samples were imaged with a JEOL 6400 SEM (Department of Geology and Soil Science, UGent) with accelerating voltage of 12 kV.

On a selection of tephra layers, glass major element geochemistry was determined on polished grain mounts by electron microprobe analysis (JEOL JXA-8600 Superprobe) by K. Fontyn at the Research Laboratory for Archaeology and the History of Art, University of Oxford. Calibration was performed using natural mineral standards and accuracy was monitored using natural glass standards. Analyses were performed using 15 kV accelerating voltage, 6 nA beam current and 10 µm beam width. In addition to glass chemistry, mineral compositions were determined semi-quantitatively by SEM-EDS

(JEOL JSM-840A) at the Department of Earth Sciences, University of Oxford (K. Fontyn).

2.4.9 X-ray fluorescence (XRF)

X-ray fluorescence (XRF) is the emission of characteristic "*fluorescent*" X-rays from a material after being bombarded (and excited) with high-energy X-rays. XRF is used to determine the elemental composition of a material. It is a semi-quantitative method, meaning that elemental counts represent relative variations in concentration, but are not directly convertible to absolute elemental concentrations. In order to eliminate density effects in a first-order approximation, ratios between two elemental counts can be used (Weltje and Tjallingii, 2008).

XRF core scanning

The Avaatech XRF core-scanner performs XRF measurements on a line along the long axis of a split sediment core. Its Rh X-ray tube and detector are physically moved to the sediment surface for every consecutive measurement and along-core resolution is determined by a slit (e.g., Richter et al., 2006). Measurements were performed at 2 and 5 mm resolution and measured at 10 and 30 kV (elements Al to Fe and Fe to Bi, respectively) at MARUM Institute in Bremen.

µXRF mapping

Micron-scale elemental studies on the sediment blocks were performed by acquiring µXRF spectra with an EDAX EAGLE-III µ-probe (X-ray Micorspectroscopy and Imaging Group; XMI, UGent), equipped with a Rh X-ray tube, using a glass polycapillary for X-ray focusing. Source voltage and current were 40 kV and 140 µA respectively, and the measuring time was 11 s/pixel (live time). A small 2D map consisting of five 100-µm-spaced scan lines were measured and averaged out. One scan line consisted of successive 100-µm-spaced pixels using a µ-beam with about the same radius. Subsequently, data of the successive sediment blocks was combined to create a composite µXRF data set for each core.

2.4.10 X-ray computed tomography (CT)

X-ray computed tomography (CT) can be used to investigate the external and internal structure of objects in a three-dimensional space (Kak and Slaney, 1988). The studied object is placed in between an X-ray source and detector, and rotated relatively to the latter two. An additional translational movement (together with the rotation resulting in a spiral) allows scanning elongated objects. Digital radiographs are taken at different rotation angles and afterwards cross-sections (or slices) through the object are calculated (Cnudde et al., 2006). This technique allows discriminating between sediment volumes with a different X-ray attenuation, which is a function of the material composition (effective atomic number) and density (Cnudde et al., 2004).

Split sediment cores were scanned using a Siemens, SOMATOM Definition Flash medical X-ray CT scanner (Ghent University Hospital). The scanner has been employed at 100 kV, with an effective mAs of 100 and a pitch of 0.55. The reconstructed images have a voxel size of 0.5 mm and a down-core step size of 0.3 mm. It is therefore possible to distinguish individual particles and aggregates of very coarse sand and gravel size. The data was visualized and analyzed with the VGStudio Max 2.0 software.

2.4.11 Varve counting

Varves are annual laminations in sediments and can –when proven to be indeed annual– be used as a dating method (De Geer, 1912; Zolitschka, 2007). The counting and measuring was carried out with an Olympus SZX12 stereomicroscope in combination with a RINNTECH LINTAB dynamic positioning "measuring" table and the associated TSAPWin software (developed for tree-ring analysis; Department of Forest and Water Management, UGent). Each section was counted (and measured) three times to improve measurement reliability, after which the intermediate curve was retained. Overlapping parts of the sections were wiggle-matched to construct a continuous varve chronology.

2.4.12 Radionuclide dating

Radionuclide dating is based on the gradual decay of fallout ^{210}Pb (half-life = 22.3 years) and the peaking ^{137}Cs (half-life = 30 years) fallout succeeding weapon tests and nuclear accidents in the second part of the 20th century. This dating method allows dating sediments deposited during the last ~150 years. Radionuclide dating was performed by S. Schmidt (Environnements et Paléoenvironnements Océaniques, Université de Bordeaux) and ages were calculated using excess activity of ^{210}Pb ($^{210}Pb_{xs}$), which is incorporated rapidly into the sediment from atmospheric fall-out and water-column scavenging. Excess ^{210}Pb was calculated by subtracting the activity supported by its parent isotope, ^{226}Ra, from the total ^{210}Pb activity in the sediment. Errors in $^{210}Pb_{xs}$ were calculated by propagation of errors in the corresponding pair (^{210}Pb and ^{226}Ra). The sedimentation rate was calculated from $^{210}Pb_{xs}$ profiles using the constant initial concentration model (CIC) model (Robbins and Eglington, 1975):

$$t = \frac{1}{\lambda} ln\left(\frac{A_0}{A}\right)$$

where t is the age (in years) of the considered layer, A_0 and A are the activities of excess ^{210}Pb at surface and depth z, and λ is the decay constant of ^{210}Pb (0.0311 an^{-1}).

To corroborate the ^{210}Pb data, we used also ^{137}Cs, an artificial radionuclide of well-known pulse inputs (maximum nuclear weapon test fall-out in 1965 in the Southern Hemisphere; Arnaud et al., 2006). ^{210}Pb, ^{226}Ra and ^{137}Cs were measured using a low-background, high-efficiency, well-shaped γ-detector (CANBERRA; Schmidt et al, 2009). Calibration of the γ-detector was achieved using certified reference materials (IAEA-RGU-1; SOIL-6). Activities are expressed in mBq.g^{-1} and errors are based on 1 standard-deviation counting statistics. For the construction of the radionuclide-dated age-depth model, all EDs were removed following the procedure described by von Gunten et al. (2009).

References

Arnaud, F., Magand, O., Chapron, E., Bertrand, S., Boes, X., Charlet, F. and Melieres, M. (2006) Radionuclide dating ((210)Pb, (137)Cs, (241)Am) of recent lake sediments in a highly active geodynamic setting (Lakes Puyehue and Icalma-Chilean Lake District). *Sci Total Environ*, **366,** 837-850.

Blott, S.J. and Pye, K. (2001) GRADISTAT: A grain size distribution and statistics package for the analysis of unconsolidated sediments. *Earth Surface Processes and Landforms*, **26,** 1237-1248.

Boës, X. and Fagel, N. (2005) Impregnation method for detecting annual laminations in sediment

cores: An overview. *Sedimentary Geology*, 179, 185-194.

Cnudde, V., Cnudde, J.P., Dupuis, C., Jacobs and P.J.S. (2004) X-ray micro tomography used for the localisation of water repellents & consolidants inside natural building stones. *Materials Characterization,* **53,** 259-271.

Cnudde, V., Masschaele, B., Dierick, M., Vlassenbroeck, J., Van Hoorebeke, L. and Jacobs, P. (2006) Recent progress in X-ray CT as a Geosciences Tool. *Applied Geochemistry,* **21,** 826-832.

De Geer, G. (1912) A geochronology of the last 12,000 years. In: *International Geological Congress 2010***,** pp. 241-257, Stockholm, Sweden.

Folk, R.L. and Ward, W.C. (1957) Brazos River bar: a study in the significance of grain size parameters. *Journal of Sedimentary Petrology*, **27,** 3-26.

Heiri, O., Lotter, A.F. and Lemcke, G. (2001) Loss on ignition as a method for estimating organic and carbonate content in sediments: reproducibility and comparability of results. *Journal of Paleolimnology*, **25,** 101-110.

Kak, A.C. and Slaney, M. (1988) *Principles of computerized tomographic imaging*. IEEE press, New York, 344 pp.

Mitchum, R.M., Vail, P.R. and Sangree, J.B. (1977) Seismic Stratigraphy and Global Changes of Sea Level, Part 6: Stratigraphic Interpretation of Seismic Reflection Patterns in Depositional Sequences. Seismic Stratigraphy-Applications to Hydrocarbon Exploration. *American Association of Petroleum Geologists Memoir*, **26,** 117-133.

Ndiaye, M. (2007) *A multipurpose software for stratigraphic signal analysis*, Université de Genève, Genève, 118 pp.

Nederbragt, A.J. and Thurow, J.W. (2004) Digital sediment colour analysis as a method to obtain high resolution climate proxy records. In: *Image analysis, sediments and paleoenvironments* (Ed P. Francus), pp. 105-124. Kluwer Academic Publishers, Dordrecht, The Netherlands.

Richter, T.O., Van Der Gaast, S., Koster, B., Vaars, A., Gieles, R., De Stigter, H.C., De Haas, H. and Van Weering, R.C.E. (2006) The Avaatech XRF Core Scanner: technical description and applications to NE Atlantic sediments. In: *New Techniques in Sediment Core Analysis* (Ed R.G. Rothwell), **267,** pp. 39-50. Geological Society Special Publications, London.

Robbins, J.A. and Eglington, D.N. (1975) Determination of recent sedimentation rates in Lake Michigan using Pb-210 and Cs-137. *Geochimica and Cosmochimica Acta,* **39,** 285-304.

Schmidt S., Howa H., Mouret A., Lombard F., Anschutz P. and Labeyrie L. (2009) Particle fluxes and recent sediment accumulation on the Aquitanian margin of Bay of Biscay. *Continental Shelf Research,* **29,** 1044-1052.

von Gunten, L., Grosjean, M., Beer, J., Grob, P., Morales, A. and Urrutia, R. (2009) Age modeling of young non-varved lake sediments: methods and limits. Examples from two lakes in Central Chile. *Journal of Paleolimnology*, **42,** 401-412.

Weltje, G.J. and Tjallingii, R. (2008) Calibration of XRF core scanners for quantitative geochemical logging of sediment cores: Theory and application. *Earth and Planetary Science Letters*, **274,** 423-438.

Wolff, C., Haug, G.H., Timmermann, A., Damsté, J.S.S., Brauer, A., Sigman, D.M., Cane, M.A. and Verschuren, D. (2011) Reduced Interannual Rainfall Variability in East Africa During the Last Ice Age. *Science*, **333,** 743-747.

Zolitschka, B., Mingram, J., van der Gaast, S., Jansen, F.J.H. and Naumann, R. (2001) Sediment logging techniques. In: *Tracking Environmental Change Using Lake Sediments. Volume 1: Basin Analysis, Coring, and Chronological Techniques* (Eds W.M. Last and J.P. Smol), **1,** pp. 137-153. Kluwer Academic Publishers, Dordrecht, The Netherlands.

Zolitschka, B. (2007) Varved Lake Sediments. In: *Encyclopedia of Quaternary Science* (Ed A.E. Scott)**,** pp. 3105-3114. Elsevier, Oxford.

“Primero vino del Concepción, y después de las montañas”

“First it came from Concepción, afterwards from the mountains”

A local inhabitant living in an according-to-compass-points-oriented house, showing how his house first moved in north-south direction and afterwards in east-west direction during the 2010 earthquake. What he was actually feeling was the arrival of the P-waves and subsequently the S-waves.

Chapter 3

Multi-proxy analysis of annually laminated sediments from three neighboring lakes in South-Central Chile: a continuous record of regional volcanic activity for the past 600 years

Modified version submitted for publication as:

Van Daele, M., Moernaut, J., Silversmit, G., Schmidt, S., Fontijn, K., Heirman, K., Vandoorne, W., De Clercq, M., Van Acker, J., Wolff, C., Pino, M., Urrutia, R., Roberts, S.J., Vincze, L. and De Batist, M. Multi-proxy analysis of annually laminated sediments from three neighboring lakes in South-Central Chile: a continuous record of regional volcanic activity for the past 600 years. *Bulletin of the Geological Society of America*.

Abstract

Lake sediments contain valuable information about past volcanic and seismic events that affect the lake catchment, and provide unique records of the recurrence rate and magnitude of such events. This study uses a multi-lake and multi-proxy analytical approach to obtain reliable and high-resolution records of past natural catastrophes from c. 600 year old annually-laminated (varved) lake sediment sequences extracted from three lakes, Villarrica, Calafquén and Riñihue, in the volcanically and seismically active Chilean Lake District. Using a combination of µXRF scanning, microfacies analysis, grain-size analysis, color analysis and magnetic susceptibility, we detected and characterized four different types of event deposits (EDs) (lacustrine turbidites; tephra-fall layers; runoff cryptotephras; lahar deposits) and revised the eruption record for the nearby volcanoes (i.e. Villarrica, El Mocho), which is unprecedented in its continuity and temporal resolution. Time series analysis shows 112 eruptions with a Volcanic Explosivity Index (VEI) ≥ 2 from Villarrica Volcano in the last c. 600 years. Mocho-Choshuenco Volcano has been significantly less active since 1900 compared to preceding centuries. Also deposits of eruptions from the more remote Carrán-Los Venados Volcanic Complex, Quetrupillán and Lanín or Huanquihue volcanoes were identified in the studied lake sediments. The last VEI ≥ 2 eruption of Villarrica Volcano occurred in 1991. We estimate the probability of the occurrence of future eruptions from Villarrica Volcano, and statistically demonstrate that the probability of a 21-year repose period (anno 2012) without eruptions is ≤ 1.9 %. This new perspective on the recurrence interval of eruptions and historical lahar activity will help improve volcanic hazard assessments for this rapidly expanding tourist region.

3.1 Introduction

The unforeseen eruption of Chaitén Volcano in 2008 (Carn et al., 2009; Lara, 2009; Watt et al., 2009) and the unanticipated magnitude of the 2010 Maule earthquake (M_w 8.8) (Ruegg et al., 2009) illustrate the lack of detailed information concerning the recurrence intervals, modes and magnitudes of such catastrophic natural events in Chile. To assess these parameters, reliable records of past catastrophes (e.g., earthquakes, volcanic eruptions and floods) are of vital importance. Unfortunately, historical accounts of such events are limited in time, and often incomplete and unreliable, especially in remote regions. To make robust probability estimates of repose times and improve hazard assessments, new and better-resolved time series of past earthquakes and eruption events, and their impacts are needed.

An eruption record can be established by tephrostratigraphic studies in the area near the volcano. However, classic tephrostratigraphic studies, such as the ones presented for southern Patagonia by Stern (2008) or for the Hualaihue region by Watt et al. (2011), are, as a result of terrestrial preservation constraints, typically limited to relatively large-scale eruptions with regionally

widespread tephra-fall deposits, ignimbrites and/or voluminous lava flows. Establishing a well-dated record of relatively small-scale but locally significant eruption events, which produce less substantial tephra deposits, remains a major challenge and is often biased towards the available historical record (e.g., Dzierma and Wehrmann, 2010). Between events, erosion and soil formation can alter terrestrial deposits, while lahars often re-use the same pathways during subsequent events, eroding older deposits (Naranjo and Moreno, 2004). Therefore, a new type of dataset is required, one that can improve both the temporal and spatial resolution of the eruption record as well as incorporate smaller eruption events.

In comparison to subaerial environments, sediment deposition in lakes is relatively constant and often continuous. In Lake Puyehue, located in the Chilean Lake District, hemipelagic sediments (henceforth referred to as background sedimentation) are annually laminated (varved) between volcanic events (Boës and Fagel, 2008), providing robust age control. Furthermore, volcanic ash layers and lahar deposits (henceforth referred to as event deposits or EDs) are often deposited in the catchment, but not always directly into the lake. These EDs are usually washed into the lake during the subsequent rainfall events; hence, the lake sediments have the potential to contain a record of all eruptions that affected the lake's catchment. Records from several lakes, whose combined catchments are influenced by the entire volcano, potentially provide a complete eruption record for that particular volcano.

EDs recorded in lacustrine sediments can sometimes be subtle features, represented by only very fine laminae (100-200 µm thick), and traditional sedimentological techniques are therefore often inadequate for their identification and analysis. In contrast, µXRF scanning and geochemical mapping (Kylander et al., 2011 and references therein) have proven to be very useful in detecting and characterizing very thin EDs in impregnated sediment slabs of annually laminated sediments, thereby providing an especially powerful technique when cross-validated by independent methodologies (Katsuta et al., 2007).

In this study, we applied µXRF scanning in combination with magnetic susceptibility (MS) and color, grain-size and microfacies analysis to varve-counted sediment cores extracted from three lakes in the Chilean Lake District of South-Central Chile. We also used electron microprobe major element data on selected tephra-fall layers to support inter-lake correlations. Our aims are to: 1) detect, characterize and classify EDs; 2) determine ED formation processes; 3) establish a new, high-resolution eruptive history for Villarrica Volcano, El Mocho Volcano and other nearby volcanoes; and 4) use statistical analysis to establish a new eruption time series for Villarrica Volcano and provide estimates of the probability of future eruptions.

3.2 Regional setting

3.2.1 Site description

Lake Villarrica (214 m asl, 21 x 9 km), Lake Calafquén (204 m asl, 24 x 2-6 km) and Lake Riñihue (107 m asl, 28 x 2-4 km) are three large glacigenic lakes situated at the foot of the Chilean Andes between 39° and 40° S (Fig. 3.1). The lakes all lie in glacially overdeepened valleys dammed at their western border by large frontal moraines of late Pleistocene age (Laugenie, 1982). The present-day climate in this part of Chile is humid-temperate. Precipitation mainly occurs during austral winter, driven by the southern Westerlies (Heusser, 2003) (in Villarrica: ~1600 mm from April through September;

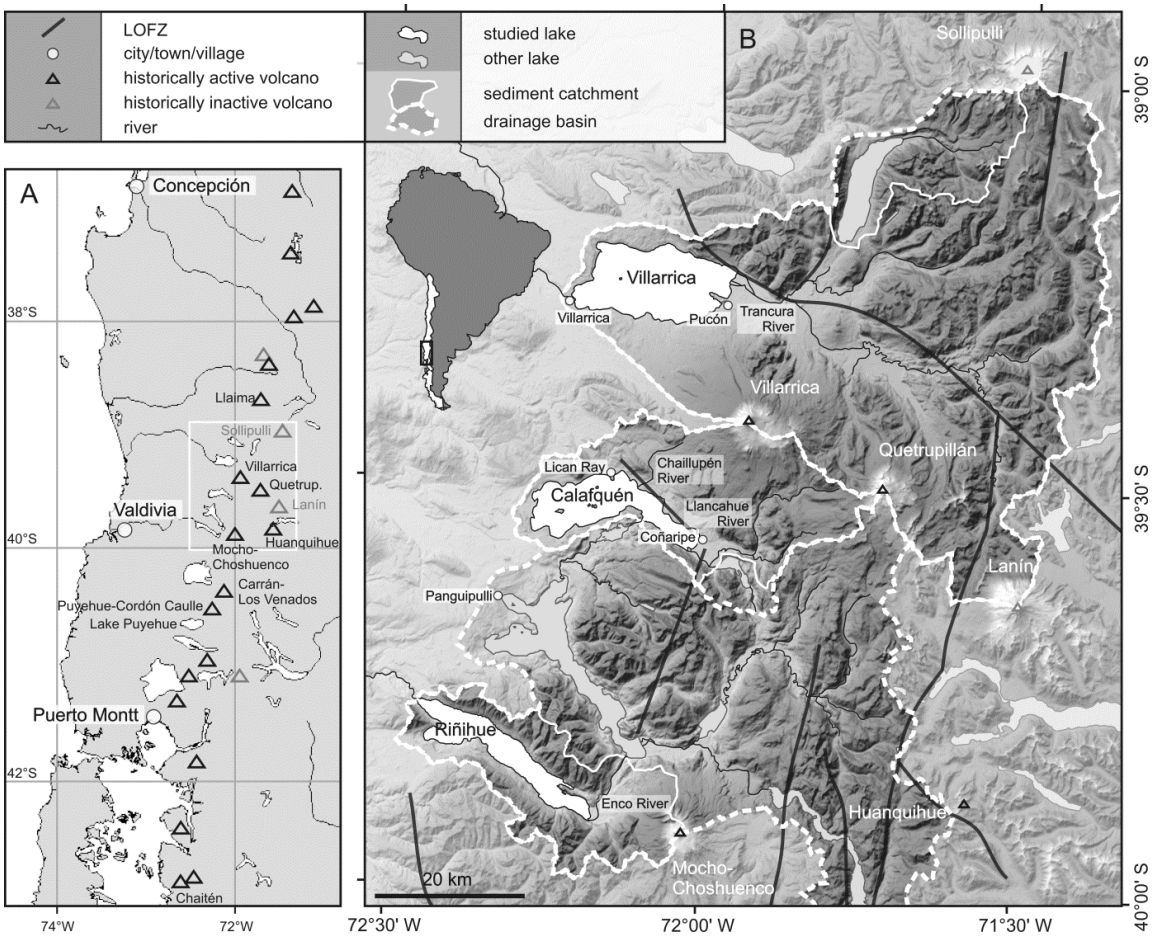

Fig. 3.1 *A) Setting of the study area in South-Central Chile. B) The three studied lakes (black font) and their drainage basins and sediment catchments are indicated. Volcanoes within the lakes catchments are indicated in white. Historically active (black triangle) and inactive (gray triangle) volcanoes in the region are indicated. Faults belonging to the Liquiñe-Ofqui Fault Zone (LOFZ) are in black lines (after Rosenau et al., 2006).*

Dirección General de Aguas, Chile, unpublished data). The perennially high amount of winter precipitation suggests that the availability of easily erodible material in the sediment catchment (i.e. the part of the drainage basin that drains directly to the lake, without other lakes functioning as sediment traps in between) is the controlling factor on sediment transport to the lakes. The soils in the study area are andosols that developed in volcanic ash. Amorphous clays (allophanes) are the product of post-depositional weathering of this ash, which mainly consists of glass and plagioclase crystals (Bertrand and Fagel, 2008).

Lake Villarrica has a large sediment catchment (2650 km²) comprising the northern slopes of Villarrica, Quetrupillán and Lanín volcanoes and the southern slopes of Sollipulli Volcano (Fig. 3.1). The Trancura River is its main tributary.

Lake Calafquén has a smaller sediment catchment (554 km²) comprising the southern slopes of Villarrica Volcano and the southwestern slopes of Quetrupillán Volcano (Fig. 3.1). The Llancahue River is its main tributary.

Lake Riñihue has the largest drainage basin (3211 km²) of the three studied lakes, but is the furthest downstream of seven inter-connected lakes, and its sediment catchment is relatively small (382 km²). Its main tributary is the Enco River. The western flank of Mocho-Choshuenco Volcano is the main source area for the detrital fraction of the sediment in this lake (Fig. 3.1; Laugenie, 1982).

3.2.2 Geology and eruptive history

Villarrica Volcano (39°25'12''S, 71°56'23''W, 2847 m asl; Fig. 3.1) is a composite Pleistocene-Holocene stratovolcano comprised of a late Pleistocene caldera with an internal late Holocene cone. Its products are of basaltic to andesitic composition (e.g., Lara, 2004). There has been frequent recorded volcanic activity since the arrival of the Spanish colonists in 1551, and it is one of the most active volcanoes in Chile. Its first reported eruption, in 1558, destroyed the town of Villarrica, which was located at the present location of Pucón. The town was rebuilt at its present location, but was abandoned from 1602 to 1882, due to a war between the Spanish colonists and the Mapuche, the native inhabitants of Southern Chile. As a result, there is a lack of historical reports for this period. From 1750 to 1882, the area was gradually repopulated by Spanish colonists and reports of volcanic eruptions become more common and reliable (Petit-Breuilh, 2004). Records of 20th century eruptions are more or less complete, and show that Villarrica, in its most recent history, produced lava flows, relatively small-scale pyroclastic fall and, more importantly, lahars capable of destroying infrastructure. For example, in 1964, lahars generated during an eruption destroyed the village of Coñaripe (Fig. 3.1; Petit-Breuilh, 2004; González-Ferrán, 1994; Urrutia de Hazbún and Lanza Lazcano, 1993; Naranjo and Moreno, 2004; Keller et al., 2008, Castruccio et al., 2010). Many 20th-century eruptions caused fatalities, and rapidly expanding tourist activity in the region is increasing the risk of future fatalities, as well as destruction of property.

The basaltic to dacitic compound Mocho-Choshuenco Volcano comprises the dormant Choshuenco Volcano (39°54'50''S, 72°02'25''W, 2360 m asl; Fig. 3.1) on the rim of a 4-km-wide caldera, and the post-glacial and historically active El Mocho Volcano (39°55'50''S, 72°01'40''W, 2430 m asl; Fig. 3.1) that has grown in the caldera. Historically, it has not shown the same degree of activity as Villarrica Volcano, but because of its more remote location, records are scarce, possibly incomplete and/or unreliable. Moreover, the name *Mocho* has in the past also been used for Quetrupillán Volcano, and some locals still do so, adding uncertainty to eruptions historically attributed to *Mocho*. Depending on the source, two to seven eruptions of El Mocho Volcano have been reported, the oldest dating to 1759. In historical illustrations of the 18th century, El Mocho Volcano was often shown in an active state (Petit-Breuilh Sepúlveda, 2004), indicating that it was possibly more active than it currently is. A major Plinian-style eruption produced the Neltume Pumice about 10,300 years ago, suggesting that El Mocho Volcano, located in a fast-growing tourist area, is a potentially hazardous volcano (González-Ferrán, 1994; Petit-Breuilh, 2004; Siebert et al., 2010).

No historical eruptions of Sollipulli or Lanín volcanoes have been recorded and depending on the source only one to four historical eruptions have been reported for Quetrupillán Volcano, all in the 19th century (Fig. 3.1; Petit-Breuilh, 2004; Siebert et al., 2010).

The Huanquihue Group is located just east of the Riñihue drainage basin, and it has had one known historical eruption. More active nearby volcanoes (< 100 km) are Llaima Volcano in the north, and the Carrán-Los Venados and Puyehue-Cordón Caulle volcanic complexes in the south (Fig. 3.1; Petit-Breuilh, 2004; Siebert et al., 2010).

3.2.3 Tectonic and seismic history

Volcano-tectonic processes in this region are a consequence of the oblique subduction of the Nazca Plate under the South American Plate (Fig. 1.1). The current convergence rate between these two

plates is estimated between 66 mm/y (Angermann et al., 1999) and 78 mm/y (DeMets et al., 1994). The plate boundary has produced numerous megathrust earthquakes. For example, the 1960 Great Chilean Earthquake along the Valdivia rupture zone was to this date the largest earthquake ever recorded instrumentally (M_w 9.5) and had a rupture length of 1000 km (Cifuentes, 1989). Other major historical earthquakes along the Valdivia rupture zone occurred in 1575, 1737 and 1837. The 1575 earthquake was of similar magnitude as the 1960 earthquake (Lomnitz, 2004; Cisternas et al., 2005). On 27th February 2010, the Maule earthquake (M_w 8.8) ruptured about 500 km of the megathrust and closed a seismic gap on the Concepción-Valparaíso rupture zone, just north of the Valdivia rupture zone (Fig. 1.1; Moreno et al., 2012).

Additionally, the Liquiñe-Ofqui Fault Zone (LOFZ) is a 1000-km-long, dextral strike-slip lineament, which has been accommodating the oblique subduction since the Middle Miocene. The fault zone separates the north-moving (6.5 mm/y) Chiloé sliver (in the west) from the rest of the South American Plate (in the east) (Cembrano et al., 2000; Wang et al., 2007; Melnick et al., 2009). In the study area, the main strands of the fragmented LOFZ run about 10-20 km to the east of both Villarrica Volcano and Mocho-Choshuenco Volcano (Fig. 3.1; Rosenau et al., 2006).

3.3 Methodology

3.3.1 Bathymetry and seismic data acquisition

Dense grids of seismic data were acquired using a 3.5 kHz sub-bottom profiler (pinger) and a CENTIPEDE sparker of the Renard Centre of Marine Geology (Ghent University) and were interpreted using SMT's KingdomSuite (more details can be found in Chapter 2).

Bathymetric maps of lakes Villarrica and Calafquén were constructed by means of interpolation between seismic data (acoustic velocity derived by depth measurements at coring sites; Moernaut et al., 2009) and data points of bathymetric soundings of the Servicio Hidrográfico y Oceanográfico de la Armada de Chile (SHOA, 1987; 2008). For Lake Riñihue, the bathymetric map of Campos et al. (1987) is used.

3.3.2 Sedimentology, geochemistry and chronology

We collected a total of 87 gravity cores (10-130 cm) from the three studied lakes using a Swiss corer or a UWITEC gravity corer. Cores were taken during the austral summers of 2007-2008 (CAGC and RINGC), 2008-2009 (CB, CGC and VILLSC) and 2010-2011 (CALA and VI) and 24 of these cores are presented in this study (Table 3.1). Cores were shipped to Belgium, opened, described and photographed. Subsequently, the magnetic susceptibility (MS) was measured on all cores. The employed methods are briefly described in this section. More detailed descriptions can be found in Chapter 2.

For each lake, one or two master cores, which contain EDs that are not –or to a limited extent– erosional, were selected for more detailed analysis (i.e. VILLSC01 (Lake Villarrica), CAGC02bis (Lake Calafquén), RINGC03 and RINGC04 (Lake Riñihue)). Color analysis, analysis of grain-size distribution and of organic-matter content, and Scanning Electron Microscope (SEM) imaging were performed at Ghent University using standard procedures. On selected samples, bulk X-Ray Diffraction (XRD) was performed to determine the different sediment mineral components. On a selection of tephra layers, glass major-element geochemistry and mineral compositions were determined using electron

Table 3.1 *Locations, water depth, length and sampling year of sediment cores discussed in this study.*

Lake	Core name	Lat (°N)	Long (°E)	Depth (m)	Length (cm)	Sampling year
Villarrica	VILLSC01	-39,28111	-72,14298	112	81	2009
Villarrica	VILLSC02	-39,25664	-72,17123	81	86	2009
Villarrica	VILLSC05	-39,26319	-72,11601	158	49	2009
Villarrica	VI4	-39,28075	-72,18710	85	81	2011
Villarrica	VI7	-39,27097	-72,18065	98	110	2011
Villarrica	VI9	-39,26934	-72,14557	109	106	2011
Villarrica	VI11	-39,26147	-72,14358	160	130	2011
Villarrica	VI13	-39,28201	-72,12283	148	55	2011
Villarrica	VI14	-39,26218	-72,08209	160	59	2011
Villarrica	VI17	-39,28264	-72,04797	90	62	2011
Villarrica	VI18	-39,28082	-72,08030	154	21	2011
Calafquén	CAGC02bis	-39,54586	-72,21898	142	90	2008
Calafquén	CAGC03	-39,54917	-72,25014	63	51	2008
Calafquén	CAGC05	-39,53685	-72,18983	112	76	2008
Calafquén	CB4	-39,54820	-72,06489	173	54	2009
Calafquén	CB9	-39,53046	-72,14298	170	45	2009
Calafquén	CGC01	-39,55566	-72,06033	177	25	2009
Calafquén	CALA01	-39,53970	-72,20990	160	123	2011
Calafquén	CALA04	-39,55054	-72,18385	93	120	2011
Calafquén	CALA05	-39,54848	-72,17941	88	119	2011
Calafquén	CALA06	-39,54146	-72,16435	94	123	2011
Calafquén	CALA07	-39,53595	-72,15231	172	96	2011
Riñihue	RINGC03	-39,79383	-72,38781	113	80	2008
Riñihue	RINGC04	-39,80537	-72,38469	120	89	2008

microprobe analysis and SEM at the University of Oxford. The master cores also were impregnated for microscopic analyses. On the sediment blocks, Micro-X-ray Fluorescence (µXRF) scanning and mapping was used to differentiate between Si-rich diatoms, Al-rich clays, fine detrital silts and Fe-rich tephras. Furthermore, the thin sections and sediment blocks were used for microfacies analysis and lamination/varve counting. Finally, radionuclide dating was performed on the upper part of core CAGCO2bis at the Université de Bordeaux, France.

3.4 Results and discussion

3.4.1 Bathymetry and core location

The bathymetry of all studied lakes is characterized by a deep basin and a shallower area with platforms and channels. The deep basins occur in the eastern or northern parts of the lakes, have deltaic fans linked to the main inflows and are usually delimited by steep, non-sediment-bearing slopes. The shallower areas, where most of the cores were taken, occur in the western or southwestern parts of the lakes, away from the main inflows.

Lake Villarrica has a maximum depth of about 165 m, in the central to northwestern part of the lake (Fig. 3.2). In the east and the south of the deep basin gentle slopes (<0.5°) rise towards the coastlines and the deltas. Six cores were taken in the southern part of this main basin; in the east it was not

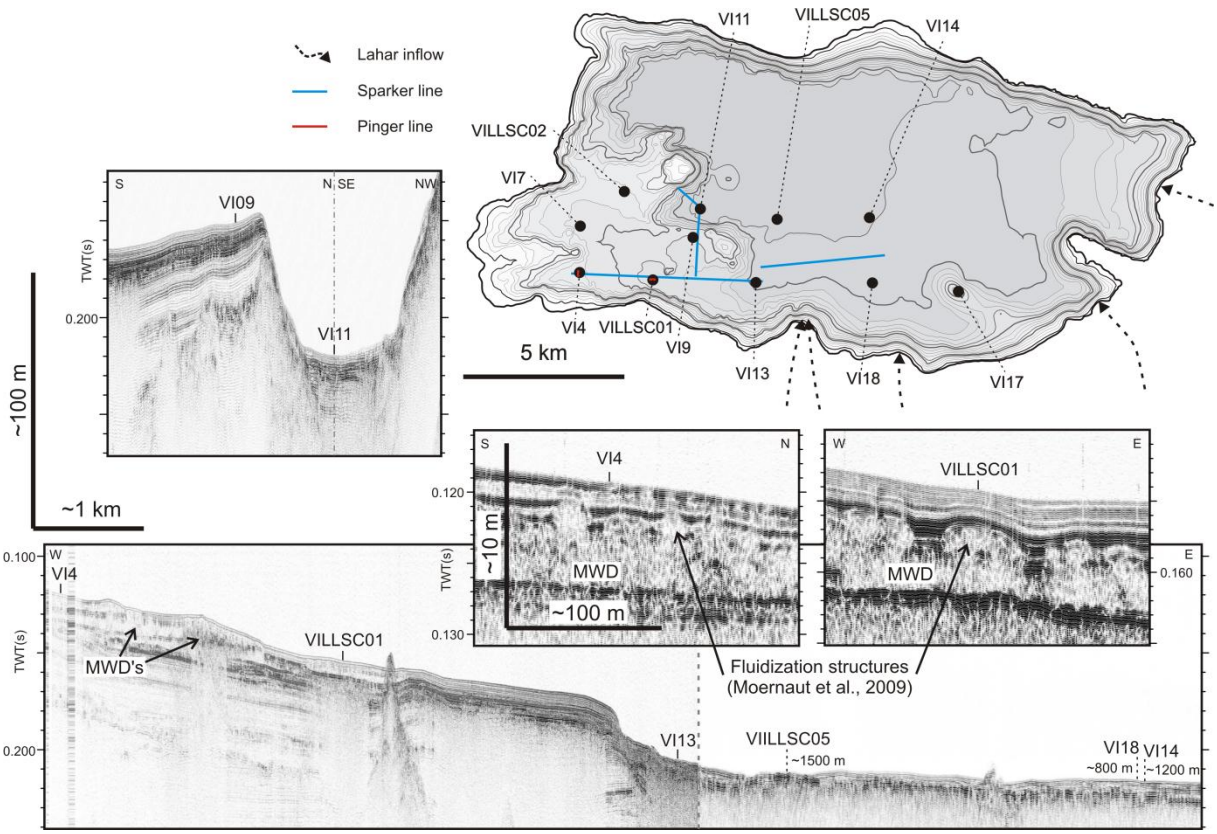

Fig. 3.2 *Selected reflection-seismic profiles (sparker and pinger) and projected coring locations in Lake Villarrica. Interpretation of mass-wasting deposits (MWD) and fluidization structures after Moernaut et al. (2009). Lake bathymetry was constructed by means of interpolation between seismic data (Moernaut et al., 2009) and data points of bathymetric soundings of the Servicio Hidrográfico y Oceanográfico de la Armada de Chile (SHOA, 1987). Isobaths are plotted every 10 m.*

possible to retrieve cores due to the presence of coarse-grained sediments (i.e. coarse sand). Five more cores are located on the platforms and channels in the southwestern part of the lake. Reflection-seismic data show that on the core locations there are no signs of erosion or other disturbances in the upper meters of the sedimentary infill (Fig. 3.2). We only found evidence of an erosional channel east of VI13, linked to one of the largest lahar inflows on the southern shores (Fig. 3.2).

The maximum depth of Lake Calafquén is about 211 m and is located in the northern part of the lake (Fig. 3.3). The depth gradually decreases towards the east to a depth of about 170 m at the foot of the Llancahue River delta. Four cores were taken in these deepest areas of the lake. Large water depth and coarse sediments did not permit coring in the northwestern and northeastern parts, respectively. In the northeast, offshore the Chaillupén River inlet, a fan-like structure with no seismic penetration is observed. Unsuccessful coring attempts in this area make us attribute this lack of penetration to the presence of sandy sediments. Seven cores were taken in the southwestern part of the lake, which is characterized by an irregular bathymetry with several channels and platforms, interrupted by islands. CALA01 was taken in a channel with parallel and conformable reflectors in the upper meters. All other cores were taken on locations without erosional features (Fig. 3.3).

Lake Riñihue (max. depth of 323 m) is the deepest of the studied lakes, impeding coring in the entire central and southeastern part. In the west, a gently sloping platform at a depth of about 120 m is

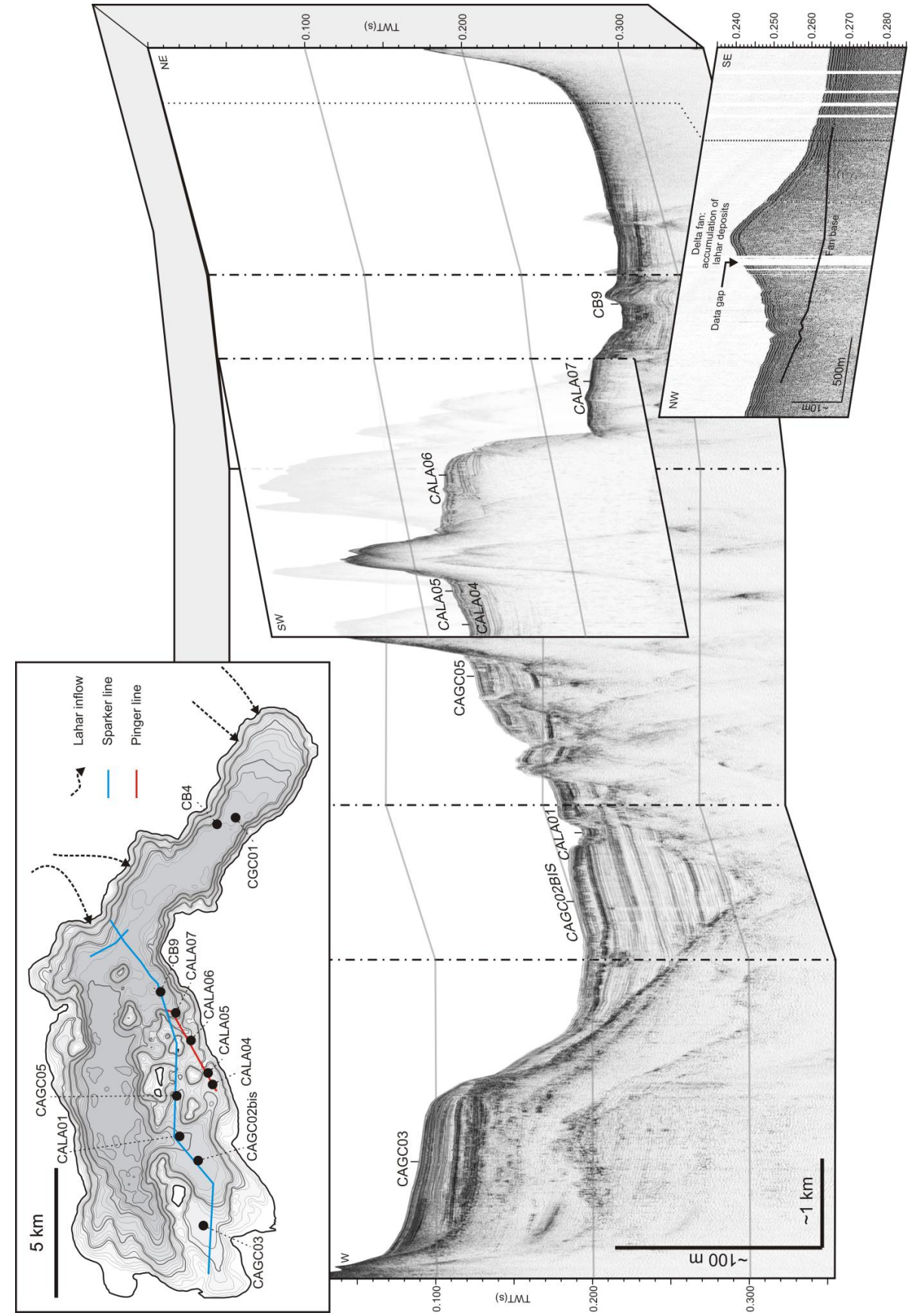

Fig. 3.3 *Selected reflection-seismic profiles (sparker and pinger) and projected coring locations in Lake Calafquén. Lake bathymetry was constructed by means of interpolation between seismic data (Moernaut et al., 2009) and data points of bathymetric soundings of the Servicio Hidrográfico y Oceanográfico de la Armada de Chile (SHOA, 2008). Isobaths are plotted every 10 m.*

prolonged towards two sub-basins. The two cores presented in this study are taken in conformable sediment sequences of the northern sub-basin and between the two sub-basins (Fig. 3.4).

The master cores, on which most analyses were performed, were selected from sites with a maximum amount of EDs, but minimum disturbance or erosion.

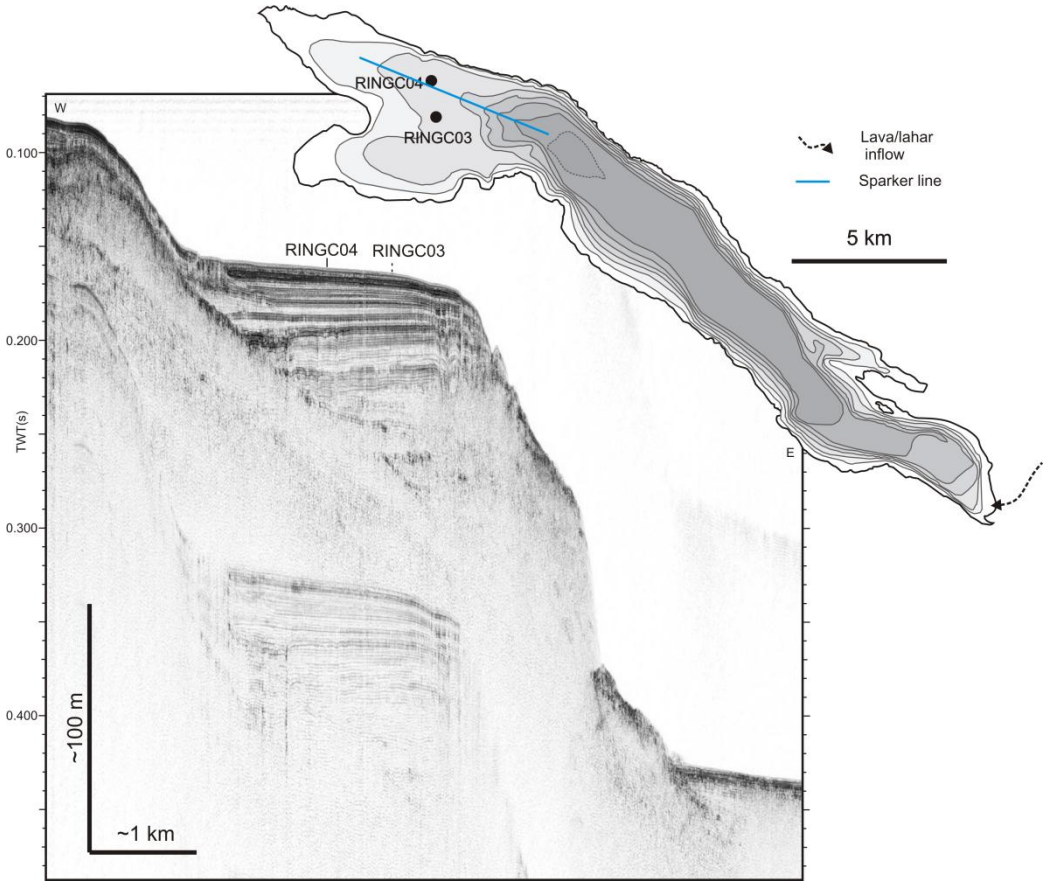

Fig. 3.4 *Selected reflection-seismic profile (sparker) and projected coring locations in Lake Riñihue. The bathymetric map of Campos et al. (1987) was used and isobaths are plotted every 50 m, except for the deepest isobath, which represents a depth of 320 m.*

3.4.2 Sedimentology and geochemistry

In all cores, the predominantly biogenic (background) sediments consist of laminated brown to green clayey silts (Fig. 3.5 and 3.6). The sediment is composed of a silt fraction rich in diatom frustules and a terrigenous clay to silt fraction. After impregnation, couplets composed of diatom-enriched laminae alternating with clay and organic matter-enriched laminae were observed in thin section (central column of Fig. 3.5).

The three main components of the sediment (i.e. diatom frustules, terrestrial clays and volcanic ash) are characterized by high concentrations of specific chemical elements (i.e. respectively Si, Al and Fe), which is reflected in the µXRF elemental counts. Diatom frustules are composed of amorphous silica and characterized by high Si-counts on the µXRF spectra and a low MS. In contrast, the clay fraction consists mainly of amorphous allophane, which is enriched in Al (Bertrand and Fagel, 2008), and a distinctive elemental component of (mafic) volcanic ash is Fe. Hence, ratios between these three elements were used to depict variations in occurrence of diatom frustules, terrestrial clays and volcanic ash in the sediment (Fig. 3.6).

In all three studied lakes, the laminated background sediments are frequently interrupted by volcanically derived EDs, in which terrestrial components produced by onshore events occur in unusually high abundance. Al/Si and Fe/Si µXRF ratios proved in the studied lakes particularly useful for separating these EDs from background sediment (Fig. 3.6).

The three lakes differ in their sediment character, requiring an adapted study method for each lake. In Lake Calafquén, which has a low catchment-to-lake-surface ratio, the background sediments consist predominantly of diatoms; hence, there is a strong contrast between the diatom-rich background sediment and the detrital EDs. Lakes Villarrica and Riñihue generally receive higher amounts of detrital input. Small mineral grains and glass particles are present throughout their background sediment, resulting in higher mean MS values and Al/Si and Fe/Si ratios. This makes EDs more difficult to identify by their µXRF signature alone; hence, other indicators (normal grading, homogeneity of color and grain size and/or anomalous color) were also used to confirm the presence of EDs.

3.4.3 Event deposit classification and formation

Based on color, grain-size characteristics, MS, µXRF signature and microscopic texture, we divided EDs in all three lakes into two main types: lacustrine turbidites and volcanic-eruption-induced EDs. Volcanic-eruption-induced EDs were further subdivided into three groups: tephra fall, Fe-rich clay to fine silt laminae (FeLs), and detrital fining-upwards EDs (interpreted as lahar deposits). The EDs were also correlated between the sediment cores of each lake (Fig. 3.7, 3.8 and 3.9), allowing us to describe the deposits not only based on occurrence in one core, but also to describe their spatial distribution and variations (e.g., thickness, grain size), and to detect possible erosion.

3.4.3.1 Lacustrine turbidites

Lacustrine turbidites have a thickness ranging from a few millimeters to several centimeters. They fine upwards, with the largest changes in grain size occurring at the top and the base (Fig. 3.6). The basal component is at most a few millimeters thick and consists of fine to coarse sand. The top component is maximum a few millimeters thick and consists of a lamina of broken diatoms (low Al/Si ratio), covered by fine silts and clays (high Al/Si and Fe/Si ratios). The middle (and main) part of the turbidite is homogeneous in grain size and sometimes darker than the background sediment. The composition of this part is similar to the background sediment (i.e., a mixture of diatoms, clays, organic matter and mineral/glass particles), which is also reflected in grain size (mode: 20-30 µm) and µXRF elemental counts ($0.011 < Al/Si < 0.062$; $0.29 < Fe/Si < 1.50$; Fig. 3.5 and 3.6). The similarity in composition suggests that these EDs are distal turbidites created by sublacustrine slope failures. By inter-core correlation, it was possible to verify that the base is rarely erosional, or that erosion is limited to some millimeters. Only lacustrine turbidite LT-1 in core CALA01, located in a channel, erodes about 10 cm of underlying sediment (Fig. 3.8). Similar turbiditic EDs have been found in other Andean and Alpine lakes where they have been used as paleoseismic indicators (Chapron et al., 2006, Bertrand et al., 2008a; Beck, 2009). These are the same turbidites as the lacustrine turbidites type 1 (LT1) in Chapter 4.

3.4.3.2 Volcanic-eruption induced EDs

Tephra-fall layers. The tephra-fall layers typically consist of dark, coarse-grained (fine to coarse sand, i.e. medium/coarse ash) glass shards and mineral grains (mainly plagioclase, clinopyroxene, olivine

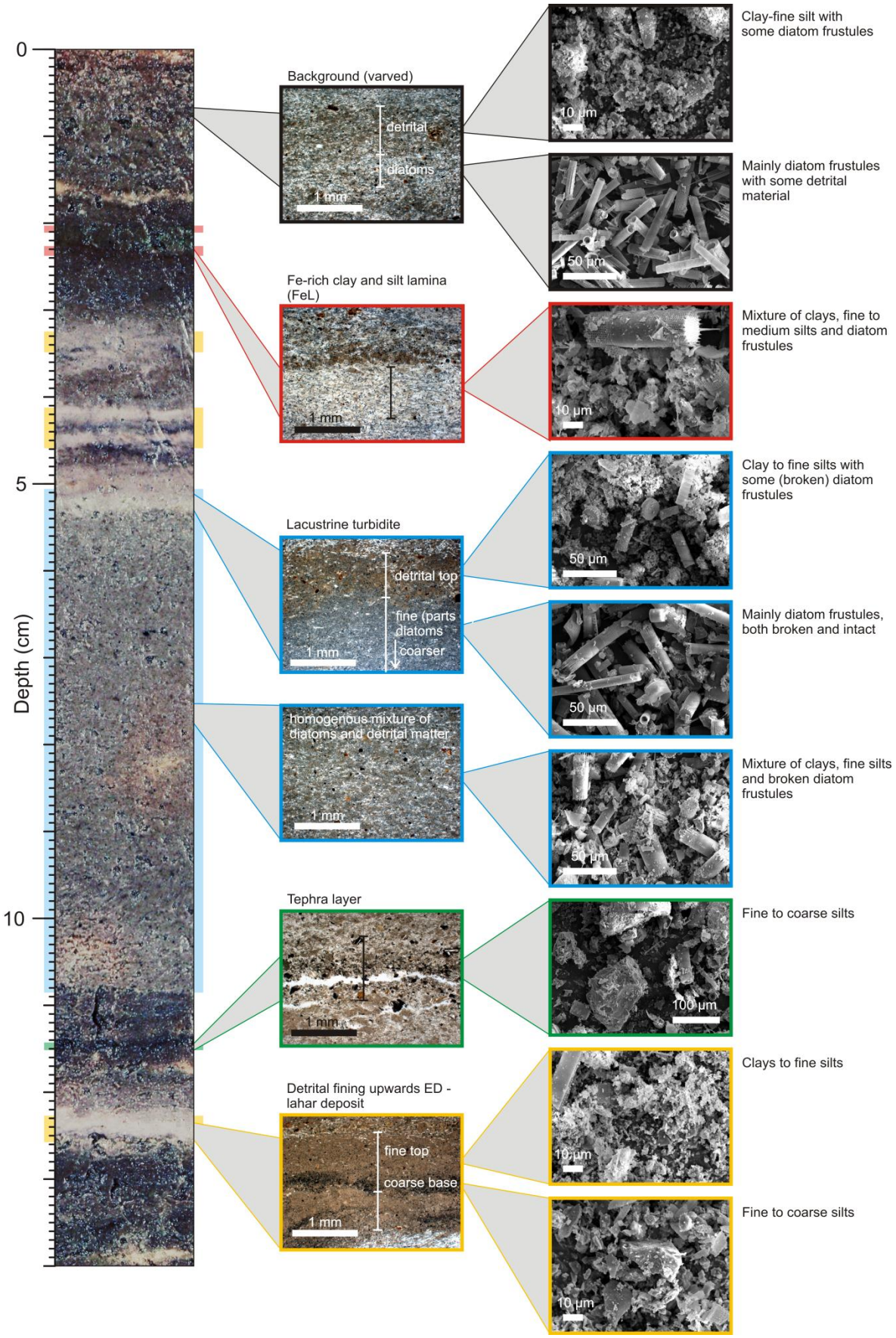

Fig. 3.5 *Left: zoom of the picture in Fig. 3.6, with EDs indicated; middle: optical microscope images of thin sections of varved background sediment and the four types of EDs; right: SEM images of the background sediment and the four types of EDs. EDs are color coded in the same way as in Fig. 3.6.*

and Ti-magnetite) in a matrix of background sediment (Fig. 3.5). Deposits are usually not thicker than 5 mm and are characterized by higher-than-background Al/Si and especially Fe/Si ratios (Al/Si > 0.062, Fe/Si > 1.50; Fig. 3.6). The strong scatter is attributed to coarse ash grains influencing the average composition and background sediment acting as a matrix. The thickness of the deposits at different locations in one lake is independent of the water depth, suggesting they result from direct tephra fallout on the lake surface. EDs with similar characteristics have been attributed to tephra fallout in nearby lakes Puyehue (40°40'S, 72°28'W) and Icalma (38°48'S, 71°17'W) (Bertrand et al., 2008a; Bertrand et al., 2008b).

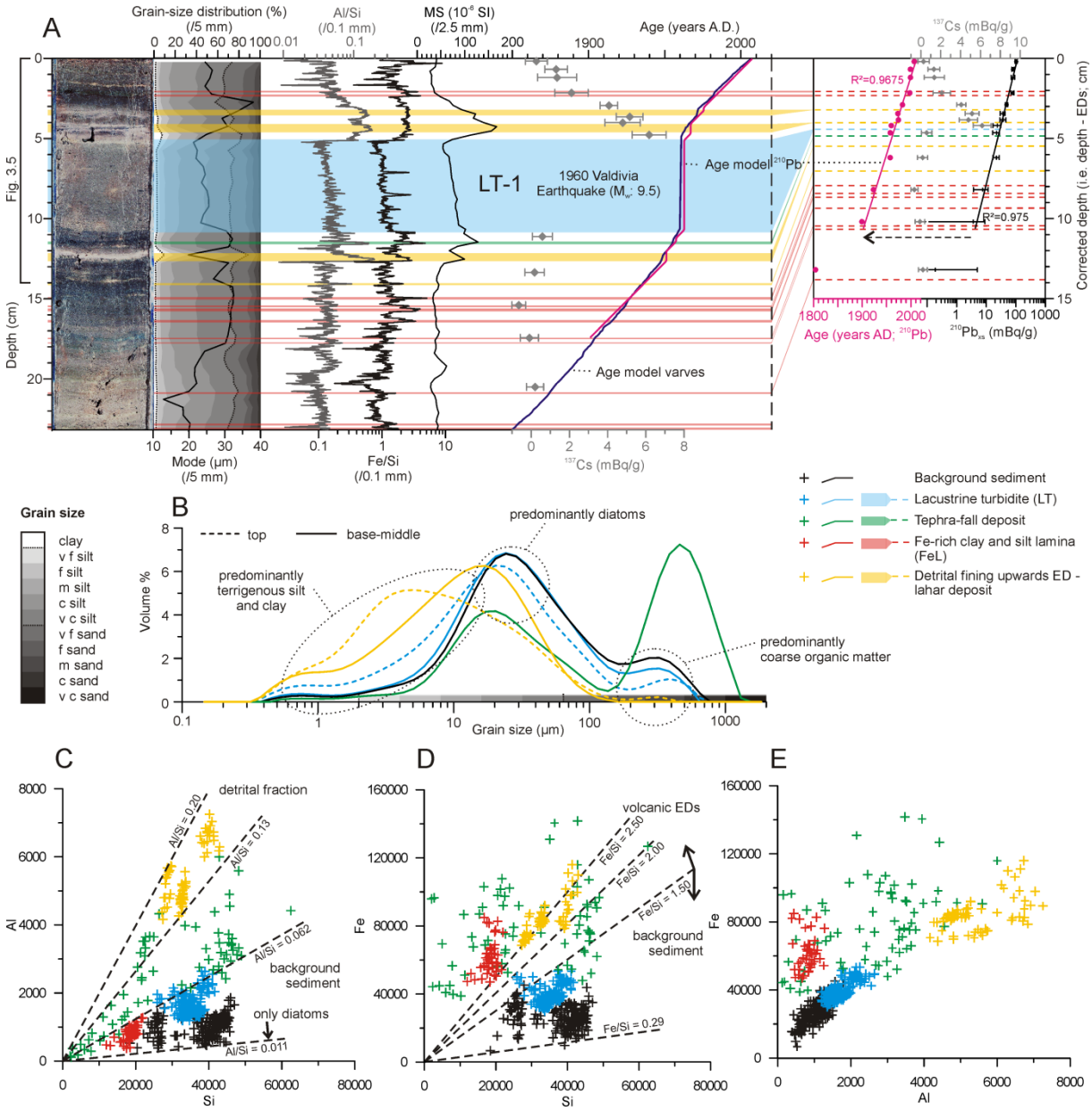

Fig. 3.6 *A: left: Picture of CAGC02bis, grain-size distribution, µXRF ratios and magnetic susceptibility (MS). The four different types of EDs are indicated with colored transparent bars: lacustrine turbidites (LT; blue), tephra layers (green), Fe-rich clay and silt laminae (FeL; red) and detrital fining upwards EDs (yellow); right: Age model CAGC02bis for the last 150 years, based on 137Cs (gray diamonds), 210Pb (pink line) and varve counts (dark blue line). B: Grain-size distribution of background sediment (black), tephra-fall deposits (green; bimodal distribution due to the finer background sediment acting as a matrix for the coarser tephra) and both base/middle (solid) and top (dashed) of detrital fining upwards EDs (yellow) and lacustrine turbidites (blue); C, D and E: µXRF elemental counts in CAGC02bis of Al versus Si (C), Fe versus Si (D) and Fe versus Al (E), dashed lines represent elemental ratios differentiating between background sediment and EDs.*

Fe-rich clay to fine silt laminae (FeLs). The FeLs have a yellowish appearance in thin section (Fig. 3.5) and are present as single thin laminae or thicker zones with yellowish clays crossing varve boundaries. They are characterized by very high Fe/Si ratios (Fe/Si > 2.50), but MS values do not exceed the background values (Fig. 3.6). Occasionally, these laminae occur immediately above tephra-fall deposits and, based on varve chronology, young FeLs can be unambiguously linked to historical eruptions of Villarrica Volcano (e.g., 1980 and 1984; see further). Hence, we interpret these laminae as a product of a volcanic eruption, representing fluvially transported very fine ash, or cryptotephra, which was originally deposited in the catchment area by an eruption. This implies that an eruption does not necessarily have to cause tephra fall on the lake surface to be represented in the sedimentary record. Since precipitation is significantly higher during the winter months, remobilization and redeposition of the cryptotephra can be delayed by several months to a year.

Detrital fining-upwards EDs (lahar deposits). The detrital fining-upwards EDs are brown layers or laminae with a light beige or light gray top component. Both the basal and the top component show high MS values. The basal component is normally graded (coarse or fine sand to medium silt) and characterized by very high Fe/Si ratios (Fe/Si > 2.50). Thin-section analysis shows that it is exclusively composed of crystals and volcanic glass, without any diatom frustules (Fig. 3.5). Occasional parallel- or cross-laminated sediment structures occur, consisting of alternations between coarser and finer sands (i.e. coarse ash). The grain size of the top component ranges from clay to fine silt (mode: 3-20 µm; i.e. fine ash) and is characterized by very high Al/Si ratios and high Fe/Si ratios (0.13 < Al/Si < 0.20, Fe/Si > 2.00; Fig. 3.6). Tops with a more grayish color have the highest Fe/Si ratios. Thin-section analysis shows that these top components consist of brownish amorphous detritus, with diatom frustules virtually absent (Fig. 3.7 and 3.8). The exclusively mineral and glass composition of the detrital fining-upwards EDs is indicative of a volcanic origin. However, the depth-dependent thickness of the deposits as well as occasional cross-lamination argue against an interpretation of tephra-fall deposits.

The detrital fining-upwards EDs are thickest and coarsest in cores in the deepest parts and closest to historical lahar inflows into lakes Villarrica and Calafquén (Urrutia de Hazbún and Lanza Lazcano, 1993; González-Ferrán, 1994; Petit-Breuilh, 2004; Naranjo and Moreno, 2004; Keller et al., 2008; Fig. 3.7 and 3.8). The brown coarse basal parts are well developed in the deepest parts and close to historical lahar inflows, while the light-colored top components drape the entire lake floor, but is thinner and less obvious in shallower areas (Fig. 3.7 and 3.8). The formation of these deposits can be explained by a combination of a hyperpycnal and a homopycnal flow once the lahar reaches the lake shore. A hyperpycnal flow –transporting medium silts to boulders– will result in a deposit mainly in the proximal (including the boulders on a deltaic fan) and deep parts. The homopycnal flow –carrying the finer fraction– will spread sediments all over the lake, however still in higher amounts in the proximal and deep areas (Fig. 3.10). Deposits with a light gray top, in contrast to light beige, are considered to contain a higher amount of fresh ash compared to reworked terrestrial clays and soils.

Volland et al. (2007) already suggested that lahars might have a major impact on the sedimentary infill of Lake Calafquén, but concluded that the characteristics of lahar deposits on seismic profiles would be very similar to those of floods. Except for the deltaic fans close to the lahar inflows, which are probably mostly built up by lahars, the lahar deposits are too thin to be detected by seismic profiling. The flood deposits encountered in Lake Puyehue by Chapron et al. (2007) are indeed quite similar to the lahar deposits we find in this study, but the former are located at only 2.5 km from the

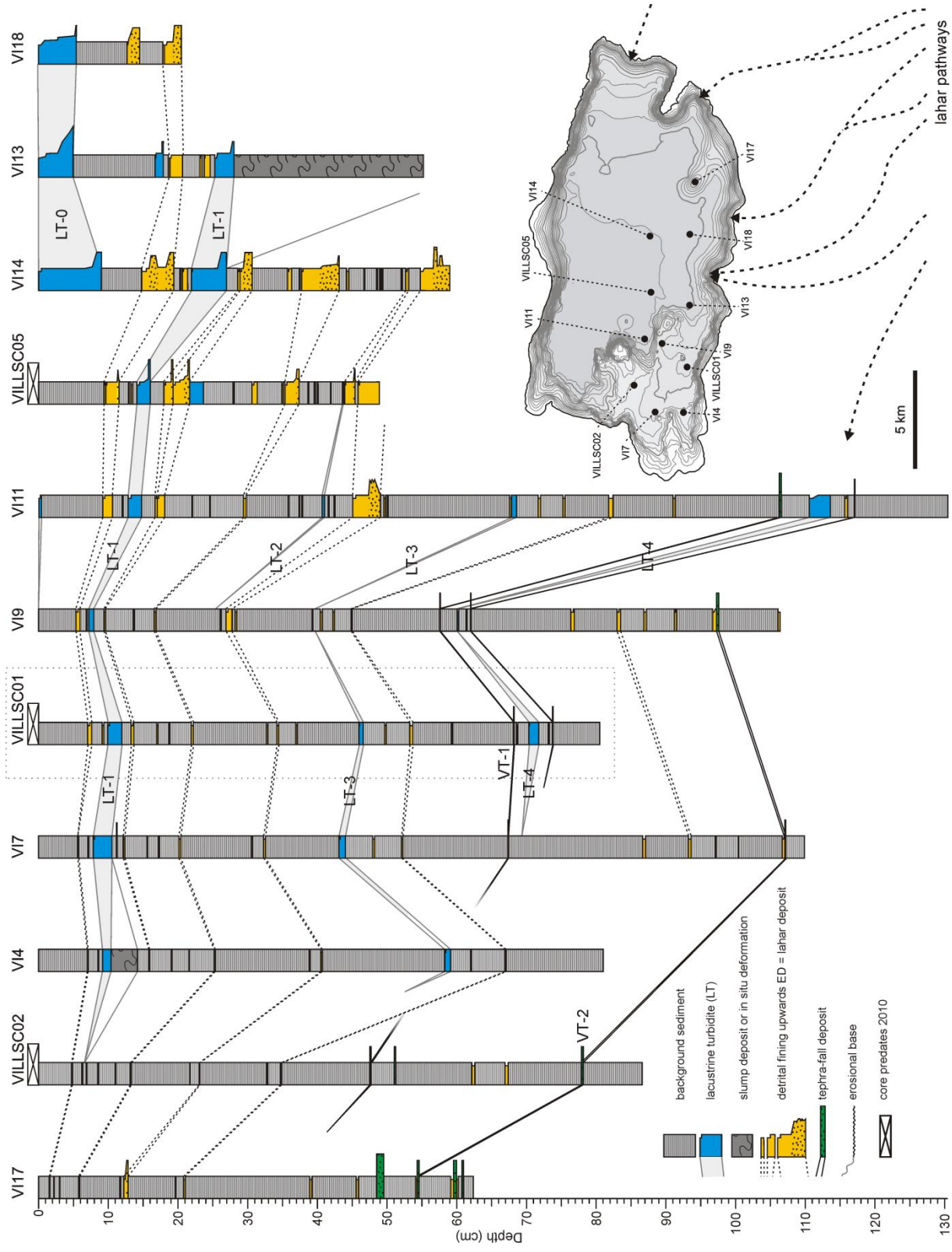

Fig. 3.7 *Lithologs of the sediment cores and correlation of the EDs (color coded in the same way as in Fig. 3.6) in Lake Villarrica. In the right hand corner the lake bathymetry with isobaths every 10 m, core locations and lahar inflows. Dotted rectangle: master core; LT: lacustrine turbidite; VT: analyzed tephra-fall deposit.*

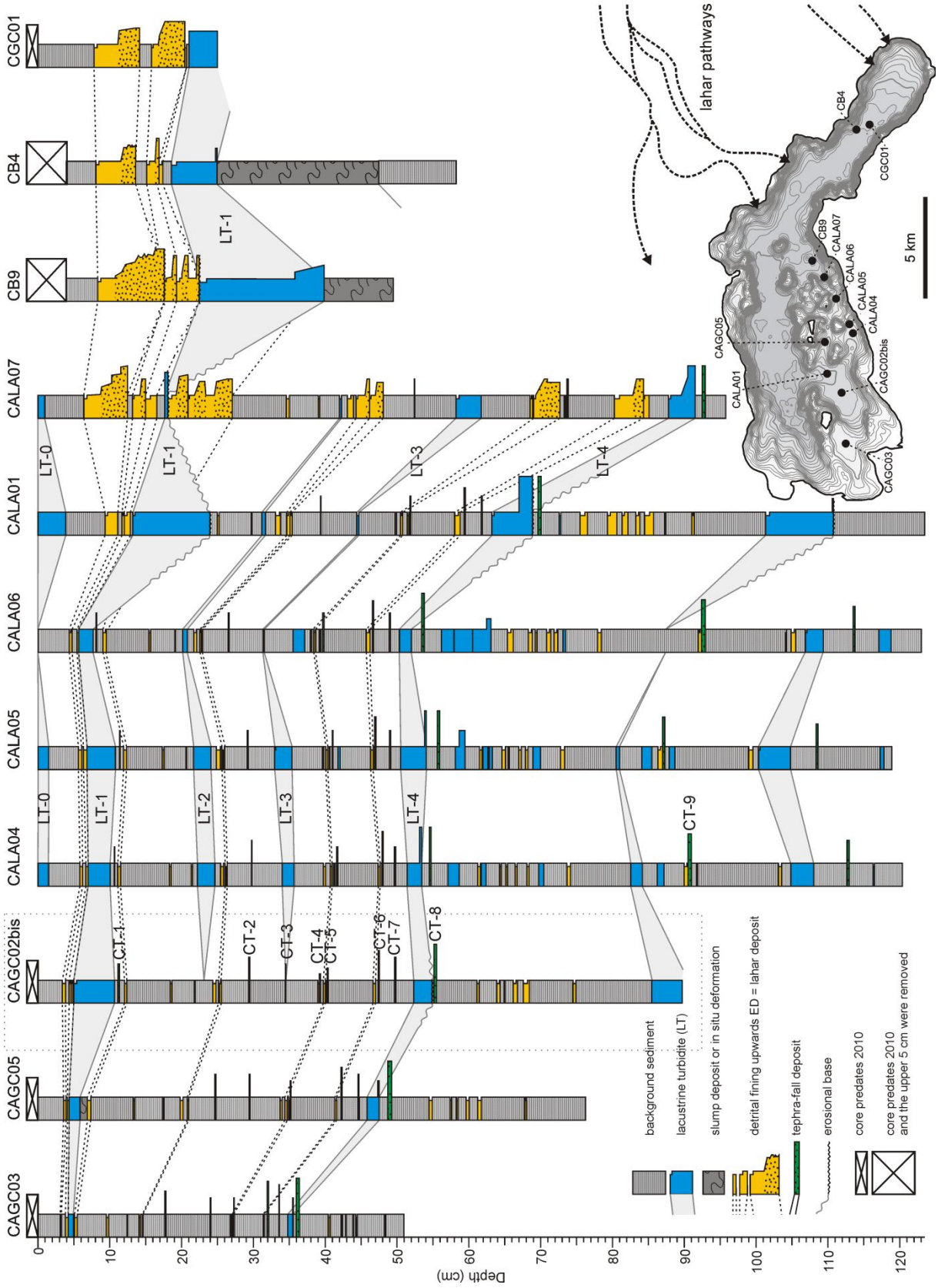

Fig. 3.8 *Lithologs of the sediment cores and correlation of the EDss (color coded in the same way as in Fig. 3.6) in Lake Calafquén. In the right hand corner the lake bathymetry with isobaths every 10 m, core locations and lahar inflows. Dotted rectangle: master core; LT: lacustrine turbidite; CT: analyzed tephra-fall deposit.*

main river inlet, and are much finer grained than the lahar deposits in lakes Calafquén and Villarrica at more distal locations. This coarser nature of the latter is due to the potential of lahars to carry much coarser material into the lake (boulders of several cubic meters; Vallance, 2000; Naranjo and Moreno, 2004; Castruccio et al., 2010). Moreover, historical lahar inflows are not necessarily located in the same areas as the main river inflows (Fig. 3.1, 3.7 and 3.8). For our detrital fining-upwards EDs, a lahar origin is considered most likely because flood deposits would all be coarser and thicker towards the Trancura or Llancahue River deltas in lakes Villarrica and Calafquén, respectively. Finally, the chronological link of these deposits with historical lahars (e.g., 1964 and 1971; see further) confirms the interpretation as a lahar deposit.

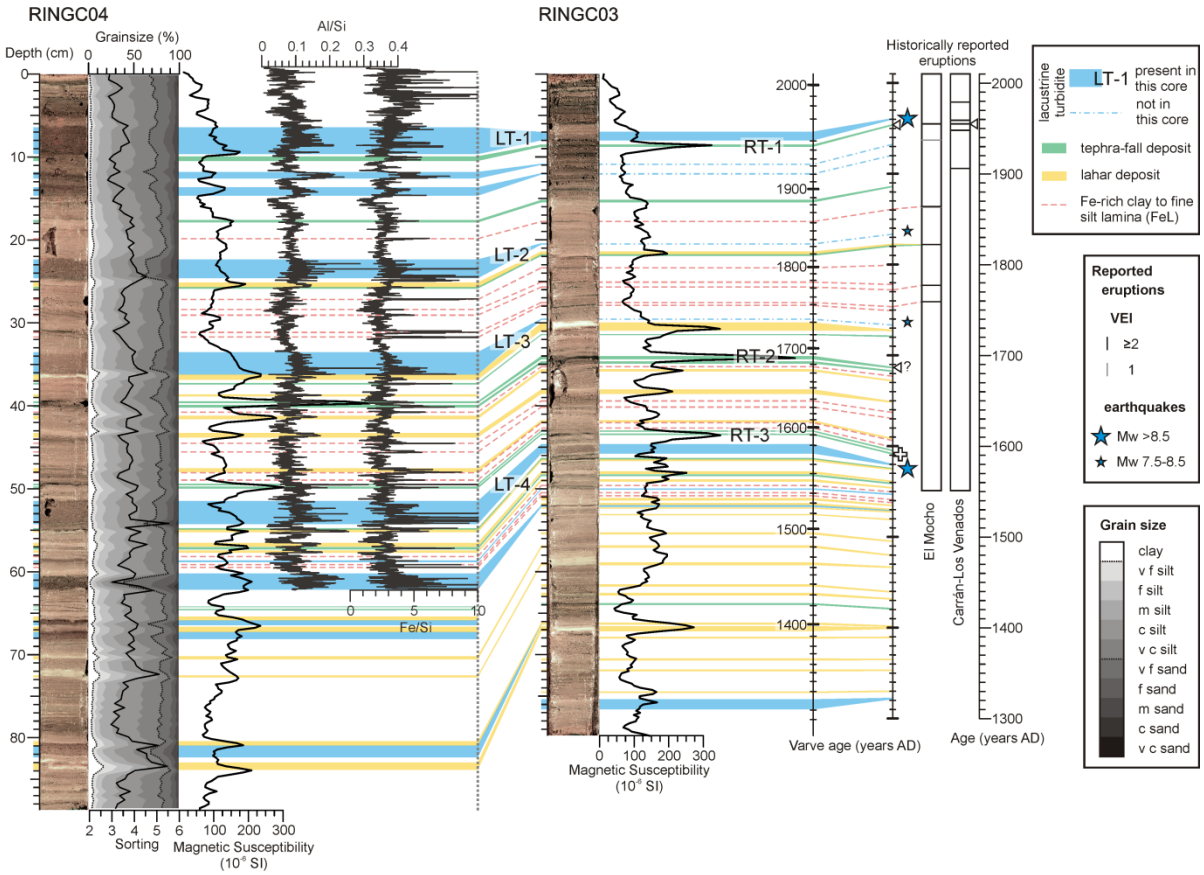

Fig. 3.9 *Left: picture, grain-size distribution, MS and µXRF ratios of RINGC04; right: picture, MS and age model (varve counting) of core RINGC03. EDs (color coded in the same way as in Fig. 3.6) are correlated between both cores and projected on the age axis. When possible, EDs are correlated with strong historical earthquakes in the region (stars) and eruptions of El Mocho Volcano, the Carrán-Los Venados Volcanic Complex (triangles) and Lanín or Huanquihue volcanoes (cross). LT: lacustrine turbidite; RT: analyzed tephra-fall deposit.*

3.4.4 Varve formation and chronology

The couplets that are observed in the background sediment of the three studied lakes are interpreted as varves, formed by processes similar to those that generate varve couplets observed in Lake Puyehue. Lake Puyehue is also a glacigenic lake, approximately 90 km south of Lake Riñihue (Fig. 3.1), with limnological characteristics similar to the lakes studied here (Campos et al., 1983; 1987; 1989). In Lake Puyehue, annual biogenic varve couplets are composed of a lamina of organic-rich clayey to silty terrestrial material depositing during increased winter runoff, and a lamina of diatom frustules deposited in spring; the later result from diatom blooms that are triggered by winter nutrient turn-over (Arnaud et al. 2006; Boës and Fagel, 2008; Campos et al., 1989). Similar couplets

are observed in this study and are therefore inferred to have been formed in the same way and deposited annually.

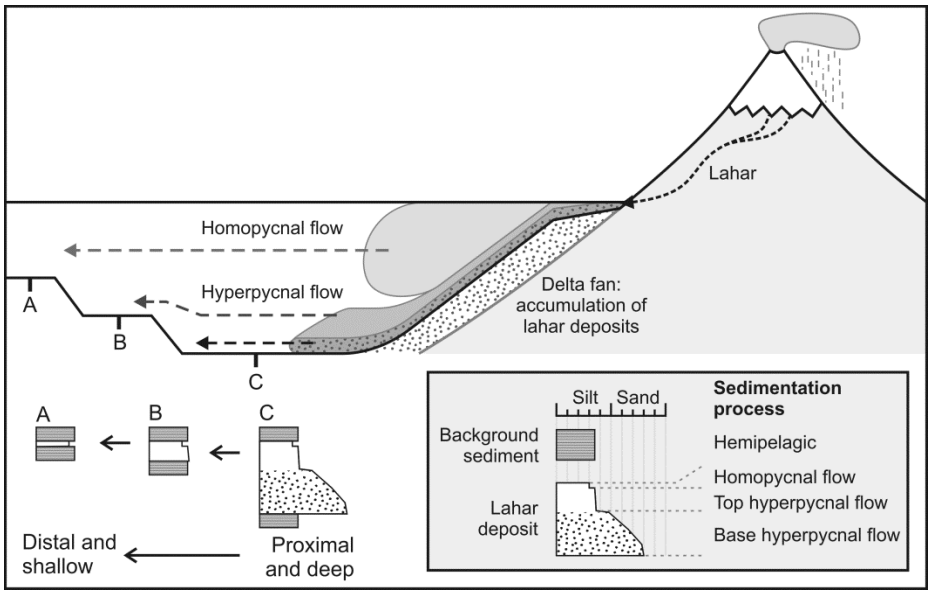

Fig. 3.10 *Schematic illustration of the formation of lahar deposits in lacustrine environments. When the lahar enters the lake, the coarsest grains (coarse silts and coarser) will be transported in a hyperpycnal flow and be deposited on deltaic fans and in (proximal) deep basins. Medium silts and finer grains will be transported by means of a homopycnal flow (or interflow) and will be distributed over the entire lake (homo- and hyperpycnal flows after Mulder and Alexander, 2001).*

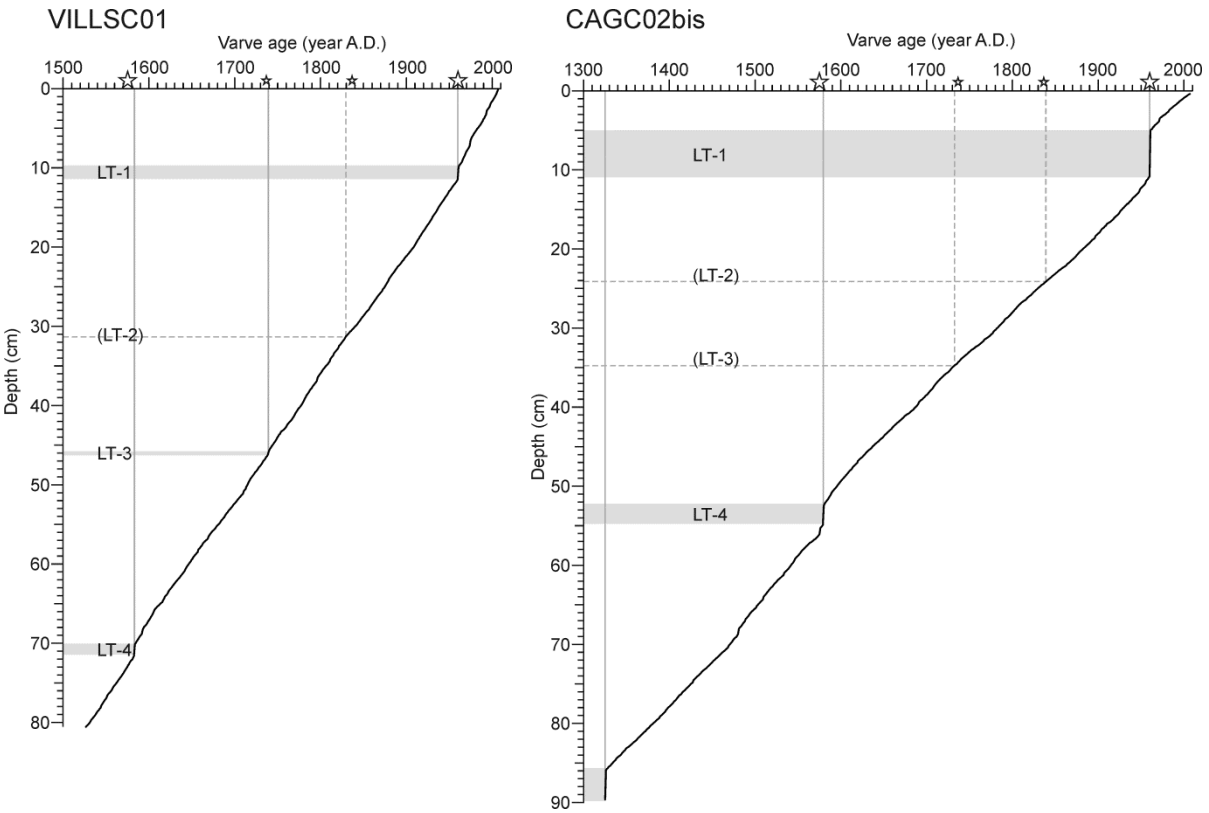

Fig. 3.11 *(left) Varve age-depth model for VILLSC01 in Lake Villarrica. Gray bar: lacustrine turbidites (LT) in this core; gray dashed line: lacustrine turbidites (LT) in other cores; star: historical earthquakes.*
Fig. 3.12 *(right) Varve age-depth model for CAGC02bis in Lake Calafquén. Gray bar: lacustrine turbidites (LT) in this core; gray dashed line: lacustrine turbidites (LT) in other cores; star: historical earthquakes.*

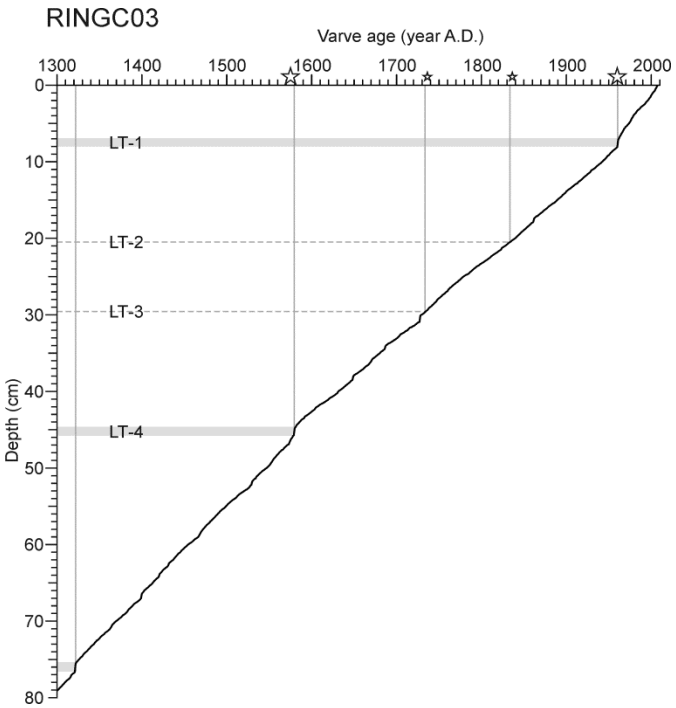

Fig. 3.13 *Varve age-depth model for RINGC03 in Lake Riñihue. Gray bar: lacustrine turbidites (LT) in this core; gray dashed line: lacustrine turbidites (LT) in other cores; star: historical earthquakes.*

In all three studied lakes, one master core was dated by varve counting (i.e. VILLSC01 in Villarrica, CAGC02bis in Calafquén and RINGC03 in Riñihue; Fig. 3.11, 3.12 and 3.13). The calculated average sedimentation rates, after removal of EDs are 1.53, 1.04 and 1.0 mm/yr, respectively, and the basal varve ages are 1523, 1325 and 1301, respectively. The youngest buried lacustrine turbidite LT-1 has a varve age of 1960 in Villarrica and Calafquén and 1961 in Riñihue (Fig. 3.11, 3.12 and 3.13; Table 3.2). This turbidite is attributed to the Great Chilean earthquake of 22 May 1960. In all three lakes the sediment deposited after 1900 has a darker color than that deposited before 1900, a higher organic-matter content and a different diatom composition with different predominant species, which is reflected in the grain-size mode (Heirman, 2011; Van de Vijver, pers. comm., 2012; Fig. 3.6, 3.9, 3.14 and 3.15). We attribute these synchronous changes in sediment characteristics to rapid increases in population, deforestation, changes in land use in the catchment, and lake eutrophication since the start of the 20th century (Campos, 1987; Petit-Breuilh, 2004).

Core CAGC02bis was also dated by radionuclide analysis (^{210}Pb and ^{137}Cs; Fig. 3.6). In the upper 5 cm, samples were taken at 0.5 cm intervals between EDs, whereas below this depth samples were taken at 1.0 cm intervals. Two samples were taken in lacustrine turbidite LT-1 for comparison. At 4.0-4.5 cm corrected depth (i.e. depth without EDs) a clear ^{137}Cs-peak can be observed, which gradually decreases in the overlying samples. The base of the ^{137}Cs-peak can be linked to fall-out of the ^{137}Cs that had culminated in the atmosphere by the early 1960s (Arnaud et al., 2006; Von Gunten et al., 2009), thereby confirming the correlation of the lacustrine turbidite below the ^{137}Cs-peak (LT-1) to the 1960 earthquake. This correlation is strengthened by the $^{210}Pb_{xs}$ specific activity and age-depth profile with a derived sedimentation rate of 0.95 mm/y throughout the last 100 years. The age-depth model based on the radionuclide activities confirms the annual character of the couplets and hence their usefulness in dating the rest of the core. The maximum offset between both age-depth models is 5 calendar years near the EDs, which is likely due to imperfect removal of the EDs, and only 2 years in intervals without EDs. The varve counting is therefore considered to be a sufficiently reliable dating method.

Year		Calafquén				Villarrica			
	Rep. VEI	VY	FeL	TEF	LAH	VY	FeL	TEF	LAH
2009	1								
2008	1								
2004	1								
2003	1								
1998	1								
1996	1								
1995	1								
1994	1								
1992	1								
1991	2					1993			X
1984	2	1984	X						
1983	1								
1980	2	1982	X						
1977	1								
1971	**2**	1971			X	1974			X
1964	**2**	1965			X	1965			X
1963	**3**	1963			X	1964			X
1961	1								
1960	1								
1960	EQ	1960		LT-1		1960		LT-1	
1958	1								
1956	1								
1948	**3**	1948			X	1949			X
1948	2?								
1947	1								
1938	2	1938			X				
1935	1								
1933	2					1935	X		
1929	1								
1927	2	1929	X						
1922	2	1924	X						
1921	2?								
1920	**2**					1927			X
1915	1	1918	X						
1909	**2**	1910	X			1918			X
1908	**2**					1916			X
1907	2								
1906	2	1906	X						
1904	**2**	1904	X			1910			X
1902						1908	X		
1897	2					1902			X
1893	2	1894			X	1897			X
1890						1891	X		
1883	2	1887	X						
1880	2					1880			X
1879	2					1878			X
1877	2					1876	X		
1875	2								
1874	2					1872	X		
1871		1877	X						
1869	2	1875	X			1867	X		
1864	2								
1859	2								
1853	2	1860	X			1848		X	
1852						1846			X
1850						1843	X		
1841		1846	X						
1837	2	1841	X						
1837	EQ	1839		LT-2		1830		LT-2	
1836		1839	X						
1832	2	1834	X			1821			X
1826		1829	X			1815	X		
1822	2	1825			X	1811			X
1815	1					1807	X		
1806	2	1807	X			1796			X
1798		1799	X						
1790	1								
1787	2	1790		X		1781			X
1780	1					1775	X		
1777	1								
1775	**2**	1782			X	1772			X
1771		1777	X						
1767		1773	X						

Year		Calafquén				Villarrica			
	Rep. VEI	VY	FeL	TEF	LAH	VY	FeL	TEF	LAH
1761		1766	X						
1759	1	1764	X						
1751	1	1750	X			1753			X
1745	1								
1742	2					1742	X		
1737	2	1734		X		1739	X		
1737	EQ	1732		LT-3		1739		LT-3	
1730	2	1725			X	1728			X
1721		1717			X				
1716	1	1712		X		1715			X
1715						1713	X		
1709		1707	X			1707		X	
1708		1706			X				
1705		1703			X				
1688	1	1690			X	1691			X
1682		1684		X		1684			X
1675	?	1676	X						
1672		1673	X						
1669						1672			X
1657	1								
1647	1	1648		X		1651			X
1645						1649	X		
1642						1647	X		
1640		1639			X	1645			X
1638		1637	X						
1632						1638			X
1625		1627	X						
1617		1620			X	1625			X
1612		1617			X	1619			X
1610		1614		X					
1604						1612	X		
1600		1606	X						
1594	2	1601	X			1603	X		
1584		1590	X			1592			X
1582		1587	X						
1579						1587	X		
1576						1584	X		
1575	EQ	1579		LT-4		1583		LT-4	
1564						1577			X
1562	2					1575			X
1558	2	1576		X		1571		X	
1553		1571	X			1566	X		
1543		1560	X			1557			X
1539						1551			X
1538						1548	X		
1537						1545	X		
1526		1544	X			1533			X
1523		1541	X						
1521		1539	X						
1516		1534	X						
1515		1533			X				
1509		1527	X						
1503		1521	X						
1497		1515	X						
1494		1512	X						
1492		1510			X				
1483		1501			X				
1479		1497	X						
1474		1492	X						
1471		1489			X				
1466		1484	X						
1463		1481			X				
1454		1472	X						
1448		1466	X						
1433		1451	X						
1417		1435	X						
1413		1431	X						
1410		1428			X				
1404		1422		X					
1392		1410	X						
1388		1406	X						
1384		1402	X						

---------- erosion

Table 3.2 *(left) Historically reported eruptions of Villarrica Volcano (Siebert et al., 2010) including reported VEI and lahars (bold), and the volcanic EDs (light gray) attributed to Villarrica Volcano with varve year and inferred calendar year. Historical earthquakes (EQ) and their lacustrine turbidites (LT; dark gray) are used as tie-points and added as a reference. Rep.: reported; VY: varve year; FeL: Fe-rich lamina; TEF: tephra; LAH: lahar.*

3.4.5 Event deposit chronology

The combined sedimentary records of the lakes contain a robust and virtually complete event deposit chronostratigraphy of major earthquakes, volcanic eruptions with a Volcanic Explosivity Index (VEI; Newhall and Self, 1982; Table 3.3) ≥ 2 and eruption-induced lahars for the last c. 500 years. All three lakes contain the four types of event deposits. In this section, we present a new event deposit chronology for each of these four depositional types.

Lacustrine turbidites

The four strongest earthquakes that ruptured the Valdivia rupture zone in historical times occurred in 1575, 1737, 1837 and 1960; and are all represented by lacustrine turbidites in the lakes' sedimentary sequences (LT-4, LT-3, LT-2 and LT-1, respectively). Additionally, a fifth lacustrine turbidite (LT-0) occurs at the top of some cores taken in the 2010-11 field season (Fig. 3.7 and 3.8). This lacustrine turbidite has a spatial extent comparable to that of the 1737 and 1837 turbidites and was not found in cores taken at the same locations during previous field seasons. Therefore, we

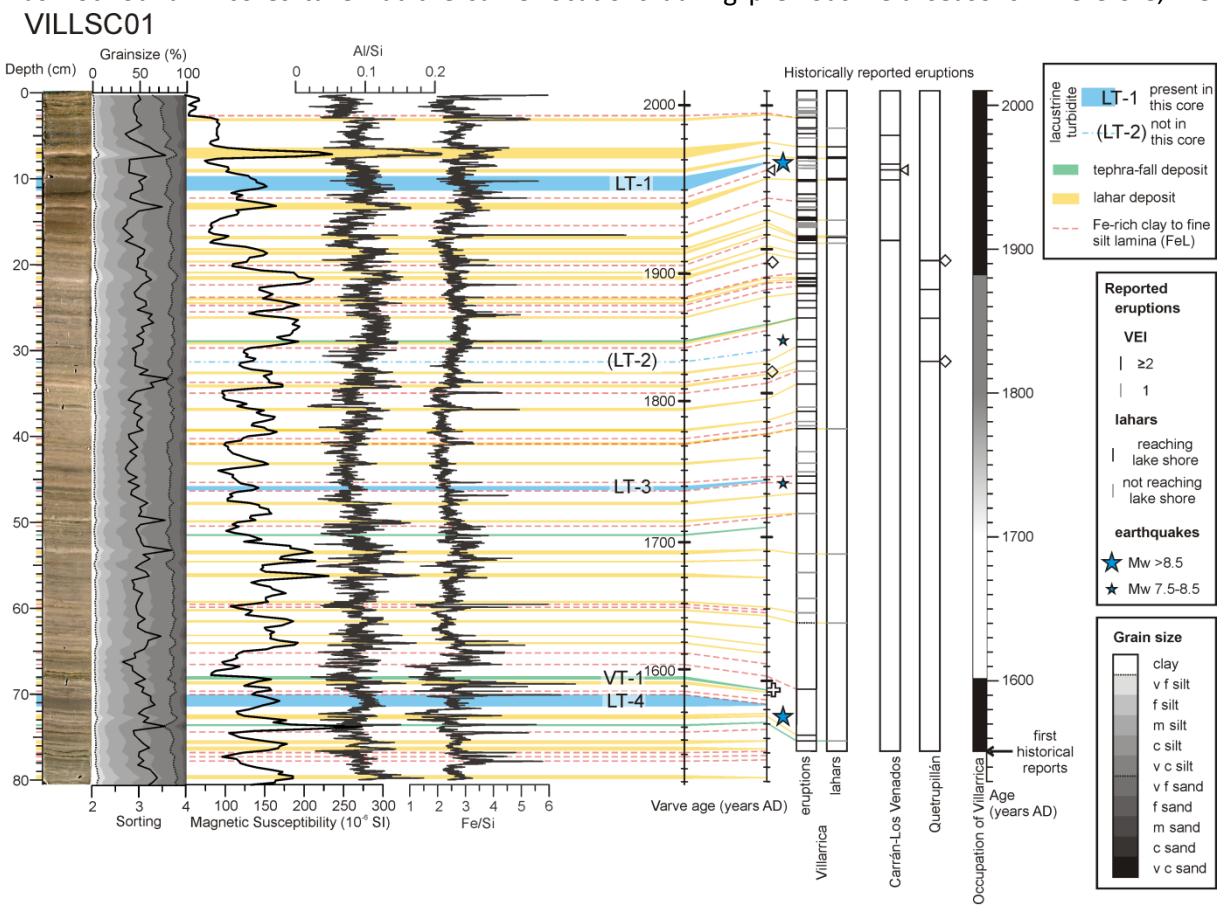

Fig. 3.14 *Picture, grain-size distribution, MS, µXRF ratios and age model (varve counting) of core VILLSC01. EDs (color coded in the same way as in Fig. 3.6) are projected on the age axis and, when possible, correlated with strong historical earthquakes in the region (stars) and eruptions of Villarrica Volcano, Quetrupillán Volcano (diamonds), the Carrán-Los Venados Volcanic Complex (triangles) and Lanín or Huanquihue volcanoes (cross). LT: lacustrine turbidite; VT: analyzed tephra-fall deposit.*

attribute LT-0 to the 2010 Maule earthquake. This observation is consistent with a seismic origin of the lacustrine turbidites observed in the studied lakes.

The youngest buried lacustrine turbidite (LT-1) present in most cores from all three lakes is attributed to the 1960 Great Chilean earthquake. The European Macroseismic Intensity of the 1960 earthquake in the study area has been estimated at VII to VIII (Lazo Hinrichs, 2008), which is equal to or higher than the minimum intensity necessary to induce subaquatic landslides and lacustrine turbidites in Alpine lakes (Monecke et al., 2004; Strasser et al., 2011). Most cores contain another lacustrine turbidite (LT-4), which has a varve age of 1583 in Lake Villarrica and 1579 in lakes Calafquén and Riñihue (Fig. 3.9, 3.11, 3.12, 3.13, 3.14 and 3.15; Table 3.2). We attribute LT-4 to the 1575 earthquake that struck Valdivia with a seismic intensity similar to that of the 1960 earthquake (Lomnitz, 2004; Cisternas et al., 2005). Between these two lacustrine turbidites, two more turbidites occur in some cores of each lake (i.e. LT-3 and LT-2). With varve ages of 1739 and 1830 in Villarrica, 1732 and 1839 in Calafquén and 1733 and 1833 in Riñihue (Fig. 3.9, 3.11, 3.12, 3.13, 3.14 and 3.15; Table 3.2), we attribute these to the major subduction earthquakes that occurred in 1737 and 1837, respectively, along the Valdivia Rupture Zone (Lomnitz, 2004; Moernaut, 2010).

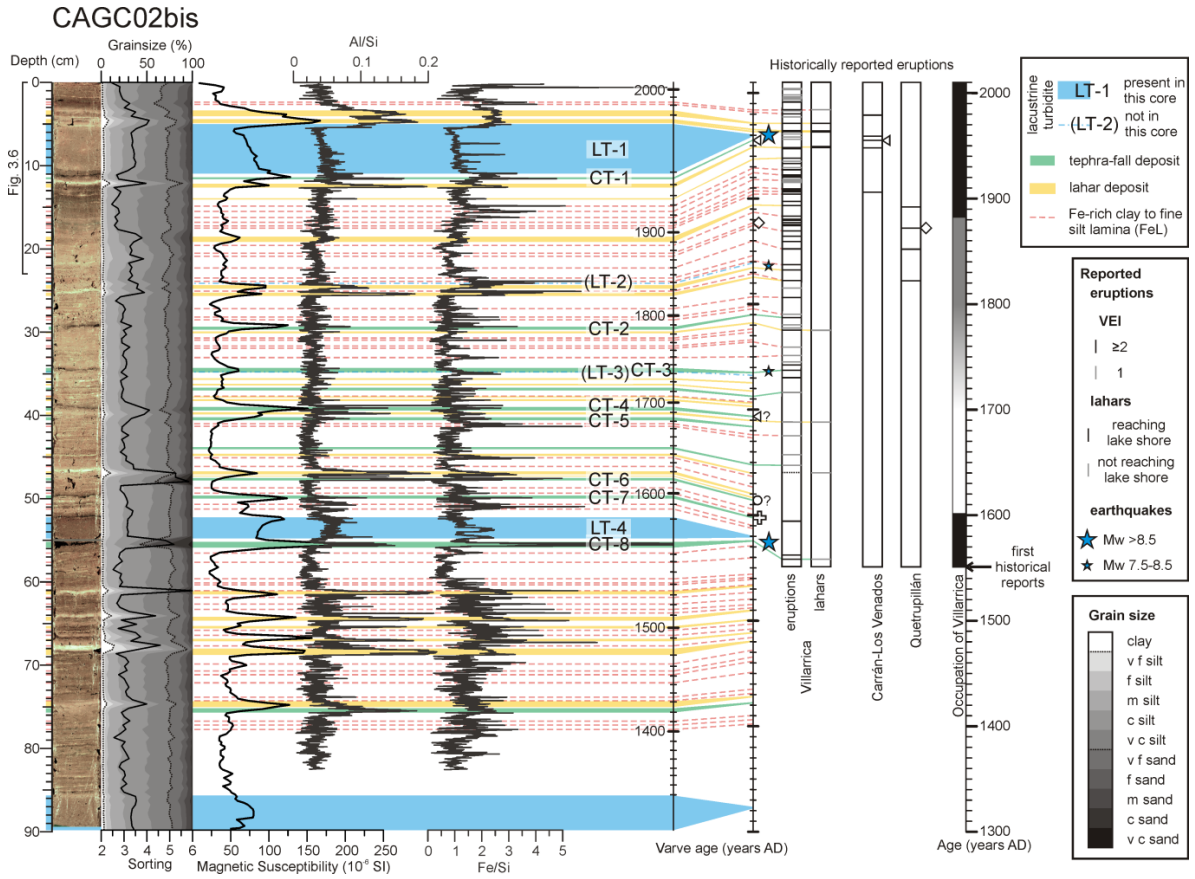

Fig. 3.15 *Picture, grain-size distribution, MS, µXRF ratios and age model (varve counting) of core CAGC02bis. EDs (color coded in the same way as in Fig. 3.6) are projected on the age axis and, when possible, correlated with strong historical earthquakes in the region (stars) and eruptions of Villarrica Volcano, Quetrupillán Volcano (diamonds), the Carrán-Los Venados Volcanic Complex (triangles), El Mocho Volcano (circle) and Lanín or Huanquihue volcanoes (cross). LT: lacustrine turbidite; CT: analyzed tephra-fall deposit.*

In addition to these five main lacustrine turbidites that occur in all three lakes, some local turbidites are also present that are inferred to be the product of small subaquatic landslides (Fig. 3.7, 3.8 and 3.9). These were probably generated by small, local earthquakes or by more distant, large earthquakes.

Table 3.3 *Criteria for estimation of the Volcanic Explosivity Index (VEI), listed in order of reliability. Adapted from Newhall and Self (1982).*

	not recorded		recorded in the studied lakes						
Criteria ***VEI***	**0**	**1**	**2**	**3**	**4**	**5**	**6**	**7**	**8**
Description	non-explosive	small	moderate	mod-large	large	very large			
Volume of ejecta (m³)	$<10^4$	10^4-10^6	10^6-10^7	10^7-10^8	10^8-10^9	10^9-10^{10}	10^{10}-10^{11}	10^{11}-10^{12}	$>10^{12}$
*Column height (km)**	<0.1	0.1-1	1-5	3-15	10-25	>25			
Qualitative description	gentle, effusive		explosive		cataclysmic, paroxysmal, colossal				
				severe, violent, terrific					
Classification		Strombolian			Plinian				
	Hawaiian		Vulcanian			Ultraplinian			
Duration		<1			>12				
of continuous blast			1-6						
				6-12					
Tropospheric injection	negligible	minor	moderate	substantial					

* For VEI's 0-2, uses km above crater; for VEI's 3-8, uses km above sea level

Volcanic-eruption-induced EDs

Apart from one lahar pathway on the western slope of Villarrica Volcano, the catchment areas of lakes Villarrica and Calafquén cover all the slopes of the volcano (Fig. 3.1). This near-complete coverage of the volcano ensures that all events that altered the volcano's surface to a certain degree are likely to be detected somehow in at least one of the lakes.

In this section, we attribute the three types of volcanic eruption-induced EDs to historically known eruptions using age-depth models with lacustrine turbidites as correlation tie-points. From the 20th century onwards, historical reports are more or less complete and reliable, and we were able to calibrate the sedimentary record by comparing historical reports to the record of volcanic EDs in lakes Villarrica and Calafquén. For each of the 17 VEI ≥ 2 eruptions of Villarrica Volcano described in 20th century historical records, as well as one VEI 1 eruption (1915-1918), an ED was identified in lakes Calafquén and/or Villarrica, under the form of tephra-fall, FeLs or lahar deposits. The robust correlation for the 20th century record allows the reconstruction of a volcanic eruptive event stratigraphy for Villarrica Volcano for the last c. 500 years (Table 3.2). Volcanic-eruption induced EDs were correlated between lakes (especially lakes Villarrica and Calafquén) and matched to historical eruptions, resulting in a calibrated varve age or calendar age. Where no historical match exists, a calendar age was calculated for the ED from the varve age by linear interpolation between calendar ages of the previous and next ED linked to a historical earthquake or eruption. Inter-lake correlation of some of the EDs revealed local offsets (of the order of a few years) in the varve-based age model, especially in Lake Villarrica. These offsets are due to parts in the core in which varves are unclear because of higher amounts of terrestrial input, masking the diatom bloom bed.

Tephra fall-out layers and FeLs. Several thin FeLs occur in the 20th century sediments from lakes Calafquén and Villarrica. Only one of these laminae could not be linked to a historically described eruption of Villarrica Volcano. The two youngest FeLs occur in varve years 1982 and 1984 and are correlated to the two VEI 2 eruptions of 1980 and 1984, respectively (Fig. 3.6 and 3.15). Above these events, the Fe/Si ratio of the background sediment gradually decreases (Fig. 3.6). This is interpreted as the result of fine ash deposited in the catchment area, gradually getting washed into rivers and the lakes for months to years after the eruption.

Numerous FeLs observed in Lake Calafquén at varve years 1904, 1907, 1910, 1918, 1924 and 1929 can be correlated to historical Villarrica eruptions in 1904, 1906, 1909, 1915-1918, 1922 and 1927, respectively (Fig. 3.15, Table 3.2). All have a VEI of 2, with the exception of the VEI 1 1915-1918 eruption. Lake Villarrica contains FeLs in varve years 1908, 1935, 1955 and 1994, the latter three of which can be correlated to the eruptions of 1933, 1955-56 and 1991, respectively (Fig. 3.14; Table 3.2). In the entire studied time period, 73 FeLs were detected in lakes Calafquén and/or Villarrica and because of the strong correlation with historical eruptions in the 20th century record, we also attribute older FeLs to VEI ≥ 2 eruptions of Villarrica Volcano.

Since 1400, 10 Villarrica eruptions directly deposited tephra fall in lakes Villarrica and/or Calafquén (Table 3.2). This number is much lower than the 73 FeLs in our records. This can be explained by the predominant westerly wind directions in this region (Kalnay et al., 1996; Meruane et al., 2005), blowing ash clouds towards the east, away from the lakes.

The glass major element geochemistry of the tephra-fall deposits (CT-2, CT-3, CT-5 and CT-8; Fig. 3.8 and 3.15) attributed to Villarrica Volcano corresponds well with previously published whole-rock data of deposits from Villarrica Volcano (Hickey-Vargas et al., 1989; Costantini et al., 2011; Lohmar et al., 2012; Fig. 3.16, Table 3.4). Also CT-6 follows this trend, however, a significant amount of Cr in the Ti-magnetites differentiate this tephra from the other tephras and might indicate a different subduction-proximal source, such as El Mocho Volcano. The phenocryst assemblage of the Villarrica tephras is characterized by plagioclase, olivine, Ti-magnetite and clinopyroxene (clinoenstatite pigeonite), in decreasing order of abundance.

Not all tephra-fall layers can be attributed to Villarrica Volcano. Tephra-fall deposits CT-9 and VT-2 have distinct glass geochemistry (Fig. 3.16; Table 3.4) with significant higher K_2O contents than the Villarrica tephra-fall deposits and similar to the whole-rock data for dacitic rocks from the historically active Quetrupillán Volcano (Hickey-Vargas et al., 1989; Fig. 3.16). Moreover, the tephra-fall deposits are covered by a lahar deposit in both lakes Calafquén and Villarrica, confirming the link with Quetrupillán Volcano, the slopes of which contribute to both of the lakes' catchments.

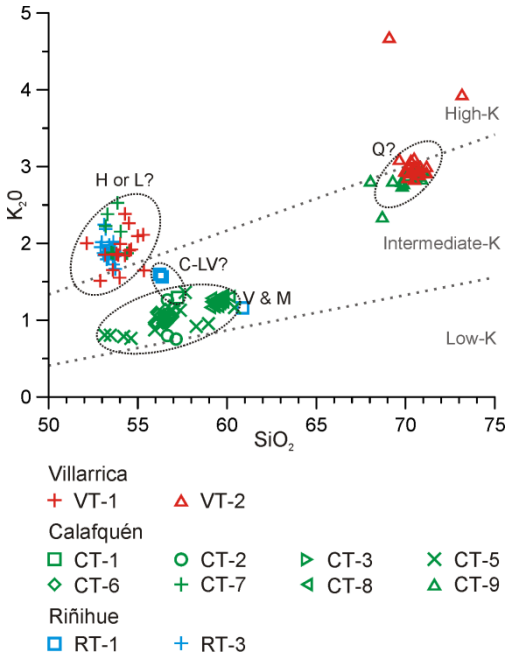

Fig. 3.16 *K_2O/SiO_2 (wt%) diagram of glass shards in the analyzed tephra-fall deposits in lakes Villarrica (red; location: Fig. 3.7 and 3.14), Calafquén (green; location: Fig. 3.8 and 3.15) and Riñihue (blue; location: Fig. 3.9), and the inferred source volcanoes. Source volcanoes: C-LV: Carrán-Los Venados; H: Huanquihue; L: Lanín; M: El Mocho; Q: Quetrupillán; V: Villarrica. K-divisions are taken from Gill (1981).*

Tephras CT-1 and RT-1 occur in varve years 1956 (Fig. 3.15) and 1954 (Fig. 3.9), respectively. Both tephras have a very similar mineralogy: they show signs of contamination by a granite-like basement (occurrence of free quartz, biotite, zircon, clinopyroxene (augite) and titanite). This is not found in the tephra-fall deposits linked to Villarrica, so we infer that these free xenocrysts are not part of the background sediment, but were indeed erupted and deposited together with the juvenile tephra. The high number of microlites in the glass complicates geochemical characterization, but nevertheless we attribute this higher-K_2O tephra-fall deposit to the 1955 VEI 4 eruption of the Carrán-Los Venados Volcanic Complex (Petit-Breuilh, 2004; Siebert et al., 2010). During this eruption southerly winds caused fine ashfall as far north as Santiago (Stern et al., 2007). A single FeL in the more remote Lake Villarrica in varve year 1955 (Fig. 3.14) was linked to the same eruption.

Tephras CT-4 and RT-2 were mineralogically linked, but also here lacking microlite-free glass inhibited characterization of glass geochemistry. Just like CT-1 and RT-1, there are signs for granitic contamination, in this case by the occurrence of free quartz, biotite, alkali feldspar, augite and titanite. Based on mineralogy, the high amount of microlites and the coarser grain size of RT-2, this tephra-fall deposit is also tentatively attributed to the Carrán-Los Venados Volcanic Complex.

Table 3.4 *Averaged electron microprobe analyses on glass shards of selected tephra-fall deposits, normalized to 100%. Number of analyzed shards (n°) and if applicable, standard devation (SD) is added.*

	Villarrica				Calafquén														Riñihue			
	VT-1		**VT-2**		**CT-1**		**CT-2**		**CT-3**		**CT-5**		**CT-6**		**CT-7**		**CT-8**		**CT-9**		**RT-1**		**RT-3**	
	wt.%	SD	wt.%	SD	wt.%	SD	wt.%	SD	wt.%	SD	wt.%	SD	wt.%	SD	wt.%	SD	wt.%	SD	wt.%	SD	wt.%	SD	wt.%	SD
SiO_2	54,09	0,86	70,54	0,83	57,23		56,82	0,28	57,05		56,21	2,46	56,54	0,33	53,70	0,43	59,52	0,28	70,07	0,81	57,82	2,65	53,41	0,25
TiO_2	2,16	0,17	0,65	0,08	1,98		1,53	0,28	2,00		1,54	0,22	1,46	0,06	2,23	0,16	1,38	0,05	0,67	0,08	2,02	0,56	2,21	0,06
Al_2O_3	14,72	0,68	14,06	0,35	13,44		15,76	0,92	14,86		14,96	0,58	15,62	0,18	14,14	0,79	15,86	0,17	14,38	0,53	14,65	0,22	14,37	0,35
FeO	12,21	0,75	3,92	0,18	12,19		10,07	0,27	11,21		11,05	1,19	9,25	0,18	12,72	0,82	8,32	0,23	3,97	0,32	9,75	0,69	12,79	0,51
MnO	0,25	0,06	0,11	0,05	0,38		0,21	0,08	0,17		0,25	0,07	0,18	0,04	0,27	0,05	0,21	0,07	0,13	0,06	0,21	0,07	0,27	0,05
MgO	3,29	0,57	0,54	0,12	2,96		2,87	0,34	2,53		3,73	1,15	4,11	0,10	3,37	0,48	2,74	0,06	0,60	0,11	3,07	0,51	3,51	0,19
CaO	6,92	0,29	1,88	0,26	6,32		6,91	0,24	6,40		7,22	1,41	7,70	0,17	6,73	0,36	5,76	0,15	2,17	0,33	6,28	0,72	6,88	0,17
Na_2O	3,89	0,35	5,06	0,43	3,88		4,53	0,08	4,31		3,79	0,42	3,85	0,20	4,16	0,35	4,64	0,16	5,04	0,22	4,28	0,33	4,12	0,26
K_2O	1,90	0,24	3,12	0,46	1,30		0,94	0,28	1,19		0,94	0,20	1,04	0,05	2,13	0,27	1,25	0,04	2,84	0,15	1,44	0,24	1,91	0,13
P_2O_5	0,57	0,05	0,12	0,02	0,32		0,37	0,15	0,28		0,29	0,10	0,26	0,02	0,55	0,04	0,31	0,02	0,13	0,03	0,47	0,11	0,54	0,03
Total	100	0,39	100	0,71	98,58		100	0,78	99,76		99,10	0,61	99,37	0,53	100	0,76	99,54	0,50	99,58	0,44	97,22	0,47	97,93	0,53
n°		16		18		1		3		1		11		25		7		21		16		3		24

VT-1, CT-7 and RT-3 have a distinct glass geochemistry (Fig. 3.16, Table 3.4). In absence of thorough geochemical characterization of most volcanoes in the study area, it is difficult to firmly attribute a source volcano to this tephra. However, the high K_2O values and the similar grain size in the three lakes suggest this tephra fall could potentially be attributed to Lanín Volcano or the historically active Huanquihue Volcano Complex (Hickey-Vargas et al., 1989; Lara et al., 2001), both more easterly (i.e. further away from the subduction zone) located volcanoes. The varve years of these three deposits are 1594, 1598 and 1592, respectively. After correction of the varve years –aided by the correlation of LT-4 to the 1575 earthquake– the tephra-fall deposited was assigned to the year 1591. The inter-lake correlation of several of these tephra-fall deposits and the limited offsets in varve age between these deposits support the varve-based age models for the three studied lakes.

Lake Riñihue has climatic and limnological conditions similar to those of lakes Villarrica and Calafquén. Its different volcanic setting make it ideal for testing the detection and characterization method for EDs. El Mocho Volcano has had fewer but larger eruptions in historical times and all of its reported 18th and 19th century eruptions (VEI ≥ 2) are recorded in Lake Riñihue. Three eruptions (1759, 1777 and 1864) are represented by FeLs, while one eruption (1822) is represented by a lahar deposit covering a tephra lamina. The two 20th century eruptions (1937 and 1955-56 (uncertain)) are not present in the Lake Riñihue sediment cores. During the last two centuries, only one tephra deposit could not be linked to a historical eruption of El Mocho Volcano (at the end of the 19th century). Before 1800 however, many FeLs and several tephra-fall deposits, which were not historically reported, occur. In general, lower in the cores, Lake Riñihue contains more FeLs and tephra-fall deposits, perhaps indicating the decreasing frequency of activity of El Mocho Volcano between the start of the 17th and the start of the 21st century (Fig. 3.9).

Detrital fining-upwards EDs (lahar deposits). All nine historically documented lahar events at Villarrica Volcano in the 20th century are represented by detrital fining-upwards EDs in lakes Calafquén and/or Villarrica. The five youngest lahar events, in 1948, 1949, 1963, 1964 and 1971, were reported to have reached both lakes Calafquén and Villarrica (Fig. 3.17, Table 3.2). All of these events are indeed represented by lahar deposits in both lakes (Fig. 3.14 and 3.15). For the four oldest 20th century events, in 1904, 1908, 1909 and 1920, lahars were only reported in the Lake Villarrica catchment, and only the 1908 lahars reached the lake shore (Fig. 3.17, Table 3.2). Indeed, these lahars are only represented in Lake Villarrica (Fig. 3.14). Lakes Calafquén and Villarrica each contain one thin (< 1 mm) lahar deposit that does not correspond to reported lahars, but which can be linked to the historical eruptions of 1938 and 1991, respectively (Fig. 3.14 and 3.15; Table 3.2). They are possibly the imprint of small lahars in the catchment.

The variations in thickness and maximum grain size of each lahar deposit in the different sediment cores correlate well with both the lake water depth and the distance to the location where the lahars entered the lake according to the historical records. Furthermore, the extent of the reported lahars correlates well with the characteristics of the lahar deposits in both lakes. When lahars were reported in channels draining towards a certain lake, but without reaching the lake shore, the lahar deposit consists of a clay to silt lamina without a coarser silt base, never exceeding a total thickness of 1 cm. Cores in the shallowest parts of the lakes only comprise a faint clay/silt lamina or no visible deposit. Lahars that were reported to have entered the lake are almost always represented by deposits that are locally thicker than 1 cm and that have coarse silt to sand bases. Major lahars (e.g., 1948 and 1971) are always represented by thick deposits in the deepest parts of the lake, locally thicker than 5 cm. Close to the shore, where core retrieval was not possible, lahar deposits are probably much thicker. The thick and coarse deposits of the 1964 lahars in the eastern part of Lake Calafquén correlate well with the large reported lahars that destroyed the village of Coñaripe at the eastern tip of the lake (Fig. 3.1 and 3.17). In shallower coring locations, the reported extent of the lahars correlates with the thickness and type of the deposit. That is, lahars not reaching the lake shore, small lahars entering the lake and large lahars entering the lake will be represented by no, faint or clear silt to clay laminae, respectively (Fig. 3.17).

Almost half of the volcanic events related to Villarrica Volcano produced a lahar deposit in lakes Villarrica and/or Calafquén, but Lake Villarrica contains more lahar deposits than Lake Calafquén. This discrepancy can be explained by the larger number of lahar pathways in Lake Villarrica's

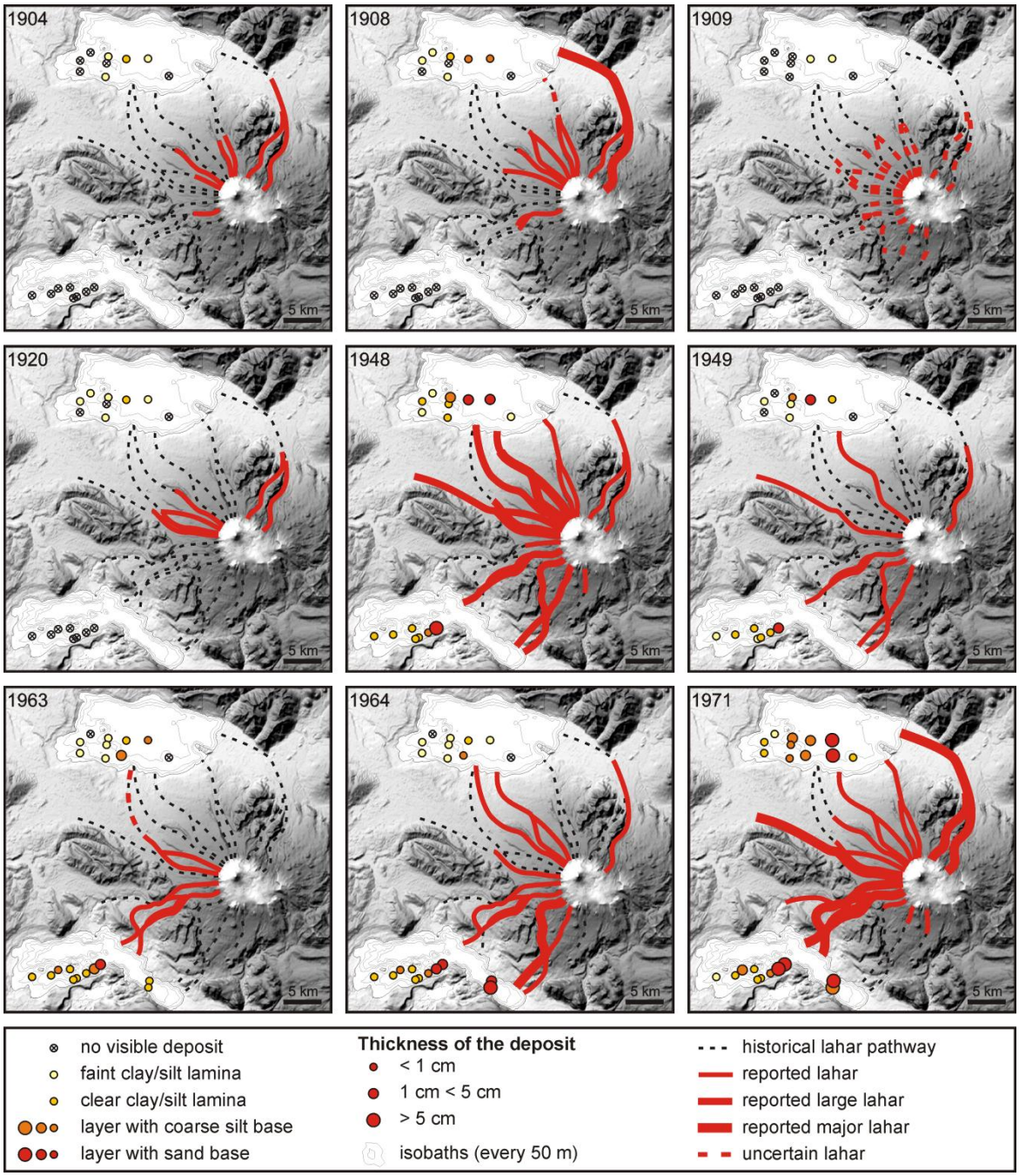

Fig. 3.17 *Historical lahar pathways compared with the thickness and maximum grain size of the linked lahar deposits.*

catchment. Most lahar deposits in Lake Villarrica are smaller or comparable in size to the 1908 lahars, which reached the lake shore. Only the 1893 and 1822 lahars seem to have been of a size similar to that of the large 1948 or 1971 lahars (Fig. 3.6, 3.15). In Lake Calafquén, several similar-sized lahar deposits occur, e.g., 1617 and 1688 lahars. In 1822, just like in 1948-49 or 1963-64, two lahar events occurred in a short period of time and are interpreted to belong to the same eruptive event (Fig. 3.8 and 3.15). Since 1400, at least 22 events occurred during which lahars reached the shores of lakes Villarrica and/or Calafquén; hence, on average almost 4 potentially destructive lahar events per 100 years. The cluster of lahar deposits between 1470 and 1530 and the lack of such deposits in the previous ~300 years (determined by extrapolation in other cores; Fig. 3.8 and 3.18) are in strong contrast with the constant activity of the volcano. The formation of lahars during an eruption

depends on many factors: i) the type of eruption, ii) the morphology of the upper volcano, iii) the availability of erodible material on the lower slopes of the volcano, iv) the availability and state of the snow cover, and v) the amount of vegetation on the slopes (Vallance, 2000). The last two variables are climate-related and are important in lahar formation and hence, might be important for this clustering. Based on the historical data however, we believe that all lahar deposits are linked to an eruption of Villarrica Volcano. Rather than rainfall or gradual snowmelt, which occur yearly, it is the sudden snowmelt during an eruption, which is the determining factor for lahar formation in this region. Hence, climatic changes can enhance or reduce the chance for a lahar to form during an eruption by providing, but not produce the lahar on its own.

In Lake Riñihue –in line with the evolution of the tephra-fall deposits and the FeLs– the lahar deposits indicate a decreasing activity of El Mocho Volcano during the past few centuries. From the start of the 14th until the start of the 18th century, lahar deposits occur frequently in the Riñihue sedimentary record. The sequence ends around 1731 with the most prominent lahar deposit. The eruption record of El Mocho Volcano in Lake Riñihue is however not complete, as only a third of the volcano's slopes are part of the Lake Riñihue sediment catchment and it can thus be expected that several eruptions are missing from the record.

3.4.6 The eruptive record of Villarrica Volcano

Due to the nearly total coverage of Villarrica Volcano by the combined catchments of lakes Villarrica and Calafquén, we do have a complete VEI ≥ 2 eruptive record for this volcano. The correlation between the number of reported eruptions and our eruption record is closely linked with the development of the town of Villarrica. Essentially, the number of reported eruptions is larger during periods of increased population in the region. Before 1860, the number of historically reported eruptions is much smaller than the number of actual volcanic EDs. During the last 150 years the reports gradually became more detailed and the assignment of an accurate VEI has improved. The number of reported small eruptions (VEI 1; Table 3.3) is higher in the last century and has significantly increased since the start of the Villarrica Volcano Visual Observation Project (POVI; http://www.povi.cl) in 1996 (Fig. 3.18).

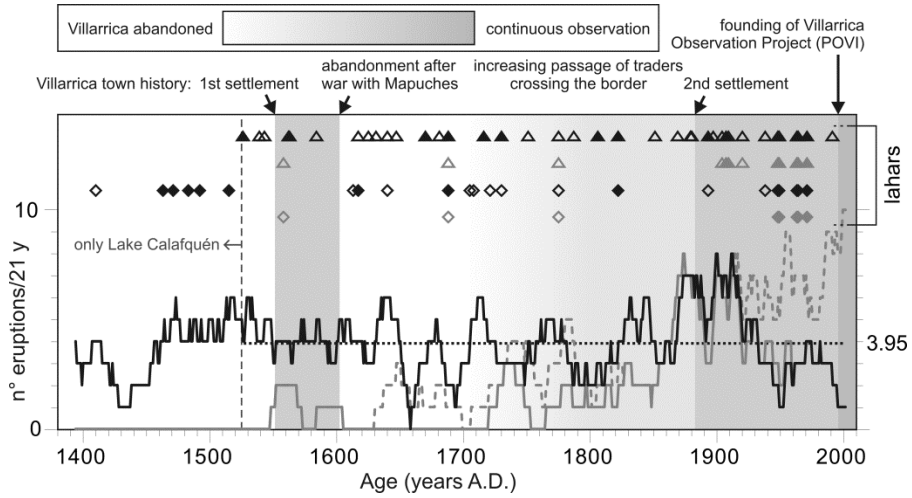

Fig. 3.18 *Eruption record of this study compared to historical records. Amount of eruptions per 21 years according to this study (black solid line), retrieved from historical reports (gray dashed line) and VEI ≥ 2 eruptions retrieved from historical reports (gray solid line). Lahars towards Lake Villarrica are indicated with a triangle and towards Lake Calafquén with a diamond (black: lahar deposits; gray: historical reports; filled: lahars reaching the lake shore; open: not reaching the lake shore).*

Overall, our record comprises 112 EDs of which 47 could be matched with historically known eruptions. Half of the historically known eruptions were large enough to be detected in both lakes, while three quarters of the newly described eruptions were smaller and found only in one of the lakes (Table 3.2). Between 1523 and 2011, when data from both lakes Calafquén and Villarrica are available, our eruption record contains 88 EDs, with on average 1 eruption (VEI ≥ 2) every 5.32 years (or 3.95 eruptions/21 years; Fig. 3.18, 3.19B). The period between 1870 and 1910 is marked by higher volcanic activity (Fig. 3.18 and 3.19A). During this period a VEI ≥ 2 eruption occurred once every 2.68 years.

3.4.7 Probability of a future eruption

The new VEI ≥ 2 eruption time series of Villarrica Volcano –with 88 eruptions since 1523– was statistically examined to provide a probability estimate for the occurrence of future eruptions. Dzierma and Wehrmann (2010) applied statistical techniques on the time series of historical records of Villarrica and Llaima eruptions. However, Fig. 3.18 highlights the comparative incompleteness of the pre-1860 historical records used by Dzierma and Wehrmann (2010). Here we repeat the same statistical analyses based on the new (and more complete, i.e. 45 new VEI ≥ 2 eruptions) combined Villarrica-Calafquén lacustrine eruption record from 1523 to 1991, the year of the last VEI 2 eruption (Fig. 3.18). We also refer to Dzierma and Wehrmann (2010) for more detailed information on the analysis technique.

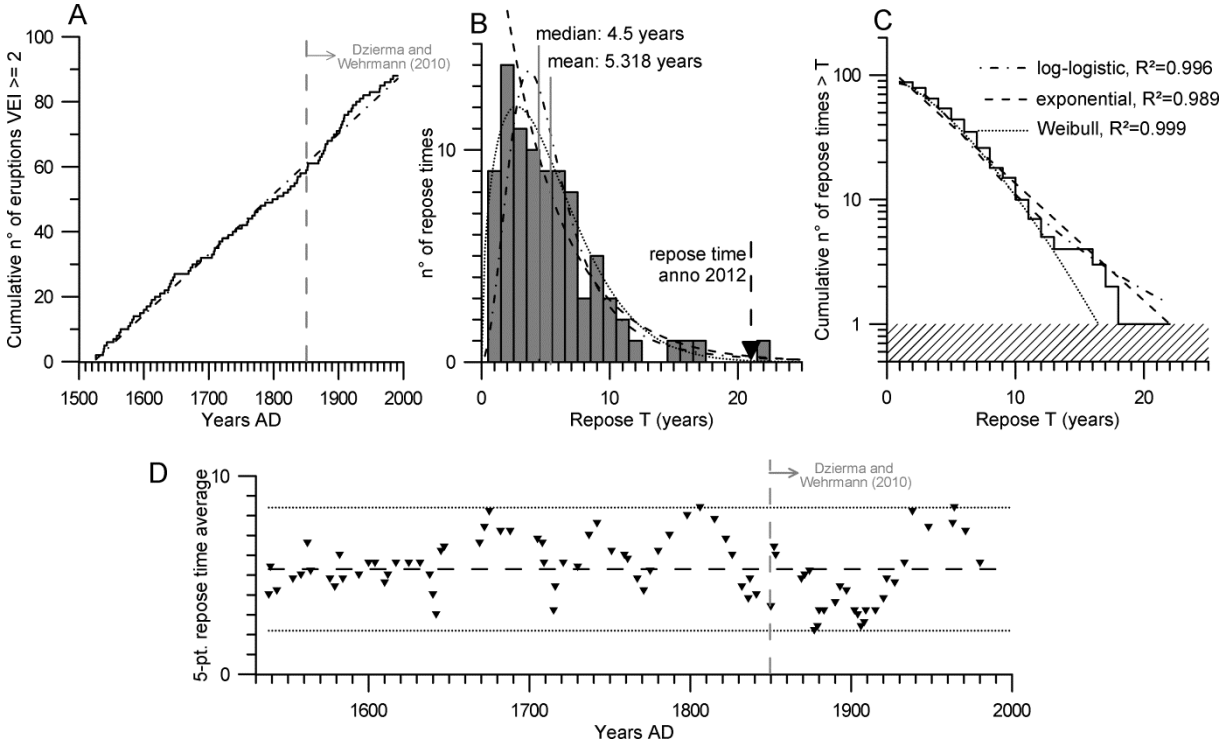

Fig. 3.19 *Statistical analyses of Villarrica Volcano eruption (VEI ≥ 2) time series obtained in this study (1523 – 1991, the period for which both lakes provide a record), based on Dzierma and Wehrmann (2010). A: cumulative number of eruptions over the studied time period; B: histogram of repose times (time between 2 consecutive eruptions) and log-logistic (dash-dot), exponential (dashed) and Weibull (dotted) distributions; C: cumulative repose time distributions: log-logistic, exponential and Weibull; and D: test for stationarity: 5-point moving average of repose times over time (triangles) with mean (dashed line) and its 95 % confidence interval (dotted line).*

We first tested if the eruptions in the time series occur independently from one another, by calculating the correlation coefficient of all successive repose times. The resulting correlation coefficient R=0.073 is even lower than the R=0.16 of Dzierma and Wehrmann (2010) and is therefore consistent with the hypothesis of no correlation, meaning that memory effects between successive eruptions are lacking and the time series can be modeled as a Poisson process (three distributions will be modeled).

To test whether the repose time series is stationary, with one distribution explaining the entire examined time interval, a moving-average test was implemented. The average of each five successive repose times was calculated. The 5-point repose time averages for the last 500 years fall within the 95% confidence interval, but approximate both upper and lower boundaries closely (Fig. 3.19D). The repose time series can be regarded as stationary (i.e. a stable eruption regime through time), although the occurrence of clusters cannot be ruled out. Both results are in contrast with the results of Dzierma and Whermann (2010), who could not confirm stationarity for the early eruption record. They attributed this result to a change in eruption frequency or incompleteness of the early eruption record. Based on our new data, we can reject the first option and confirm the latter. Moreover, some large repose times in their early record widened the confidence interval, leading to the flawed conclusion of stationarity in the most recent period. A critical review of the completeness of historical records by e.g. comparison with the local or regional history –as we did in Fig. 3.18– is highly recommended for other study areas as well.

Three types of distributions were fitted to the cumulative number of repose times: a Weibull (favoring stationarity, i.e. continuous rising of the probability of an eruption in a certain year after the last eruption), a log-logistic (favoring some clustering, i.e. initial fast rising probability, followed by a decrease) and an exponential (intermediate, i.e. a constant identical probability) distribution (Fig. 3.19B and C). The best model for the histogram of the repose times is a Weibull distribution (based on highest R^2 and best Kolmogorov-Smirnov test results; Fig. 3.19C), which is for the short repose times (<10 years) visible in Fig. 3.19B. However, for longer repose times (>10 years), the log-logistic and exponential distributions provide more reliable estimates (Fig. 3.19B and C).

At the time of writing, the last VEI ≥ 2 eruption happened 21 years ago in 1991, an uncommonly long repose in the past 600 years. The probability of a 21-year period without VEI ≥ 2 eruptions is ≤ 1.9%: the Weibull model reached a 99.9% (= 100% - 0.1%) probability, the log-logistic and exponential models resulted in probabilities of 98.1% (= 100% - 1.9%) and 99.0% (= 100% - 1.0%), respectively (Fig. 3.20). In the Weibull model, the probability of a new VEI ≥ 2 eruption in a certain year or period –given that no VEI ≥ 2 eruption has occurred in the meantime– is at this moment continuously rising, for the exponential model this probability stays equal, while for the log-logistic model the probability of a new eruption decreases with time (Fig. 3.20B and C). The better model for longer repose times of the latter two distributions suggests that there might be some clustering for VEI ≥ 2 eruptions. This raises the question of whether the high number of reported VEI 1 eruptions and continuous degassing from an active lava lake during the last two decades (Witter et al., 2004) is only due to more continuous observations (we do not have information on the existence of a lava lake and thus an open conduit system before this period) or also reflects real changes in eruptive mode. In the latter case, this activity may decrease the probability of a VEI ≥ 2 eruption, favoring the log-logistic and exponential models.

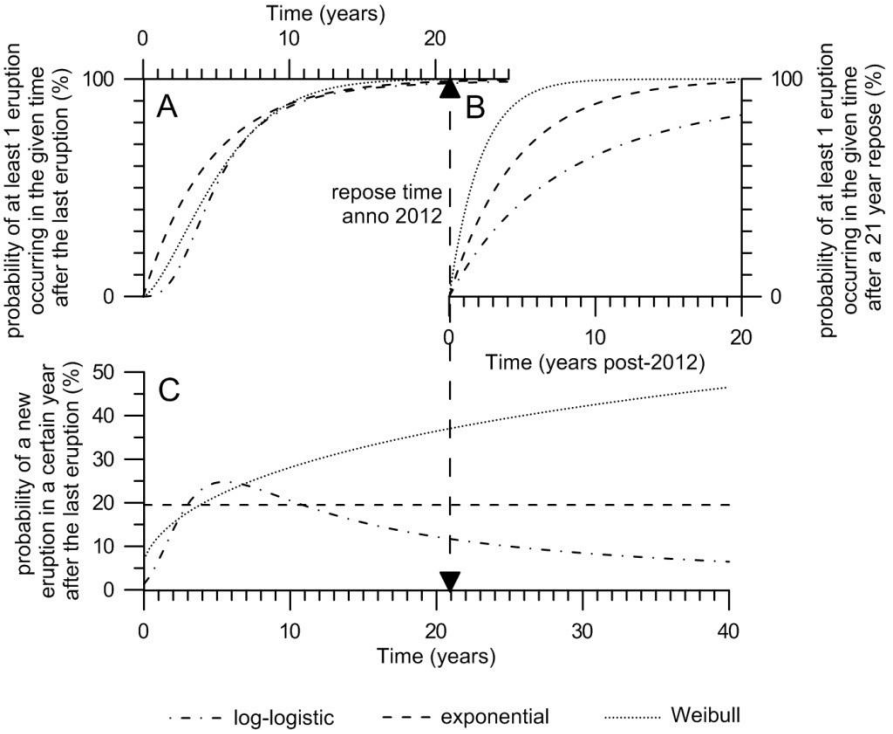

Fig. 3.20 *Probability of at least one VEI ≥ 2 eruption occurring in the given time after A) the last eruption and B) a 21 year repose; C) probability of a new eruption in a certain year after the last eruption.*

To summarize, our new lacustrine-based eruption time series suggests that a VEI ≥ 2 eruption from Villarrica in the near future is likely. This study is an addition to previous studies on volcanic hazards in the Villarrica region such as the volcanic hazard map by Moreno (2000) and the overview presented by Lara (2004). We provide time series that can be used to better assess the hazards in different areas of the volcano already depicted by Moreno (2000). In particular, improved hazard assessments for lahars on the many historical lahar pathways should be a priority because of their flat morphology and proximity to beaches which are usually preferred for building tourist accommodation. We note, however, that lahars occur on a more irregular basis especially in the Lake Calafquén catchment, and a possible climatic control on lahar formation must be further examined to be able to provide probability estimates for lahar occurrence.

3.5 Conclusions

1) Using high-resolution multi-proxy analyses of sediment cores in lakes Villarrica, Calafquén and Riñihue we have constructed a new, more detailed and reliable 500-year-long eruption record for Villarrica and surrounding volcanoes in the Chilean Lake District between 39° and 40° S.

2) A combination of µXRF scanning combined with standard sedimentological techniques allowed the systematic detection of very thin event deposits (EDs) in an objective and efficient manner down to a thickness of 100 µm. We detected and classified four types of EDs and divided them into two groups, lacustrine turbidites and volcanic eruption-induced EDs.

(i) Lacustrine turbidites are homogenous deposits that fine upwards and have a composition similar to that of the background sediment. They can all be attributed to known megathrust earthquakes

(ii) Volcanic eruption-induced EDs were subdivided into three sub-types: ***a) tephra fall-out layers:*** characterized by draping coarse ash with very high Fe/Si and high Al/Si ratios; ***b) Fe-rich clay to fine silt laminae (FeLs):*** clays and fine silts with a high Fe/Si ratio, that record fluvial erosion and transport of cryptotephra into the lake; ***c) lahar deposits:*** fining upwards EDs with coarse basal deposits close to the inflow (high Fe/Si) and a fine silt to clay with the same composition as the detrital component of the background sediment (high Al/Si and Fe/Si)

3) Our lacustrine dataset significantly improves the eruption record of Villarrica Volcano, with a total 88 VEI ≥ 2 eruptions identified between 1523 and 1991, and incomplete since ~1350 (only Lake Calafquén), with 112 eruptions. Villarrica Volcano has experienced nearly constant eruptive activity during the past 600 years with an average and median since 1523 of one eruption (VEI ≥ 2) every 5.32 and 4.5 years, respectively. The last VEI ≥ 2 eruption occurred in 1991. The probability of a 21-year repose period (anno 2012) is ≤ 1.9 %. Based on the last 600 years, we conclude that there is a high probability of a VEI ≥ 2 eruption in the near future. However, the possibility of cluster occurrence and hence, a temporarily decreasing activity, cannot be excluded.

4) Probability estimates should be used to improve existing hazard assessments for Villarrica Volcano region.

5) Apart from Villarrica, tephra-fall deposits have been geochemically and mineralogically linked to the Carrán-Los Nevados Volcanic Complex, El Mocho, Quetrupillán and Huanquihue or Lanín volcanoes. El Mocho Volcano has possibly experienced a decrease in activity frequency during the last centuries.

Acknowledgements

This research was funded mainly by the Fund for Scientific Research Flanders (FWO-Vlaanderen) and by the Special Research Fund of Ghent University (BOF). We thank the GSA Limnogeology Division for the Kerry Kelts award and IAS for the postgraduate student grant, both used in the last field season. M. Vinckx is acknowledged for the use of the Malvern Mastersizer 2000. We thank Ph. De Smedt for sharing the Bartington MSE2 point sensor. Special thanks to J. Yurcika for the help during thin-section preparation and to P. Van den haute for putting the thin-section lab at our disposal. We are grateful to V. Cnudde for use of the petrographic microscope and J. Mortier for help with the use of the SEM. We thank N. Fagel for performing the XRD measurements. We are grateful to R. Brümmer for help with logistics etc. in Valdivia. Finally we thank A. Peña for the invaluable assistance on the field. We acknowledge the constructive reviews of W. Scott and an anonymous reviewer. K. Fontijn is supported by NERC grant NE/I013210/1. J. Moernaut acknowledges the support of the Research Foundation Flanders (FWO-Vlaanderen) and the Swiss National Science Foundation (grant 133481). M. Van Daele is currently funded by FWO-Vlaanderen.

References

Angermann, D., Klotz, J. and Reigber, C. (1999) Space-geodetic estimation of the nazca-south america euler vector. *Earth and Planetary Science Letters*, **171,** 329-334.

Arnaud, F., Magand, O., Chapron, E., Bertrand, S., Boes, X., Charlet, F. and Melieres, M. (2006) Radionuclide dating ((210) Pb,(137) Cs,(241) Am) of recent lake sediments in a highly active

geodynamic setting (Lakes Puyehue and Icalma-Chilean Lake District). *Sci Total Environ*, **366,** 837-850.

Beck, C. (2009) "Late Quaternary lacustrine paleo-seismic archives in north-western Alps: Examples of earthquake-origin assessment of sedimentary disturbances". *Earth-Science Reviews*, **96,** 327-344.

Bertrand, S. and Fagel, N. (2008) Nature, origin, transport and deposition of andosol parent material in south-central Chile (36-42°S). *Catena*, **73,** 10-22.

Bertrand, S., Charlet, F., Chapron, E., Fagel, N. and De Batist, M. (2008a) Reconstruction of the Holocene seismotectonic activity of the Southern Andes from seismites recorded in Lago Icalma, Chile, 39°S. *Palaeogeography, Palaeoclimatology, Palaeoecology*, **259,** 301-322.

Bertrand, S., Castiaux, J. and Juvigné, E. (2008b) Tephrostratigraphy of the Late Glacial and Holocene sediments of Puyehue Lake (Southern Volcanic Zone, Chile 40°S). *Quaternary Research*, **70,** 343-357.

Boës, X. and Fagel, N. (2008) Relationship between southern Chilean varved lake sediments, precipitation and ENSO for the last 600 years. *Journal of Paleolimnology*, **39,** 237-252.

Campos, H., Steffen, W., Román, C., Zúñiga, L. and Agüero, G. (1983) Limnological studies in Lake Villarrica: Morphometric, physical, chemical, planktonical factors and primary productivity. *Archiv für Hydrobiologie Supplement*, **65,** 371-406.

Campos, H., Steffen, W., Agüero, G., Parra, O. and Zúñiga, L. (1987) Limnology of lake Riñihue. *Limnologica*, **18,** 339-357.

Campos, H., Steffen, W., Agüero, G., Parra, O. and Zúñiga, L. (1989) Estudios limnologicos en el Lago Puyehue (Chile) : Morfometria, factores fisicos y quimicos, plancton y productividad ad primaria. *Medio Ambiente*, **10,** 36-53.

Carn, S.A., Pallister, J.S., Lara, L., Ewert, J.W., Watt, S., Prata, A.J., Thomas, R.J. and Villarosa, G. (2009) The unexpected awakening of Chaitén Volcano, Chile. *EOS, Transactions, American Geophysical union*, **90**.

Castruccio, A., Clavero, J. and Rivera, A. (2010) Comparative study of lahars generated by the 1961 and 1971 eruptions of Calbuco and Villarrica volcanoes, Southern Andes of Chile. *Journal of Volcanology and Geothermal Research*, **190,** 297-311.

Cembrano, J., Schermer, E., Lavenu, A. and Sanhueza, A. (2000) Contrasting nature of deformation along an intra-arc shear zone, the Liquine-Ofqui fault zone, southern Chilean Andes. *Tectonophysics*, **319,** 129-149.

Chapron, E., Ariztegui, D., Mulsow, S., Villarosa, G., Pino, M., Outes, V., Juvignié, E. and Crivelli, E. (2006) Impact of the 1960 major subduction earthquake in Northern Patagonia (Chile, Argentina). *Quaternary International*, **158,** 58-71.

Chapron, E., Juvigné, E., Mulsow, S., Ariztegui, D., Magand, O., Bertrand, S., Pino, M. and Chapron, O. (2007) Recent clastic sedimentation processes in Lake Puyehue (Chilean Lake District, 40.5°S). *Sedimentary Geology*, **201** 365-385.

Cifuentes, I.L. (1989) The 1960 Chilean earthquakes. *Journal of Geophysical Research-Solid Earth and*

Planets, **94,** 665-680.

Cisternas, M., Atwater, B.F., Torrejon, F., Sawai, Y., Machuca, G., Lagos, M., Eipert, A., Youlton, C., Salgado, I., Kamataki, T., Shishikura, M., Rajendran, C.P., Malik, J.K., Rizal, Y. and Husni, M. (2005) Predecessors of the giant 1960 Chile earthquake. *Nature*, **437,** 404-407.

Costantini, L., Pioli, L., Bonadonna, C., Clavero, J. and Longchamp, C. (2011) A Late Holocene explosive mafic eruption of Villarrica volcano, Southern Andes: The Chaimilla deposit. *Journal of Volcanology and Geothermal Research*, **200,** 143-158.

DeMets, C., Gordon, R.G., Argus, D.F. and Stein, S. (1994) Effect of recent revisions to the geomagnetic reversal time scale on estimates of current plate motions. *Geophysical Research Letters*, **21,** 2191-2194.

Dzierma, Y. and Wehrmann, H. (2010) Eruption time series statistically examined: Probablilities of future eruptions at Villarrica and Llaima Volcanoes, Southern Volcanice Zone, Chile. *Journal of Volcanology and Geothermal Research*, **193,** 82-92.

González-Ferrán, O. (1994) *Volcanes De Chile*. Instituto geografico militar, Santiago, 642 pp.

Gill, J.B. (1981) *Orogenic Andesites and Plate* Tectonics. Springer Verlag, Berlin Heidelberg, New York, 385 p.

Heirman, K. (2011) *'A Wind of Change': Changes in Position and Intensity of the Southern Hemisphere Westerlies during Oxygen Isotope Stages 3, 2 and 1.* Unpublished PhD Thesis, Ghent University, Ghent, 227 p.

Heusser, C. (2003) Ice age Southern Andes - A chronicle of palaeoecological events. Elsevier, Amsterdam.

Hickey -Vargas, R., Roa, H.M., Escobar, L.L. and Frey, F.A. (1989) Geochemical variations in Andean basaltic and silicic lavas from the Villarrica-Lanin volcanic chain (39.5Â° S): an evaluation of source heterogeneity, fractional crystallization and crustal assimilation. Contributions to Mineralogy and Petrology, **103,** 361-386.

Kalnay, E., Kanamitsu, M., Kistler, R., Collins, W., Deaven, D., Gandin, L., Iredell, M., Saha, S., White, G., Woollen, J., Zhu, Y., Leetmaa, A., Reynolds, R., Chelliah, M., Ebisuzaki, W., Higgins, W., Janowiak, J., Mo, K.C., Ropelewski, C., Wang, J., Jenne, R. and Joseph, D. (1996) The NCEP/NCAR 40-Year Reanalysis Project. Bulletin of the American Meteorological Society, **77,** 437-471.

Katsuta, N., Takano, M., Kawakami, S.I., Togami, S., Fukusawa, H., Kumazawa, M. and Yasuda, Y. (2007) Advanced Micro-XRF method to separate sedimentary rhythms and event layers in sediments: Its application to lacustrine sediment from Lake Suigetsu, Japan. Journal of Paleolimnology, **37,** 259-271.

Keller, W., Bacher, H., Marfull, V. and Koller, A. 2008. Historia Eruptiva. Villarrica Volcano Visual Observation Project (POVI), last accessed september 2011.

Kylander, M.E., Lind, E.M., Wastegård, S. and Löwemark, L. (2011) Recommendations for using XRF core scanning as a tool in tephrochronology. The Holocene, **22,** 371-375.

Lara, L., Rodríguez, C., Moreno, H. and Pérez de Arce, C. 2001. Geocronología K-Ar y geoquímica del volcanismo plioceno superior-pleistoceno de los Andes del sur (39-42°S), **28,** pp. 67-90. scielocl.

Lara, L.E. (2004) Overview of Villarrica Volcano. In: Villarrica Volcano (39.5°S), Southern Andes, Chile (Eds L.E. Lara and J. Clavero), **61,** pp. 5-12. Servicio Nacional de Geología y Minería.

Lara, L.E. (2009) The 2008 eruption of the Chaiten Volcano, Chile: a preliminary report. Andean Geology, **36,** 125-129.

Laugenie, C. (1982) La région des lacs, Chili méridional, Université de Bordeaux III, Bordeaux, France, 822 pp.

Lazo, R.G. (2008) Estudio de los daños de los terremotos del 21 y 22 de mayo de 1960, Universidad de Chile, Santiago, 427 pp.

Lohmar, S., Parada, M., Gutierrez, F., Robin, C. and Gerbe, M.C. (2012) Mineralogical and numerical approaches to establish the pre-eruptive conditions of the mafic Lican Ignimbrite, Villarrica Volcano (Chilean Southern Andes). Journal of Volcanology and Geothermal Research, **235,** 55-69.

Lomnitz, C. (2004) Major earthquakes of Chile: A historical survey, 1535-1960. Seismological Research Letters, **75,** 368-378.

Melnick, D., Bookhagen, B., Strecker, M.R. and Echtler, H.P. (2009) Segmentation of megathrust rupture zones from fore-arc deformation patterns over hundreds to millions of years, Arauco peninsula, Chile. Journal of Geophysical Research-Solid Earth, **114**.

Meruane, C., Niño, Y. and Garreaud, R. (2005) Response of the thermal structure of lake Villarrica (Chile) to strong foehn like wind: field study and numerical simulations. In: MECOM**,** pp. 37. Universidad de Chile, Santiago de Chile.

Moernaut, J. (2010) Sublacustrine landslide processes and their paleoseismological significance: Revealing the recurrence rate of giant earthquakes in South-Central Chile. PhD, Ghent University, Ghent, 274 pp.

Moernaut, J., De Batist, M., Heirman, K., Van Daele, M., Pino, M., Brümmer, R. and Urrutia, R. (2009) Fluidization of burried mass-wasting deposits in lake sediments and its relevance for paleoseismology: Results from a reflection seismic study of lakes Villarrica and Calafquén (South-Central Chile). Sedimentary Geology, **213,** 121-135.

Monecke, K., Anselmetti, F.S., Becker, A., Sturm, M. and Giardini, D. (2004) The record of historic earthquakes in lake sediments of Central Switzerland. Tectonophysics, **394,** 21-40.

Moreno, H. 2000. Mapa de Peligros del Volcán Villarrica, Regiones de la Araucanía y de Los Lagos**,** pp. 1 sheet. Servicio Nacional de Geología y Minería, Documento de Trabajo, N°17, Santiago.

Moreno, M., Melnick, D., Rosenau, M., Baez, J., Klotz, J., Oncken, O., Tassara, A., Chen, J., Bataille, K., Bevis, M., Socquet, A., Bolte, J., Vigny, C., Brooks, B., Ryder, I., Grund, V., Smalley, B., Carrizo, D., Bartsch, M. and Hase, H. (2012) Toward understanding tectonic control on the Mw 8.8 2010 Maule Chile earthquake. Earth and Planetary Science Letters, **321-322,** 152-165.

Mulder, T. and Alexander, J. (2001) The physical character of subaqueous sedimentary density flows and their deposits. *Sedimentology*, **48,** 269-299.

Naranjo, J.A. and Moreno, H. (2004) Laharic debris-flows from Villarrica Volcano. In: Villarrica Volcano (39.5°S), Southern Andes, Chile (Eds L.E. Lara and J. Clavero), **61,** pp. 28-38. Servicio Nacional de Geología y Minería.

Newhall, C.G. and Self, S. (1982) The Volcanic Explosivity Index (VEI) - An Estimate of Explosive Magnitude for Historical Volcanism. Journal of Geophysical Research-Oceans and Atmospheres, **87,** 1231-1238.

Petit-Breuilh, M.E. (2004) La Historia Eruptiva De Los Volcanes Hispanoamericanos (Siglos XVI Al XX): El Modelo Chileno. Casa de los Volcanes. Servicio de publicaciones exmo. cabildo insular de Lanzarote, 435 pp.

Rosenau, M., Melnick, D. and Echtler, H. (2006) Kinematic constraints on intra-arc shear and strain partitioning in the southern Andes between 38 degrees S and 42 degrees S latitude. Tectonics, **25**.

Ruegg, J.C., Rudloff, A., Vigny, C., Madariaga, R., de Chabalier, J.B., Campos, J., Kausel, E., Barrientos, S. and Dimitrov, D. (2009) Interseismic strain accumulation measured by GPS in the seismic gap between Constitucion and Concepcion in Chile. Physics of the Earth and Planetary Interiors, **175,** 78-85.

Siebert, L., Simkin, T. and Kimberly, P. (2010) *Volcanoes of the World – Third Edition.* University of California Press, Berkeley and Los Angeles, California, 551 pp.

SHOA (Servicio Hidrográfico y Oceanográfico de la Armada de Chile) (1987) *Lago Villarrica,* scale 1:40 000, 1 sheet.

SHOA (Servicio Hidrográfico y Oceanográfico de la Armada de Chile) (2008) *Lago Calafquén,* scale 1:30 000, 1 sheet.

Stern, C. (2008) Holocene tephrochronology record of large explosive eruptions in the southernmost Patagonian Andes. *Bulletin of Volcanology*, **70,** 435-454.

Stern, C.R., Moreno, H., López-Escobar, L., Clavero, J.E., Lara, L.E., Naranjo, J.A., Parada, M.A. and Skewes, M.A. (2007) Chilean Volcanoes. In: *The Geology of Chile* (Eds T. Moreno and W. Gibbons)**,** pp. 147-178. The Geological Society of London, London.

Strasser, M., Hilbe, M. and Anselmetti, F. (2011) Mapping basin-wide subaquatic slope failure susceptibility as a tool to assess regional seismic and tsunami hazards. *Marine Geophysical Research*, **32,** 331-347.

Urrutia de Hazbún, R. and Lanza Lazcano, C. (1993) *Catástrofes en Chile, 1541-1992,* Editorial La Noria, Santiago, Chile, 440 p.

Vallance, J.W. (2000) Lahars, In: *Encyclopedia of Volcanoe* (Eds H. Sigurdsson, B. Houghton, S.R. McNutt, H. Rymer, and J. Stix), pp. 601- 616, Encyclopedia of Volcanoes: Academic Press.

Volland, S., Sturm, M., Lukas, S., Pino, M. and Müller, J. (2007) Geomorphological and

sedimentological evolution of a lake basin under strong volcano-tectonic influence: Lake Calafquén (South Central Chile). *Quaternary International*, **161,** 32-45.

Von Gunten, L., Grosjean, M., Beer, J., Grob, P., Morales, A. and Urrutia, R. (2009) Age modeling of young non-varved lake sediments: methods and limits. Examples from two lakes in Central Chile. *Journal of Paleolimnology*, **42,** 401-412.

Wang, K., Hu, Y., Bevis, M., Kendrick, E., Smalley, R. and Lauria, E. (2007) Crustal motion in the zone of the 1960 Chile earthquake: Detangling earthquake-cycle deformation and forearc-sliver translation. *Geochemistry Geophysics Geosystems*, **8,** 14.

Watt, S.F.L., Pyle, D.M., Mather, T.A., Martin, R.S. and Matthews, N.E. (2009) Fallout and distribution of volcanic ash over Argentina following the May 2008 explosive eruption of Chaiten, Chile. *Journal of Geophysical Research-Solid Earth*, **114**.

Watt, S.F.L., Pyle, D.M., Naranjo, J.A., Rosqvist, G., Mella, M., Mather, T.A. and Moreno, H. (2011) Holocene tephrochronology of the Hualaihue region (Andean southern volcanic zone, ~42° S), southern Chile. *Quaternary International*, **246,** 324-343.

Witter, J.B., Kress, V.C., Delmelle, P. and Stix, J. (2004) Volatile degassing, petrology, and magma dynamics of the Villarrica Lava Lake, Southern Chile. *Journal of Volcanology and Geothermal Research*, **134,** 303-337.

“Fue fuerte, pero nada comparado con lo del ’60, esto si fue fuerte!”

“It was strong, but nothing compared to the one of 1960, that one was really strong!”

Local inhabitant living at the shores of Lake Lanalhue, comparing the 2010 with the 1960 earthquake.

Chapter 4

Sedimentary imprint of the giant 1960 and 2010 Chilean earthquakes in variable lacustrine environments

Modified version must be streamlined to be submitted for publication as:

Van Daele, M., Moernaut, J., Doom, L., Boes, E., Heirman, K., Vandoorne, W., Hebbeln, D., Pino, M., Urrutia, R., Brümmer, R. and De Batist, M. Sedimentary imprint of the giant 1960 and 2010 Chilean earthquakes in variable lacustrine environments. *Sedimentology*.

Abstract

Recent, well-described, giant earthquakes provide an ideal opportunity to calibrate seismites in lakes with different settings. We used mainly short sediment cores, sometimes combined with high-resolution reflection seismics, to study the sedimentary impact of the 1960 M_w 9.5 Valdivia and the 2010 M_w 8.8 Maule earthquakes in 19 lakes in South-Central Chile (from north to south: Negra, Lo Encañado, Aculeo, Vichuquén, Laja, Lanalhue, Butaco, Villarrica, Calafquén, Pullinque, Pellaifa, Panguipulli, Neltume, Riñihue, Ranco, Maihue, Puyehue, Rupanco and Llanquihue). By using image-analysis, magnetic susceptibility and grain-size analysis, we identified five types of event deposits (seismites) that were attributed to one of the aforementioned megathrust earthquakes: i) mass-transport deposits (MTDs), ii) in-situ deformation, iii) lacustrine turbidites with a similar composition as the background sediments (LT1s), iv) lacustrine turbidites with a different composition as the background sediments (more terrestrial; LT2s), and v) homogenites. These seismites were compared to local seismic intensities, eyewitness reports, post-earthquake observations, vegetation and geomorphology of the catchment. Homogenites consistently represent lake seiches and LT2s can be a result of local near-shore mass wasting, a delta collapse or onshore landslides surging into the lake (direct imprint), but also of debris or mud flows entering the lake, or of fluvial reworking of landslide debris in the catchment (indirect imprint). LT1s are the most reliable seismites, since they can have almost no other triggers then earthquake shaking. Moreover, they most sensitively record different seismic intensities, which is reflected in a different thickness and distribution in a certain lake. For the other seismites, the lake sub-basins only have a minimum intensity threshold. In general, the minimum encountered intensity threshold for most seismites is VI, but it can differ between the lakes and/or sub-basins. Finally, coastal lakes on the border between Valdivia rupture zone and Concepción-Valparaíso rupture zone (i.e. lakes Lanalhue and Butaco), where seismic shaking is frequent, appear to record lake-level rise due to the coastal uplift rather than the seismic shaking itself.

4.1 Introduction

During the past decade, several megathrust earthquakes have struck subduction zones around the globe (2004 M_w 9.1 Sumatra-Andaman, Indonesia; 2010 M_w 8.8 Maule, Chile; and 2011 M_w 9.0 Tohoku-Oki, Japan), which together represent half of the top 6 of largest instrumentally recorded earthquakes. The top position in this list is still occupied by the 1960 M_w 9.5 Valdivia (Great Chilean) earthquake, which ruptured 1000 km of megathrust just south of the 500 km that would 50 years later be ruptured by the 2010 Maule earthquake. These two earthquakes form the topic of this study.

Due to the inaccessibility of the megathrust fault at subduction zones, paleoseismological information can only be obtained by indirect studies, in which deposits of events that were triggered by the earthquake, such as landslides or tsunamis, are investigated. Turbidites in submarine channels

have proven to be good recorders of megathrust earthquakes in the Cascadia subduction zone, although several channels and their confluences need to be examined in order to confirm the earthquake trigger (Goldfinger et al., 2012). It has been demonstrated that onshore deposits of tsunamis are valuable for reconstructing these destructive waves (e.g., Cisternas et al., 2005). However, to exclude storms and tsunamis originating in other parts around the ocean, site conditions –which can change through time– should be optimal. Both tsunami deposits and submarine turbidites can provide very useful information (timing and rupture zone) concerning prehistoric earthquakes, but add little information on onshore seismic intensities and impact of the earthquake. Sedimentary sequences in lakes have proven to be good recorders of past earthquakes in French and Swiss Alpine lakes (e.g., Schnellmann et al., 2002; Beck, 2009; Strasser et al., accepted). Several types of event deposits have been attributed to earthquakes in these studies: mass-transport deposits (MTDs; slumps and slides), turbidites (including megaturbidites or homogenites), liquefaction structures and in-situ deformation (microfaults and -folds). Monecke et al. (2004) linked deposits to seismic intensities in different Swiss lakes. These results were then used by Strasser et al. (2006) to estimate paleo-epicenters of these earthquakes. Also outside the European Alps, lake deposits are increasingly used as paleoseismological archives. In Japan and Turkey lake turbidites were used to reconstruct prehistoric earthquakes (e.g., Shiki et al., 2000; Schwab et al., 2009), while in Chilean and Argentinian lakes, in addition to turbidites, MTDs were used to reconstruct past earthquakes (Moernaut et al., 2007; Bertrand et al., 2008; Waldmann et al. 2011), and even fluidization structures of buried MTDs (Moernaut et al., 2009). Chapron et al. (2006) and Howarth et al. (2012) also observed postseismic turbidites originating from hyperpycnal flows, which were formed by fluvial remobilization of landslide debris in the catchment.

By comparing all these studies it becomes clear that not all lakes record earthquakes in the same way. Not only the seismic intensity (Macroseismic intensity: Medvedev–Sponheuer–Karník (MSK) or Modified Mercalli Intensity (MMI); Musson et al., 2010; Table 4.1), but also the regional climate, vegetation and the morphology of the catchment, the bathymetry of the lake and its tectonic setting may influence the earthquake recording capability (ERC) of a lake. Comparative studies in which similar seismic intensities of similar earthquakes in different settings are compared, were, up to now, lacking. The 1960 and 2010 Chilean earthquakes affected together about 1400 km of the Chilean subduction zone. The presence of many lakes, especially in the central part of this zone, make this an ideal study area to compare the impact of recent earthquakes on different types of lake records. In the present study, we compared the sedimentary imprints left by the iconic 1960 Great Chilean earthquake and by the recent 2010 Maule earthquake in 19 different lakes with reports, seismic intensities and their setting, and we created a catalog of different lake types and the type of seismites (i.e. earthquake-triggered event deposits) they can contain.

4.2 Setting

4.2.1 Geomorphologic, tectonic and geologic setting

The study area, which extends over a latitudinal distance of 900 km, from Santiago in the North to Puerto Montt in the South, is composed of three basic geomorphologic zones, from west to east: the Coastal Range, the Intermediate Depression and the Andean Cordillera (Fig. 4.1). The Coastal Range generally reaches altitudes between 500 and 1000 m asl; however, it reaches heights of 1500 m asl and 2250 m asl east of the Arauco Peninsula and around Santiago, respectively. The Intermediate

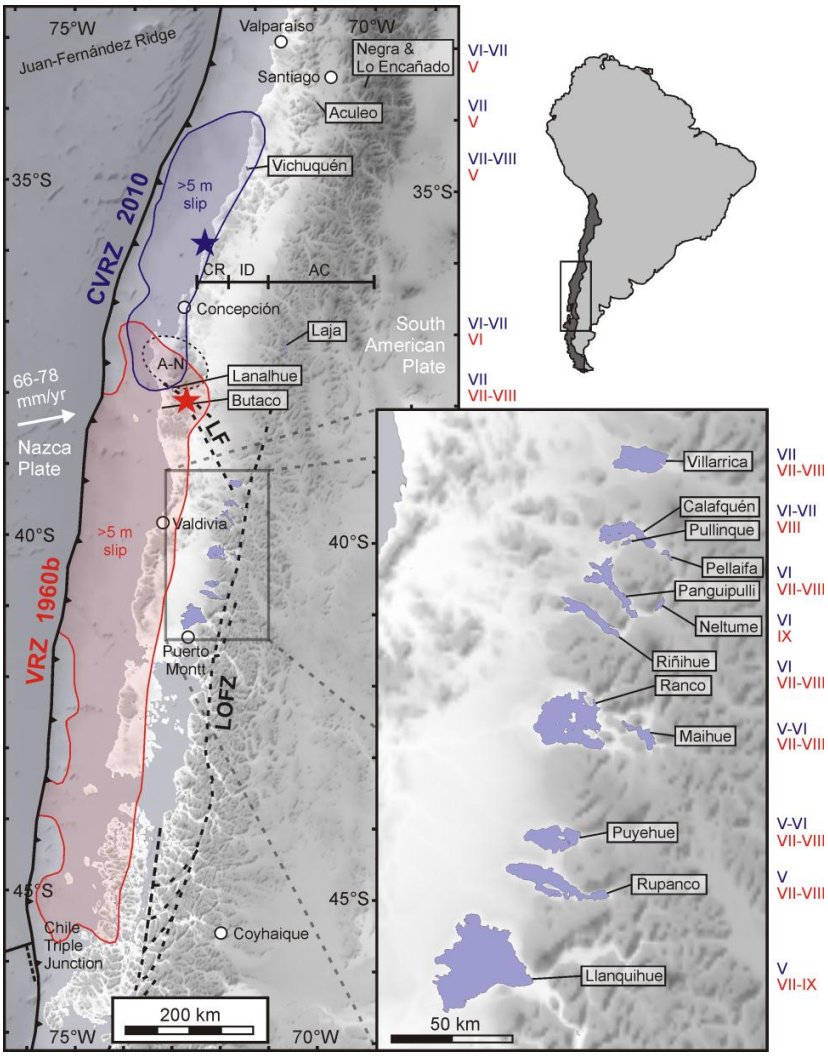

Fig. 4.1 *Overview of the study area in South-Central Chile and location of all studied lakes with on the right hand side of each lake or group of lakes the seismic intensities during the 1960 (MSK of Lazo (2008); red) and 2010 (MMI of USGS (2012) Did you feel it?; blue) earthquakes. Coseismic slip area (>5 m) for the 1960 and 2010 events (Moreno et al., 2009; 2012). CR: Coastal Range; ID: Intermediate Depression; AC: Andean Cordillera; A-N: Arauco Peninsula-Nahuelbuta Range; LF: Lanalhue Fault; and LOFZ: Liquiñe-Ofqui Fault Zone.*

Depression (10-100 km wide, 0-600 m asl) is widest and lowest in the south and becomes narrower and higher towards the north, reaching 600 m asl in Santiago. At the latitude of Valdivia and just south of Santiago the Intermediate Depression is locally not present, because the Coastal Range extends more towards the east. Also the Andean Cordillera tends to decrease in altitude towards the south, generally reaching over 6000 m asl around Santiago and 1500 to 2000 m asl in the south (with the volcanoes reaching more than 3000 m asl; Fig. 4.1).

The regional tectonic setting of the study area is determined by the oblique subduction of the Nazca Plate under the South American Plate (Fig. 4.1). The current convergence rate between these two plates is estimated between 66 mm/y (Angermann et al., 1999) and 78 mm/y (DeMets et al., 1994). In our study area, the megathrust can be subdivided in two historical rupture areas: the Valdivia rupture zone (VRZ) and the Concepción-Valparaíso rupture zone (CVRZ). The VRZ is delimited by the Chile Triple Junction in the south and the Arauco-Nahuelbuta buttress (bordered by the Lanalhue Fault) in the north. The CVRZ extends from the latter in the south to the Juan-Fernández Ridge in the north (Melnick et al., 2009). At the latitudes of the VRZ, the stress resulting from the oblique subduction is accommodated by the 1000-km-long Liquiñe-Ofqui Fault Zone (LOFZ) (Cembrano et al., 2000), a long-lived dextral strike-slip lineament. The LOFZ separates the north-moving (6.5 mm/y) Chiloé sliver (in the west) from the rest of the South American Plate (in the east) (Cembrano et al., 2000; Wang et al., 2007; Melnick et al., 2009). Between Lake Villarrica in the southeast and the Arauco Peninsula in the northwest, the counterclockwise rotation of the northern Chiloé sliver is accommodated by the Lanalhue Fault (Moreno et al., 2008; Fig. 4.1).

Table 4.1 *Description of the Macroseismic-Intensity scales referred to in this chapter (Medvedev–Sponheuer–Karník, Medvedev et al., 1964; Modified Mercalli Intensity, Wood and Neumann, 1931).*

Medvedev–Sponheuer–Karník (MSK)	Modified Mercalli Intensity (MMI)
I. Not perceptible Not felt, registered only by seismographs. No effect on objects. No damage to buildings.	**I. Instrumental** Not felt except by a very few under especially favorable circumstances.
II. Hardly perceptible Felt only by individuals at rest. No effect on objects. No damage to buildings.	**II. Weak** Felt only by a few persons at rest, especially on upper floors of buildings. Delicately suspended objects may swing.
III. Weak Felt indoors by a few. Hanging objects swing slightly. No damage to buildings.	**III. Slight** Felt quite noticeably indoors, especially on upper floors of buildings, but many people do not recognize it as an earthquake. Standing motor cars may rock slightly. Vibration like passing truck. Duration estimated.
IV. Largely observed Felt indoors by many and felt outdoors only by very few. A few people are awakened. Moderate vibration. Observers feel a slight trembling or swaying of the building, room, bed, chair etc. China, glasses, windows and doors rattle. Hanging objects swing. Light furniture shakes visibly in a few cases. No damage to buildings.	**IV. Moderate** During the day felt indoors by many, outdoors by few. At night some awakened. Dishes, windows, and doors disturbed; walls make creaking sound. Sensation like heavy truck striking building. Standing motorcars rock noticeably.
V. Fairly strong Felt indoors by most, outdoors by few. A few people are frightened and run outdoors. Many sleeping people awake. Observers feel a strong shaking or rocking of the whole building, room or furniture. Hanging objects swing considerably. China and glasses clatter together. Doors and windows swing open or shut. In a few cases window panes break. Liquids oscillate and may spill from fully filled containers. Animals indoors may become uneasy. Slight damage to a few poorly constructed buildings.	**V. Rather strong** Felt by nearly everyone; many awakened. Some dishes, windows, etc., broken; a few instances of cracked plaster; unstable objects overturned. Disturbance of trees, poles, and other tall objects sometimes noticed. Pendulum clocks may stop.
VI. Strong Felt by most indoors and by many outdoors. A few persons lose their balance. Many people are frightened and run outdoors. Small objects may fall and furniture may be shifted. Dishes and glassware may break. Farm animals may be frightened. Visible damage to masonry structures, cracks in plaster. Isolated cracks on the ground.	**VI. Strong** Felt by all; many frightened and run outdoors. Some heavy furniture moved; a few instances of fallen plaster or damaged chimneys. Damage slight.
VII. Very strong Most people are frightened and try to run outdoors. Furniture is shifted and may be overturned. Objects fall from shelves. Water splashes from containers. Serious damage to older buildings, masonry chimneys collapse. Small landslides.	**VII. Very strong** Everybody runs outdoors. Damage negligible in buildings of good design and construction slight to moderate in well built ordinary structures; considerable in poorly built or badly designed structures. Some chimneys broken. Noticed by persons driving motor cars.
VIII. Damaging Many people find it difficult to stand, even outdoors. Furniture may be overturned. Waves may be seen on very soft ground. Older structures partially collapse or sustain considerable damage. Large cracks and fissures opening up, rockfalls.	**VIII. Destructive** Damage slight in specially designed structures; considerable in ordinary substantial buildings, with partial collapse; great in poorly built structures. Panel walls thrown out of frame structures. Fall of chimneys, factory stacks, columns, monuments, walls. Heavy furniture overturned. Sand and mud ejected in small amounts. Changes in well water. Persons driving motor cars disturbed.
IX. Destructive General panic. People may be forcibly thrown to the ground. Waves are seen on soft ground. Substandard structures collapse. Substantial damage to well-constructed structures. Underground pipelines ruptured. Ground fracturing, widespread landslides.	**IX. Violent** Damage considerable in specially designed structures; well-designed frame structures thrown out of plumb; great in substantial buildings, with partial collapse. Buildings shifted off foundations. Ground cracked conspicuously. Underground pipes broken.
X. Devastating Masonry buildings destroyed, infrastructure crippled. Massive landslides. Water bodies may be overtopped, causing flooding of the surrounding areas and formation of new water bodies.	**X. Intense** Some well-built wooden structures destroyed; most masonry and frame structures destroyed with foundations; ground badly cracked. Rails bent. Landslides considerable from river banks and steep slopes. Shifted sand and mud. Water splashed over banks.
XI. Catastrophic Most buildings and structures collapse. Widespread ground disturbances, tsunamis.	**XI. Extreme** Few, if any (masonry), structures remain standing. Bridges destroyed. Broad fissures in ground. Underground pipelines completely out of service. Earth slumps and land slips in soft ground. Rails bent greatly.
XII. Very catastrophic All surface and underground structures completely destroyed. Landscape generally changed, rivers change paths, tsunamis.	**XII. Catastrophic** Damage total. Waves seen on ground surfaces. Lines of sight and level distorted. Objects thrown upward into the air.

Both the VRZ and the CVRZ have produced a megathrust earthquake in recent times.

The 22 May 1960 Great Chilean Earthquake along the VRZ was the largest earthquake ever recorded instrumentally (M_w 9.5) and had a rupture length of 1000 km (Cifuentes, 1989). Medvedev–Sponheuer–Karník (MSK) Macroseismic Intensities were estimated and compiled by Lazo (2008) (Table 4.1). Between the Arauco Peninsula in the north and Chiloé in the south, a zone with MSKs between VII and VIII covers the coastal range and most of the Intermediate Depression. However, Weishet (1963) concluded that the Mercalli Intensities can fluctuate strongly depending on the soil conditions. For example, Mercalli intensities of X were reached in Valdivia, located on alluvium, while only 20 km east and west of the city, where the crystalline basement outcrops, MMIs did not reach VII. Therefore care should be taken when interpreting these intensities. Around Concepción and even up to Santiago, the foreshock on 21 May (1960 Concepción earthquake; M_w 7.9 (USGS, 2012a) to 8.3 (Vigny et al., 2011)) caused larger MSKs than the main shock (up to IX). Several studies with reports of phenomena associated to the earthquake have been published (e.g., Tazieff, 1960; Weishet, 1963; Wright and Mella 1963; Sievers, 2000).

On 27 February 2010, the Maule earthquake (M_w 8.8) ruptured about 500 km of the megathrust and probably closed a seismic gap on the CVRZ (Moreno et al., 2012). Modified Mercalli Intensities (MMIs; Table 4.1) of USGS *´Did you feel it?´* reports and the USGS *´Shakemap´* give different values (USGS, 2012b). At similar latitudes as the rupture (i.e. between Concepción and Santiago), the *´Shakemap´* systematically overestimates the '*Did you feel it?*' reports (VII-VIII versus VI-VII, respectively). South of the rupture zone (i.e., between Puerto Montt and Concepción) the *´Shakemap´* underestimates *´Did you feel it?´* reports (IV-VI versus V-VII, respectively). For the coastal areas, inventories of observed co-seismic vertical movements, geomorphologic changes and tsunami run-up have been established (Quezada et al., 2010; Fritz et al., 2011).

4.2.2 Lake settings

The 19 investigated lakes cover the entire CVRZ and the northern part of the VRZ (Fig. 4.1). The lakes are located in different climate zones ranging from warm temperate Mediterranean climates in the north to temperate rainy climates in the south, and some of the Andean lakes at high altitudes are even located in steppe climate zones (Table 4.2). Lakes in coastal areas, in mountainous areas and in intermediate settings, usually at the piedmont of the Andes, were included in the study. The coastal lakes Butaco, Lanalhue and Vichuquén were formed due to coastal uplift and isolation of old river valleys. Lake Vichuquén is the most recent; it was still connected to the Pacific Ocean during the war of the Pacific (AD 1879-1883). Lake Lanalhue was disconnected from the Pacific Ocean approximately 8000 years BP (Stefer et al., 2010). Lake Aculeo is a tectonic lake in the Coastal Range and with a maximum depth of 6 m it is the shallowest of the studied lakes (Jenny et al., 2002). Most of the lakes in or at the foot of the Andes (from north to south: Villarrica, Calafquén, Pellaifa, Panguipulli, Neltume, Riñihue, Ranco, Maihue, Puyehue, Rupanco and Llanquihue) are overdeepened glacigenic lakes, in most cases dammed by frontal moraines (Laugenie, 1982). Andean lakes Negra and Lo Encañado have a similar origin, although Lo Ecañado is partially landslide dammed. Lake Laja is dammed by volcanic deposits (Melnick et al., 2006) and Lake Pullinque is dammed by deep-seated landslides that probably formed during (pre)historic earthquakes (Laugenie, 1982; Fig. 4.1).

Table 4.2 provides general information on all the studied lakes and references to more detailed descriptions of local settings.

4.3 Methods

4.3.1 Reports

An inventory was made of all reported events in and around the lakes during and after the 1960 and 2010 earthquakes. In order to make an assessment of the events related to the 1960 earthquake, publications were consulted (Weishet, 1963; Wright and Mella, 1963; Sievers, 2000, Lazo, 2008). Moreover, where available, aerial photographs taken in the 1940's and 1961 were examined. Events related to the 2010 earthquake were documented by interviewing local inhabitants during the 2011 and 2012 field campaigns and consulting the reports of Quezada et al. (2010). The nocturnal time of the earthquake (at 03:34 am), however, did complicate obtaining detailed records. Also, the remoteness of some lakes resulted in lacking reports.

Table 4.2 *General information on setting, bathymetry and seismic intensities (MMI for the 1960 earthquake and MSK for the 2010 earthquake) for all studied lakes. Sedimentation rates in black: directly from other studies; in blue: from cores in this study after correlation with cores from the same lake in other studies; in green: from this study.*

Lake	MMI 2010 (USGS, 2012)		MSK 1960 (Lazo, 2008)	
	Did you feel it?	Shakemap	21 May	22 May
Negra	VI-VII	VII	(V)	(II-IV)
Lo Encañado	VI-VII	VII	(V)	(II-IV)
Aculeo	VII	VII1/2	(V)	(II-IV)
Vichuquén	VII-VIII	VIII		
Laja	VI-VII	VII	VI	<VI?
Lanalhue	VII	VII1/4	VII-VIII	(VII-VIII)
Butaco	VII	VII	VII-VIII	(VII/-III)
Villarrica	VII	VI		VII-VIII
Calafquén	VI-VII	V1/2		VIII
Pullinque	VI-VII	V1/2		(VIII)
Pellaifa	VI	V1/4		(VII-VIII)
Panguipulli	VI	V1/2		VII-VIII
Neltume	VI	V		IX
Riñihue	VI	V		(VII-VIII)
Ranco	VI	V		(VII-VIII)
Maihue	V-VI	IV3/4		(VII-VIII)
Puyehue	V-VI	IV3/4		>VII
Rupanco	V	IV1/2		(VII-VIII)
Llanquihue	V	IV1/4		VII-IX

***Table 4.2** (continuation)*

Lake	Climate	Vegetation	Sedimentation rate (mm/y)	Study sedimentation rate
Negra	Steppe due to high altitude (ETH)	Andean scrubland/steppe	~1	von Gunten et al., 2009a
Lo Encañado	Steppe due to high altitude (ETH)	Andean scrubland/steppe	~1.75	Salvetti, 2006
Aculeo	Warm temperate (Csb) Mediterranean	Sclerophyllous and deciduous forest	1.25-3.8	von Gunten et al., 2009b; Jenny et al., 2002
Vichuquén	Warm temperate (Csbn's) Mediterranean	Sclerophyllous forest	?	-
Laja	Steppe due to high altitude (ETH)	Andean scrubland/steppe	~1.7	Quiroz et al., 2005
Lanalhue	Warm temperate rainy (Cfsb)	Humid coastal forest	~2.5	Stefer et al., 2010
Butaco	Warm temperate rainy (Cfsb)	Humid coastal forest	?	-
Villarrica	Temperate rainy (Cfs)	Deciduous forests	~1.5	Van Daele et al., submitted
Calafquén	Temperate rainy (Cfs)	Deciduous forests	~1	Van Daele et al., submitted
Pullinque	Temperate rainy (Cfs)	Deciduous forests	0.4-1.4	this study
Pellaifa	Temperate rainy (Cfs)	Valdivian rainforests	1.25-1.7	this study
Panguipulli	Temperate rainy (Cfs)	Deciduous forests	1.15-1.75	this study
Neltume	Temperate rainy (Cfs)	Valdivian rainforest	~5	this study
Riñihue	Temperate rainy (Cfs)	Valdivian rainforest	~1	Van Daele et al., submitted
Ranco	Temperate rainy (Cfs)	Valdivian rainforest	0.8-1.4	this study
Maihue	Temperate rainy (Cfs)	Valdivian rainforest	2.2-4	this study, varve counting
Puyehue	Temperate rainy without dry season (Cfb-c)	North Patagonian forests	1.05-2.3; 1.0-1.9	Boës and Fagel, 2008; this study
Rupanco	Temperate rainy without dry season (Cfb-c)	North Patagonian forests	1.1-2.85	this study
Llanquihue	Temperate rainy without dry season (Cfb-c)	North Patagonian forests	0.6-1	this study

Table 4.2 *(continuation)*

Lake	Lat (°S)	Long (°W)	Altitude (m asl)	Lake surface (km^2)	Catchment area (km^2)	Catchment/Lake ratio	Max. depth (m)	Origin of bathymetry
Negra	33.65	70.13	2703	5.8	53.5	9.2	>350	von Gunten et al. (2009a) + single datapoints
Lo Encañado	33.67	70.13	2492	0.5	38.5	77.0	32	Salvetti (2006)
Aculeo	33.85	70.92	356	12.1	81.2	6.7	6	Jenny et al. (2002); von Gunten et al. (2009b)
Vichuquén	34.80	72.06	4	11.9	187.1	15.7	30	SHOA (2002)
Laja	37.35	71.30	1361	84.6	892.4	10.5	92	Reflection seismics (Melnick et al., 2006)
Lanalhue	37.92	73.31	8	32.4	326.6	10.1	25	Reflection seismics (Stefer et al., 2010)
Butaco	38.21	73.44	11	0.99	11.31	11.4	15	Single datapoints
Villarrica	39.25	72.10	215	174	2287	13.1	167	SHOA (1987) + reflection seismics (Moernaut et al., submitted)
Calafquén	39.52	72.18	204	117.8	555.2	4.7	212	SHOA (2008) + reflection seismics (Moernaut et al., submitted)
Pullinque	39.56	72.15	199	5.4	32.6	6.0	25	Westermayer (2005)
Pellaifa	39.60	71.96	221	6.9	47.1	6.8	93	Reflection seismics
Panguipulli	39.70	72.24	131	114.2	703.8	6.2	268	Campos et al. (1981)
Neltume	39.79	71.98	197	9.8	731.2	74.6	86	Reflection seismics
Riñihue	39.80	72.38	107	89.6	382.4	4.3	323	Campos et al. (1987) + reflections seismics (Moernaut et al., submitted)
Ranco	40.23	72.42	64	429.3	1538.7	3.6	199	SHOA (2003)
Maihue	40.28	72.03	90	49.5	1320.5	26.7	205	Reflection seismics + single datapoints
Puyehue	40.67	72.50	187	157.7	1055.3	6.7	123	SHOA (2000)
Rupanco	40.82	72.50	123	231.2	691.8	3.0	269	SHOA (2001)
Llanquihue	41.13	72.83	53	867.5	709.5	0.8	317	SHOA (1992)

4.3.2 Modified Mercalli (MMI) and Medvedev–Sponheuer–Karník (MSK) Intensities

Our inventory was compared with MSKs and MMIs at the lakes during both earthquakes. For the 1960 Great Chilean earthquake, MSKs were estimated using the results of Lazo (2008). To estimate MMIs of the 2010 Maule earthquake, we used absolute values of the USGS (2012) ´*Did you feel it?*´ reports, locally extrapolated by using relative changes in the USGS (2012) ´*Shakemap*´, to cover areas where reports are lacking (Fig. 4.1). Available intensities for both earthquakes are expressed on different scales (MSK versus MMI), but since the effects assigned to the values on both scales are similar and comparable (Musson et al., 2010), we will further refer to intensities as *Seismic Intensity* (SI) when discussing intensities of both earthquakes at the same time.

4.3.3 Seismic data acquisition and bathymetry

In some of the studied lakes, high-resolution seismic data was acquired using a Geopulse sub-bottom profiler (pinger) and/or a Centipede multi-electrode sparker developed by the Renard Centre of Marine Geology (Ghent University). The 3.5 kHz pinger transducer was mounted on a Cataraft system and towed by the RV Huala II of the Universidad Austral de Chile in Valdivia. The sparker, operated at 300-400 J, produces a broad-spectrum seismic signal, with a mean frequency of ~1.3 kHz. A single-channel streamer with 10 hydrophones and a total group length of 2.7 m, was used as a receiver. Both pinger and sparker data were acquired at an average survey speed of 4 knots. Seismic and GPS data were digitally recorded and converted to SEG-Y format with the IXSEA™ Delph Seismic Acquisition system. Seismic-stratigraphic interpretation was done using SMT's KingdomSuite. In lakes Pellaifa, Panguipulli and Neltume, seismic data was used to map the location and extent of earthquake-induced deposits (Fig. 4.2).

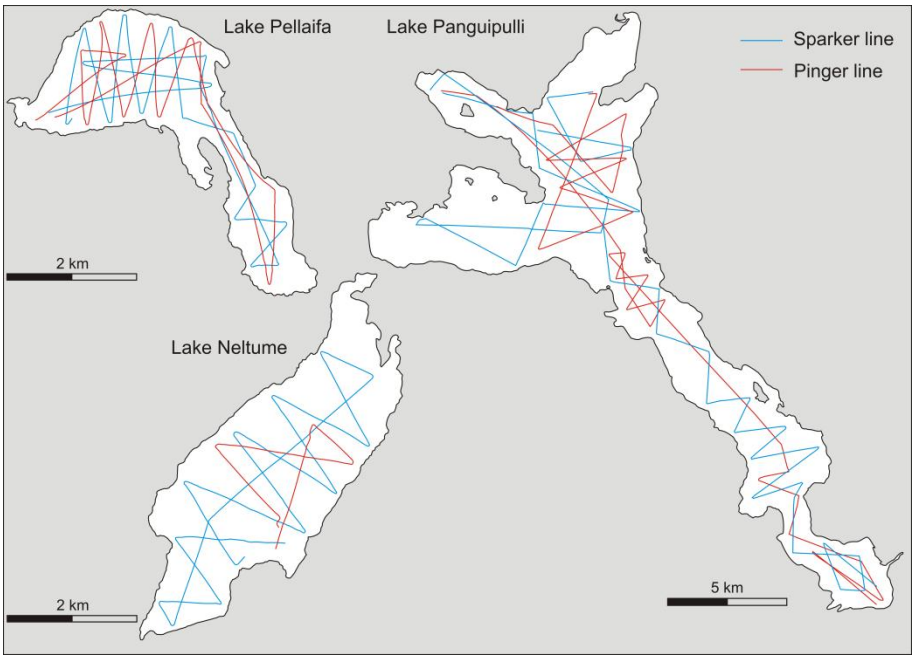

Fig. 4.2 *High-resolution seismic sparker (blue) and pinger (red) profiles in lakes Pellaifa, Neltume and Panguipulli.*

Bathymetric maps were constructed either by interpolation between seismic lines (acoustic velocity derived by depth measurements at coring sites), by single echosounder data points, by data points of bathymetric soundings of the Servicio Hidrográfico y Oceanográfico de la Armada de Chile (SHOA), by previously published studies of the lakes, or by a combination of the above (Table 4.2).

4.3.4 Coring and sedimentology

The 121 gravity cores presented in this study were taken during three field seasons (2008, 2009 and 2011) using a Swiss corer (UACH, Valdivia) or a UWITEC gravity corer (British Antarctic Survey or Ghent University). Cores were shipped to Belgium, opened, described and photographed. Subsequently the magnetic susceptibility (MS) was measured with a Bartington MSE2 point sensor (3.5 mm resolution) at a step size of 2.5 mm. On some cores, AVAATECH XRF-core scanning was performed at MARUM (Bremen) at down-core resolutions of 2 or 5 mm. Grain-size analyses of some of the event deposits were conducted at variable downcore intervals with a Malvern Mastersizer 2000 at Ghent University.

Basic information (location, depth, length) of every core can be found in Table 4.3.

4.3.5 Chronology

Both the 1960 and 2010 earthquakes are recent events. Deposits resulting from these events should therefore show little burial and, hence, occur close to the top of the sediment cores.

Deposits related to the 2010 earthquake are assumed to occur at the top of the cores that were taken less than 1 year after the 2010 earthquake, during the 2011 field season. In lakes, in which cores had already been taken during the 2008 or 2009 field seasons, pre- and post-2010 cores were compared to confirm this hypothesis.

Deposits related to the 1960 earthquake are dated by correlation with dated cores from other studies, by varve counting or by inter-lake correlation. For some of the studied lakes age models are available and sedimentation rates in the last 50-100 years range between 0.65 and 2.5 mm/yr (Negra (von Gunten et al., 2009a), Lo Encañado (Salvetti, 2006), Aculeo (Jenny et al., 2002; von Gunten et al., 2009b), Laja (Quiroz et al., 2005), Lanalhue (Stefer et al., 2010), Villarrica, Calafquén and Riñihue (Chapter 3), and Puyehue (Boës and Fagel, 2008; Table 4.2). Based on this range of sedimentation rates, the top of a potential 1960 seismite is expected to occur at a depth between 3 and 12.5 cm in these lakes. This depth range was also used to detect 1960 seismites in some of the other lakes that were not previously studied (i.e. lakes Pellaifa, Pullinque, Panguipulli, Ranco, Rupanco and Llanquihue; Table 4.2). Sedimentation rates in lakes Panguipulli and Ranco were confirmed by inter-lake correlation of marked volcanic event deposits also present in Lake Riñihue. In lakes Panguipulli and Pullinque, the timing of start of eutrophication (i.e. around AD 1900, and evidenced by a clear darker color of the sediment) was used for inter-lake correlation with lakes Calafquén and Riñihue (Chapter 3). These four lakes are connected by rivers, allowing this correlation to be made. The upper part of the Lake Maihue sedimentary infill was dated by varve counting, which was confirmed by a resulting age of 1960 for the youngest seismite (corresponding to the 1960 earthquake). The resulting sedimentation rates in the main basin are about 4 mm/yr, which is considerably higher than for the other lakes. This discrepancy compared to the other lakes is easily explained by the high catchment to lake surface ratio (26.7), which is much higher than the median (6.8) and average (15.6) of all studied lakes. Another lake with a very high catchment to lake surface ratio is Lake Neltume (74.6), thereby supporting the relatively deep burial (below 23 cm of background sediments) of the event deposits that were attributed to the 1960 earthquake. The resulting sedimentation rates for all studied lakes can be found in Table 4.2.

Table 4.3 *General information for all cores presented in this study and thickness of the seismites that were attributed to the 1960 (red) or 2010 (blue) earthquake.*

Lake	Core name	Sampling year	Lat	Long	Depth (m)	Length (cm)	Thickness of deposits (cm) in situ	MTD	LT1	LT2	Homog.
Negra	NEG1	2011	-33.63	-70.12	170	21				>21	
	NEG2	2011	-33.63	-70.13	80	32				2+1.5	
	NEG3	2011	-33.64	-70.13	115	24				0.3+1	
	NEG6	2011	-33.65	-70.13	255	62				1	
Lo Encañado	ENC1	2011	-33.67	-70.13	30	62				24	
	ENC2	2011	-33.67	-70.13	32	94				4	
Aculeo	ACU2	2011	-33.85	-70.90	5	62					
	ACU3	2011	-33.85	-70.91	6	59					
	ACU4	2011	-33.85	-70.91	6	78					
	ACU6	2011	-33.84	-70.92	6	59					
	ACU8	2011	-33.84	-70.93	6	56					
Vichuquén	VIC07	2011	-34.82	-72.06	27	122			3-4?		
	VIC12 I	2011	-34.80	-72.07	28	85					
	VIC13 I	2011	-34.81	-72.04	30	84			2.5		
Laja	LAJ1	2011	-37.36	-71.36	92	48			7		
	LAJ2	2011	-37.35	-71.33	79	69			3		
	LAJ3	2011	-37.33	-71.29	78	105					
	LAJ4	2011	-37.29	-71.32	72	102			2		
	LAJ5	2011	-37.27	-71.31	77	93					
Lanalhue	LAN01	2011	-37.89	-73.38	20	67			2		
	LAN02	2011	-37.91	-73.36	24	68			2.5		
	LAN03	2011	-37.92	-73.35	25	75			2		
	LAN04	2011	-37.92	-73.33	21	78					
	LAN05	2011	-37.93	-73.31	16	83					
	LAN06	2011	-37.93	-73.30	18	86			0.5		
	LAN07	2011	-37.92	-73.30	21	76			1.5		
	LAN08	2011	-37.93	-73.28	19	82					
	LAN09	2011	-37.94	-73.26	15	61					
	LAN10	2011	-37.97	-73.26	5	43					
Butaco	BUT1	2011	-38.21	-73.45	12	45					
	BUT2	2011	-38.21	-73.44	15	78			2		
	BUT3	2011	-38.21	-73.44	11	18			2		
Villarrica	VILLSC02	2009	-39.26	-72.17	82	87					
	VILLSC05	2009	-39.26	-72.12	160	49				2.5	
	VI3	2011	-39.28	-72.20	79	91		1.5	1		
	VI4	2011	-39.28	-72.19	85	81		4.5	1		
	VI5	2011	-39.27	-72.19	85	95			1.5		
	VI6	2011	-39.27	-72.19	93	104			3.5		
	VI7	2011	-39.27	-72.18	98	110			3		
	VI8	2011	-39.28	-72.16	113	95			5 + 1		
	VI9	2011	-39.27	-72.15	109	106			1		
	VI10	2011	-39.26	-72.15	155	120			2 + 1		
	VI11	2011	-39.26	-72.14	160	130			2 + 0.5		
	VI12	2011	-39.26	-72.14	165	129			3 + 0.5		
	VI13	2011	-39.28	-72.12	148	55		26	2.5	5	
	VI14	2011	-39.26	-72.08	160	59				5 + 9	
	VI15	2011	-39.26	-72.05	157	38		≥9			
	VI16	2011	-39.28	-72.02	150	28		≥6.5		3.5	
	VI17	2011	-39.28	-72.05	90	63					
	VI18	2011	-39.28	-72.08	154	21			3	2.5	
Calafquén	CAGC01bis	2008	-39.55	-72.23	135	59		≥49	3		
	CAGC03	2008	-39.55	-72.25	63	51			1		
	CAGC05	2008	-39.54	-72.19	112	76	3		1.5		
	CGC01	2009	-39.56	-72.06	178	25				4	
	CB4	2009	-39.55	-72.06	173	54		≥26		6	
	CB9	2009	-39.53	-72.14	170	45		>9		9+7.5	
	CALA01	2011	-39.54	-72.21	160	123			11 + 4		
	CALA02	2011	-39.55	-72.22	147	104			6		
	CALA04	2011	-39.55	-72.18	93	120			3 + 1		
	CALA05	2011	-39.55	-72.18	88	119			4.5 + 1.5		
	CALA06	2011	-39.54	-72.16	94	123			2.5		
	CALA07	2011	-39.54	-72.15	172	96			0.5 + 1		
	CALA08	2011	-39.52	-72.15	194	20				12	
	CALA09	2011	-39.52	-72.13	195	22				22	

Table 4.3 *(continuation)*

Lake	Core name	Sampling year	Lat	Long	Depth (m)	Length (cm)	Thickness of deposits (cm) in situ	MTD	LT1	LT2	Homog.
Calafquén	CALA10	2011	-39.52	-72.11	194	22		>10		12	
	CALA11	2011	-39.54	-72.08	186	19		>14		5	
Pullinque	PULGC01	2008	-39.57	-72.16	8.5	45			5		
	PULGC02	2008	-39.57	-72.15	24.7	38					
	PULGC04	2008	-39.55	-72.14	18.5	45					
	PULGC08	2008	-39.57	-72.17	10	54					
Pellaifa	PEGC01	2008	-39.59	-71.97	89	65				3.5+2.5+1+1	50
	PEGC02	2008	-39.59	-71.96	90	83				3+2+0.5+1	>71
	PEGC03BIS	2008	-39.62	-71.94	25	83				9	
Panguipulli	PAGC03	2008	-39.67	-72.27	135	64			5.5		
	PAGC04	2008	-39.66	-72.24	160	53		>40	5		
	PAGC05	2008	-39.67	-72.25	170	60			5		
	PAGC06	2008	-39.73	-72.21	260	63					48
	PAGC07	2008	-39.65	-72.31	18,2	50					
	PAGC10	2008	-39.71	-72.23	260	78					>72
Riñihue	RINSC04	2009	-39.82	-72.38	113	70		40	2.5		
	RI1	2011	-39.82	-72.40	115	85			5		
	RI2	2011	-39.82	-72.39	119	81			7		
	RI3	2011	-39.81	-72.38	122	82			5.5		
	RI4	2011	-39.81	-72.38	124	78			1.5		
	RI5	2011	-39.80	-72.39	121	62			5.5	2.5	
	RI6	2011	-39.79	-72.39	120	58			0.5	3 + 2	
	RI7	2011	-39.79	-72.39	118	62			1	3.5 + 3	
	RI8	2011	-39.79	-72.40	118	73			5.5		
Neltume	NEL02	2009	-39.80	-71.98	82	73				6	26
	NEL04	2009	-39.79	-71.98	86	73				9	>33
Ranco	RAN1	2011	-40.16	-72.41	168	45		37	1		
	RAN2	2011	-40.16	-72.45	165	57		22	2	0.5	
	RAN3	2011	-40.18	-72.45	181	72			10		
	RAN4	2011	-40.19	-72.51	178	65		28	1.5		
	RAN5	2011	-40.20	-72.50	175	36					
	RAN6	2011	-40.23	-72.53	135	83		8 + 8	1 + 1		
	RAN7	2011	-40.23	-72.49	143	83	5		1		
	RAN8	2011	-40.14	-72.35	53	66					
Maihue	MAI01	2009	-40.29	-72.05	93	58		>28		4.5	
	MAI02	2009	-40.28	-72.04	203	70		>58		3	
	MAI03	2009	-40.28	-72.04	203	45		>17		3	
	MAI04	2009	-40.29	-72.01	205	80				2	32
	MAI06	2009	-40.31	-72.01	195	62					8
	MAI12	2009				102					15.5
Puyehue	PUY01	2011	-40.67	-72.57	102	39			9		
	PUY02	2011	-40.67	-72.54	93	71			1		
	PUY03	2011	-40.69	-72.51	97	70			1		
	PUY04	2011	-40.70	-72.51	80	49			0.5		
	PUY05	2011	-40.70	-72.49	90	75			2.5		
	PUY06	2011	-40.70	-72.46	83	75			2		
	PUY07	2011	-40.68	-72.42	108	108			1		
	PUY08	2011	-40.65	-72.48	116	76			5.5		
	PUY09	2011	-40.65	-72.55	90	59			2.5		
Rupanco	RUP01BIS	2009	-40.85	-72.38	213	55					>45
	RUP02BIS	2009	-40.88	-72.24	262	81				5	>62
	RUP03TRIS	2009	-40.82	-72.51	268	44				10	
	RUP04	2009	-40.87	-72.49	97	59				13	
	RUP05	2009	-40.88	-72.31	226	67				3+6+3+2	>28
Llanquihue	LLA3	2011	-41.12	-72.97	92	22				>22	
	LLA4	2011	-41.14	-72.83	298	37			3		

4.4 Results

4.4.1 Background sediments

Background sediments are the sediments that occur in between the seismites (earthquake-triggered event deposits) and represent the normal steady-state sedimentation processes not influenced by earthquakes or other extreme events. At our coring locations, the background sediments are usually composed of hemipelagic sediments. In the deep (> 50 m) southern lakes, located at the foot of the Andes, these hemipelagic sediments are composed of laminated diatomaceous muds. However, lakes with a very large catchment-to-surface ratio, such as the varved Lake Maihue, but also Lake Neltume, have a larger clastic component. In these lakes, a larger part of the background sediment is expected to be deposited by hyperpycnal flows. The shallow lakes (< 30 m) at low altitudes (< 500 m, i.e. Aculeo, Vichuquén, Lanalhue, Butaco and Pullinque) are characterized by homogenous to faintly layered mud, very rich in organic matter; only Lake Vichuquén contains a finely laminated sediment infill. The background sediment of the Andean lakes Negra, Lo Encañado and Laja is composed of laminated clastic-rich mud.

4.4.2 Seismites

The background sediments can be interrupted by event deposits. Based on structure, composition (color, MS, XRF) and grain size, we were able to differentiate between 5 types of event deposits that can be attributed to seismic triggering (i.e. seismites): mass-transport deposits (MTDs), in-situ deformation and three types of lacustrine turbidites. A certain seismite can have different characteristics depending on the lake or location in the lake, but will always contain some key features that are discussed in this section (Fig. 4.3). The definitions given here are based on the seismites we encountered in the studied Chilean lakes. Hence, this section should not be considered to be an overview of seismites that have previously been described in literature.

Mass-transport deposit (MTD)

In a MTD, sediments that were initially deposited on the lacustrine slopes have become deformed (inclined, folded, contorted and/or faulted) while moving downslope. The MTDs usually have an erosional base and can reach a thickness of up to several decimeters or meters. The deformation of the sediments occurs when the sediment package slides or flows downslope. Sometimes, however, the original stratification is preserved and entire sediment packages within an MTD may appear to be undisturbed (Fig. 4.3). On seismic profiles, MTDs are characterized by intercalating deposits with a positive relief and a transparent to chaotic seismic facies.

In-situ deformation

In an in-situ deformed layer, the original laminae or layers are still present (i.e. no laminae or layers are removed or added to the original stratigraphy), but deformed (i.e. inclined, folded and faulted). This can only occur in areas without a significant slope, since the presence of a slope would cause the deforming sediments to start moving. The deformation in these deposits is therefore caused only by the earthquake shaking (Fig. 4.3). Even a thin layer (centimeter-scale) affected by in-situ deformation can be represented on pinger profiles by a chaotic reflection.

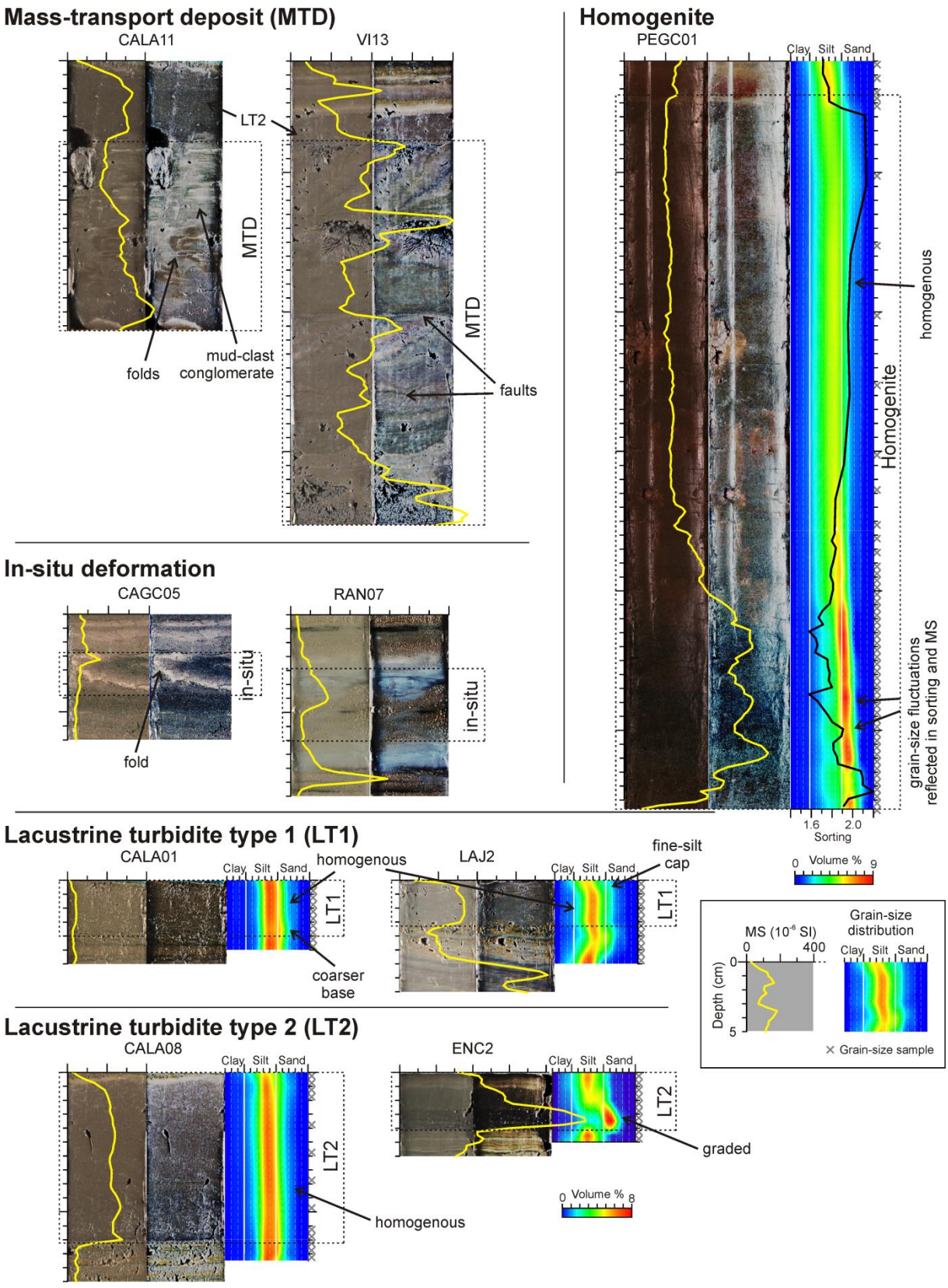

Fig. 4.3 *Different types of seismites that have been encountered in the studied lakes: i) mass-transport deposits (MTD); ii) in-situ deformation; iii) lacustrine turbidites type 1 (LT1); iv) lacustrine turbidites type 2 (LT2) and v) homogenites. Original (left) and processed (Histogram equalization; right) images with magnetic susceptibility (MS; yellow line) and grain-size distribution for the turbidites (samples: gray crosses). Depth scales ar all in cm.*

Turbidites

The encountered turbidites are divided into three groups. Two types of lacustrine turbidites (LT) have a T_a and/or T_e Bouma division (Bouma, 1962) and are distinguished by their composition being similar (LT type 1) or different (LT type 2) to the background sediment. Homogenites have one or more T_a divisions and a thick (>10 cm) T_e division.

Lacustrine turbidite type 1 (LT1). Type 1 lacustrine turbidites (LT1s) are generated by mass-wasting from gentle lateral slopes (i.e. draped with hemipelagic lacustrine sediments) and correspond to the lacustrine turbidites described in Chapter 3. The source area of these turbidites has similar background sediments as those in the area where the turbidite is deposited, resulting in a composition and grain-size distribution of the lacustrine turbidite that is similar to the background sediment at the coring location. Due to the well-sorted nature of the background sediments, the LT1s are mostly homogenous (T_e), with a very thin coarser base (< 2 mm; T_a) and thin fine grained top (< 5 mm; top of T_e; Fig. 4.3). These are the same turbidites as the lacustrine turbidites (LT) in Chapter 3.

Lacustrine turbidite type 2 (LT2). Type 2 lacustrine turbidites (LT2s) are turbidites of which the source area is composed of more terrestrial, usually coarser-grained and more poorly sorted sediments, sometimes also richer in macro-organic matter. This different composition is reflected in higher MS values, darker color and leads to the deposition of a homogenous to well-graded turbidite with a T_a and T_e division (Fig. 4.3), and locally also a T_b, T_c and/or T_d division. Proximal to the source area, these turbidites can contain gravel-size clasts (Lowe (1982) S_3 to T_a) and will therefore be deposited by (hyper-)concentrated density flows with basal laminar flow pattern. Strictly spoken, the deposits are therefore density-flow deposits and not turbidites (Mulder and Alexander, 2001). However, more distally –where most of our cores are located– only the overriding turbulent flow will be left and hence, the resulting deposit can be considered as a turbidite.

Homogenite. A homogenite is a mass-wasting-generated turbidite shaped by a lake seiche. It can reach a thickness of up to a meter or more. A homogenite has a coarse-grained base (T_a) and a thick package of homogenous mud on top, covered by a fine-grained (clay to fine silt) cap (T_e; Fig. 4.3). On seismic profiles, a homogenite is characterized by a transparent seismic facies and its lens-shaped, ponding geometry. The mass-wasting at the origin of the deposit can have occurred onshore or offshore, but has to be large enough to cause a lake tsunami and subsequent seiche. The fluctuating bottom currents linked to the lake seiche cause grain-size fluctuations in the coarse base of the deposit (best represented by the sorting index; Fig. 4.3) and the ponding geometry of the homogenous mud (i.e. the main part of the deposit; Chapron et al., 1999; Bertrand et al., 2008; Beck, 2009; Mulder et al., 2009).

4.4.3 2010 reports and seismites

In the next two sections the reports and deposits of the 2010 and 1960 earthquakes are discussed per lake. From this point onward, the lakes will always be listed from north to south.

Lake Negra

Reports. Lake Negra is a very remote Andean lake. Hence, no reports of the events related to the 2010 earthquake are available. However, most slopes in the area are bare (i.e. not covered by vegetation), and rock slides and avalanches were reported in the entire area, causing valleys to fill

entirely with dust (Fig. 4.4).

Deposits. In both sub-basins of Lake Negra LT2s are present at the top of the cores. In the northern part of the eastern sub-basin (NEG1, a proximal location), a >21 cm thick LT2 occurs with a very coarse gravel bed at the base of the core. In the northern part of the western sub-basin (NEG2), a double (amalgamated) LT2 occurs, of which the two sub-deposits are still distinguishable on a deeper location to the south (NEG3), but not anymore in the deepest areas of this sub-basin (NEG6), where only one thin (1 cm) LT2 is recognized (Fig. 4.4; Table 4.3).

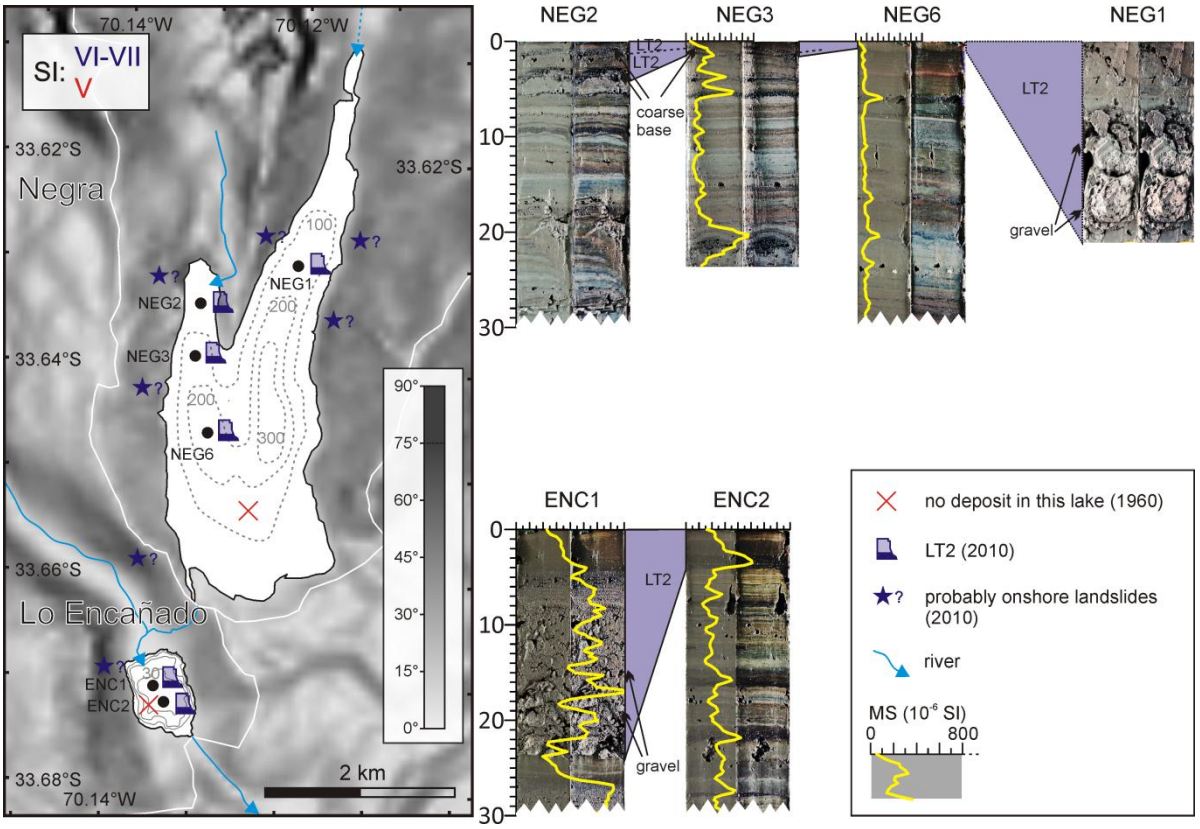

Fig. 4.4 *Slope-shaded SRTM map of the area around lakes Negra (NE) and Lo Encañado (SW) with onshore reports, seismic intensity (SI) of the 1960 (red) and 2010 (blue) earthquakes, bathymetries (gray lines; Table 4.2), coring locations and the encountered seismites. Probably onshore landslides (rockslides) affected the catchments (borders: solid white line) of both lakes. On all coring locations LT2s are attributed to the 2010 earthquake. On the right: LT2s in some cores on original and processed images with MS. Depth scales are in cms.*

Lake Lo Encañado

Reports. Reports for Lake Lo Encañado are equally scarce as for Lake Negra. It has compared to the latter a relatively large catchment area with one main inflowing river and a delta at the river mouth (Fig. 4.4).

Deposits. Both Lo Encañado cores have a well-graded LT2 at their top. Proximal to the delta (ENC1) the deposit is thickest (24 cm) and coarsest (up to coarse gravel at its base), while on a more distal location (ENC2) the deposit has a thickness of 4 cm and a sandy base (Fig. 4.3 and 4.4; Table 4.3).

Lake Aculeo

Reports. Only one irregularity was reported at Lake Aculeo. Some local inhabitants reported having observed approximately 1-m-high (standing) waves. These waves were unusual in regard of the windless conditions. These waves could be interpreted as a type of seiche, caused by the entire water body that moves due to the shaking, resulting in high waves especially close to the shore. No landslides have been reported nor observed in the catchment (Fig. 4.5).

Deposits. After comparing the data with the cores of von Gunten et al. (2009b), which were taken prior to the 2010 earthquake, no seismites were present at the top of any of the cores (Fig. 4.5; Table 4.3).

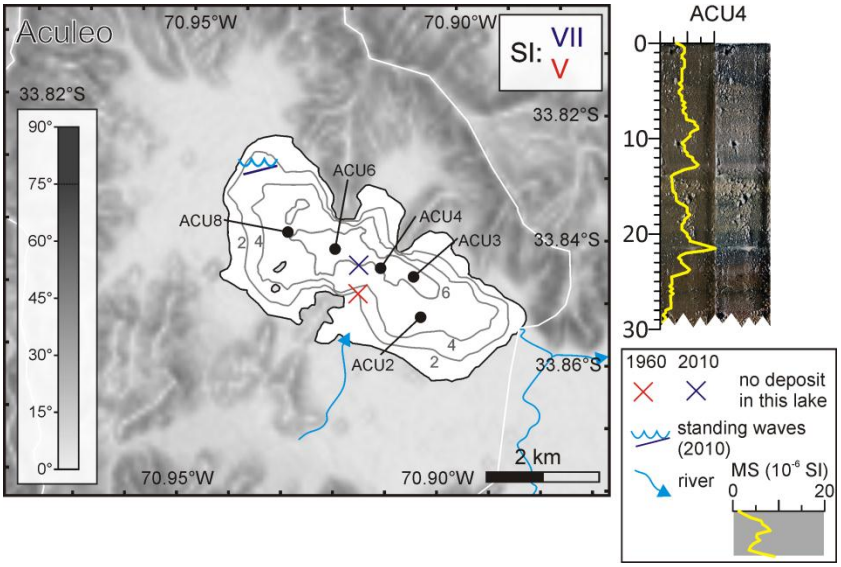

Fig. 4.6 *Slope-shaded SRTM map of the area around Lake Aculeo with onshore reports, seismic intensity (SI), bathymetry (Table 4.1) and coring locations. Standing waves were reported along the shores and no seismites have been encountered in any of the cores. On the right: original and processed image with MS of ACU4. More detailed information in the caption of Fig. 4.3 and 4.4.*

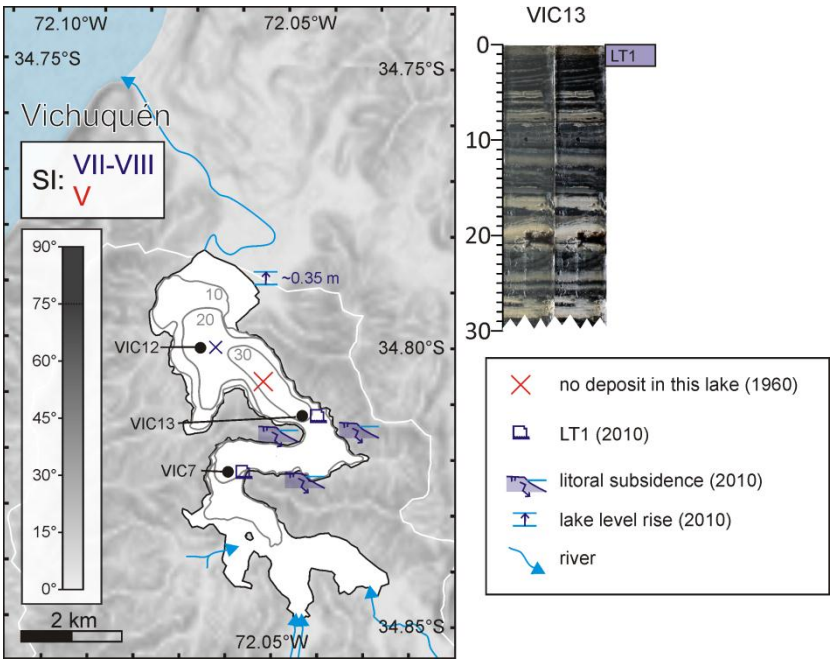

Fig. 4.5 *Slope-shaded SRTM map of the area around Lake Vichuquén with onshore reports, seismic intensity (SI), bathymetry (Table 4.1), coring locations and the encountered seismites. Local subsidence of beaches was reported and Quezada et al. (2010) reported a lake level rise of ~0.35 m at the outlet. On two coring locations LT1s are attributed to the 2010 earthquake. The LT1 in VIC13 on the original and processed image. More detailed information in the caption of Fig. 4.3 and 4.4.*

Lake Vichuquén

Reports. Similar to Lake Aculeo, no landslides were reported in the catchment of Lake Vichuquén. In some areas around the lake, however, local subsidence along the shorelines was observed (e.g., quays disappeared into the lake and cracks formed in beaches). There are no reports of a seiche on the lake. Quezada et al. (2010) reports a rise of the lake level around the outlet of about 35 cm, due to co-seismic subsidence (Fig. 4.6).

Deposits. In the elongated, sinuous basin, thin (1-2.5 cm) LT1s are present at the top of the cores (VIC07 and 13). No seismite was detected in the northern main sub-basin (VIC12; Fig. 4.6; Table 4.3).

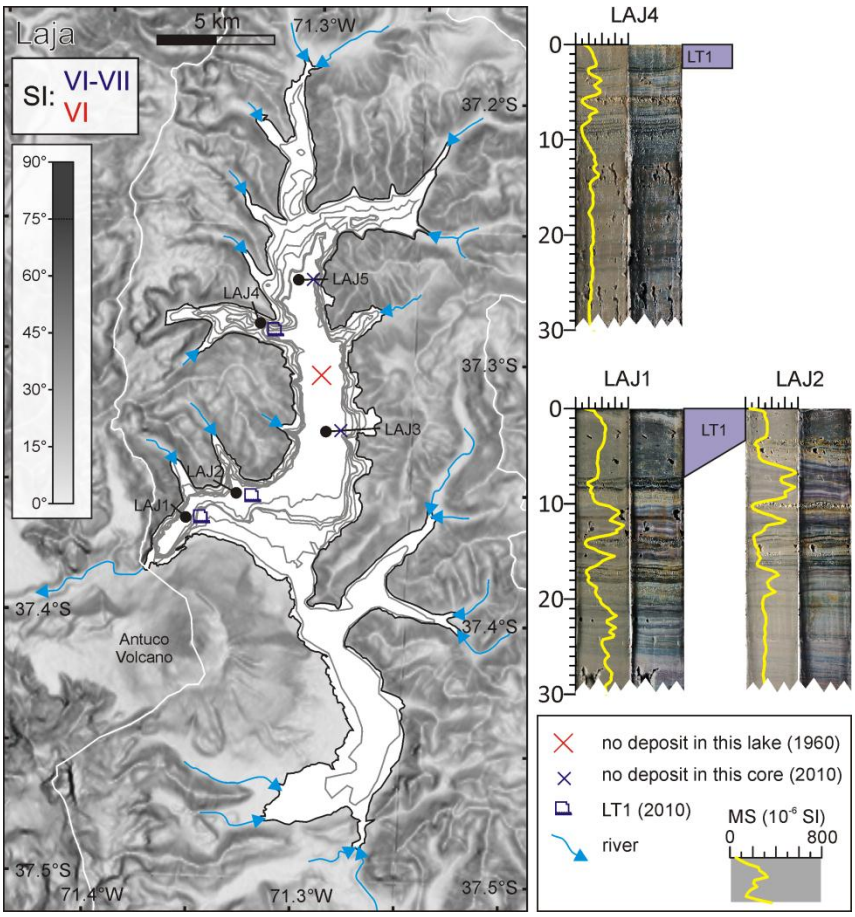

Fig. 4.7 *Slope-shaded SRTM map of the area around Lake Laja with onshore reports, seismic intensity (SI), bathymetry (Table 4.1), coring locations and the encountered seismites. In the western sub-basins LT1s are attributed to the 2010 earthquake. All LT1s on the original and processed images with MS. More detailed information in the caption of Fig. 4.3 and 4.4.*

Lake Laja

Reports. During the summer season only two people live at this remote lake, who did not report any irregularities. No onshore landslides were observed in the catchment.

Deposits. In the two western sub-basins (LAJ1, 2 and 4) of the lake, LT1s (≤ 7 cm) occur in the top of the cores. In the central basin (LAJ3 and 5) no seismites were encountered (Fig. 4.3 and 4.7; Table 4.3).

Lake Lanalhue

Reports. In the catchment of Lake Lanalhue only minor landslides occurred, some of which along the lake's shores. On the flat delta plains of Elicura River at the eastern shores of the lake, a small (~20 cm), temporary lake-level drop was observed after the earthquake. In the days after the earthquake

the outlet (in the west) temporarily dried out, indicating that there was coastal uplift, resulting in tilting of the lake. This resulted in a permanent lake-level rise at the eastern side of the lake, causing beaches and quays to become drowned. These observations match the observations of Quezada et al. (2010), who reported a lake-level rise of about 40 cm in the eastern sector of camping Chanchán and a minor drop (~10 cm) in the La Vaina sector. However, we have reports of a lake-level rise of several tens of centimeters at the peninsula just south of La Vaina, indicating that some of these lake-level changes can be very local (Fig. 4.8).

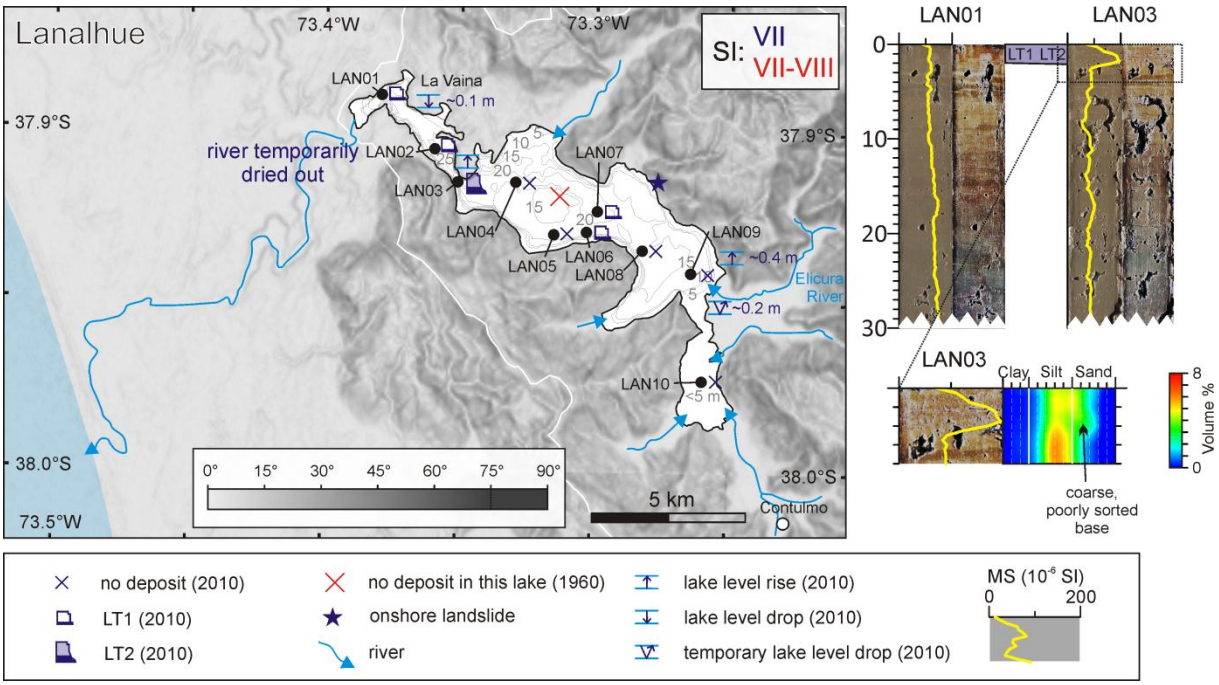

Fig. 4.8 *Slope-shaded SRTM map of the area around Lake Lanalhue with onshore reports, seismic intensity (SI), bathymetry (Table 4.2), coring locations and the encountered seismites. Lake level changes were reported at several locations (Quezada et al., 2010) and the outlet temporarily dried out. LT1s and LT2s are attributed to the 2010 earthquake. On the right: seismites in two cores on the original and processed images with MS; below: a zoom of LAN03 with grain-size distribution. More detailed information in the caption of Fig. 4.3 and 4.4.*

Deposits. Lacustrine turbidites were detected only in the deepest areas of the lake, close to steep slopes. In LAN03, located in both the deepest basin (~25 m) and narrowest part of the lake (~350 m across) a LT2 occurs at the top of the core. In other depocenters (LAN01, 02, 06 and 07), thin (0.5-2.5 cm) LT1s occur (Fig. 4.8; Table 4.3).

Lake Butaco

Reports. Similar to Lake Lanalhue, the outlet of Lake Butaco temporarily (i.e. a couple of days) dried out after the earthquake. These observations are corroborated by the uplift of approximately 30 cm at Playa Quidica (~2 km southwest of Lake Butaco), reported by Quezada et al. (2010). Furthermore, some cracks were observed in beaches along the northwestern shore of the lake (Fig. 4.9 and 4.10).

Deposits. In the central part of the lake (BUT2) a thin (2 cm) LT1 is present, while closer to the outlet (northeast; BUT3) a thin erosional LT2 (2 cm) was observed. In the southwestern part no deposit is present (Fig. 4.9; Table 4.3).

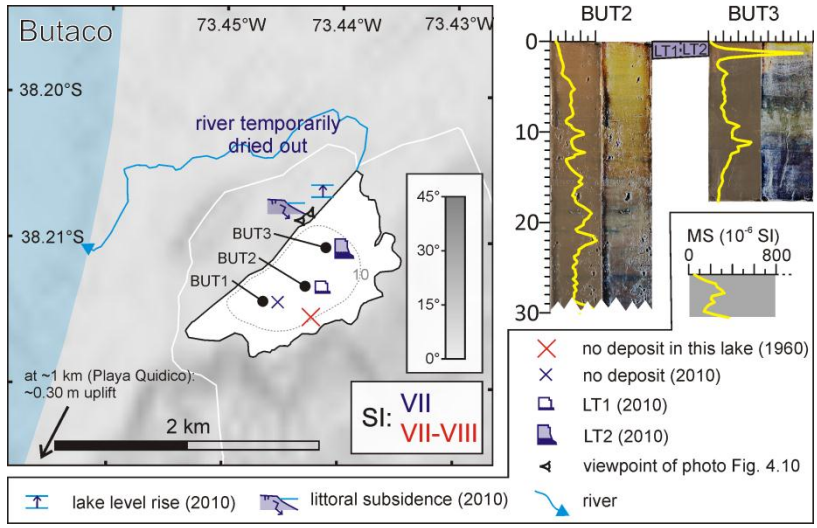

Fig. 4.9 *(left) Slope-shaded SRTM map of the area around Lake Butaco with onshore reports, seismic intensity (SI), bathymetry (Table 4.1), coring locations and the encountered seismites. Co-seismic uplift was reported by Quezada et al. (2010) at Playa Quidico, the outlet temporarily dried out and locally some littoral subsidence was reported. One LT1 and LT2 are attributed to the 2010 earthquake. On the right: seismites in two cores on the original and processed images with MS. More detailed information in the caption of Fig. 4.3 and 4.4.*

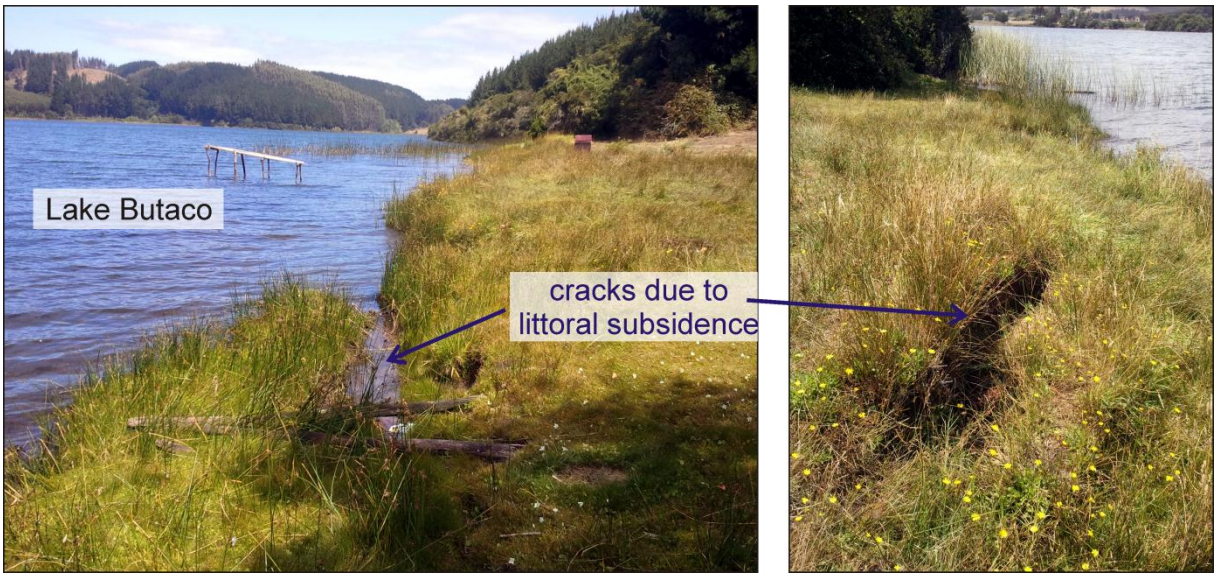

Fig. 4.10 *Cracks along the northwestern shore of Lake Butaco indicating littoral subsidence (February 2012; location: see Fig. 4.9).*

Lake Villarrica

Reports. In Lake Villarrica a small tsunami crossed the lake after the earthquake. At the eastern end of the lake (around Pucón), the lake level dropped 2 to 3 m immediately after the earthquake, then rose until about 1-1.5 m above its normal level with an incoming wave. After this oscillation the lake level returned to its original level. Buoys of harbors in and around Pucón drowned permanently due to subsidence in the near-shore zone (Fig. 4.11). Also the beach south of the Trancura River inlet subsided and disappeared. Some of the local inhabitants consider the effects worse than those that were induced by the 1960 earthquake. On the western side of the lake (in the Villarrica-town harbour) the lake level first rose about 80 cm, then dropped, to finally return to its normal level. On the beach of Villarrica town some sand blows were observed, indicating liquefaction. All the observations point to a tsunami-like effect, propagating from the east to the west. The event apparently did not evolve into a lake seiche. No alterations were observed in the catchment of Lake Villarrica (Fig. 4.12).

Fig. 4.11 *Coastal subsidence induced by the 2010 earthquake at the Trancura River delta north of Pucón (February 2012; location: see Fig. 4.12), evidenced by the disappearance of beaches previously bordering the forests.*

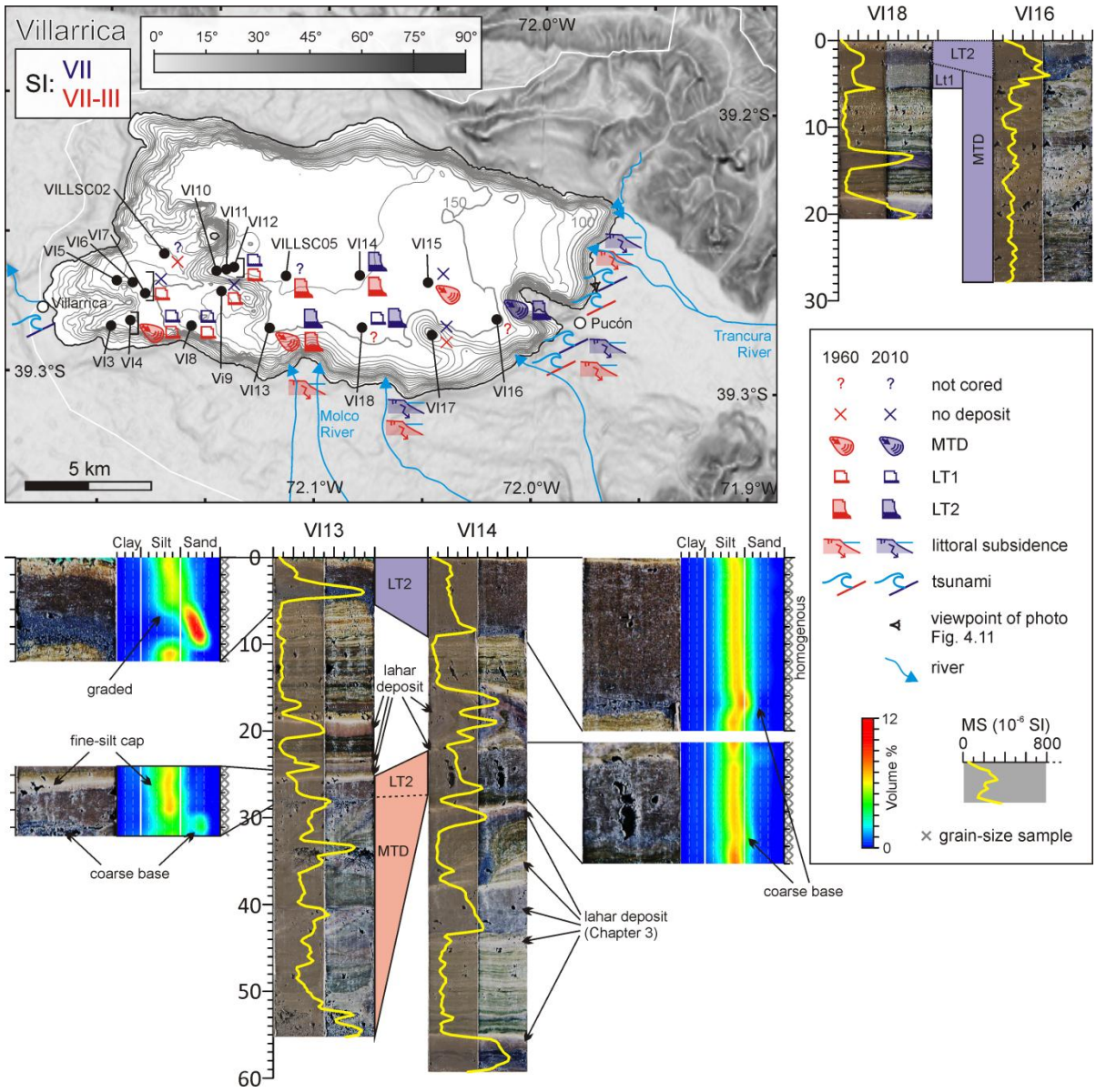

Fig. 4.12 *Slope-shaded SRTM map of the area around Lake Villarrica with onshore reports, seismic intensity (SI), bathymetry (Table 4.2), coring locations and the encountered seismites. Littoral subsidence and tsunamis were reported in both 1960 (red; Weischet, 1963; Sievers, 2000) and 2010 (blue). MTDs, LT1s and LT2s are attributed to both earthquakes. On the right and below: seismites in several cores on the original and processed images with MS, and grain-size distribution of some LT2s. More detailed information in the caption of Fig. 4.3 and 4.4.*

Deposits. In the southwestern sub-basins of the lake, locally some thin (< 1.5 cm) LT1s occur (Moernaut et al., submitted). In the southeastern corner of the lake (VI16), a MTD is present and covered by a LT2. Furthermore, a well graded 5 cm thick LT2 occurs northwest of the Molco delta (VI13) and a mostly homogenous LT2 was found in the main basin (VI14). West of the ridge in the southeastern part of the lake (VI18) a LT1 (2.8 cm) is covered by a LT2 (2.7 cm), indicating 2 density flows reaching this location (Fig. 4.12; Table 4.3).

Lake Calafquén

Reports. Local near-shore subsidence was observed in Lake Calafquén. On Playa Chica in Lican Ray (east of the peninsula; Fig. 4.13) some buoys disappeared below the water surface due to subsidence. On Playa Grande (west of the peninsula; Fig. 4.13), nothing out of the ordinary was observed. In Coñaripe, similarly to reports in Lake Aculeo, large (standing) waves were observed during the earthquake. Shortly after the earthquake, the lake level rose up to approximately 1 m above normal lake level (first row of trees) and subsequently returned to its normal level. Also, the lake-ward limit of the submerged part of the beach moved landward after the earthquake, indicating littoral subsidence (Fig. 4.13).

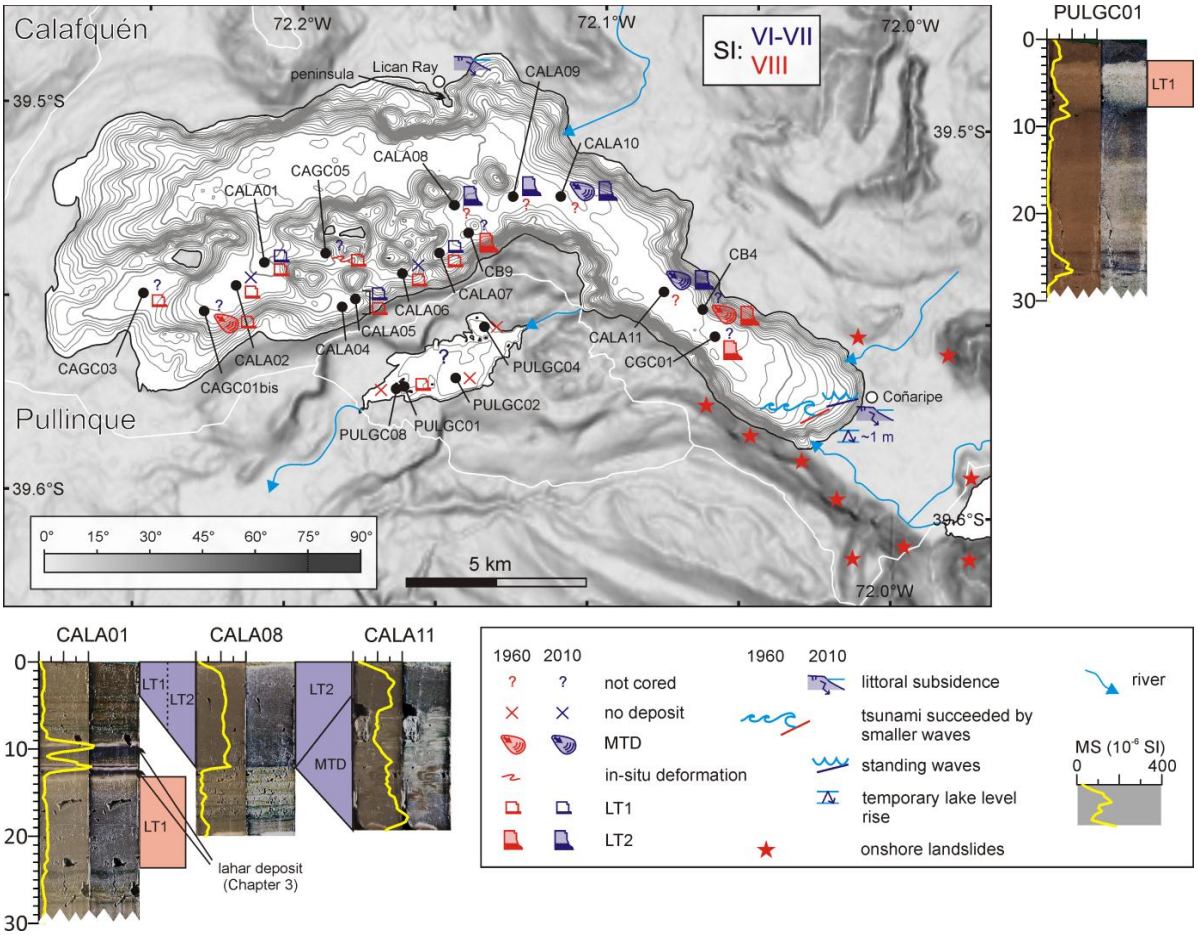

Fig. 4.13 *Slope-shaded SRTM map of the area around lakes Calafquén and Pullinque with onshore reports, seismic intensity (SI), bathymetry (Table 4.2), coring locations and the encountered seismites. Large waves were reported in Coñaripe in both 1960 (red; Weishet, 1963; Wright and Mella, 1963; Sievers, 2000) and 2010 (blue). In Lake Calafquén, MTDs, LT1s and LT2s are attributed to both earthquakes; one in-situ deformation was attributed to the 1960 earthquake. In Lake Pullinque (cored in 2008), one LT1 is attributed to the 1960 earthquake (see original and processed image with MS on the right). Below: seismites in several cores on the original and processed images with MS. More detailed information in the caption of Fig. 4.3 and 4.4.*

Deposits. In the southwestern sub-basins, LT1s occur locally (CALA1, 4, 5 and 7; Moernaut et al., submitted). Both cores in the eastern sub-basin (CALA10 and 11) have a MTD which is covered by a LT2. In CALA10, the base of this LT2 contains rip-up mud clasts and more distally (CALA09) the LT2 is a 21.5 cm thick, well-graded turbidite. Similar to Lake Villarrica, the LT2 becomes more homogenous towards the central areas of the basin (CALA08; Fig. 4.13; Table 4.3).

Lake Riñihue

Reports. There are no reports of any unusual events in or around Lake Riñihue. However, since the 1960 earthquake (see further) few people live along the coastline (Fig. 4.14).

Deposits. Southeast of a small delta on the northern shore of the northwestern sub-basin, a LT2 was encountered on two locations. A 3 cm thick graded LT2 on the most proximal location (RI7) and more distally (RI6) a thinner (2 cm) homogenous LT2 (Moernaut et al., submitted; Fig. 4.14; Table 4.3).

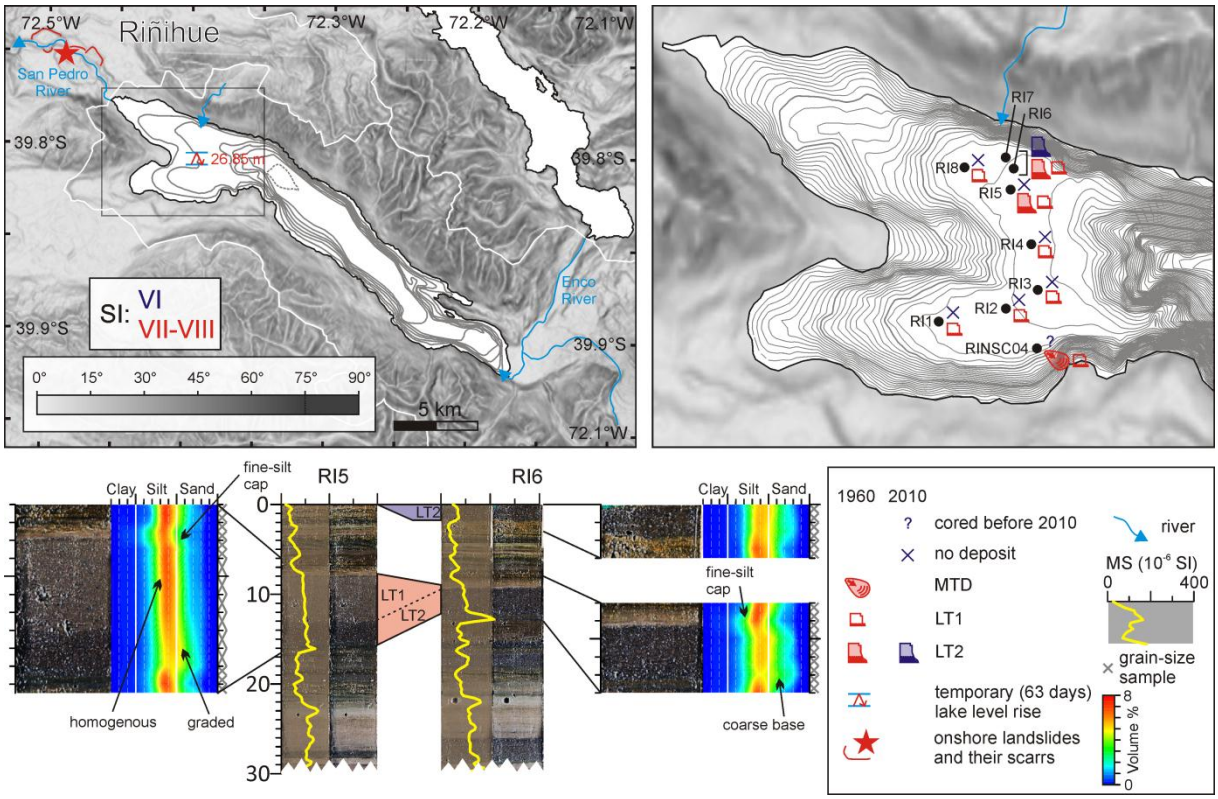

Fig. 4.14 *Slope-shaded SRTM map of the area around Lake Riñihue with onshore reports, seismic intensity (SI), bathymetry (Table 4.2); and coring locations and the encountered seismites in the zoom on the right. After the 1960 earthquake, the lake level rose 26.85 m due to landslides blocking the outlet (Davis and Karzulovíc, 1963; Weishet, 1963; Wright and Mella, 1963; Sievers, 2000). One MTD, several LT1s and some LT2s are attributed to the 1960 earthquake, only LT2s to the 2010 earthquake. Below: seismites in two cores on the original and processed images with MS, and grain-size distributions of the seismites. More detailed information in the caption of Fig. 4.3 and 4.4.*

Lake Ranco

Reports. There are no reports of any unusual events in or around Lake Ranco.

Deposits. Along the western flanks of the western sub-basin (RAN6) a 8 cm thick MTD is covered by a thin (2 cm), homogenous LT1. Along the northern flanks of the northwestern sub-basin (RAN2) a LT2

occurs that is mainly composed of its sandy base (0.5 cm). In the central parts of both sub-basins (RAN7 and RAN3, respectively) no deposit was detected (Fig. 4.15; Table 4.3).

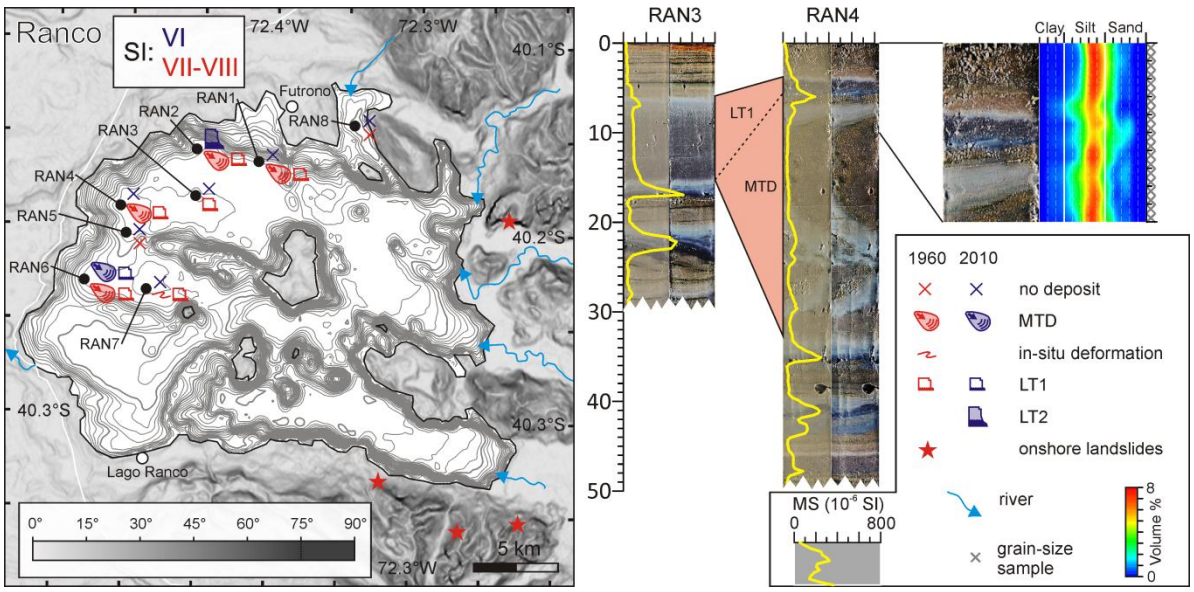

Fig. 4.15 *Slope-shaded SRTM map of the area around Lake Ranco with onshore reports, seismic intensity (SI), bathymetry (Table 4.2), coring locations and the encountered seismites. Few landslides were reported in the catchment after the 1960 earthquake. Several MTDs and LT1s are attributed to the 1960 earthquake, locally seismites are attributed to the 2010 earthquake. Below: seismites in three cores on the original and processed images with MS, and grain-size distribution of the upper part of RAN4. More detailed information in the caption of Fig. 4.3 and 4.4.*

4.4.4 1960 reports and seismites

General remarks

The 1960 earthquake triggered many onshore landslides, often concentrated in certain areas. Most affected was a 8-20 km broad zone between Reloncaví Fjord and Villarrica Volcano, about 25 km east of the western foot of the Andes (Weishet, 1963). The high local concentration of landslides in this region results probably from a combination of the Liquiñe-Ofquí Fault Zone, causing fracturing of the substrate in this area making it more susceptible to landsliding, and the presence of volcanoes in this region, causing thick ash layers and andosols on top of the bedrock, which are also more susceptible to sliding. Finally, in the catchments of many lakes (e.g., Llancuihue, Rupanco, Calafquén, Ranco and Villarrica) minor soil slumps were reported (Wright and Mella, 1963).

Lakes Lanalhue, Butaco and Laja

Reports. We do not have reports on any of these lakes.

Deposits. In both lakes Lanalhue and Laja, no seismites are present around the depths that – according to existing age models (Quiroz et al., 2006; Stefer et al., 2010)– have an age of AD 1960. In Lake Butaco some deposits occur that are similar to the 2010 seismite (e.g., and LT2 with very high MS at 25 cm in BUT1). However, lack of an age model prevents attributing any of these deposits to the 1960 earthquake (Fig. 4.7, 4.8 and 4.9).

Lake Villarrica

Reports. At the eastern end of Lake Villarrica, the earthquake was followed by a rise of the water level in northern Pucón, while it synchronously dropped in southern Pucón. The water returned to its normal level after about 15 minutes. In northern Pucón the water was reported to be *boiling*. On many beaches around the lake subsidence was reported. In the catchment of Lake Villarrica no major landslides were reported (Weischet, 1963; Sievers, 2000; Fig. 4.12).

Deposits. LT1s are present on all coring locations in the southwestern sub-basins (VI3, 4, 5, 6, 7, 8, 10, 11 and 12), only on the plateau (VILLSC02) not deposit was encountered. Also, thin (<5 cm) MTDs were detected in the two cores in the most southwesterly located sub-basin (VI3 and 4) (Moernaut et al., submitted). Northwest of the Molco delta (VI13), a > 27 cm thick MTD covered by a 2 cm thick LT2 was found. Also in the eastern part of the main basin (VI15) an MTD occurs, and both cores in the central part of the main basin (VI14 and VILLSC05) contain a LT2 (Fig. 4.12; Table 4.3).

Lake Calafquén

Reports. In contrast to the catchment of Lake Villarrica, many landslides occurred in the catchment and along the southern shores of the eastern sub-basin of Lake Calafquén. These landslides triggered a main wave and subsequently some small secondary waves in the upper eastern end of the lake (Weishet, 1963; Wright and Mella, 1963; Sievers, 2000; Fig. 4.13).

Deposits. In the southwestern sub-basins (CAGC01bis, 02bis, 03 and 05, CALA01, 02, 04, 05, 06 and 07) several LT1s were attributed to the 1960 earthquake. In CAGC05, this LT1 covers a 3 cm thick layer affected by in-situ deformation. At the foot of the southwestern sub-basin slopes (CAGC01bis), the LT1 is covering a ~67 cm thick MTD that is clearly visible on the pinger profiles (Moernaut et al., submitted). More MTDs occur in the eastern and northern sub-basins (CB4 and 9, respectively 22 and > 9.5 cm thick) and are overlain by one or in CB9 even two LT2s (Chapter 3; Fig. 4.13; Table 4.3).

Lake Pullinque

Reports. This is one of the few lakes in this region where lake conditions were observed to be unaffected by the seismic activity (Sievers, 2000).

Fig. 4.16 *Southeastern shore of Lake Pellaifa (January 2008; location: see Fig. 4.17), showing the 5 m lake-level rise after the 1960 earthquake, evidenced by the drowned trees.*

Fig. 4.17 *(right) Slope-shaded SRTM map of the area around Lake Pellaifa with onshore reports, seismic intensity (SI), bathymetry (Table 4.2), mapped homogenite and chaotic seismic facies, coring locations and the encountered seismites. Many landslides were reported in the catchment after the 1960 earthquake, several of which*

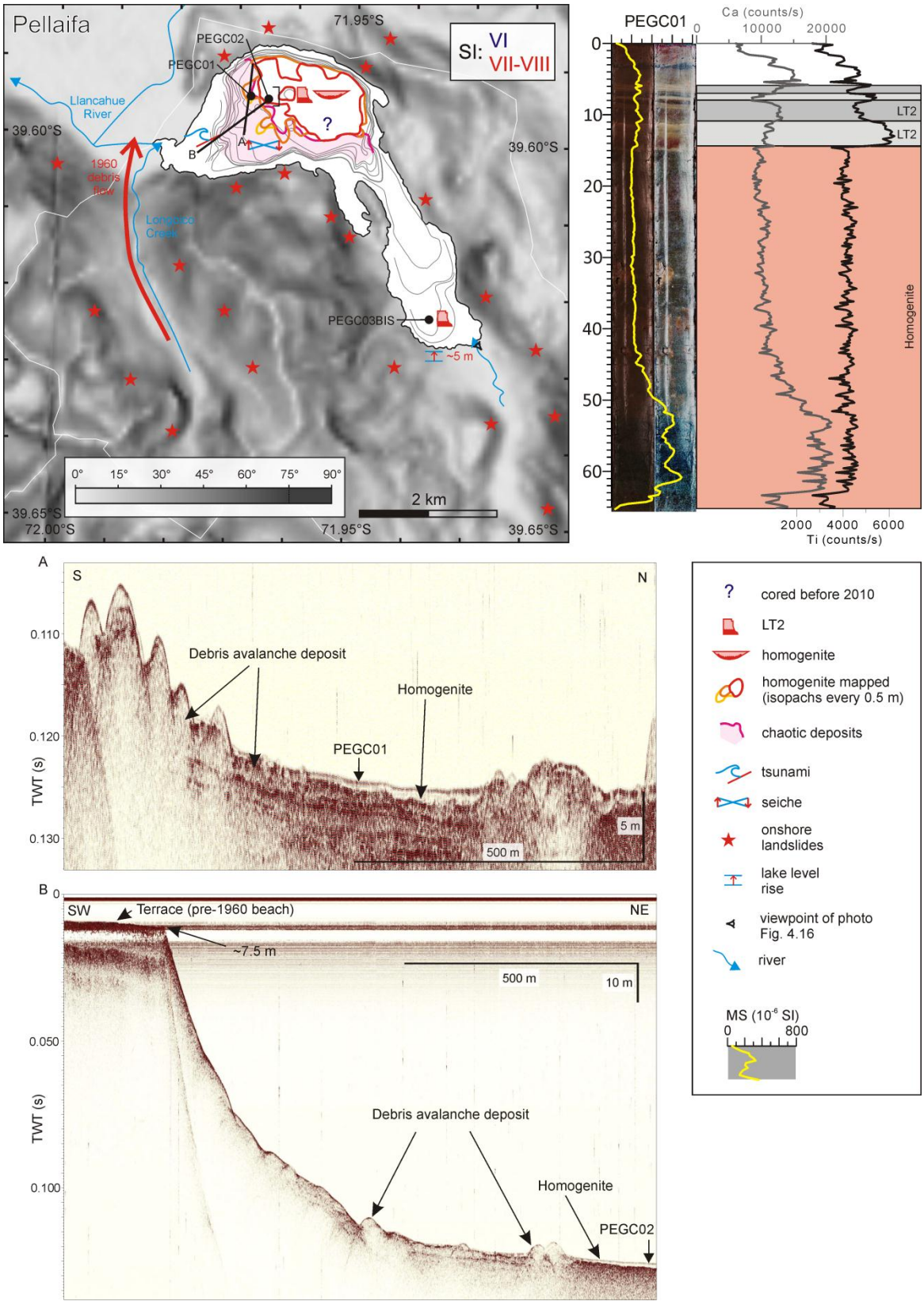

(continuation Fig.4.17) directly surging into the lake, causing a tsunami and subsequent lake seiche, a debris flow dammed the lake and caused a permanent 5 m lake level rise (Weishet, 1963; Wright and Mella, 1963; Sievers, 2000). A homogenite in the main basin is covered by several LT2s, all attributed to the 1960 earthquake. On the right: homogenite in PEGC01 on the original and processed images with MS and XRF Ca- and Ti-counts, indicating different source areas of the overlaying LT2s. Below: A) seismic pinger profile of debris-avalanche deposits and homogenite; B) seismic pinger profile that also shows a drowned terraces, interpreted as the pre-1960 beach (locations: solid black lines on map). More detailed information in the caption of Fig. 4.3 and 4.4.

Deposits. In only one location, at the foot of a small slope the western sub-basins (PULGC01), a 5 cm thick LT1 interrupts the background sediments (Fig. 4.13; Table 4.3).

Lake Pellaifa

Reports. Landslides occurred both within the catchment and along almost all the shores of Lake Pellaifa. The landslides that impacted the lake surface caused a large impact wave, after which smaller secondary waves ricocheted back and forth on the lake some time afterwards. A debris flow originating in the Longoico Creek catchment blocked the outlet, causing a permanent lake-level rise of about 5 m (Fig. 4.16). The same debris flow also caused changes in the course of the Llancahue River (Weishet, 1963; Wright and Mella, 1963; Sievers, 2000; Fig. 4.17).

Deposits. In the main basin of Lake Pellaifa (PEGC02), a >70 cm thick homogenite occurs (≥51.5 cm in PEGC01). In PEGC01, the homogenite has at least six grain-size fluctuations in its coarse basal part (Fig. 4.3) and is covered by four LT2s, of which the first, the third and especially the fourth have a pronounced fine grained cap. Also, the first and the third LT2 have a clearly distinct geochemistry (high Ti and low Ca counts), while the geochemistry of the other two turbidites resembles more that of the homogenite. In the southern end of the southeastern sub-basin (PEGC03BIS) a 9 cm thick LT2 occurs. On the reflection seismic profiles in the southern and western part of the main basin, the homogenite (up to 1.5 m thick) is onlapping a chaotic seismic facies with several separate blocks, interpreted as the deposits of the earthquake-triggered onshore landslides that surged into the lake. On the reflection-seismic profiles, also a drowned terrace was identified in the western part of the lake (Fig. 4.17; Table 4.3).

Lake Panguipulli

Reports. Almost simultaneously with the earthquake, a wave with a height of approximately 6 m reached Puerto de Panguipulli (this locality does not exist anymore and we do not know where it used to be located) and had a run-up of locally 100 m. The tsunami, which destroyed all harbours except that of Panguipulli in the western sub-basin and Puñire in the southeastern part of the lake, was followed by a seiche (Weishet, 1963; Wright and Mella, 1963; Sievers, 2000; Fig. 4.18).

Deposits. In the deepest (main) basin a homogenite occurs (PAGC06 and 10) and reaches a maximum thickness of >72 cm. In the western part of the basin (PAGC06) this homogenite is covered by two thin (0.8 and 0.7 mm) LT1s; in the central part of the basin (PAGC10) only one LT1 remains. The reflection-seismic profiles show how the homogenite is filling the deepest parts of the deep basin and is thicker towards the western sub-basin. In this sub-basin, the profiles also show how a chaotic deposit fills the western extremity of the deep basin. In the eastern and northern sub-basins, a ~5 cm thick LT1 occurs (PAGC03, 04 and 05). In the northern sub-basin (PAGC04) this turbidite is covering a >40.5 cm thick MTD (Fig. 4.18; Table 4.3).

Lake Neltume

Reports. Many landslides were reported in the catchment and along the shores of Lake Neltume. There are no reports on irregularities of the lake level (Tazieff, 1960; Weishet, 1963; Fig. 4.19).

Deposits. Both cores from Lake Neltume contain a homogenite that is overlain by a LT2. Close to the northwestern border (NEL2), the homogenite has a thickness of 27.5 cm and shows three grain-size

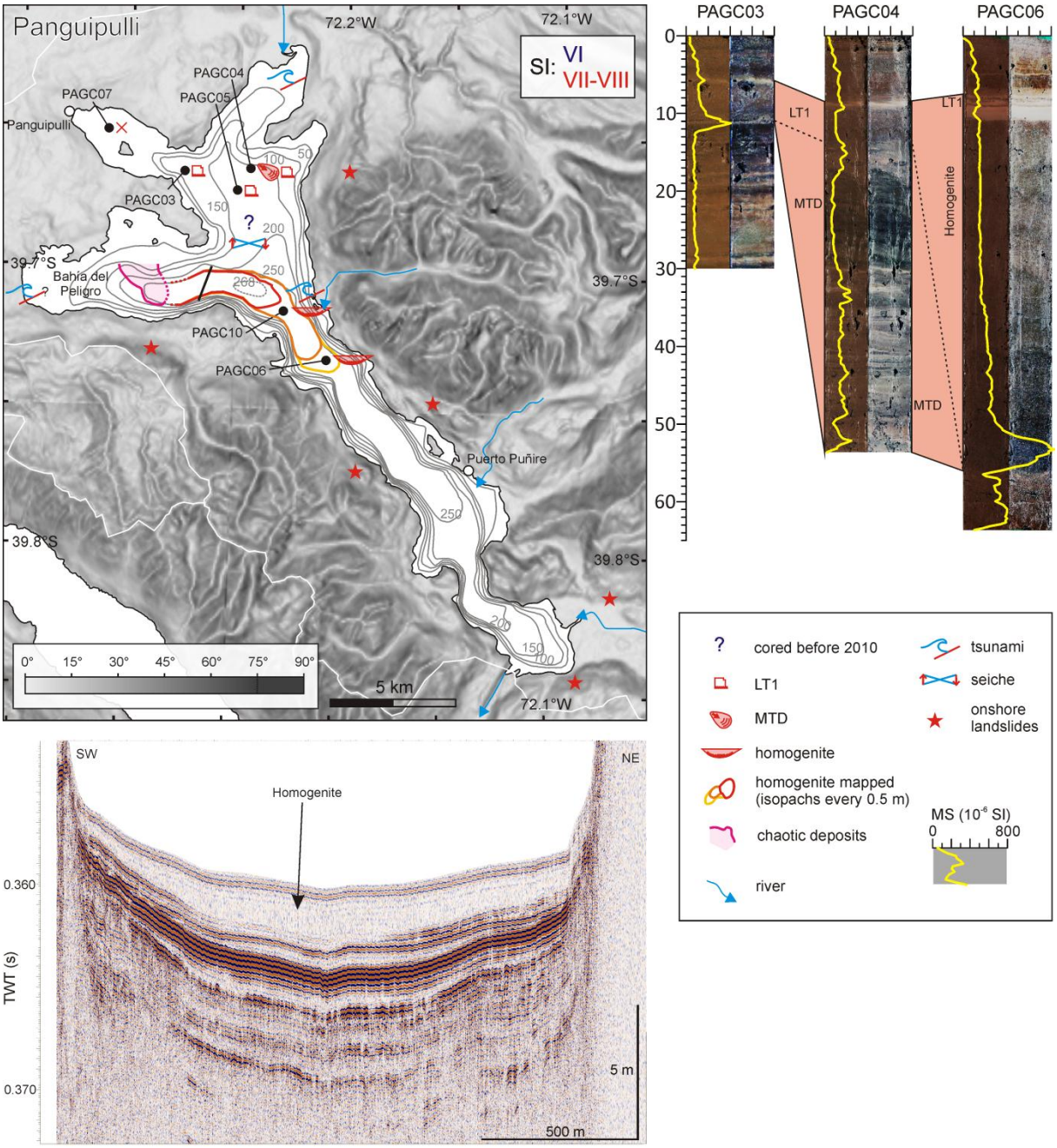

Fig. 4.18 *Slope-shaded SRTM map of the area around Lake Panguipulli with onshore reports, seismic intensity (SI), bathymetry (Table 4.2), mapped homogenite and chaotic seismic facies, coring locations and the encountered seismites. Several landslides were reported in the catchment after the 1960 earthquake and a tsunami and subsequent lake seiche were reported on the lake (Weishet, 1963; Wright and Mella, 1963; Sievers, 2000). A homogenite is present in the deep basin and some LT1s and an MTD in the western sub-basins, these are all attributed to the 1960 earthquake. On the right: seismites in several cores on the original and processed images with MS. Below: seismic pinger profile of homogenite (location: solid black line on map). More detailed information in the caption of Fig. 4.3 and 4.4.*

fluctuations at its sandy base. Towards the southeastern border (NEL4BIS), the homogenite is thicker (>30 cm) and the base was not reached by coring. Along the foot of both the northwestern and southeastern slopes, a chaotic seismic facies with single blocks is observed on the reflection-seismic profiles. It is covered by a homogenous unit with a thickness of less than 1.5 ms two-way travel time. These chaotic deposits are interpreted as the deposits of the onshore landslides that surged into the lake (Fig. 4.19; Table 4.3).

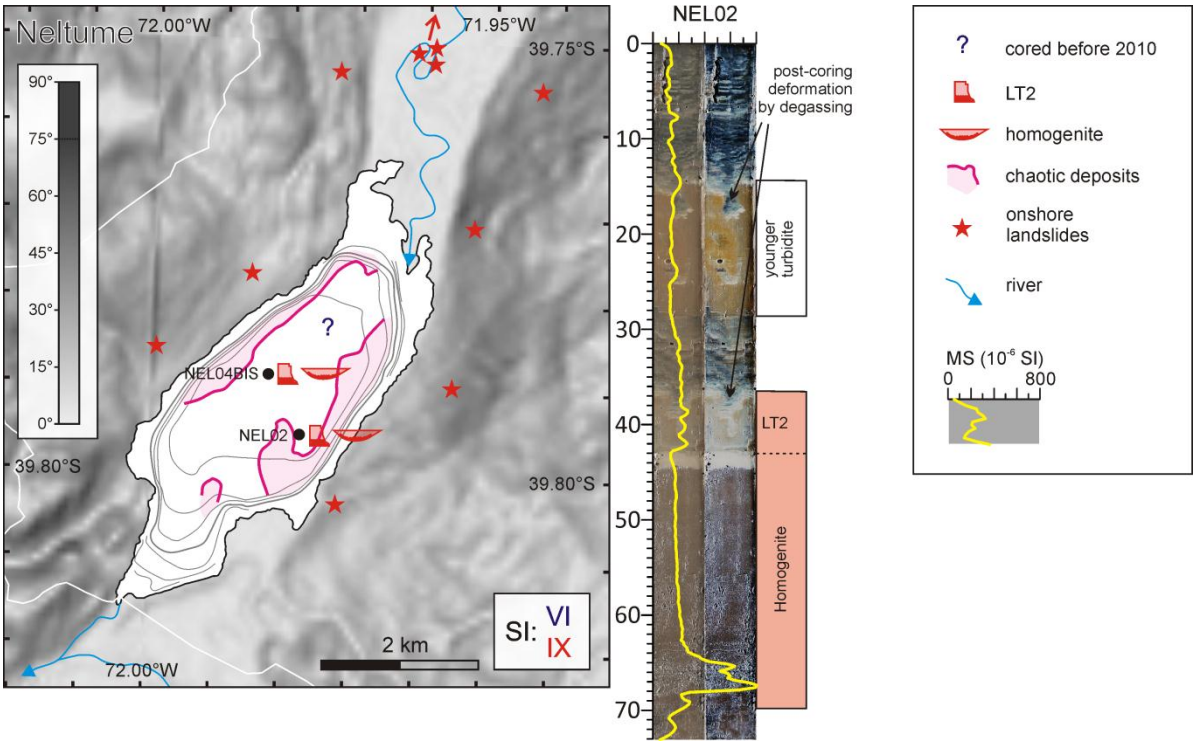

Fig. 4.19 *Slope-shaded SRTM map of the area around Lake Neltume with onshore reports, seismic intensity (SI), bathymetry (Table 4.2), mapped chaotic seismic facies, coring locations and the encountered seismites. Many landslides were reported in the catchment after the 1960 earthquake, several of which directly surging into the lake (Tazieff, 1960; Weishet, 1963). A homogenite that covered by one LT2 are both attributed to the 1960 earthquake. On the right: homogenite and LT2 in NEL02 on the original and processed images with MS. More detailed information in the caption of Fig. 4.3 and 4.4.*

Lake Riñihue

Reports. No irregularities of lake behavior were induced as a direct consequence of the earthquake. However, major onshore landslides blocked the outflowing San Pedro River, causing the lake level to rise 26.85 m during 63 days and connect with Lake Panguipulli. Several attempts were made to open the natural dam, with all then available techniques and manpower. When the dam finally broke (Riñihuazo), the outflow was partially controlled, but the disastrous flooding of Valdivia could not be prevented (Davis and Karzulovíc, 1963; Weishet, 1963; Wright and Mella, 1963; Sievers, 2000; Fig. 4.14).

Deposits. In both western sub-basins LT1s are present in every core (RINSC04, RI1, 2, 3, 5, 6, 7 and 8; Moernaut et al., submitted). At the foot of the southern slopes of the southern sub-basin (RINSC04), the LT1 is covering a 40 cm thick MTD. Southeast of a small delta on the northern shore of the northwestern sub-basin, a LT2 was encountered on 3 locations. On the most proximal location (RI7) the LT2 is 3.5 cm thick graded turbidite with a coarse sandy base, distally (RI6 and RI5) the LT2 becomes thinner (2-3 cm) and more homogenous (Moernaut et al., submitted; Fig. 4.14; Table 4.3).

Lake Ranco

Reports. Scattered landslides on the northern flanks of the Puyehue-Cordón Caulle Volcanic Complex were observed on aerial photographs. However no landslides directly surged into the lake and also no other disturbances were reported (Fig. 4.15).

Deposits. Along the western flanks of the western sub-basin (RAN6) an MTD (8.5 cm) is overlain by a thin (1 cm) LT1. In the central part of this basin (RAN7) a 5 cm thick in-situ deformation is also covered by a thin (1 cm) LT1. In the northwestern sub-basin (RAN1, 2 and 4) MTDs (>35, 23 and 28 cm, respectively) are present along all the slopes bordering the lake shores. The MTDs are covered by a thin (1-1.5 cm) LT1, while in the central part of the basin (RAN3) a thick (9.5 cm) LT1 is present. Sandy sediments inhibited coring in the eastern sub-basins (Fig. 4.15; Table 4.3).

Lake Maihue

Reports. Lake Maihue has a large catchment in which the Pillanleufú River is one of the main rivers. A large part of the slopes of the Pillanleufú valley failed during the earthquake (Weishet, 1963). On the southwestern lake shore, a major landslide occurred in the northeastern slopes of Cerro Carrán (Los Guindos; part of the Carrán-Los Venados volcanic complex; Fig. 4.20) and entered the lake. This landslide must have caused a large wave crossing the lake, however, no detailed reports on this event are available (Fig. 4.21).

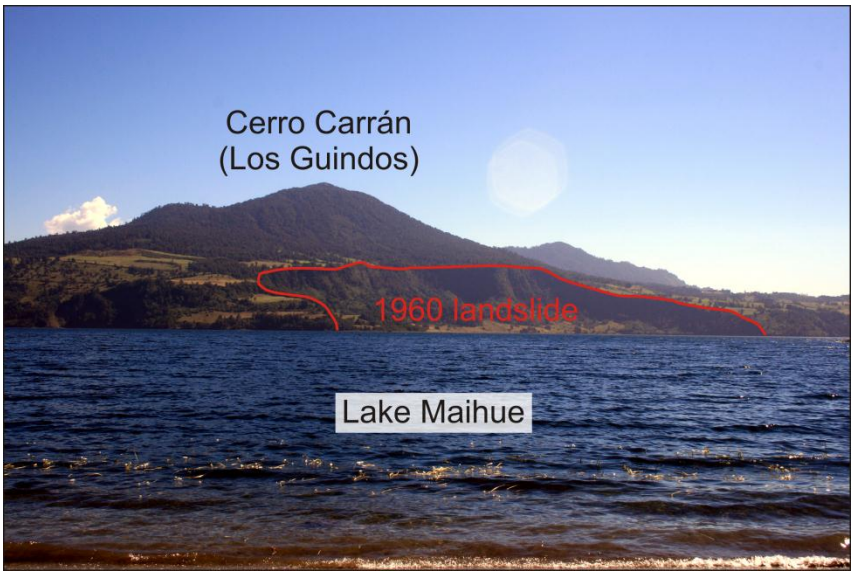

Fig. 4.20 *View from a beach on the northeastern shore of Lake Maihue on the scar of a large onshore landslide triggered by the 1960 earthquake on the northern slopes of Cerro Carrán (May, 2009; locations: see Fig. 4.21).*

Deposits. In the southwestern part of the main basin an MTD with a thickness of >20 cm is present in the cores which are located on top and in front of an irregular bathymetric high northeast of the onshore landslide scarp (MAI01, 02 and 03). In the central part of the main basin (MAI04) a homogenite occurs (32 cm), while in the south (MAI06) only an 8 cm thick LT2 is present. Both the MTDs and the homogenite in the central part of the basin are overlain by a 2-4.5 cm thick LT1/LT2 (MAI01, 02, 03 and 04). It is not possible to clearly distinguish between LT1s and LT2s, since the background sediment consistes of clastic sediments. Therefore LT1s would have a similar composition as LT2s. In the central part of the western sub-basin (MAI12) a 15.5 cm thick homogenite is encountered. In most of the cores these deposits that all have a fine-silt cap are covered by one or two LT1/LT2s with a thickness of 1 to 4 cm (Fig. 4.21; Table 4.3).

Lake Puyehue

Reports. In the catchment of Lago Puyehue several landslides occurred, some of which temporarily dammed the Golgol River. These landslide dams broke through in the following weeks by *floods* following the earthquake. No irregularities in the lake level during or after the earthquake have been reported (Tazieff, 1960; Wright and Mella, 1963; Fig. 4.22).

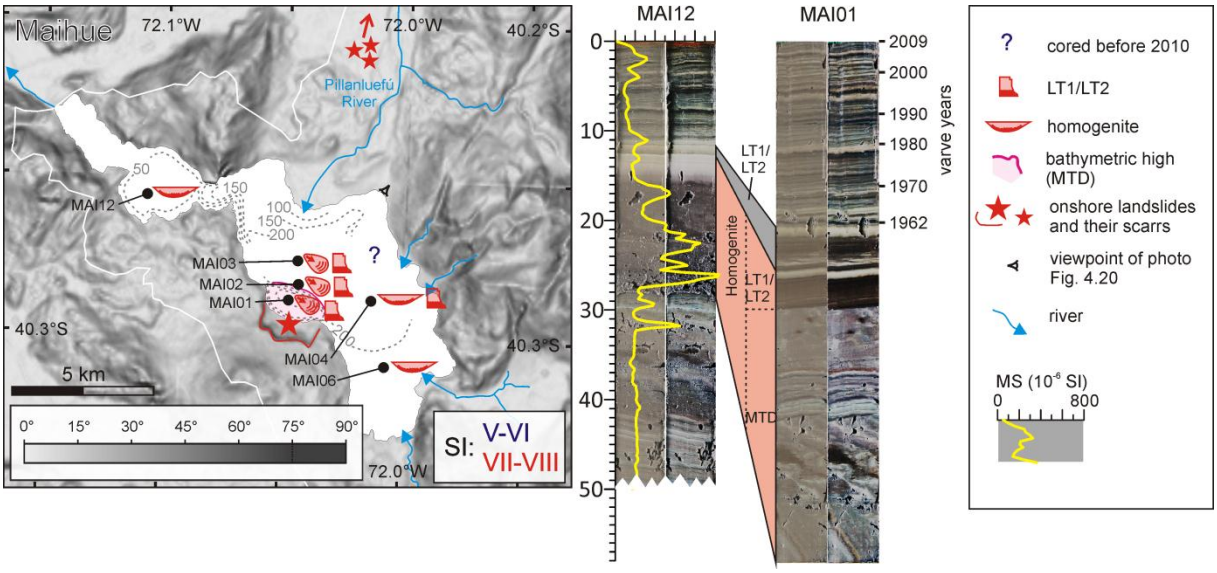

Fig. 4.21 *Slope-shaded SRTM map of the area around Lake Maihue with onshore reports, seismic intensity (SI), bathymetry (Table 4.2), coring locations and the encountered seismites. Many landslides were reported in the catchment after the 1960 earthquake (especially the Pillanleufú River), one landslide directly surged into the lake (Weishet, 1963). Cores in the bathymetric high in front of this landslide contain MTDs covered by LT2s, in the deeper basin homogenites occur. On the right: seismites in two cores on the original and processed images with MS, and varve years on MAI1. More detailed information in the caption of Fig. 4.3 and 4.4.*

Deposits. In all cored sub-basins (northern, southwester and central) LT1s are present. In most cores (PUY2-7 and 9) these LT1s are rather thin (<3 cm), but in the northern sub-basin (PUY8) the LT1 is 5.5 cm thick and in the western end of the southwestern sub-basin (PUY1) the LT1 has a thickness of 9 cm. In all cores the LT1s are covered by a finer grained lamina (0.5-1.5 cm thick) that becomes thicker towards the east and is clearly distinguishable from the LT1 in PUY7 (Fig. 4.22; Table 4.3). Based on high-resolution reflection seismic, Moernaut et al. (2007) describes 17 mass-wasting deposits that were attributed to the 1960 earthquake in the eastern and southeastern sub-basins of Lake Puyehue.

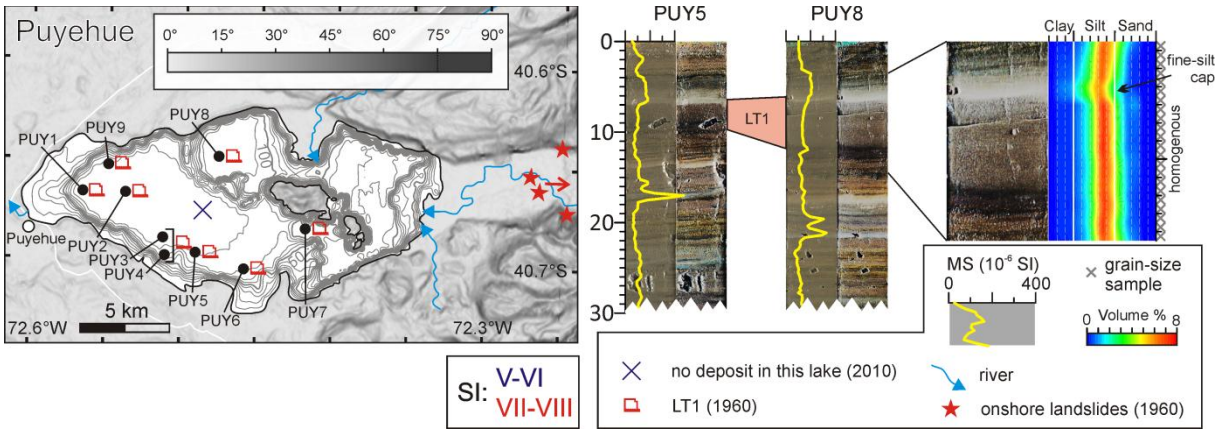

Fig. 4.22 *Slope-shaded SRTM map of the area around Lake Puyehue with onshore reports, seismic intensity (SI), bathymetry (Table 4.2), coring locations and the encountered seismites. Several landslides were reported in the catchment after the 1960 earthquake, some of which blocked the Golgol River (Tazieff, 1960; Wright and Mella, 1963). In all cores LT1s are attributed to the 1960 earthquake. On the right: LT1s in two cores on the original and processed images with MS, and grain-size distribution of LT1 in PUY8. More detailed information in the caption of Fig. 4.3 and 4.4.*

Lake Rupanco

Reports. Many landslides occurred in the catchment of Lake Rupanco. Mud flows formed where landslides converged and flowed into the lake at two places in the east. Moreover, many landslides occurred along the shores and propagated directly into the lake. The debris surging into the lake caused a large lake wave followed by more waves. Also, narrow beaches disappeared by subsidence of the unconsolidated sediments (Weishet, 1963; Wright and Mella, 1963; Fig. 4.23).

Deposits. In the eastern sub-basin (RUP02BIS and 05) a >58 cm thick homogenite is covered by two LT2s with a thickness of 4 and 4.5 cm. Also in the central sub-basin (RUP01BIS) a homogenite is present (34 cm thick), but not covered by additional turbidites. In the western (RUP03TRIS) and southern (RUP04) sub-basins, thick (7.5 and 13 cm, respectively) LT2s occur (Fig. 4.23; Table 4.3).

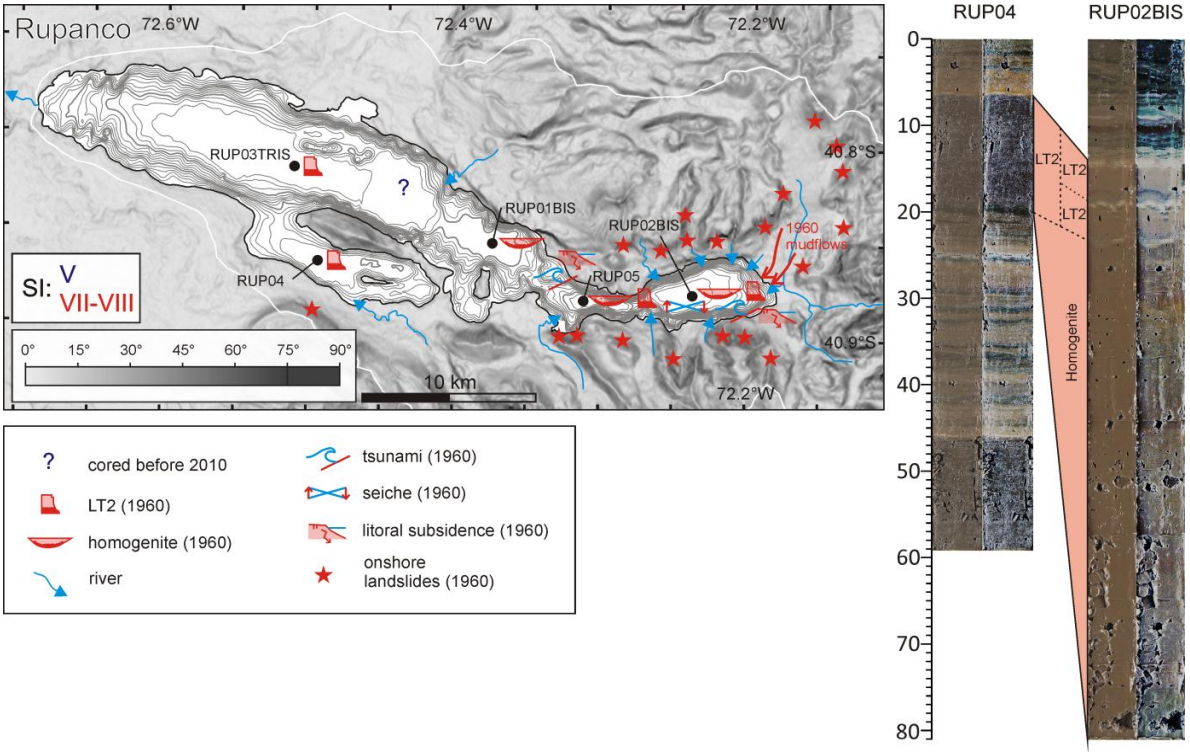

Fig. 4.23 *Slope-shaded SRTM map of the area around Lake Rupanco with onshore reports, seismic intensity (SI), bathymetry (Table 4.2), coring locations and the encountered seismites. Many landslides were reported in the catchment after the 1960 earthquake, several of which directly surging into the lake, causing a tsunami and subsequent lake seiche in the eastern sub-basins, two mud flows entered the eastern sub-basin and subsidence of several beaches was reported (Weishet, 1963; Wright and Mella, 1963). Homogenites in the eastern sub-basins are covered by one or two LT2s, and are all attributed to the 1960 earthquake. On the right: LT2s and homogenites in two cores on the original and processed images. More detailed information in the caption of Fig. 4.3 and 4.4.*

Lake Llanquihue

Reports. Minor slumping and surface fissures were reported along the shores of the lake (Wright and Mella, 1963; Fig. 4.24).

Deposits. In the central basin (LLA4) a 3 cm thick LT1 is present, which is composed of three sub-deposits. The sub-deposits are each composed of homogenous silt and a finer-grained whitish top, of which the upper one is clearly thickest. In the central-western sub-basin (LLA3), a well graded LT2 with a thickness of >22 cm is present (Fig. 4.24; Table 4.3).

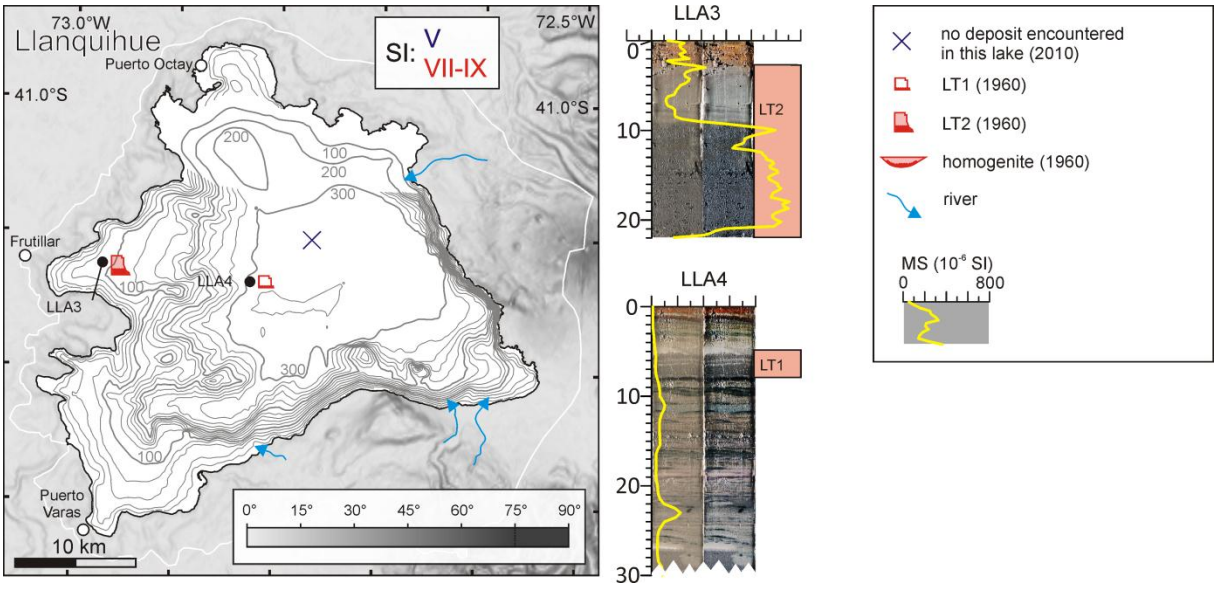

Fig. 4.24 *Slope-shaded SRTM map of the area around Lake Llanquihue with onshore reports, seismic intensity (SI), bathymetry (Table 4.2), coring locations and the encountered seismites. Minor slumping and surface fissures were reported along the shores of the lake in 1960 (Wright and Mella, 1963). A LT1 in the central basin and a LT2 in the western sub-basin are attributed to the 1960 earthquake. On the right: turbidites in both cores on the original and processed images with MS. More detailed information in the caption of Fig. 4.3 and 4.4.*

4.5 Discussion

4.5.1 Deposits versus reports

One of the main goals of this study is to compare the phenomena observed on and around the lake during and after the earthquake, with the deposits on the lake bottom. If reports and deposits show a consistent degree of correlation, these deposits can be used to better reconstruct older events.

Homogenites versus seiches

During and after the 1960 earthquake, large waves (or lake tsunamis) and subsequent seiches were reported in several of the studied lakes (i.e. Pellaifa, Panguipulli and Rupanco; Fig. 4.17, 4.18 and 4.23). In each of these lakes we find a homogenite in the basin where the waves were reported (Fig. 4.25). Also in lakes Neltume and Maihue we found homogenites, although these were markedly thinner than in the other lakes (~30 cm versus >60 cm; Fig. 4.19, 4.21). Similar to what happened in lakes Pellaifa and Rupanco, landslides surged into the main basin of lakes Neltume and Maihue during the earthquake. We infer that the lack of a reported seiche in the latter two is mainly due to the remoteness of these lakes, which resulted in incomplete reports, rather than the absence of a lake tsunami and subsequent seiche.

In Lake Panguipulli, where both a seiche was reported and a homogenite was encountered, no landslides were reported to have directly caused a tsunami and seiche. The seismic profiles show the presence of a deposit with a chaotic seismic facies that can be interpreted as an MTD reaching the western deep basin, just west of where the homogenite is thickest. We therefore deduce that this sublacustrine MTD caused the initial tsunami and the subsequent lake seiche. A tsunami originating in the western sub-basin would have had the largest wave heights and run-up along the shores of this basin where no harbours were present and therefore no reports are available. Nevertheless, the

name of this sub-basin, Bahía del Peligro (*Hazard Bay*), might have found its origin in such a tsunami flooding its shores (Fig. 4.18).

The waves that were triggered by the onshore landslides in the eastern sub-basin of Lake Calafquén can –based on the reports– not be interpreted as a lake seiche. The absence of a homogenite (in the eastern sub-basin) is therefore in agreement with the historical reports (Fig. 4.13). Also in Lake Villarrica, where during both the 1960 and 2010 earthquakes only one wave was reported, no homogenite was found (Fig. 4.12). We therefore conclude that the occurrence of a homogenite in the deepest part of a basin is representative for the occurrence of a lake seiche and can therefore be used confidently as a proxy for lake seiches in paleostudies.

LT2s versus subsidence, onshore landslides, debris flows, mud flows and floods

LT2s are turbidites that are characterized by a composition that is different (usually more terrigenous) than that of the background sediment. The source of their material can be from the lake deltas, from relatively shallow near-shore areas, but also from onshore landslides that surged directly into the lake, or that reached the lake in a more indirect way by means of debris flows, mud flows or even floods (Fig. 4.25).

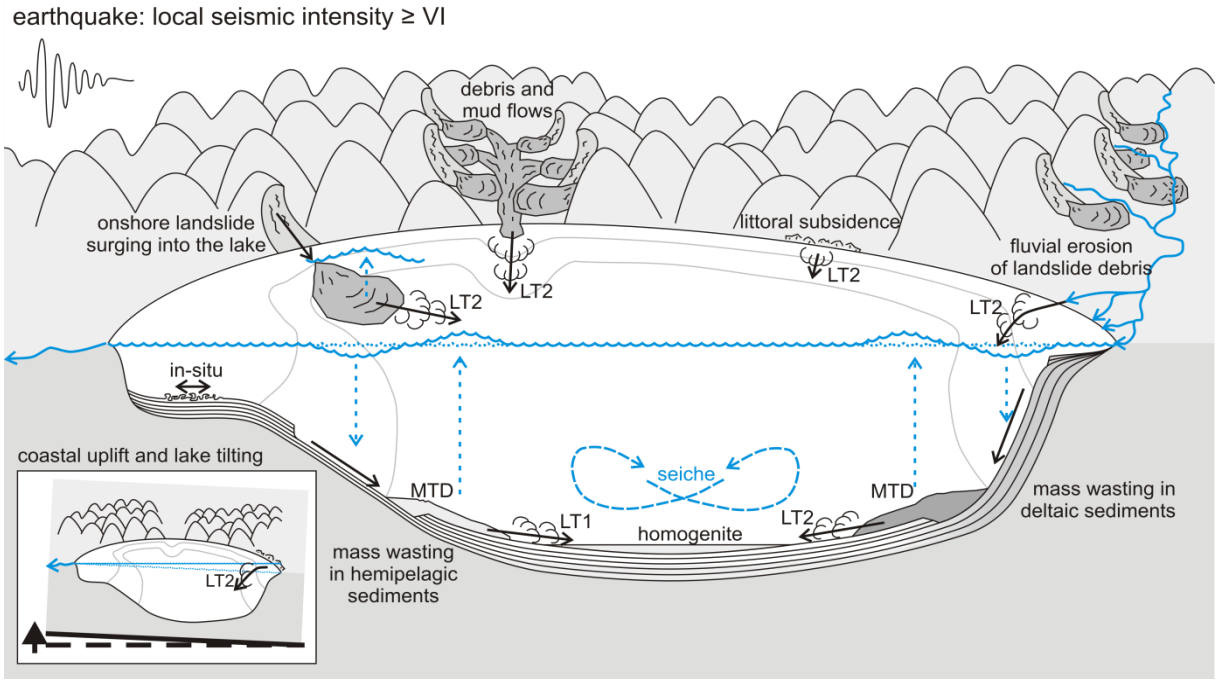

Fig. 4.25 *Cartoon summarizing the different types of seismites encountered in this study and the processes forming them. In-situ deformation occurs in flat areas. LT2s are formed by several processes such as i) delta collapse, ii) onshore landslide surging into the lake, iii) debris or mud flows flowing into the lake, iv) littoral subsidence (possibly indicating small-scale mass wasting), and v) post-seismic fluvial erosion of landslide debris in the catchment. The first two can also induce MTDs. LT1s are only formed when slopes with hemipelagic sediments fail (which can also leave MTDs). All processes that deposit MTDs potentially trigger a tsunami and/or a lake seiche. The latter is evidenced by a homogenite. Inset: coastal uplift can cause tilting of coastal lakes and therefore locally a permanent lake-level rise, resulting in erosion of littoral areas and LT2s.*

In many lakes, cracks along the shores and subsidence of beaches were observed after both the 1960 and 2010 earthquakes. In lakes Vichuquén, Lanalhue and Butaco (Fig. 4.6, 4.8 and 4.9), these cracks, subsidence or even lake-level rises along relatively steep slopes are probably an indication of local littoral sliding or slumping, or beach subsidence by liquefaction in sandy sediments. On nearby coring

locations both LT1s and LT2s were observed. In lakes Villarrica and Calafquén (Fig. 4.12 and 4.13), this littoral subsidence was –during both earthquakes– mainly observed near deltas, suggesting that the subsidence might indicate larger-scale delta collapses. In these lakes clear LT2s are present at the coring locations close to where this subsidence was observed, indicating that LT2s might indeed result from littoral sliding and slumping. Similar littoral subsidence or slumping processes in shallow lakes have usually not given rise to LT2s, but rather to LT1s. In these lakes, littoral and basinal sediments might not be dissimilar enough to produce LT2s.

In several cases, onshore landslides propagated directly into the lakes (i.e. lakes Calafquén, Pellaifa, Neltume, Maihue and Rupanco in 1960; Fig. 4.13, 4.16, 4.19, 4.20 and 4.23; and Lake Negra in 2010; Fig. 4.4). In some of these lakes the impact of the landslides created a lake tsunami and subsequent seiche, resulting in a homogenite (Fig. 4.25). In lakes where no seiche occurred or in the more proximal, shallower parts of the lakes, these onshore landslides are consequently represented by LT2s.

In lakes Pellaifa and Rupanco (Fig. 4.17 and 4.23) there are reports of respectively debris flows and mud flows composed of landslide material that reached the lakes after the earthquake. In both lakes we observe LT2s that cover poorly developed fine-silt caps (i.e. < 0.5 cm thick and thinner than the caps at the top of the overlying LT2s) at the top of homogenites. This indicates that the arrival of the LT2-forming turbidity flows is considerably delayed from the formation of the homogenite (a fine-silt cap is already being formed), but also that the LT2 was deposited not too long after the formation of the homogenite (the fine-silt cap is only poorly developed). Moreover, in Lake Pellaifa, the different geochemical composition of this LT2 (more Ti and Fe, less Ca, K and Sr) likely reflects the composition of the basalts in the Longoico Creek (the rest of the catchment is composed of (grano)diorites and tonalities; Sernageomin, 2003), where the debris flows originated. We infer that the LT2s covering the homogenites do indeed represent the debris flows and mud flows that entered the lake after the earthquake (Fig. 4.25).

In Lake Pellaifa (Fig. 4.17) this LT2 (with fine-grained cap) is covered by three more LT2s. In the same way, in lakes Neltume and Maihue (Fig. 4.19 and 4.21), homogenites or LT1/LT2s (interpreted as genetically similar to LT2s) that are covered by a well-developed fine-silt cap (i.e. > 1 cm thick and thicker than the caps at the top of any LT2s in the same lake) are overlain by one or more LT2s. These LT2s must have been deposited a considerable amount of time (more than several days) after the earthquake and are interpreted to be a result of post-earthquake flood-driven remobilization of the many landslide deposits in the large catchments of especially these two lakes (Fig. 4.25). Similar post-seismic turbidites covering a megaturbidite (or homogenite) have been described and attributed to the same origin by Howarth et al. (2012) in lakes in New Zealand.

The presence of LT2s in the lake basins corresponds very well to reports of onshore events that might have triggered turbidites. However, the variety of events that might trigger these turbidites complicates their interpretation. Nevertheless, several parameters can aid in determining the exact origin of the LT2s. The distribution of the deposit in the basin can be used to distinguish between local littoral sliding, or slumping, or a delta collapse. Also, the relation of LT2s compared to other seismites (separated by either no, a poorly or well developed fine-silt cap) can help in determining their origin. Hence, we conclude that LT2s can be used to reconstruct some of the onshore phenomena triggered by an earthquake.

4.5.2 Lake types and their seismites

Lakes with steep slopes

Lakes with steep slopes that bear no or only a thin sediment cover (e.g., lakes Negra, Lo Encañado, Vichuquén, Pellaifa, Neltume and Maihue; Fig. 4.4, 4.6, 4.17, 4.19 and 4.21) contain only event deposits that originated from deltas, from beaches and littoral areas; and onshore. The earthquake-recording capability (ERC) of these lakes will therefore be strongly dependent on the characteristics of their catchment and the vegetation in the catchment. A large catchment will potentially allow a large delta to be constructed in the lake, while steep onshore slopes with thick soils can increase the susceptibility of these slopes to fail. If these slopes border the lake, onshore landslides can directly surge into the lakes and even cause lake tsunamis. Consequently, these lakes may contain MTDs (originating from onshore landslides and deltas), LT2s, homogenites and in-situ deformation.

Lakes surrounded by steppe versus lakes surrounded by forest

In our study area, steppe vegetation occurs in the catchment of some lakes at high altitude (i.e. lakes Negra, Lo Encañado and to a lesser extent Laja; Fig. 4.4 and 4.7). Due to the topography in the catchment of these lakes, strong earthquakes can easily trigger subaerial landslides (rockslides), of which some might surge directly into the lakes, resulting in a deposit of a LT2. Such rockslides may be triggered by processes other then earthquakes (e.g., precipitation events), and LT2s can thus occur in these lakes without being a seismite. Examples of such deposits might be the sandy LT2s at 9 cm depth in NEG2, and 4 and 6 cm depth in NEG3, which all occur on different stratigraphic levels.

In lakes at lower altitudes, where the forested catchments have thick soil covers, such subaerial landslides can bring a lot of detrital material into the lake, making such lakes more prone to the formation of homogenites in case a lake seiche would occur. In more arid or higher regions, the subaerial landslides more commonly consist of rock slides or avalanches, with coarser grain sizes, making homogenite formation in the lakes less likely.

Also the sedimentary imprint of landslides in the catchment (not directly propagating into the lake) depends on the vegetation in the catchment. Landslides that occur in the forested catchment of lakes in the lower Andes such as Pellaifa, Neltume and Maihue (Fig. 4.17, 4.19 and 4.21), will provide large amounts of extra detrital material that can subsequently be eroded. Under normal conditions this material is stabilized and buffered in soils and held together by roots of trees and other plants. In contrast, in regions with little vegetation (such as Lake Negra), the erodibility of the slopes is less affected by landsliding. Therefore, subsequent flooding of these landslide deposits will not result in a clear LT2 in these lakes. To conclude, homogenites and postseismic LT2s (due to flooding of landslide deposits) are less likely to be found in lakes with little vegetation in their catchment. Also, landslides (rockslides) might occur more spontaneously (i.e. without earthquake trigger) in these environments, pointing out that one should be more careful when interpreting their deposits.

Multibasin lakes with gentle slopes acting as natural seismographs

Lakes that consist of several sub-basins (e.g., Laja, Villarrica, Calafquén, Panguipulli, Riñihue, Ranco, Puyehue, Rupanco and Llanquihue; Fig. 4.7, 4.12, 4.13, 4.14, 4.15, 4.18, 4.22, 4.23 and 4.24) will usually also have different types of slopes, of which some can bear hemipelagic sediments. Therefore, these lakes will not only potentially contain all the seismites of the previously discussed

lakes, but also LT1s (Fig. 4.25). The source areas of LT1s (slopes with hemipelagic sediments) are less diverse then the ones of LT2s or homogenites and as a result, the LT1s are more straightforward to interpret. Also, since LT1s are composed of remobilized lacustrine sediments, most trigger mechanisms other than earthquakes can be ruled out. Furthermore, different slopes appear to have a different sensitivity. For example, in lakes Villarrica, Calafquén and Ranco (Fig. 4.12, 4.13 and 4.15), almost all cores in the western basins contain LT1s triggered by the 1960 earthquake, while only some contain a thinner LT1 related to the 2010 earthquake. In these same lakes, but also in Lake Riñihue (Fig. 4.14), LT2s appear to be more sensitive recorders of earthquakes and therefore add an extra intensity threshold to the potential record. The presence of different sub-basins and slope sediments is therefore considered very useful for paleoseismological purposes, since every sub-basin and even type of deposit might have a different ERC. The use of such lakes for paleoseismological purposes is discussed in more detail by Moernaut et al. (submitted). Finally, following the reasoning used in several studies of Swiss lakes (Monecke et al., 2004; Schnellmann et al., 2006; Strasser et al., accepted), we support the strategy of using different sub-basins and/or lakes to prove synchronous triggering an hence, an earthquake origin.

Impact of coastal tilting on coastal lakes

Two phenomena linked to megathrust earthquakes will affect only coastal lakes: i) marine tsunamis (which are not the subject of this study), and ii) co-seismic coastal uplift or subsidence. The three studied coastal lakes (i.e. lakes Vichuquén, Lanalhue and Butaco; Fig. 4.6, 4.8 and 4.9) are located on the VCRZ and the latter two also on the VRZ. At Lake Vichuquén, Quezada et al. (2010) reported ~35 cm of subsidence at the lake outlet after the 2010 earthquake, locally causing a lake-level rise. In 1960 there was also subsidence in the area of lakes Lanalhue and Butaco (Cisternas et al., 2005), but coastal uplift was observed west of these lakes after the 2010 earthquake (Quezada et al., 2010). These two lakes are located on the border between the VRZ and the VCRZ, and on top of the active Lanalhue Fault (Moreno et al., 2008). Therefore, these lakes frequently suffer from small earthquakes close to the lake, locally reaching high seismic intensities. In both lakes we find a deposit related to the 2010 earthquake, but not to the 1960 earthquake, although the latter caused higher seismic intensities in that area (VII-VIII in 1960 versus VII in 2010). We infer that in this area –where earthquake shaking is common– the deposits are not originating from mass wasting of slope sediments, but from the lake-level rise caused by coastal uplift and consequent tilting of the lake. This lake-level rise causes erosion of inundated and sometimes slightly subsided shorelines, which, in turn, results in a lacustrine turbidite (Fig. 4.25). When carefully studied, these lakes could thus provide information on coastal uplift or subsidence of prehistoric earthquakes.

Shallow lakes (< 30 m) and very shallow lakes (< 10 m)

In contrast to all afore-discussed lakes, shallow lakes have usually no or few sediment-bearing slopes or large deltas. Therefore, the most common source areas for turbidites are not present in these lakes. The clearest example is the very shallow Lake Aculeo (Fig. 4.5), a eutrophic lake with a maximum depth of 6 m and no slopes nor large inflows. Changes in grain-size mode have previously been linked to earthquakes (von Gunten et al., 2009b), but as well to floods (Jenny et al., 2002). Based on our data we prefer the latter explanation. A study on Lake Shkodra (8 m deep) by van Welden et al. (2008) also shows that very shallow lakes are less well suited for recording earthquakes with seismites. Contrarily, Avsar et al. (submitted b) claim that very shallow lakes can be used as

earthquake recorders as well. They studied a Turkish lake (Lake Göllüköy, 7 m deep) in which paleoearthquakes are recorded as organic-rich intercalations with material from the littoral zone of the lake. This material is reworked by the water oscillations (seiche) due to the seismic shaking. Since such shaking was reported in Lake Aculeo, a similar deposit could potentially occur in this lake, however, the sediments should therefore be studied applying the methodology proposed by Avsar et al. (submitted b) (i.e. µXRF, organic geochemistry, principle component analysis).

Lakes that are slightly deeper might contain slopes and therefore also mass-wasting related deposits. In Lake Vichuquén turbidites are encountered in two of the three coring locations (Fig. 4.6). These cores are located in the central part of the elongated basin, but still close to the lake shore, which implies that small local near-shore mass wasting might reach them (Fig. 4.25). Alternatively, turbidity currents could have originated from local slopes in the southern bays and reach the site of VIC7, although a turbidite would then also be expected in the main northern basin. Lake Pullinque (Fig. 4.13) is a landslide-dammed lake (Laugenie, 1982) with a very irregular bathymetry, especially in the western part. Hence, it has several short slopes and at the base of one of these slopes a turbidite was encountered. The above examples illustrate that shallow lakes can directly record earthquakes. However, the occurrence of a turbidite on a certain location depends strongly on local factors which may change with time. Therefore, the distribution of earthquake-triggered turbidites is not expected to be consistent through time.

The relatively shallow lake Lo Encañado (Fig. 4.4) has a large catchment area (Table 4.2), resulting in clastic sediments and a large delta in the northern part of the lake. Cores in this lake contain a very clear LT2 originating from the delta, which is expected to react very sensitively to earthquake shaking.

We conclude that in small, shallow lakes, the occurrence of seismites very much depends on local factors and that the presence of some sort of slope is required to ensure proper recording of earthquakes. However, studies on a shallow Turkish lake by Avsar et al. (submitted a) show that although these very shallow lakes might not always contain co-seismic deposits, they can contain a clear post-seismic signature, which should not be underestimated and can potentially disturb paleoclimate records, especially when there is no seismite to link the sudden change with.

4.5.3 Implications for lacustrine paleoseismological research

Sensitivity of deltas

Deltas are more sensitive to slope failure than slopes covered with hemipelagic sediment (Strasser et al., accepted). Girardclos et al. (2007) concluded that the Lake Brienz delta collapse in 1996 occurred under normal sediment-loading conditions and without other external triggers. We believe that as long as earthquakes occur frequently enough (i.e. with a shorter recurrence interval than the time needed to build an intrinsically unstable slope sequence by continuous loading), deltas will collapse due to seismic shaking before they will collapse by continuous loading. Therefore LT2s from delta collapses can be used for paleoseismological purposes in seismically active regions, such as Chile. In seismically less active regions their use as an earthquake proxy becomes less straightforward.

LT1 versus LT2

The difference between a turbidite resulting from remobilization of slope sediments (LT1) and one resulting from a delta collapse (LT2) is easily recognized by comparing the composition of the turbidite to the background sediment. Distinguishing between both types of deposit is important when interpreting the origin of the turbidite and using it as an earthquake proxy. Due to the different, more terrestrial composition of LT2s, it is harder to exclude a flood origin for these deposits, especially when they occur in a basin with a large river delta. Our study shows, however,

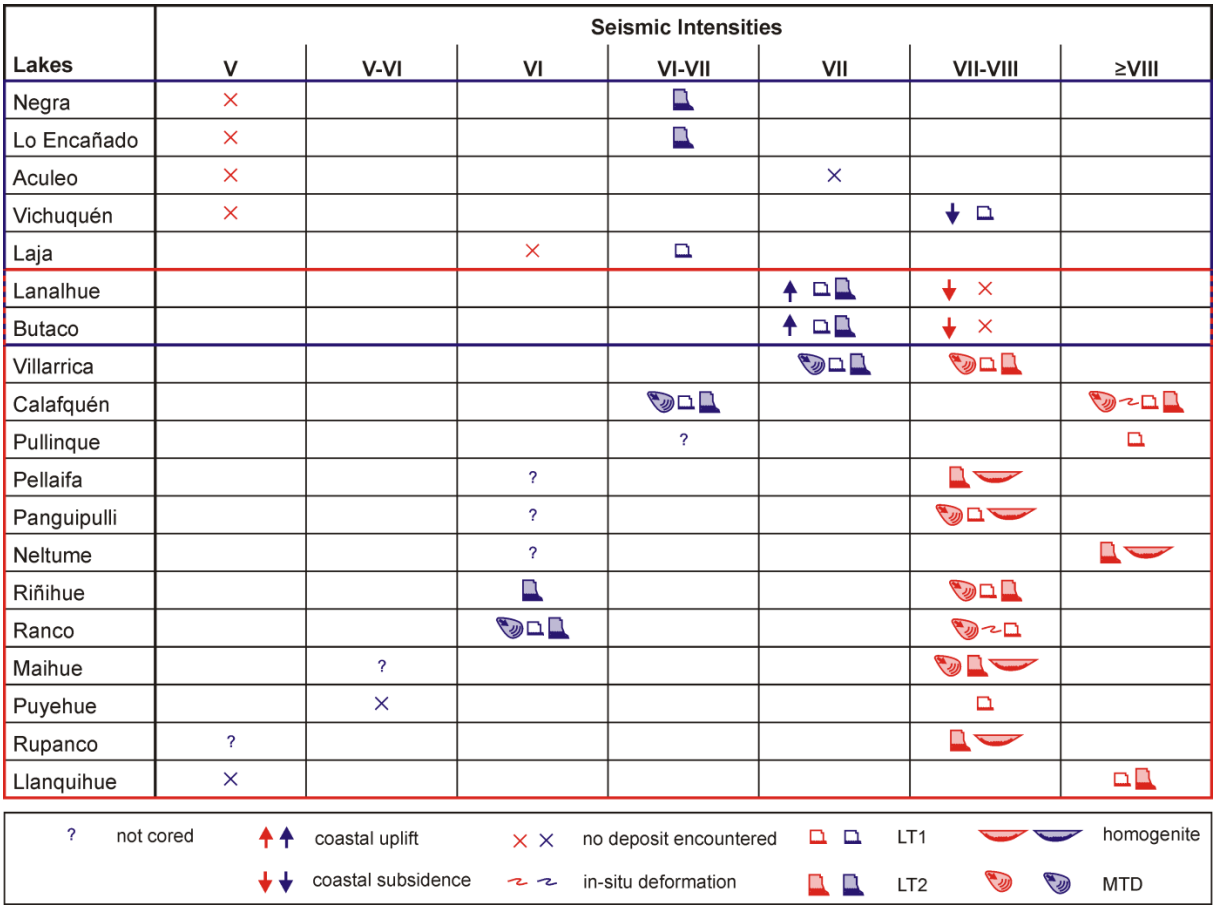

Fig. 4.26 *Overview of the types of seismites attributed to the 1960 (red) or 2010 (blue) earthquake, in every lake and according to the corresponding seismic intensity (MSK for 1960, MMI for 2010). Red box corresponds to the VRZ, blue box to the CVRZ.*

that this does not mean that LT2 turbidites cannot be used for paleoseismological purposes, but only that more care should be taken when interpreting them. The occurrence of an amalgamated LT2 (i.e. a turbidite containing the separate arrival of more than one flow; Chapter 6), such as in the western sub-basin of Lake Negra (Fig. 4.4), indicates synchronous triggering of landslides on different locations and can therefore be used as a paleoseismological indicator. Similarly, successions of a LT1 and LT2 (VI18; Fig. 4.12) or vice versa (RI5; Fig. 4.14) indicate synchronous failing of different types of slopes with different sediments, and hence, a seismic trigger.

Earthquake recording capability (ERC) of basins and their seismites

The ERC of a lake that can record seismic shaking, depends on the type of slope sediments that are available in the lake and on the geomorphology and vegetation of the catchment. In lakes with several sub-basins, each sub-basin can have a different ERC, e.g., lakes Villarrica, Calafquén and Riñihue (Moernaut et al., submitted), but also Laja, Ranco, Rupanco and Puyehue. Such lakes are very useful for paleoseismological studies since every sub-basin can record a certain earthquake separately, and sediments in the separate sub-basins can be easily correlated. Therefore, the simultaneous triggering, a necessary requirement to infer an earthquake origin, can be easily

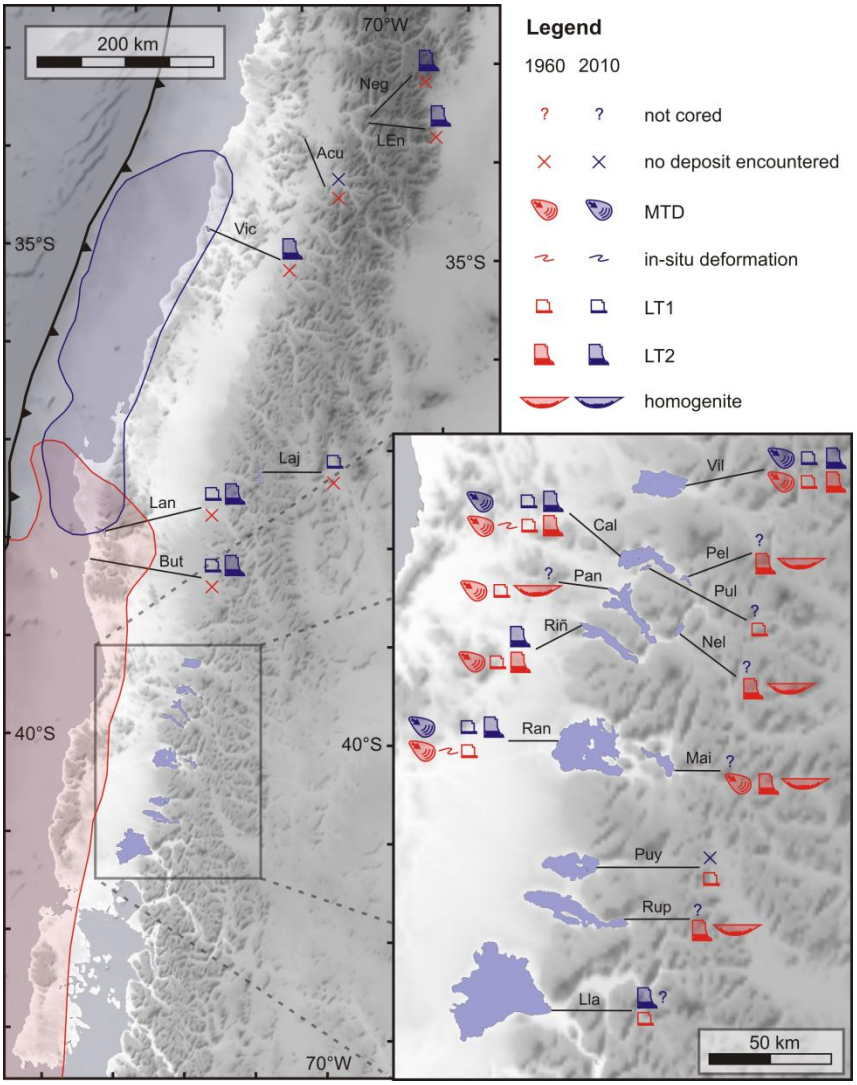

Fig. 4.27 *Overview of the study area in South-Central Chile and location of all studied lakes with types of seismites attributed to the 1960 (red) or 2010 (blue) earthquake. Coseismic slip area (>5 m) for the 1960 and 2010 events (Moreno et al., 2009; 2012).*

demonstrated. When there are no separate earthquake-recording sub-basins, different lakes close to each other are necessary. Also, the possible different ERC of the sub-basins and lakes can be used to better estimate paleo-seismic intensities in the study area.

A universally applicable intensity threshold for any of the aforementioned seismites to occur does not exist. However, our study reveals a seismic-intensity threshold of VI for most seismites. This is in agreement with the results of Monecke et al. (2004), who reported a seismic-intensity threshold of VI-VII in some Swiss lakes.

Consistency of lake records

Almost all sub-basins of lakes that are located along the rupture zone (CVRZ or VRZ), where intensities are always >VI (CVRZ; 2010) and usually >VII (VRZ; 1960), did record the earthquakes (Fig. 4.26 and 4.27). Some lake sub-basins further to the south or north also recorded the earthquakes, but only on sensitive locations. In other words, for each sub-basin there are sites at which only the earthquakes on that rupture zone are recorded. The only exceptions to this rule are i) Lake Aculeo, which does not record any earthquake because it is too shallow, and ii) lakes Lanalhue and Butaco, which only seem to register lake-level rises by tilting of the lake due to coastal uplift. The large majority of the studied lake sub-basins thus recorded the earthquakes in a consistent way. We can therefore conclude that lakes are good recorders of past earthquakes and that the studied lakes potentially provide a consistent record of ancient earthquakes with seismic-intensity values similar to or larger than the 1960 and 2010 earthquakes.

4.6 Conclusions

In 19 Chilean lakes, we encountered 5 distinct types of event deposits that could be attributed to the 1960 and 2010 earthquakes (i.e. seismites): i) mass-transport deposits (MTDs); ii) in-situ deformation; iii) lacustrine turbidites with a similar composition as the background sediments (LT1s); iv) lacustrine turbidites with a different composition as the background sediments (more terrestrial; LT2s); and v) homogenites.

The encountered deposits correspond very well to reports of local inhabitants and observations around the lake after the earthquake. Homogenites consistently represent lake seiches; and LT2s can be a result of local near-shore mass wasting, a delta collapse or onshore landslides surging into the lake (direct imprint); but also debris or mud flows entering the lake, or flooding of landslide deposits in the catchment (indirect imprint). However, distribution in the lake, composition and relation to other event deposits can clarify the origin of the deposits.

Distinguishing between LT1s and LT2s is very important, since LT2s can have several origins, while LT1s can only be formed by mass-wasting within the lake. Synchronous LT1s in different lakes and/or sub-basins are therefore a very good indicator for earthquake triggering. Moreover, LT1s appear to be the seismites that record seismic intensities in the best way. The thickness and distribution of LT1s in a certain lake sub-basin strongly depends on the local seismic intensity, while for the other seismites there only appears to be a minimum intensity threshold for each lake or sub-basin.

Special cases are coastal lakes on the border between VRZ and CVRZ (i.e. lakes Lanalhue and Butaco), where seismic shaking is frequent. These lakes record lake-level rise due to the coastal uplift rather than the seismic shaking.

Finally, apart from the very shallow (6 m) Lake Aculeo, all lake sub-basins consistently recorded one or both megathrust earthquakes.

Acknowledgements

This research was funded mainly by the Research Foundation Flanders (FWO-Vlaanderen) and by the Special Research Fund of Ghent University (BOF). We thank the GSA Limnogeology Division for the

Kerry Kelts award and IAS for the postgraduate student grant, both used in the last field season. M. Vincx is acknowledged for the use of the Malvern Mastersizer 2000. We thank Ph. De Smedt for sharing the Bartington MSE2 point sensor. We thank S. Roberts and D. Verschuren for putting their gravity corer to our disposition. We are grateful to A. Peña for the invaluable assistance on the field. We thank I. Meyer for proofreading an earlier version of this manuscript. J. Moernaut acknowledges the support of the Research Foundation Flanders (FWO-Vlaanderen) and the Swiss National Science Foundation (grant 133481). M. Van Daele is currently funded by FWO-Vlaanderen.

References

Angermann, D., Klotz, J. and Reigber, C. (1999) Space-geodetic estimation of the nazca-south america euler vector. *Earth and Planetary Science Letters*, **171,** 329-334.

Avsar, U., Hubert-Ferrari, A., De Batist, M. and Fagel, N. (submitted a) A 3400-year lacustrine paleoseismic record from the North Anatolian Fault, Turkey: 2 Insights into non-characteristic deformation and recurrence behavior. *Geophysical Research Letters*.

Avsar, U., Hubert-Ferrari, A., De Batist, M. and Fagel, N. (submitted b) Robust lacustrine paleoseismic chronology achieved by tuning Anatolian sedimentary archives, the North Anatolian Fault (Turkey). *Quaternary Science Reviews*.

Beck, C. (2009) Late Quaternary lacustrine paleo-seismic archives in north-western Alps: Examples of earthquake-origin assessment of sedimentary disturbances. *Earth-Science Reviews*, **96,** 327-344.

Bertrand, S., Charlet, F., Chapron, E., Fagel, N. and De Batist, M. (2008) Reconstruction of the Holocene seismotectonic activity of the Southern Andes from seismites recorded in Lago Icalma, Chile, 39°S. *Palaeogeography, Palaeoclimatology, Palaeoecology*, **259,** 301-322.

Boës, X. and Fagel, N. (2008) Relationship between southern Chilean varved lake sediments, precipitation and ENSO for the last 600 years. *Journal of Paleolimnology*, **39,** 237-252.

Bouma, A.H. (1962) *Sedimentology of Some Flysch Deposits: a Graphic Approach to Facies Interpretation*. Elsevier, Amsterdam, 168 pp.

Campos, H., Arenas, J., Steffen, W., Agüero, G. (1981) Morphometrical, physical and chemical limnology of Lake Panguipulli (Valdivia, Chile). *Neues Jahrbuch fur Geologie und Palaeontologie – Abhandlungen,* **10,** 603-625.

Campos, H., Steffen, W., Agüero, G., Parra, O., Zuñiga, L. (1987) Limnology of Lake Riñihue. *Limnologica,* **18,** 339-357.

Cembrano, J., Schermer, E., Lavenu, A. and Sanhueza, A. (2000) Contrasting nature of deformation along an intra-arc shear zone, the Liquine-Ofqui fault zone, southern Chilean Andes. *Tectonophysics*, **319,** 129-149.

Chapron, E., Beck, C., Pourchet, M. and Deconinck, J.F. (1999) 1822 earthquake-triggered homogenite in Lake Le Bourget (NW Alps). *Terra Nova*, **11,** 86-92.

Chapron, E., Ariztegui, D., Mulsow, S., Villarosa, G., Pino, M., Outes, V., Juvignié, E. and Crivelli, E.

(2006) Impact of the 1960 major subduction earthquake in Northern Patagonia (Chile, Argentina). *Quaternary International*, **158,** 58-71.

Cifuentes, I.L. (1989) The 1960 Chilean Earthquakes. *Journal of Geophysical Research-Solid Earth and Planets*, **94,** 665-680.

Cisternas, M., Atwater, B.F., Torrejon, F., Sawai, Y., Machuca, G., Lagos, M., Eipert, A., Youlton, C., Salgado, I., Kamataki, T., Shishikura, M., Rajendran, C.P., Malik, J.K., Rizal, Y. and Husni, M. (2005) Predecessors of the giant 1960 Chile earthquake. *Nature*, **437**, 404-407.

Davis, S.N. and Karzulovíc, J. (1963) Landslides at lake Riñihue, Chile. *Bulletin of the Seismological Society of America*, **53,** 1403-1414.

DeMets, C., Gordon, R.G., Argus, D.F. and Stein, S. (1994) Effect of recent revisions to the geomagnetic reversal time scale on estimates of current plate motions. *Geophysical Research Letters*, **21,** 2191-2194.

Fritz, H.M., Petroff, C.M., Catalán, P.A., Cienfuegos, R., Winckler, P., Kalligeris, N., Weiss, R., Barrientos, S.E., Meneses, G., Valderas-Bermejo, C., Ebeling, C., Papadopoulos, A., Contreras, M., Almar, R., Dominguez, J. and Synolakis, C.E. (2011) Field Survey of the 27 February 2010 Chile Tsunami. *Pure and Applied Geophysics*, **168,** 1989-2010.

Girardclos, S., Schmidt, O.T., Sturm, M., Ariztegui, D., Pugin, A. and Anselmetti, F.S. (2007) The 1996 AD delta collapse and large turbidite in Lake Brienz. *Marine Geology*, **241,** 137-154.

Goldfinger, C., Nelson, C.H., Morey, A.E., Johnson, J.R., Patton, J., Karabanov, E., Gutierrez-Pastor, J., Eriksson, A.T., Gracia, E., Dunhill, G., Enkin, R.J., Dallimore, A. and Vallier, T. (2012) Turbidite event history—Methods and implications for Holocene paleoseismicity of the Cascadia subduction zone. *U.S. Geological Survey Professional Paper,* **1661–F,** 170 pp, available at http://pubs.usgs.gov/pp/pp1661/f

Howarth, J.D., Fitzsimons, S.J., Norris, R.J. and Jacobsen, G.E. (2012) Lake sediments record cycles of sediment flux driven by large earthquakes on the Alpine fault, New Zealand. *Geology*.

Jenny, B., Valero-Garcés, B.L., Urrutia, R., Kelts, K., Veit, H., Appleby, P.G. and Geyh, M. (2002) Moisture changes and fluctuations of the Westerlies in Mediterranean Central Chile during the last 2000 years: The Laguna Aculeo record (33Â°50â€²S). *Quaternary International*, **87,** 3-18.

Laugenie, C. (1982) *La région des lacs, Chili méridional*, Université de Bordeaux III, Bordeaux, France, 822 pp.

Lazo, R.G. (2008) *Estudio de los daños de los terremotos del 21 y 22 de mayo de 1960*, Universidad de Chile, Santiago, 427 pp.

Lowe, D.R. (1982) Sediment gravity flows: II. Depositional models with special reference to the deposits of high-density turbidity currents. *Journal of Sedimentary Petrology*, **52,** 279-298.

Medvedev, S., Sponheuer, W. and Karník, V. (1964) Neue seismische Skala Intensity scale of earthquakes, 7. Tagung der Europäischen Seismologischen Kommission vom 24.9. *bis 30.9.1962.* In: *Jena, Veröff. Institut für Bodendynamik und Erdbebenforschung in Jena, vol 77*, pp. 69-76. Deutsche

Akademie der Wissenschaften zu Berlin.

Melnick, D., Charlet, F., Echtler, H.P. and De Batist, M. (2006) Incipient axial collapse of the Main Cordillera and strain partitioning gradient between the central and Patagonian Andes, Lago Laja, Chile. *Tectonics*, **25,** 1-22.

Melnick, D., Bookhagen, B., Strecker, M.R. and Echtler, H.P. (2009) Segmentation of megathrust rupture zones from fore-arc deformation patterns over hundreds to millions of years, Arauco peninsula, Chile. *Journal of Geophysical Research-Solid Earth*, **114**.

Moernaut, J., De Batist, M., Charlet, F., Heirman, K., Chapron, E., Pino, M., Brummer, R. and Urrutia, R. (2007) Giant earthquakes in South-Central Chile revealed by Holocene mass-wasting events in Lake Puyehue. *Sedimentary Geology*, **195,** 239-256.

Moernaut, J., De Batist, M., Heirman, K., Van Daele, M., Pino, M., Brümmer, R. and Urrutia, R. (2009) Fluidization of burried mass-wasting deposits in lake sediments and its relevance for paleoseismology: Results from a reflection seismic study of lakes Villarrica and Calafquén (South-Central Chile). *Sedimentary Geology*, **213**, 121-135.

Moernaut, J., Van Daele, M., Heirman, K., Vandoorne, W., Strasser, M., Pino, M., Urrutia? R., Brümmer, R. and De Batist, M. (in prep) Lacustrine turbidites in Chile as a tool for quantitative earthquake reconstruction. *Earth and Planetary Science Letters,* in prep.

Monecke, K., Anselmetti, F.S., Becker, A., Sturm, M. and Giardini, D. (2004) The record of historic earthquakes in lake sediments of Central Switzerland. *Tectonophysics*, **394,** 21-40.

Moreno, M.S., Klotz, J., Melnick, D., Echtler, H. and Bataille, K. (2008) Active faulting and heterogeneous deformation across a megathrust segment boundary from GPS data, south central Chile (36-39 degrees S). *Geochemistry Geophysics Geosystems*, **9,** 14.

Moreno, M.S., Bolte, J., Klotz, J. and Melnick, D. (2009) Impact of megathrust geometry on inversion of coseismic slip from geodetic data: Application to the 1960 Chile earthquake. *Geophysical Research Letters*, **36,** 5.

Moreno, M., Melnick, D., Rosenau, M., Baez, J., Klotz, J., Oncken, O., Tassara, A., Chen, J., Bataille, K., Bevis, M., Socquet, A., Bolte, J., Vigny, C., Brooks, B., Ryder, I., Grund, V., Smalley, B., Carrizo, D., Bartsch, M. and Hase, H. (2012) Toward understanding tectonic control on the Mw 8.8 2010 Maule Chile earthquake. *Earth and Planetary Science Letters*, **321-322,** 152-165.

Mulder, T. and Alexander, J. (2001) The physical character of subaqueous sedimentary density flows and their deposits. *Sedimentology*, **48,** 269-299.

Mulder, T., Zaragosi, S., Razin, P., Grelaud, C., Lanfumey, V. and Bavoil, F. (2009) A new conceptual model for the deposition process of homogenite: Application to a cretaceous megaturbidite of the western Pyrenees (Basque region, SW France). *Sedimentary Geology*, 222, 263-273.

Musson, R.M.W., Gruenthal, G. and Stucchi, M. (2010) The comparison of macroseismic intensity scales. *Journal of Seismology*, **14,** 413-428.

Quiroz, R., Popp, P., Urrutia, R., Bauer, C., Araneda, A., Treutler, H.-C. and Barra, R. (2005) PAH

fluxes in the Laja Lake of south central Chile Andes over the last 50 years: Evidence from a dated sediment core. *Science of the Total Environment*, **349,** 150-160.

Quezada, J., Jaque, E., Belmonte, A., Fernández, A., Vásquez, D. and Martínez, C. (2010) Movimientos cosísmicos verticales y cambios geomorfológicos generados durante el terremoto Mw= 8,8 del 27 de febrero de 2010 en el centro-sur de Chile. *Revista Geográfica del Sur*, **1,** 11-45.

Salvetti, C. (2006) *Palaeolimnological Analysis of Lakes in the South Central Andes in Chile: A Case Study of Laguna del Encañado (33°S/70°W*), Diplomarbeit der Philosophisch-naturwissenschaftlichen Fakultät, University of Bern, Bern, 137 pp.

Schnellmann, M., Anselmetti, F.S., Giardini, D., McKenzie, J.A. and Ward, S.N. (2002) Prehistoric earthquake history revealed by lacustrine slump deposits. *Geology*, **30,** 1131-1134.

Schnellmann, M., Anselmetti, F.S., Giardini, D. and McKenzie, J.A. (2006) 15,000 Years of mass-movement history in Lake Lucerne: Implications for seismic and tsunami hazards. *Eclogae Geologicae Helvetiae*, **99,** 409-428.

Schwab, M.J., Werner, P., Dulski, P., McGee, E., Nowaczyk, N.R., Bertrand, S. and Leroy, S.A.G. (2009) Palaeolimnology of Lake Sapanca and identification of historic earthquake signals, Northern Anatolian Fault Zone (Turkey). *Quaternary Science Reviews*, **28**, 991-1005.

Sernageomin (Servicio Nacional de Geología y Minería) (2003) *Mapa Geologico de Chile: Versión Digital.* Scale 1:1,000,000, 25 pp.

Shiki, T., Kumon, F., Inouchi, Y., Kontani, Y., Sakamoto, T., Tateishi, M., Matsubara, H. and Fukuyama, K. (2000) Sedimentary features of the seismo-turbidites, Lake Biwa, Japan. *Sedimentary Geology*, **135,** 37-50.

SHOA (Servicio Hidrográfico y Oceanográfico de la Armada de Chile) (1987) *Lago Villarrica (n° 6230).* Scale 1: 40000, 1pp.

SHOA (Servicio Hidrográfico y Oceanográfico de la Armada de Chile) (1992) *Lago Llanquihue (n° 7160)*. Scale 1:75000, 1pp.

SHOA (Servicio Hidrográfico y Oceanográfico de la Armada de Chile) (2000) *Lago Puyehue (n° 7140).* Scale 1:40000, 1pp.

SHOA (Servicio Hidrográfico y Oceanográfico de la Armada de Chile) (2001) *Lago Rupanco (n° 7150).* Scale 1:50000, 1pp.

SHOA (Servicio Hidrográfico y Oceanográfico de la Armada de Chile) (2002) *Lago Vichuquén (n° 5215).* Scale 1:15000, 1pp.

SHOA (Servicio Hidrográfico y Oceanográfico de la Armada de Chile) (2003) *Lago Ranco (n° 7120).* Scale 1:50000, 1pp.

SHOA (Servicio Hidrográfico y Oceanográfico de la Armada de Chile) (2008) *Lago Calafquén (n° 6232).* Scale 1:30000, 1pp.

Sievers, H. (2000) *El maremoto del 22 de mayo de 1960 en las costas de Chile*. Servicio Hidrográfico y Oceanográfico de la Armada de Chile, Valparaíso, 2ª Edición, 72 pp.

Stefer, S., Moernaut, J., Melnick, D., Echtler, H.P., Arz, H.W., Lamy, F., De Batist, M., Oncken, O. and Haug, G.H. (2010) Forearc uplift rates deduced from sediment cores of two coastal lakes in south-central Chile. *Tectonophysics*, **495,** 129-143.

Strasser, M., Anselmetti, F.S., Fah, D., Giardini, D. and Schnellmann, M. (2006) Magnitudes and source areas of large prehistoric northern Alpine earthquakes revealed by slope failures in lakes. *Geology*, **34,** 1005-1008.

Strasser, M., Monecke, K., Schnellmann, M. and Anselmetti, F.S. (Accepted manuscript) Lake sediments as natural seismographs: A compiled record of Late Quaternary earthquakes in Central Switzerland and its implication for Alpine deformation. *Sedimentology*.

Tazieff, H. (1960) Interprétation des glissements de terrain accompagnant le grand séisme du Chili. *Bulletin de la Société belge de Géologie*, **119,** 374-384.

USGS (Unites States Geological Survey) (2012a) Magnitude The largest earthquake in the world. *Earthquake Hazards Program – Significant earthquake archive,* http://earthquake.usgs.gov/earthquakes/world/events/1960_05_22.php, last consulted in November 2012.

USGS (Unites States Geological Survey) (2012b) Magnitude 8.8 - OFFSHORE BIO-BIO, CHILE – maps. *Earthquake Hazards Program – Significant earthquake archive,* http://earthquake.usgs.gov/earthquakes/eqinthenews/2010/us2010tfan/#maps, last consulted in November 2012.

van Welden, A., Beck, C., Reyss, J.-L., Bushati, S., Koci, R., Jouanne, F. and Mugnier, J.-L. (2008) The last 500 year of sedimentation in Shkodra Lake (Albania/Montenegro): paleoenvironmental evolution and potential for paleoseismicity studies. *Journal of Paleolimnology*, **40,** 619-633.

Vigny, C., Socquet, A., Peyrat, S., Ruegg, J.C., Métois, M., Madariaga, R., Morvan, S., Lancieri, M., Lacassin, R., Campos, J., Carrizo, D., Bejar-Pizarro, M., Barrientos, S., Armijo, R., Aranda, C., Valderas-Bermejo, M.C., Ortega, I., Bondoux, F., Baize, S., Lyon-Caen, H., Pavez, A., Vilotte, J.P., Bevis, M., Brooks, B., Smalley, R., Parra, H., Baez, J.C., Blanco, M., Cimbaro, S. and Kendrick, E. (2011) The 2010 Mw 8.8 Maule Megathrust Earthquake of Central Chile, Monitored by GPS. *Science*, **332**, 1417-1421.

von Gunten, L., Grosjean, M., Beer, J., Grob, P., Morales, A. and Urrutia, R. (2009a) Age modeling of young non-varved lake sediments: methods and limits. Examples from two lakes in Central Chile. *Journal of Paleolimnology*, **42,** 401-412.

von Gunten, L., Grosjean, M., Rein, B., Urrutia, R. and Appleby, P. (2009b) A quantitative high-resolution summer temperature reconstruction based on sedimentary pigments from Laguna Aculeo, central Chile, back to AD850. *The Holocene*, **19,** 873-881.

Waldmann, N., Anselmetti, F.S., Ariztegui, D., Austin, J.A., Jr., Pirouz, M., Moy, C.M. and Dunbar, R. (2011) Holocene mass-wasting events in Lago Fagnano, Tierra del Fuego (54 degrees S): implications

for paleoseismicity of the Magallanes-Fagnano transform fault. *Basin Research*, **23,** 171-190.

Wang, K., Hu, Y., Bevis, M., Kendrick, E., Smalley, R. and Lauria, E. (2007) Crustal motion in the zone of the 1960 Chile earthquake: Detangling earthquake-cycle deformation and forearc-sliver translation. *Geochemistry Geophysics Geosystems*, **8,** 14.

Weishet, W. (1963) Further observations of geologic and geomorphic changes resulting from the catastrophic earthquake of May 1960, in Chile. *Bulletin of the Seismological Society of America*, **53,** 1237-1257.

Westmayer, A. (2005) *Composición, distribución y origen de las facies sedimentarias del Lago Pullinque, X Región*. Tesis para optar al Título de Biólogo Marino, Universidad Austral de Chile, Valdivia, 37p.

Wood, H.O. and Neumann, F. (1931) Modified Mercalli intensity scale of 1931. *Bulletin of the Seismological Society of America*, **21,** 277-283.

Wright, C. and Mella, A. (1963) Modifications to the soil pattern of South-Central Chile resulting from seismic and associated phenomenona during the period May to August 1960. *Bulletin of the Seismological Society of America*, **53,** 1367-1402.

“La tierra se abrió y vomitó arena, arena roja, que no es de acá”

“The earth opened and vomited sand, red sand, that is not from here”

Local inhabitant living at the shores of Lake Lanalhue about sand blows on the alluvial plain after the 2010 earthquake.

Chapter 5

Widespread deformation of basin-plain sediments in Aysén fjord (Chile) due to impact by earthquake-triggered, onshore-generated mass movements

Modified version accepted for publication as:

Van Daele, M., Versteeg, W., Pino, M., Urrutia, R. and De Batist, M. Widespread deformation of basin-plain sediments in Aysén fjord (Chile) due to impact by earthquake-triggered, onshore-generated landslides. *Marine Geology*.

Abstract

The 2007 M_w 6.2 earthquake in Aysén fjord caused widespread basin-plain deformation and has had prehistoric predecessors. We mapped both superficial and buried deformed basin-plain deposits using multibeam bathymetry and seismic-reflection (sparker) profiling. The seismic signature of the sub-bottom was ground-truthed with short sediment cores on key locations. Deformed basin-plain deposits induced by the 2007 earthquake can be divided in frontally emergent and confined deformed basin-plain deposits, with a deep and shallow basal shear surface. All deformed basin-plain deposits with a deep basal shear surface are induced by the weight and impact of a slope-adjacent mass-flow wedge. The frontally emergent –most mobile– basin-plain deformation is triggered by mass flows originating from onshore mass movements (i.e. debris flows, rock slides and avalanches) propagating into the fjord. This basin-plain deformation results in vertical seafloor offsets of up to 20 m and might be even more important for tsunami generation than the impact on the sea surface of the onshore mass movements themselves. In the depressions created by the basin-plain deformation, megaturbidites occur, while more distally, sandy density-flow deposits cover the seafloor. Our data also indicates that these density flows propagate slower than the basin-plain deformation. Based on correlations with the two main eruptions of the Hudson Volcano, we hypothesize that during the Holocene three to four similar events have struck the fjord. The constant structural characteristics of the Liquiñe-Ofqui Fault Zone in the northern Patagonian fjordland and historical seismic swarms in this area make us conclude that similar hazards should be taken into account for most of the fjords in this region. Finally, we have indications that both the prehistoric events and the 2007 fluid-driven seismic swarm may have been accompanied by fluid flow from tectonic structures below the fjord to the seafloor.

5.1 Introduction

Offshore mass movements have repeatedly proven their value in paleoseismological research; both in marine and lacustrine settings (Dawson, 1999; Strasser et al., 2006; Moernaut et al., 2007; Tripsanas et al., 2008; Masson et al., 2011). They have been successfully correlated to historical earthquakes and were used to identify prehistoric events. Especially in fjords or bays, mass movements can be catastrophic (Syvitski and Schafer, 1996; Bøe et al., 2000; Urgeles et al., 2002) and potentially induce tsunamis (Tocher and Miller, 1959; Ward, 2001; L'Heureux et al., 2011; Suleimani et al., 2011). These, in turn, represent great hazards for coastal villages and harbors, which in many cases provide the best access to remote inland areas.

The northern Patagonian fjordland is a tectonically active region. Not only is it crossed from north to south by the Liquiñe-Ofqui Fault Zone, an active dextral strike-slip structural lineament, it is also located along the subduction zone that produced the largest earthquake ever instrumentally recorded (i.e. the 1960 Great Chilean earthquake) (Fig. 5.1A; Melnick et al., 2009). Nevertheless, except for the study of St.-Onge et al. (2012) in which mass-wasting events in Reloncaví fjord were

linked to megathrust earthquakes, no studies have had the objective to map and date submarine mass-movement deposits or basin-plain deformation in the Chilean fjordland. However, the 2007 Aysén fluid-driven seismic swarm (Fig. 5.1B; Legrand et al., 2011) and 21 April 2007 M_w 6.2 main shock clearly highlight that research on the characteristics and the recurrence of such catastrophic events is essential for establishing reliable hazard assessments in the region. After the extensive onshore mass movement triggered by the 2007 main earthquake, studies were performed on these mass movements and the tsunamis induced by them (Fig. 5.1C; Naranjo et al., 2009; Sepúlveda and Serey, 2009; Sepúlveda et al., 2010). Unfortunately, older (i.e. historical and prehistoric) onshore mass movements are often hard to detect, let alone to date (Jibson, 1996), which complicates any study of such older events and of possible recurrence rates between events. Ward and Day (2010) propose that the 1958 seismically induced onshore rockslide in Lituya Bay (Alaska) triggered a submarine landslide. Introducing this submarine slide into their tsunami model was necessary to fit the high run-ups –derived from eyewitness and trimline accounts– at the more remote locations. Bozzano et al. (2009) and Watt et al. (2012) have shown that seismic-reflection profiling and/or multibeam bathymetry can successfully detect deposits of onshore landslides propagating into the sea or a lake. They also show that these onshore landslides have the potential to trigger offshore mass movements, thereby demonstrating that on- and offshore mass movements can be related. Such offshore mass-movement deposits are more efficiently preserved in the sedimentary record, and can potentially be dated much easier. Finally, Schnellmann et al. (2005) proposed a model where mass movements trigger basin-plain deformation with fold and thrust belts, accompanied by a lake tsunami or seiche.

In this study, we link offshore basin-plain deformation to onshore mass movements triggered by the M_w 6.2 2007 earthquake, using seismic-reflection profiling and multibeam bathymetry data. This strategy allows identifying and mapping not only the recent, but also older (buried) basin-plain deformation. Furthermore, short sediment cores are used for ground-truthing the superficial deposits and in this way better understand the seismic signature of older deposits. A hypothesis, based on seismic stratigraphy, for the age of these older deposits is presented. Moreover, seismic-reflection data and bathymetrical data can provide information about previously suggested volcanic activity in the fjord (Lara, 2008).

5.2 Setting

5.2.1 Geographical and geomorphological setting

Aysén fjord is one of the many fjords in the Chilean part of Patagonia, located between Puerto Montt in the north and Cape Horn in the south. It is carved in the Andean Cordillera, which reaches altitudes of approximately 2000 m asl (meters above sea level) in this region. At the eastern extremity of the fjord lies Puerto Chacabuco, the largest harbor of the Aysén District and through Puerto Aysén the main access to Coyhaique, the district capital (Fig. 5.1).

The fjord was formed by glacial erosion during the Pleistocene. The ice divide of the former Patagonian Ice Cap is thought to have been centered around the eastern end of the fjord (Fig. 5.1A and 5.1B), creating an east to west ice-flow in the ice cap and its outlet glaciers through the major part of the fjord (Glasser et al., 2008).

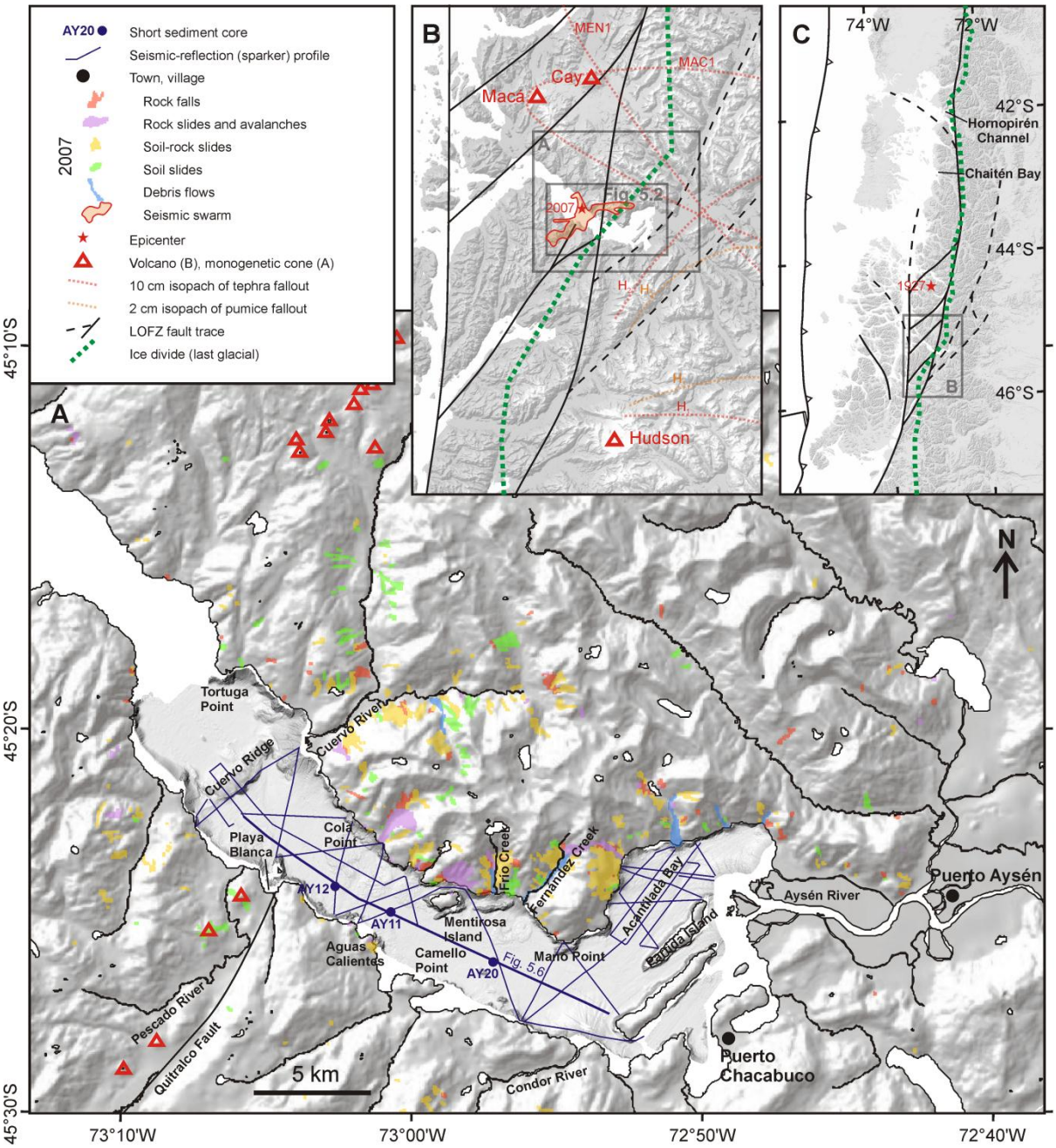

Fig. 5.1 *Setting of Aysén fjord; A: shaded relief map of the inner fjord area with indication of monogenetic volcanic cones and of the various types of onshore mass movements that were triggered by the 2007 Mw 6.2 earthquake (Sepúlveda et al., 2010). In the fjord, multibeam bathymetry coverage and location of reflection-seismic (sparker) profiles and short sediment cores are shown. B: region around Aysén fjord with indication of the Liquiñe-Ofqui Fault Zone (after Cembrano et al., 2000; Melnick et al., 2009), ice divide of the former Patagonian Ice Cap (after Glasser et al., 2008), volcanoes, tephra and pumice fallout isopachs (after Naranjo and Stern, 1998 and 2004; MEN = Mentolat, MAC = Macá, H = Hudson) and the region of the 2007 seismic swarm and main shock (after Mora et al., 2010; Legrand et al., 2011) and C: northern Patagonian fjordland with Liquiñe-Ofqui Fault Zone, ice divide of the former Patagonian Ice Cap and the epicenter of the 1927 earthquake.*

5.2.2 Geological, tectonic and volcanic setting

The geology of this area is dominated by the Patagonian Batholith. This granitic to dioritic batholith outcrops from the Llaima volcano (38°40'S) in the north to Cape Horn (56°00'S) in the south. Therefore, most of the catchment of Aysén fjord consists of this granitic to dioritic bedrock, locally

interrupted by some Quaternary volcanic centers with associated basaltic to rhyolitic volcanic rocks that cover the batholith. Also, the eastern part of the Aysén River catchment consists mainly of Mesozoic volcanic rocks (basaltic-rhyolitic composition) with some intercalated sedimentary sequences (Sernageomin, 2003).

A second important geological feature in the study area is the Liquiñe-Ofqui Fault Zone (LOFZ). The LOFZ is a 1000 km long dextral strike-slip lineament, which has been accommodating the oblique subduction of the Nazca Plate underneath the South-American Plate since the Mid Miocene. The fault zone separates the north-moving (6.5 mm/y) Chiloé sliver (in the west) from the rest of the South-American Plate (in the east) (Cembrano et al., 2000; Wang et al., 2007; Melnick et al., 2009). In the study area, the LOFZ consists of two overlapping, NNE-striking, master faults, connected by a series of NE-striking, right lateral en echelon faults (Legrand et al., 2011). In Aysén fjord, one of these en echelon faults joins the easternmost master fault (Fig. 5.1A and 5.1B).

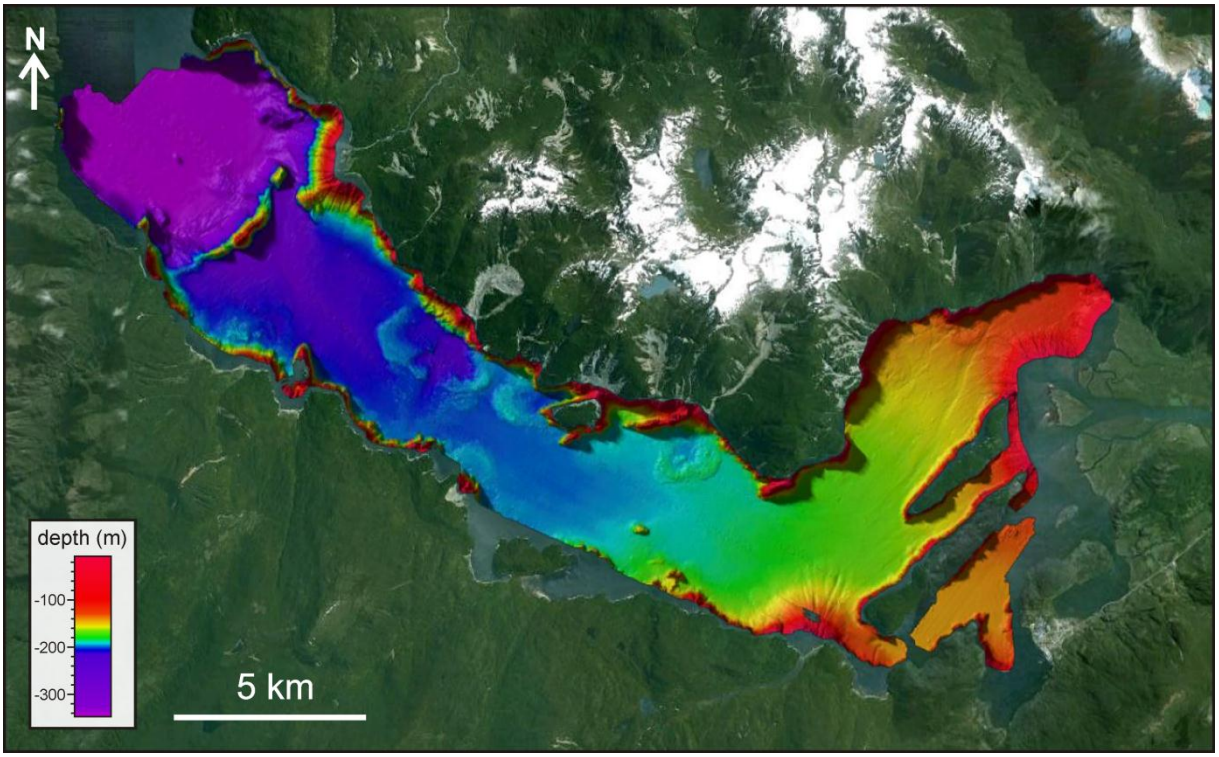

Fig. 5.2 *Post-2007 satellite photographs from Google Earth and bathymetry of the inner Aysén fjord (this study; location: Fig. 5.1).*

During the first months of 2007 a seismic swarm with more than 7000 recorded earthquakes affected the region around Aysén fjord. The series of seismic events started on 22 January 2007 and reached a maximum on 21 April 2007 with an M_w 6.2 earthquake. The epicenter of this M_w 6.2 earthquake was located in the fjord (Fig. 5.1B) and the earthquake occurred at a depth of <9 km. Intensities as high as VIII to IX on the Modified Mercalli scale were reported around the epicenter, where the largest mass movements occurred. In Puerto Chacabuco and Puerto Aysén (at the eastern end of the fjord) Modified Mercalli Intensities decreased to VII (Naranjo et al., 2009; Sepulveda and Serey, 2009; Sepúlveda et al, 2010). Multiple debris flows, rock slides and avalanches were triggered along the fjord's coastline, with a concentration of the mass movements around the LOFZ, attributed to fracturation of the bedrock by this fault zone (Fig. 5.1A and 5.2). The two most voluminous rock avalanches and one rock slide/avalanche were reported to have caused tsunamis. Several tsunami

waves with a height of up to 6 m reached the shores of the fjord, where they not only destroyed salmon farms, houses and small villages, but also resulted in 10 casualties (Sepúlveda and Serey, 2009). In 1927, a similar seismic swarm, which lasted for at least 2 months, affected the northern part of the Patagonian fjordland (i.e. Aysén to Chiloé). On 21 November 1927, an earthquake with an estimated magnitude of 7.1 occurred approximately 100 km north of Aysén fjord (Fig. 5.1A), causing landslides and tsunamis in the fjords (Naranjo et al., 2009). In August 2005 a seismic cluster with predominantly dextral strike-slip focal mechanisms and a maximum magnitude of M_w 3.8 occurred in the Hornopirén Channel (Lange et al., 2008; Fig. 5.1C). The same area was struck by a seismic swarm in May-June 2008; during this swarm magnitudes reached M_w 5.3 (Servicio Sismológico, 2012).

According to Legrand et al. (2011), the 2007 seismic swarm in Aysén fjord was related to a combined fluid-driven mechanism and tectonic activity of the LOFZ. Although such seismic swarms are typical for movement of fluids and volcanic activity, the focal mechanisms of the largest earthquakes clearly indicate a tectonic control. The presence of monogenetic volcanic cones along the LOFZ close to the fjord (Fig. 5.1C) and –based on bathymetrical data and grab samples– in the fjord (Lara, 2008), is compatible with the partly volcanic origin of the seismic swarm (Cembrano and Lara, 2009).

Apart from the monogenetic cones, several major Pleistocene-Holocene volcanoes occur close to Aysén fjord. The Macá and Cay volcanoes, 20 and 30 km north of the fjord, respectively, and the Hudson Volcano, 50 km south of the fjord, are the three southernmost volcanoes of the Andean Southern Volcanic Zone (SVZ) (Fig. 5.1B). The Hudson Volcano (45°54'S, 72°58'W, 1905 m asl) is an active volcano, with a 10 km wide, ice-filled caldera. The largest known eruptions of this basaltic-dacitic volcano are prehistoric and date from ~3600 14C yrs BP (H_2) and ~7430 14C yrs BP (~8260 cal yrs BP) (H_1), the latter probably having formed the caldera (Naranjo and Stern, 1998; Stern and Weller, 2012). The basaltic to dacitic Macá Volcano (45°06'S, 73°10'W, 2960 m asl) is the highest volcano in the region, but has only one known eruption: in AD 410±50. The Cay Volcano (45°3'33"S, 72°59'3"W, 2090 m asl) is a basaltic to dacitic stratovolcano with no historical record of eruptions (Naranjo and Stern, 2004).

5.3 Materials and methods

The data used in this study (multibeam bathymetry, high-resolution reflection-seismic profiles and short sediment cores) were acquired in December 2009 on board of the RV Don Este.

5.3.1 Multibeam bathymetry

The bathymetry of the inner part of the fjord (i.e. east of Tortuga Point; Fig. 5.1 and 5.2) was mapped using an ELAC SeaBeam 1050 multibeam sonar. The two 50 kHz transducer arrays were installed on a pole at the bow of RV Don Este. In order to correct for roll, pitch and heave an IXSEA Octans motion sensor was installed immediately above the transducers, to minimize errors. The sound-velocity profile was made using the pressure, temperature and salinity data from an IDROMAR IP039D CTD. Continuous CTD measurements at the surface were made with a Valeport CTD. The data was first cleaned with HDPedit and tide information was added in HDPpost. Final data cleaning and interpretation were done using the IVS 3D FledermausTM software.

5.3.2 Seismic-reflection data

High-resolution seismic-reflection data was acquired using RCMG's in-house designed Centipede multi-electrode sparker source. The sparker, operated at 300-400 J, produces a broad-spectrum seismic signal, with a mean frequency of ~1.3 kHz. A single-channel streamer with 10 hydrophones and a total grouplength of 2.7 m, was used as a receiver. Data was acquired at an average survey speed of 4 knots. Seismic and GPS data were digitally recorded and converted to SEG-Y format with the IXSEATM Delph Seismic Acquisition system. Interpretation of the data was done using The Kingdom SuiteTM software. In total, 35 seismic profiles with a total length of 133 km were acquired in the inner part of the fjord (Fig. 5.1A).

5.3.3 Sediment cores

In order to ground-truth the sedimentary signature of the 2007 event, we collected several short gravity cores in the inner part of the fjord. Three of these cores, taken from key locations with a particular superficial seismic facies, were used in this study (AY11, AY12 and AY20; Fig. 5.1A). The cores were taken with a Swiss gravity corer and have a length ranging between 50 and 130 cm. Magnetic susceptibility (MS) of the sediment was measured every 2.5 mm with a Bartington MS2E point sensor (3.5 mm resolution). Grain size was measured with a Malvern Mastersizer 2000 at 1-5 mm spatial resolution, depending on the sediment, without pretreatment.

5.4 Results

The combination of multibeam bathymetry and seismic stratigraphy provides insight in both the morphology of the bottom and the sedimentary infill of the fjord. The primary morphology of the fjord consists of steep slopes, presenting a continuation of the onshore mountainous morphology, with sharp lower slope breaks (Fig. 5.3). The basin plain is almost flat and has a depth of 150 m bsl (meter below sea level) in the inner fjord (i.e. at the slope break of the Aysén River delta), gradually increasing towards the outer fjord, reaching a depth of 217 m bsl east of the Cuervo Ridge. West of the Cuervo Ridge, the fjord bottom is flat and has a depth of 343 m bsl. This primary morphology, however, is interrupted by several discontinuities.

Where the acoustic basement can be observed, it has an irregular morphology with ridges and mounds, locally reaching the seafloor. The sedimentary infill can be divided into three units: i) a weakly stratified to transparent unit, only observed east of the Cuervo Ridge, ii) a ponding unit, with a discontinuous, stratified seismic facies, and iii) a draping unit with a continuous, stratified seismic facies. In the latter, some stratigraphic levels (SL) with high reflection amplitudes occur (i.e. SL-A, SL-B to SL-B', SL-C, SL-D, SL-E and SL-F). Some of these stratigraphic levels (i.e. SL-A, SL-C, SL-D and SL-F) correspond to the upper boundaries of deposits with a characteristic chaotic to transparent seismic facies. These deposits are interpreted as mass-movement deposits and/or deformed basin-plain deposits (DBPDs), based on their resemblance with other deposits with similar characteristics described elsewhere and on the geological setting (Schnellmann et al., 2005; Moernaut and De Batist, 2011). Such DBPDs occur also at the seafloor, covering large parts of the inner fjord.

5.4.1 Acoustic basement

Ridges and mounds

Across the fjord, several ridges and small mounds emerge from the flat fjord bottom (Fig. 5.3). The main morphological structure is the Cuervo Ridge, an elongated ridge that crosses the fjord perpendicularly, and bends towards the north in the northeastern part (Fig. 5.3 and 5.4). The highest point of the ridge, located at its center, reaches 57 m bsl, which corresponds to 160 and 285 m above the southeastern and northwestern basin floors, respectively. On reflection seismic data, the Cuervo Ridge can be tracked below the seafloor until a depth of at least 110 and 60 ms two-way travel time (TWT) (i.e. ~82.5 and ~45 m, based on a sound velocity of 1500 m/s) below the southeastern and northwestern basin floors, respectively (Fig. 5.5A). The average slope of the ridge on the southeastern side is 25°-35°, both above and below the seafloor. On the northwestern side, the average slope angle is also 25°-35°, but decreases to 15°-25° at 200-220 m bls, and even less below the seafloor. The ridge has no internal structure, and only some isolated hyperbolic reflections are present.

Another distinct morphological feature is an east-west oriented ridge, which is connected in the east to the steep basin walls between the Frío and Fernández Creek mouths. The ridge is interrupted east of Mentirosa Island, but seems to continue further to the west. Other prominent ridges are present west of the Cuervo River delta, east of Playa Blanca, south of Mano Point and in between Camello Point and the Condor River mouth. Furthermore two isolated mounds emerge from the flat seafloor:

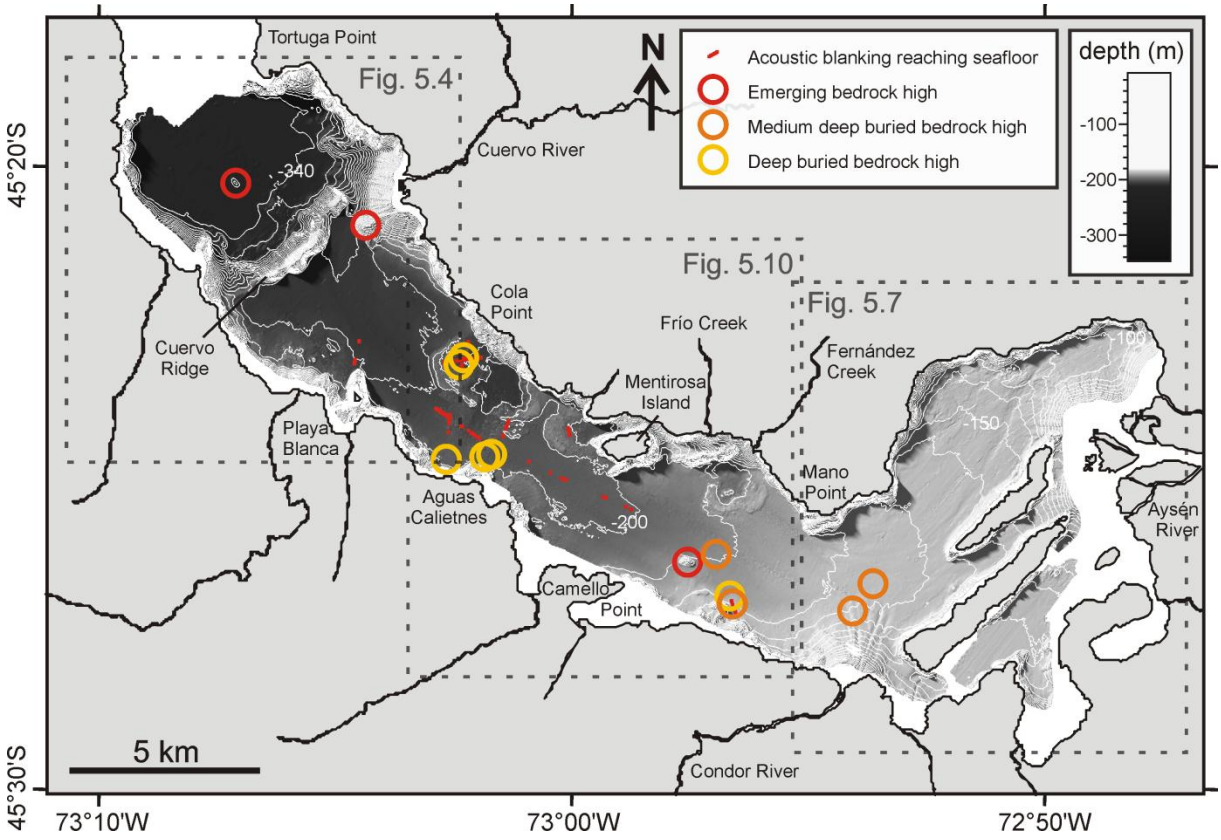

Fig. 5.3 *Multibeam bathymetry map of the inner fjord with isobaths every 10 m and occurrence of bedrock highs.*

i) one centrally in the basin west of the Cuervo Ridge, sticking out 18 m above the seafloor (i.e. 325 m bsl) and ii) a second one northeast of Camello Point, culminating at 45 m above the seafloor (i.e. 147 m bsl). The latter, however, is connected with the ridges in the southeast, by a gentle, positive bottom topography (Fig. 5.3).

Buried mounds or ridges (further called bedrock highs) with a transparent seismic facies occur in between Cola Point in the west and the Condor River mouth in the east (Fig. 5.3). Most of the bedrock highs in the western part of the fjord, between Cola Point and Mentirosa Island, are relatively deeply buried (ca. 145 m bsf; meter below sea floor), while those in the area delimited by Camello Point, Mano Point and Condor River mouth (Fig. 5.3) reach higher in the sedimentary succession (ca. 86 m bsf). The top reflection of these bedrock highs has low amplitudes and is hard to distinguish. Above the bedrock highs, subvertical acoustic wipe-out columns occur, sometimes flanked by reflections with enhanced amplitudes (Fig. 5.5B). The wipe-out columns locally reach the seafloor (concentrated under the Cola Point SE deformed basin-plain deposit (see further) and in front of Aguas Calientes), on which sometimes lens-shaped features with low amplitudes are present.

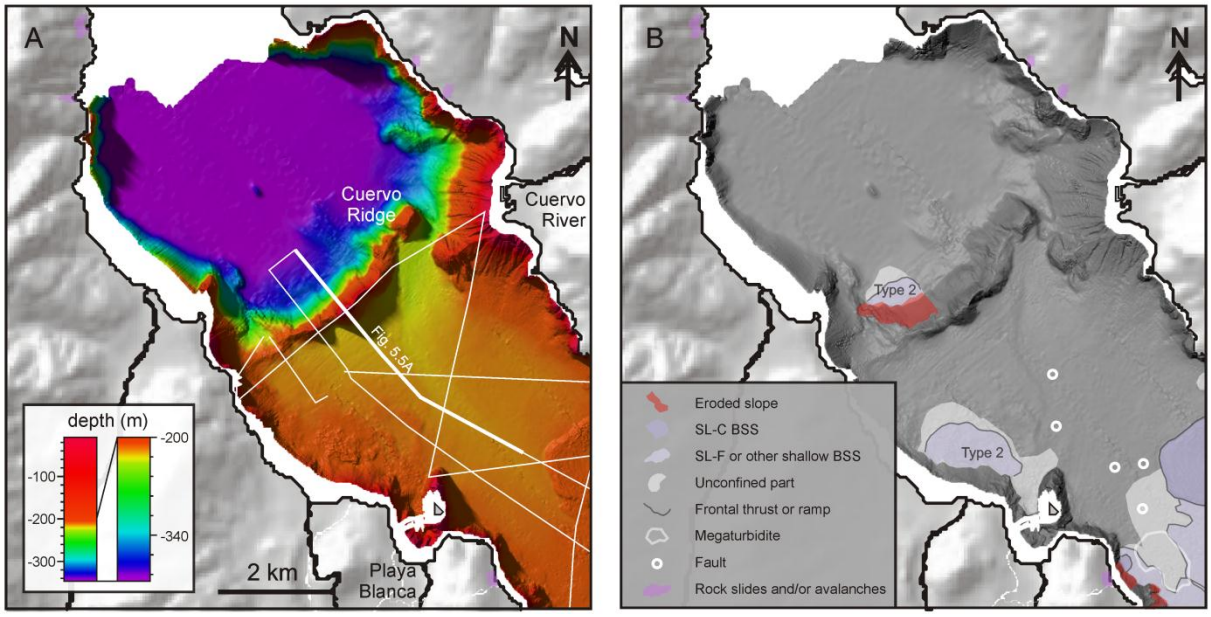

Fig. 5.4 *Shaded relief map with occurrence of onshore mass movements (after Sepúlveda et al., 2010) and bathymetry of the Cuervo Ridge area (location: Fig. 5.3); A: bathymetry and location of sparker profiles; B: grayscale bathymetry with interpretation of superficial deformed basin-plain deposits and indication of faults in the sedimentary infill of the fjord that reach the seafloor. SL: stratigraphic level; BSS: basal shear surface.*

Bedrock morphology

The acoustic basement (here interpreted as bedrock) can be observed in some parts (i.e. where it occurs shallower than the first seafloor multiple; Fig. 5.5A). At its base, the Cuervo Ridge merges with the bedrock, which occurs shallower at its southeastern than at its northwestern side. The deepening of the bedrock from the Cuervo Ridge towards the inner fjord occurs in steps. These step-downs are imaged on several seismic-reflection profiles and are aligned. The strike of these steps ranges between N-S to NE-SW, which is consistent with the dominant strike of onshore faults (Mora et al., 2010; Knight Piéshold Consulting, 2009; (Fig. 5.5A).

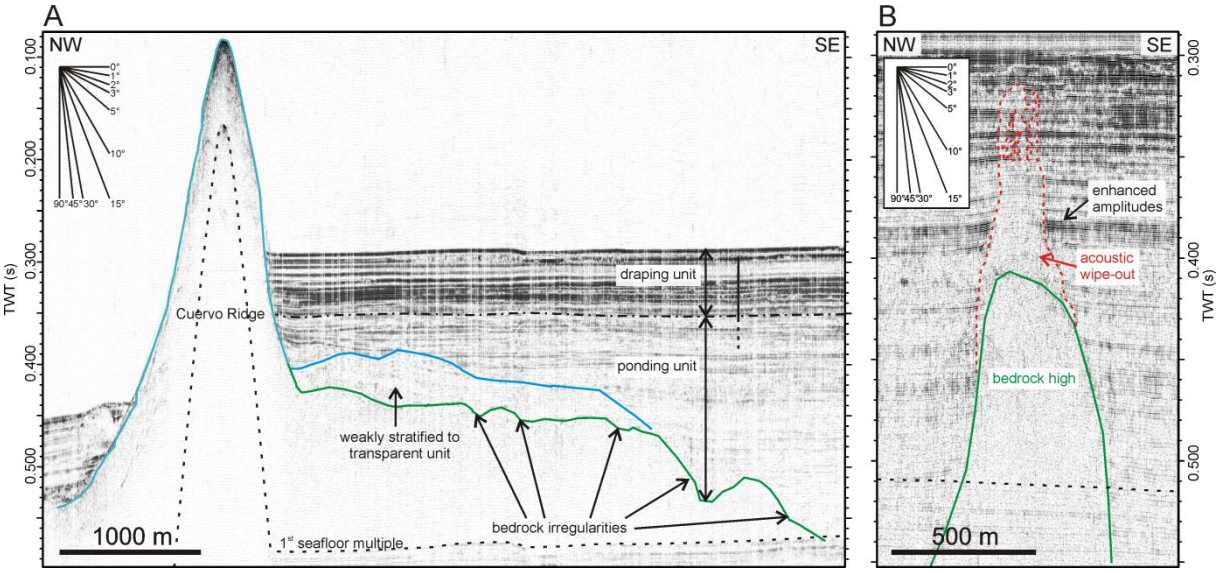

Fig. 5.5 *A: sparker profile showing the Cuervo Ridge, bedrock morphology and the sedimentary infill of the fjord, which is subdivided into three units: i) the lower weakly stratified to transparent on- and downlapping unit; ii) the middle 'ponding' unit with discontinuous reflections and iii) the upper 'draping' unit with continuous reflections; and faults in the sedimentary infill (black line) (location: Fig. 5.4A); B: deep section of a sparker profile, showing a bedrock high with acoustic wipe-out and adjacent enhanced reflections above (location: Fig. 5.10A).*

5.4.2 Sedimentary infill

Proximal to the Cuervo Ridge, the bedrock is covered by a seismic unit that is characterized by a weakly stratified to transparent seismic facies, which proximally onlaps the bedrock and Cuervo Ridge, and distally downlaps onto the bedrock. This unit, the ridge and the bedrock are all onlapped by a stratified seismic facies, which comprises the rest of the sedimentary infill of the fjord (Fig. 5.5A). The parallel stratified facies can be subdivided into two units that are separated by a gradual transition. The lower unit consists of a ponding, stratified seismic facies, but with amplitudes that vary laterally; its thickness reaches more than 200 ms TWT. The upper unit consists of a draping and continuous stratified seismic facies, with a thickness ranging between 60 and 80 ms TWT (Fig. 5.5A). In some parts of the draping unit, the basin-plain sediments are deformed.

In the stratified facies some small faults occur, either affecting the entire infill or only a part of it (Fig. 5.5A and 5.6). These faults are recognized by diffraction hyperbolae at different stratigraphic levels and sometimes there is a small offset in the stratification. The faults that do not reach the seafloor always terminate at one of the high-amplitude reflections at SL-A, SL-C, SL-D or SL-F (Fig. 5.6). When they occur underneath deformed basin-plain, the upper affected stratigraphic level cannot always be determined.

5.4.3 River deltas and fans

Aysén River delta

The Aysén River delta is situated at the eastern extremity of the fjord. Most of the subaqueous part of the delta is only a few meters deep and therefore not covered by the bathymetry map. The delta slopes extend from 20 to 120 m bsl and have a mean slope angle of 6°-8° (Fig. 5.7). The seismic penetration in the delta front sediments is limited to only a few meters and the seismic facies is

chaotic. The north-facing slopes are interrupted by multiple small channels, which are up to 5 m deep and extend straight towards the basin floor. These channels converge into a larger channel that originates at the northern foot of the delta slope, circumventing the delta to the west and then following a SW course adjacent to Partida Island, ending up at Mano Point. This channel has a width and depth of 100-250 m and 0-4 m, respectively (Fig. 5.7 and 5.8).

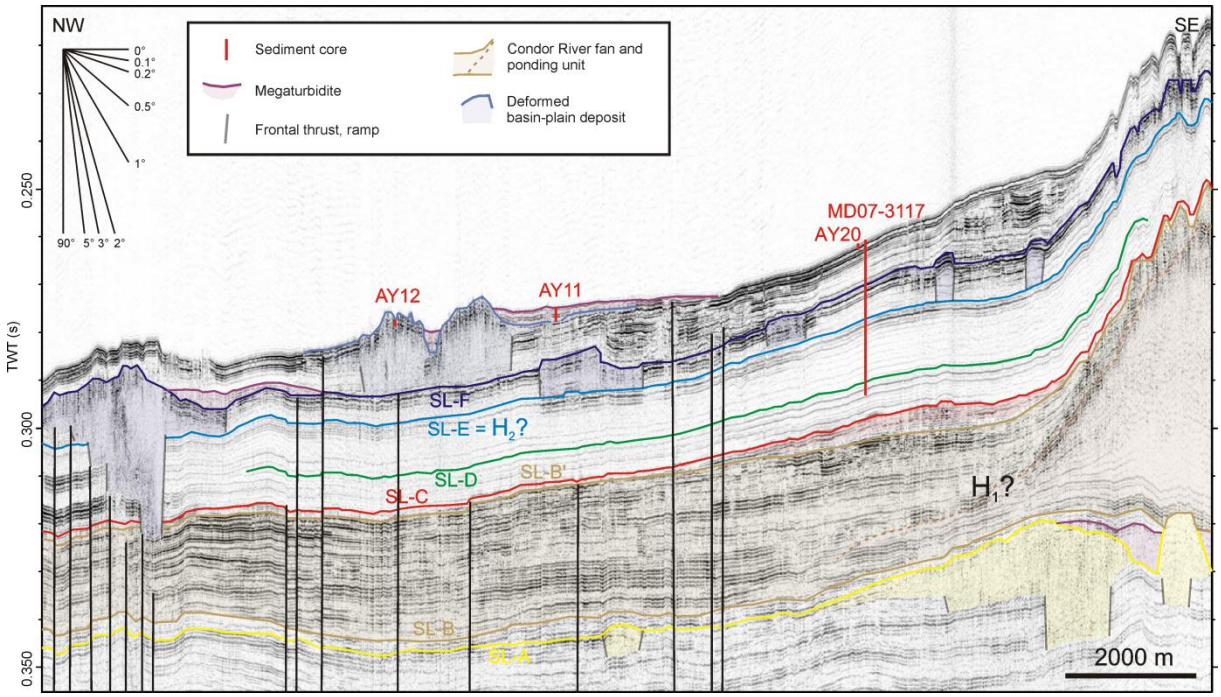

Fig. 5.6 *Sparker profile showing the upper 'draping' unit and the different stratigraphic levels (SL), deformed basin-plain deposits, transparent lens-shaped megaturbidites, the Condor River fan, the associated ponding unit, faults in the sedimentary infill and sediment cores. H_1=~7430 ^{14}C yrs BP Hudson eruption; H_2=~3600 ^{14}C yrs BP Hudson eruption, the H_1 probably formed the caldera (Naranjo and Stern, 1998; Stern and Weller, 2012; location: Fig. 5.1).*

Condor River fan

At the Condor River mouth, at SL-B, a large fan-like feature is intercalated between the sediments of the draping unit (Fig. 5.6 and 5.7). The fan is composed of a chaotic to transparent seismic facies, and is deposited on an area covering a quarter of a circle with a radius of approximately 2.5 km. The maximum thickness of this fan with a slope of 4-10° is estimated to be 130-200 ms (~100-150 m). The corresponding volume of this fan can be calculated and would be ~0.06-0.1 km³.

Towards the basin, the Condor River fan merges into a distally thinning, ponding unit. SL-B and SL-B' represent bottom and top of this unit, respectively. This unit is characterized by a basin-focusing morphology, without any draping, and high-amplitude reflections, especially close to the fan (Fig. 5.6). It has a thickness of ~20 ms (~15 m) near the fan and gradually thins out to a thickness of ~10 ms (~7.5 m) east of the Cuervo Ridge (Fig. 5.6).The thickness of this deposit gradually increases up to ~30 ms (~22.5 m) at the base of the Aysén River delta. The estimated total volume of this unit is in the order of ~0.9 km³.

SL-E is a prominent reflector with high reflection amplitudes, which are strongest close to the Condor River fan (Fig. 5.6).

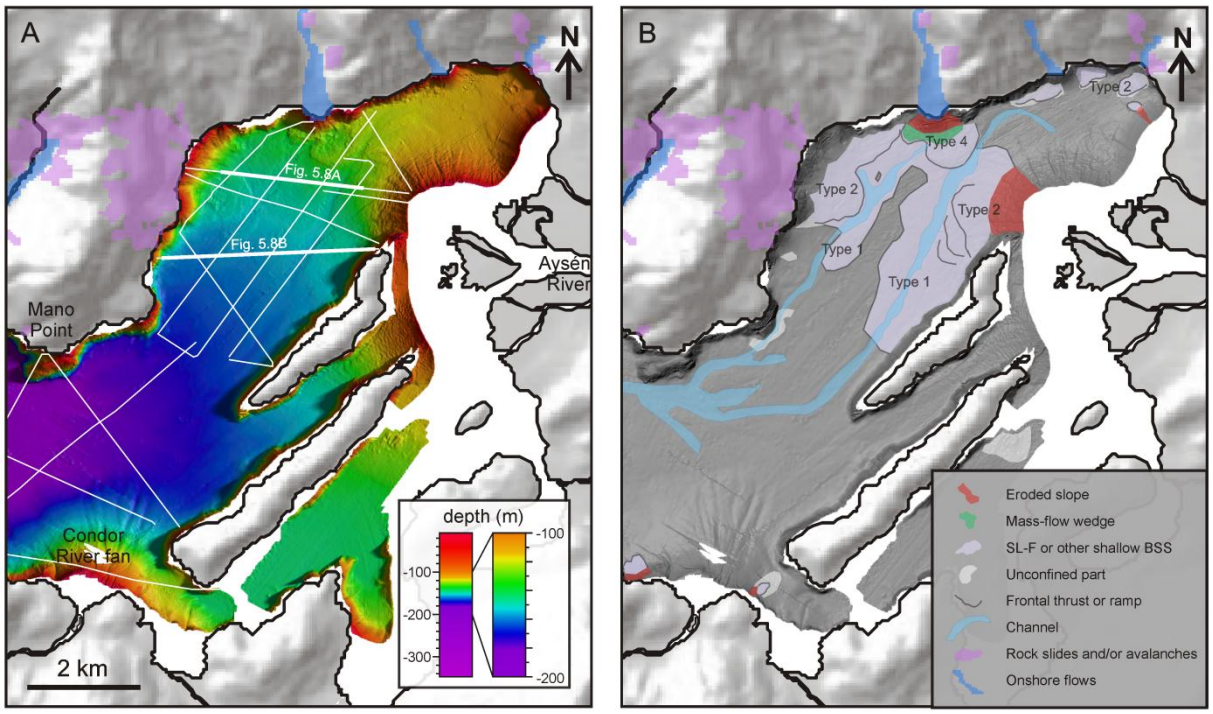

Fig. 5.7 *Shaded relief map with occurrence of onshore mass movements (after Sepúlveda et al., 2010) and bathymetry of the Acantilada Bay area (location: Fig. 5.3); A: bathymetry and location of sparker profiles; B: grayscale bathymetry with interpretation of superficial deformed basin-plain deposits and channels. SL: stratigraphic level; BSS: basal shear surface.*

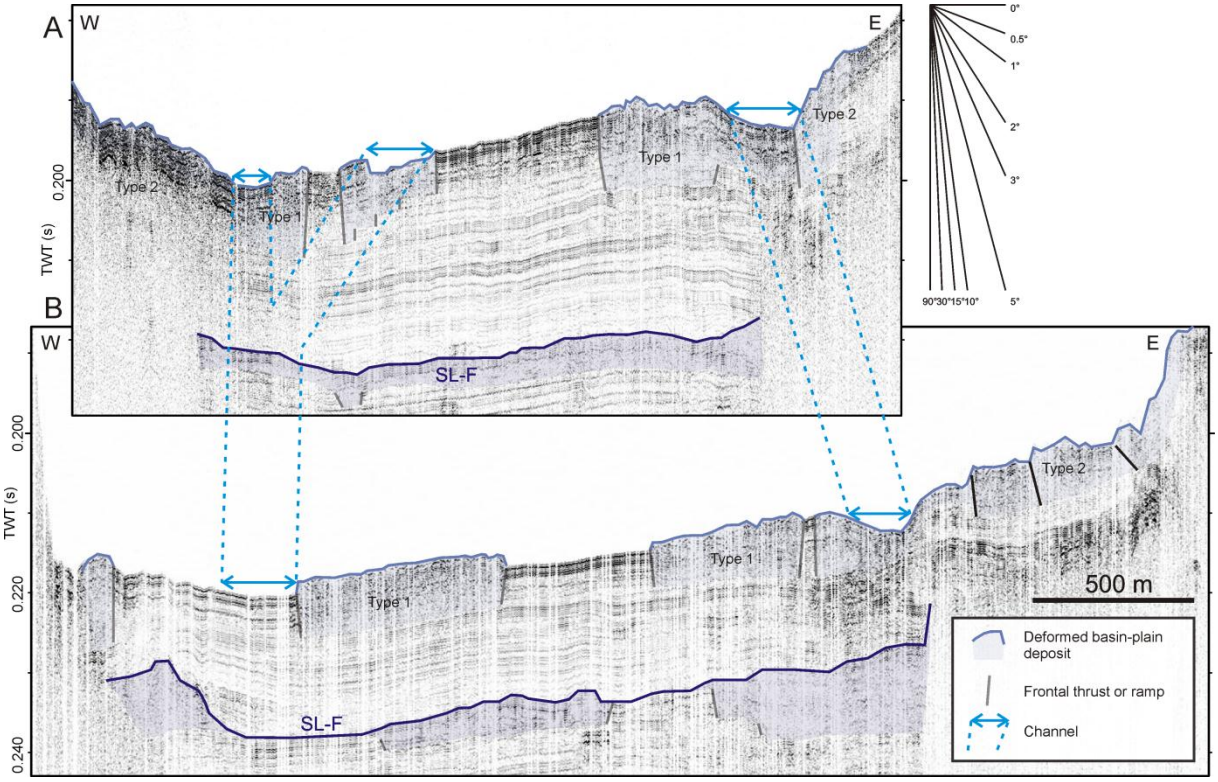

Fig. 5.8 *Sparker profiles crossing Acantilada Bay (location: Fig. 5.8A) and showing SL-F and 2007 deformed basin-plain deposits and channels; A: proximal; B: distal.*

5.4.4 Deformed basin-plain deposits (DBPDs)

Superficial DBPDs

The flat topography of the fjord floor is interrupted by large deformed basin-plain deposits (DBPDs), which are mapped using a combination of reflection-seismic profiles and multibeam bathymetry. The deposits have deformation distance that can reach up to several kilometers and reach heights of 12 m. Since a fjord can be regarded as a system intermediate between lacustrine and marine (i.e. relatively small basins, high sedimentation rate, but marine setting), we adopt the terminology used by Moernaut and De Batist (2011) to describe the morphology of the DBPDs and the characteristics of their basal shear surface (BSS). However, we use deformation distance instead of run-out distance, since this term better explains that in this specific case of DBPDs, it is the deformation that propagates, rather than a mass movement that slides and slumps. The DBPDs can be subdivided into four groups: i) long, frontally confined DBPDs with a shallow BSS (Type 1), ii) frontally emergent DBPDs with a shallow BSS (Type 2), iii) frontally confined DBPDs with a deep BSS (Type 3) an iv) frontally emergent DBPDs with a deep BSS (Type 4; Fig. 5.9).

Type 1 DBPDs (long, frontally confined DBPDs with a shallow BSS) are frontally confined DBPDs with a deformation distance of up to 3 km. The BSS is not everywhere at the same stratigraphic level, but corresponds to the first high-amplitude reflection which occurs at a depth of <10 ms bsf. These DBPDs develop distally of Type 2 DBPDs on slopes of 0.5°-1.5° and have a slope angle at the toe of 0.3° (Fig. 5.7, 5.8 and 5.9).

Type 2 DBPDs (frontally emergent DBPDs with a shallow BSS) are frontally emergent DBPDs with a deformation distance of <1 km. The BSS is not everywhere at the same stratigraphic level, but corresponds to the first high-amplitude reflection which occurs at a depth of <10 ms bsf. Proximally, some of these DBPDs have a hummocky morphology with poor seismic penetration. Some of these DBPDs occur where onshore rock slides and small debris flows propagated into the fjord (Fig. 5.9).

The Type 3 DBPD (a frontally confined DBPD with a deep BSS) is a frontally confined DBPD with a deformation distance of ~2 km. The used BSS (i.e. SL-D) occurs at a depth of ~30 ms (~22.5 m). The proximal fjord slope gradients range between 0 and 45°. On the northwestern slopes, a head scarp is present at a depth of ~60-80 m. At the foot of the slopes, side scarps merge with the frontal thrust of the DBPD and a wedge with chaotic seismic facies occurs. The proximal zone of the DBPD consists of a chaotic-transparent seismic facies forming a depression with a similar depth as the original seafloor and which is partly covered by a ponding, transparent unit. The distal part of the DBPD has a positive morphology and rises gradually towards the borders with maximum heights of 13 m above the undisturbed seafloor. In this part thrust faults cut through the still recognizable original stratigraphy (Fig. 5.9, 5.10 and 5.11A).

Type 4 DBPDs (frontally emergent DBPDs with deep BSSs) are frontally emergent DBPDs with a deformation distance of >1 km. The DBPDs have three BSSs, which are connected by two step-ups. These DBPDs occur where onshore rock avalanches or debris flows propagated into the fjord. No head or side scarps are observed in the usually steep fjord slopes. Proximally, a wedge with chaotic seismic facies and sometimes hummocky upper surface occurs. The rest of the DBPD can be subdivided in four areas: i) the inner depression, ii) the inner thrust belt, iii) the outer thrust belt and iv) the unconfined part (Fig. 5.9, 5.10 and 5.11B):

-In the inner depression the seafloor has a similar depth or is even deeper than the undisturbed basin floor, and the DBPD is partially covered by a ponding unit with a transparent seismic facies and a maximum thickness of 4 ms (~3 m). The BSS is hard to distinguish on the seismic-reflection data due to blanking by the DBPD. The seismic facies of the deposit is transparent to chaotic (Fig. 5.10 and 5.11B).

-The inner thrust belt uses SL-C as BSS, has a transparent to chaotic seismic facies forming a positive topography in which (frontal) thrusts are present close to the outer BSS step-up (Fig. 5.10 and 5.11B).

-The outer thrust belt has a positive topography, although lower than the one of the inner thrust belt. The BSS that is used in this part of the deposit is SL-F (Fig. 5.10 and 5.11B).

-The unconfined part of the deposit emerges distally or laterally from the outer thrust belt (Fig. 5.10).

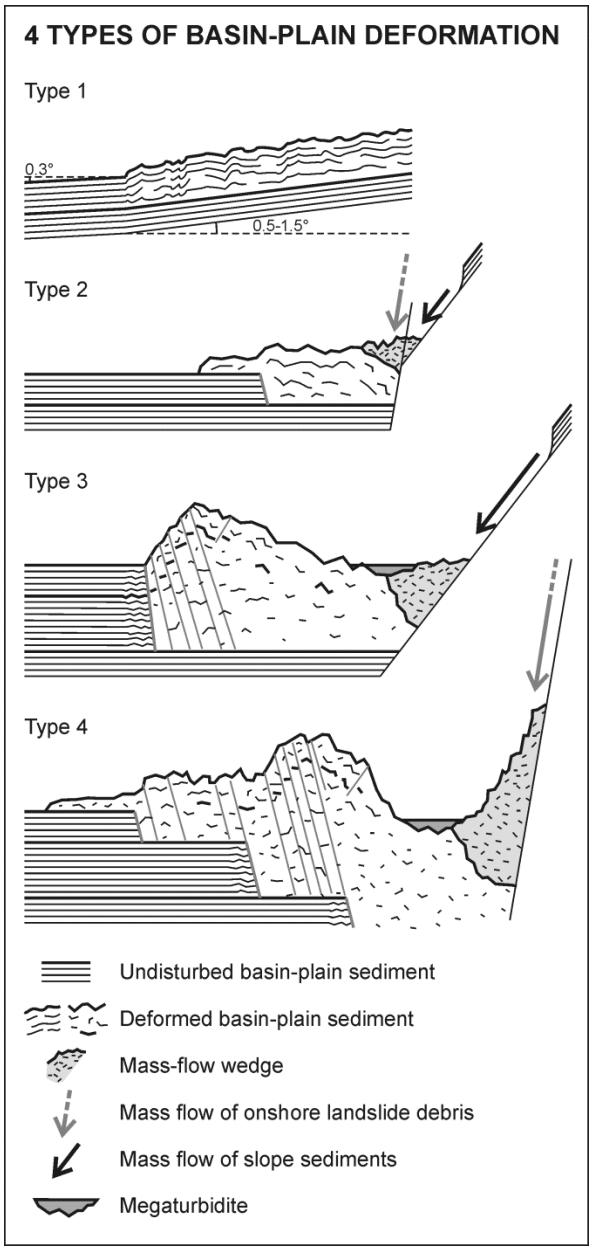

Fig. 5.9 *Schematic illustration of the 4 types of basin-plain deformation encountered in Aysén fjord.*

Acantilada Bay. Acantilada Bay is characterized by the Aysén River delta in the east and a gently SW-inclined basin floor (1.5° to 0.22° from northeast to southwest, respectively). Along Aysén River delta and the western and northern shores of Acantilada Bay, multiple Type 2 DBPDs and one Type 4 DBPD occur. The most characteristic for this area, however, are several Type 1 DBPDs, originating at the distal parts of the other DBPDs and covering a large part of Acantilada Bay (Fig. 5.7 and 5.8). Adjacent to these Type 1 DBPDs, also channels occur with widths and depths of 50-200 m and 0-3 m, respectively. These channels locally cut through the Type 1 DBPDs and the western channel only cuts through the upper sediments without disturbing deeper stratigraphic levels; they merge south of Mano Point (Fig. 5.7 and 5.8).

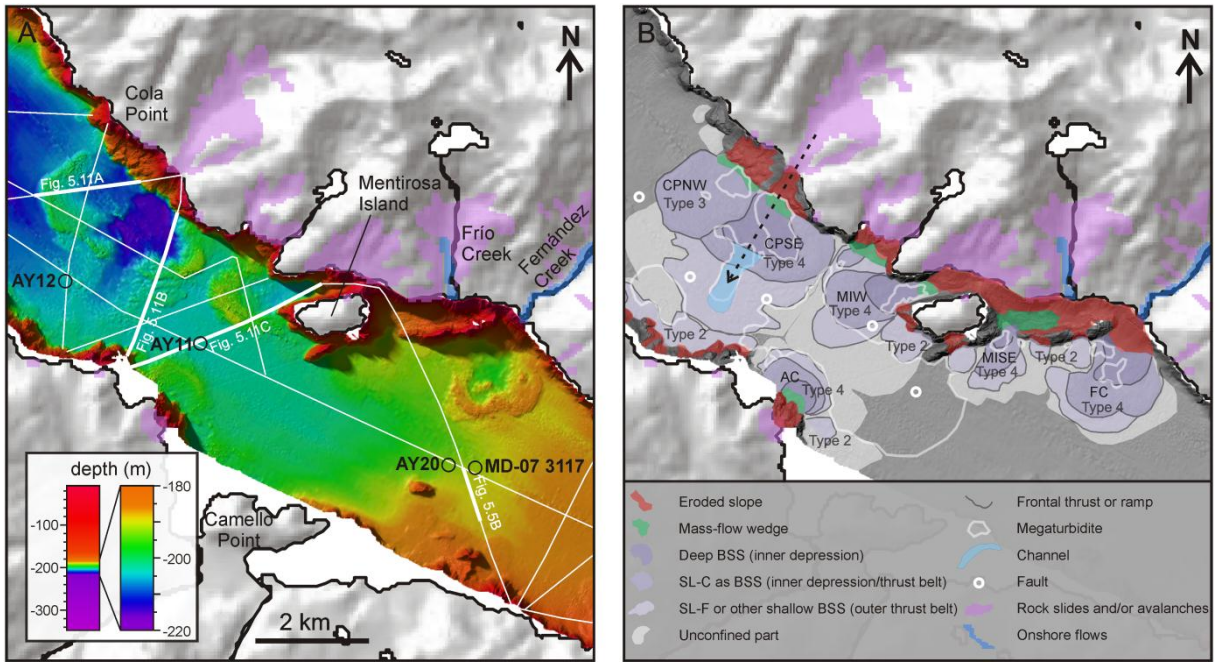

Fig. 5.10 *Shaded relief map with occurrence of onshore mass movements (after Sepúlveda et al., 2010) and bathymetry of the Mentirosa Island-Cola Point area (location: Fig. 5.3); A: bathymetry and location of sparker profiles; B: grayscale bathymetry with interpretation of superficial deformed basin-plain deposits (CPNW: Cola Point northwestern DBPD; CPSE: Cola Point southeastern DBPD; MIW: Mentirosa Island western DBPD; MISE: Mentirosa Island southeastern DBPD; FC: Fernández Creek DBPD; AC: Aguas Calientes DBPD) and faults in the sedimentary infill of the fjord that reach the seafloor. SL: stratigraphic level; BSS: basal shear surface.*

Cola Point-Mentirosa Island area. In the area comprised between Mano Point in the east and the Quitralco Fault in the west, multiple DBPDs are present. The depth of the flat basin floor ranges between 180 and 210 m bsl. Along the shores, several Type 2 DBPDs occur, but the most prominent DBPDs are of Type 3 (Cola Point NW) or Type 4 (Cola Point SE, Mentirosa Island W, Mentirosa Island SE, Fernández Creek and Aguas Calientes; Fig. 5.10 and 5.11). All these DBPDs are named after onshore geographic features where also subaerial debris flows and rock slides and avalanches occurred during the 2007 earthquake (Fig. 5.7). In the Cola Point SE DBPD, both the inner and the outer thrust belts are incised by a NNE-SSW striking channel (Fig. 5.10).

Cuervo Ridge and surroundings. In the southern part of the northwest-facing slopes of the Cuervo Ridge a Type 2 DBPD occurs. Also distally from Playa Blanca, a Type 2 DBPD with a hummocky morphology is present. Lacking seismic-reflection data in this area prevents us from making further observations concerning this DBPD (Fig. 5.4).

Ground-truthing. Southwest of Mentirosa Island, a transparent, ponding deposit can be observed on the seismic-reflection profiles. The deposit is filling a morphological depression delimited by the confined part of the DBPDs in the north, west and south, and by the gently rising undisturbed basin floor in the east (Fig. 5.6, 5.10 and 5.11). Core AY11 was taken in the central part of this deposit (Fig. 5.10 and 5.11C), and penetrates a 106 cm thick, normally graded unit (Fig. 5.12). The lower 18 cm consist of normally graded coarse to very fine sands, followed by 12 cm of normally graded fine sands to silts and finally 76 cm of homogenous silts. The upper 2 cm of the core consist of silts similar to the sediments underneath this deposit (Fig. 5.12).

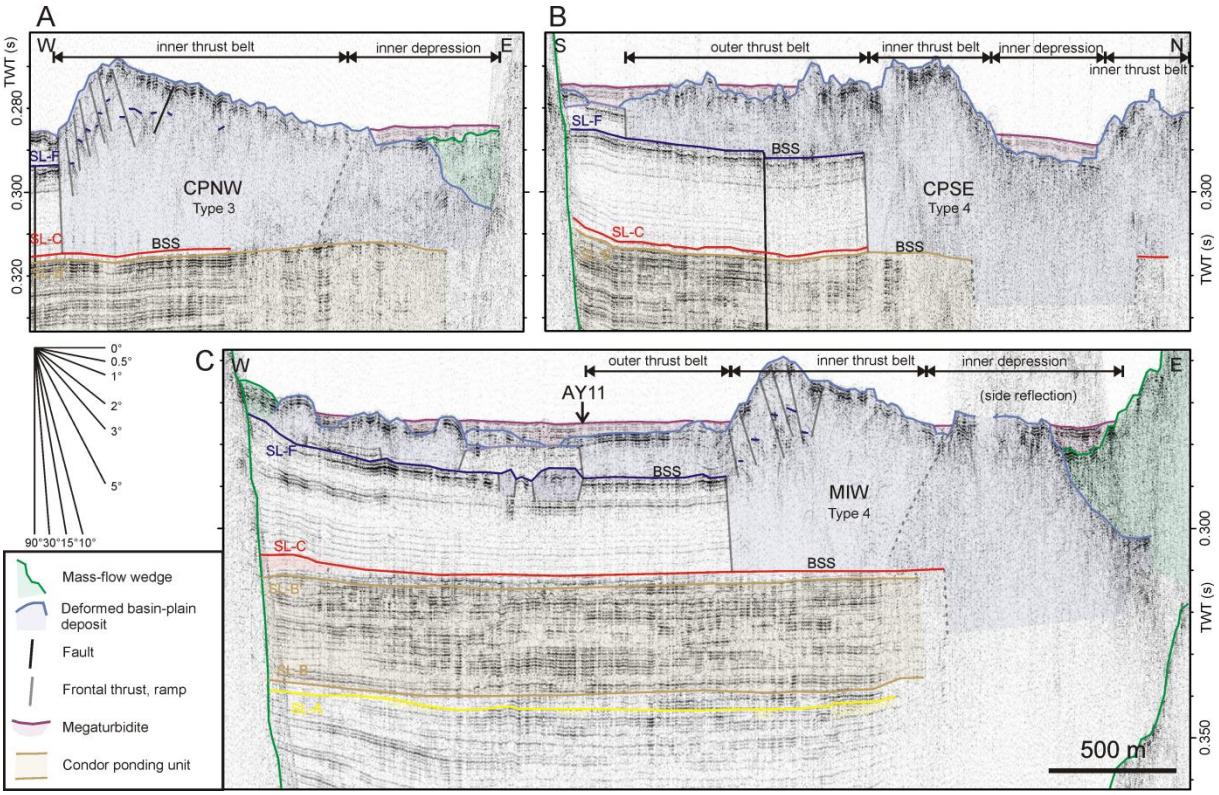

Fig. 5.11 *Sparker profiles showing three major DBPDs, their mass-flow wedge, basal shear surfaces (BSS), megaturbidites and faults in the sedimentary infill; A: CPNW: Cola Point northwestern DBPD; B: CPSE: Cola Point southeastern DBPD; C: MIW: Mentirosa Island western DBPD, DBPDs at the southwestern shores, buried DBPDs and the Condor ponding unit (location: Fig. 5.10A).*

Core AY12 was taken in the outer thrust belt of the Cola Point SE DBPD (Fig. 5.10) and clearly shows the deformations in the sediments. The lower 45 cm of the core (i.e. 6-51 cm) are characterized by folded and faulted silts. The upper limit of this unit is irregular and filled by a 3-5 cm thick normally graded unit of coarse sand to coarse silt. The upper 2.5 cm of the core consist of homogenous silt similar to the lowest unit (Fig. 5.12).

Core AY20, which was taken south of the Fernández Creek DBPD (Fig. 5.10), sampled a 12.5 cm thick sandy deposit. The lower 5 cm of this deposit consists of predominantly normally graded medium to fine sands with intercalated and silty laminae. The upper part is characterized by normally graded fine to very fine sands. On top of this unit, a 1.2 cm thick gray-brown, poorly-sorted silt layer occurs. Finally, the top of the core is formed by a 1.8 cm thick, brown, poorly sorted-sorted silt layer, similar to the sediment below the sandy unit (Fig. 5.12).

Buried DBPDs

Within the draping unit making up the upper part of the sedimentary infill of the fjord, seismic-reflection data reveal several buried DBPDs (Fig. 5.6). Some of the buried DBPDs share –similarly as the ones at the surface– the same stratigraphic level. Three stratigraphic levels comprise all except one of the buried DBPDs. The geographical extent of DBPD occurrence at the three levels is similar as for the superficial DBPDs: from the Cuervo Ridge in the west to the Aysén River delta in the east. All these stratigraphic levels are easily recognized by their basin-wide high-amplitude reflections (Fig. 5.6).

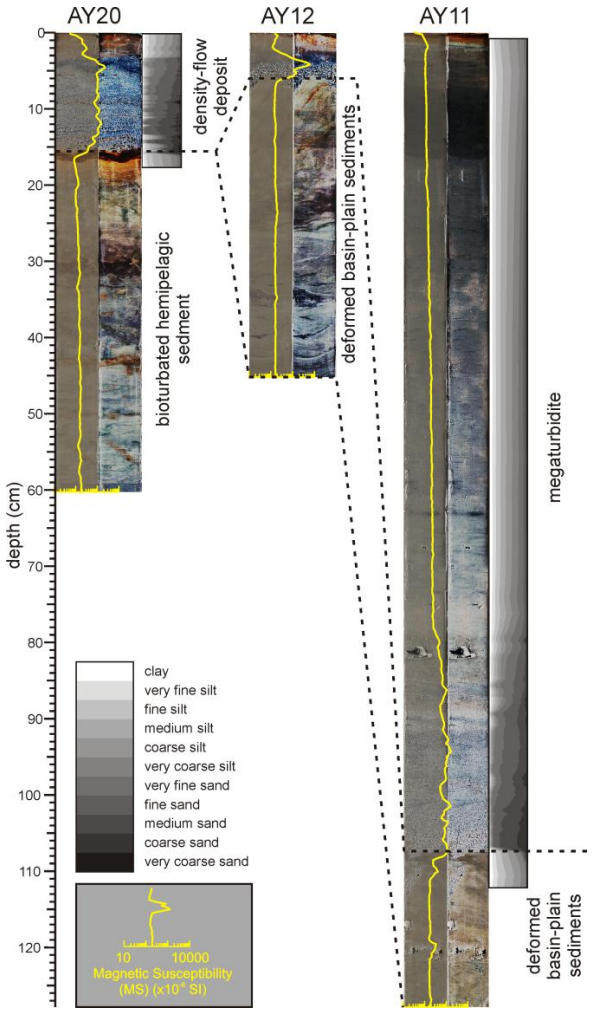

Fig. 5.12 *Three gravity cores taken in Aysén fjord showing the folded and faulted upper part of the DBPDs (AY12 and AY11), distal density-flow deposits (AY20 and AY12) and a megaturbidite (AY11). For each core: left: unprocessed core photograph; middle: photograph processed with histogram equalization; right (only for AY20 and AY11): grain-size distribution (location of the cores: Fig. 5.1, 5.5 and 5.10A).*

The largest DBPD occurs at SL-A, in the area between the Condor River mouth and Mano Point. This deposit is accompanied by a large transparent, ponding deposit, covering the northeastern part of the DBPD and the area comprised by this deposit and the Aysén River delta. Other, smaller, DBPDs occur at this level in the northwestern part of Acantilada Bay, in the Mentirosa Island-Aguas Calientes area and south of the Cuervo River delta (Fig. 5.6 and 5.13).

At SL-C, DBPDs are present in the same areas as for SL-A, with the largest one south of Mano Point. Probably some more, shallow excavating DBPDs occur in Acantilada Bay, but the resolution of the seismic-reflection data did not allow mapping out these deposits (Fig. 5.6 and 5.13).

Only a single DBPD was found at SL-D, west of the Condor River mouth. This stratigraphic level only has a high-amplitude reflection in the area close to this deposit (Fig. 5.6 and 5.13).

At SL-F, DBPDs were found in Acantilada Bay, Mentirosa Island and in the Playa Blanca-Cola Point area. East of the DBPD at Playa Blanca, a transparent lens-shaped deposit with a maximum thickness of 3 ms, occurs. This semi-ponding deposit is plastered against the southwestern slopes. Between this deposit and the fjord bottom local subvertical acoustic wipe-out occurs. Above this wipe-out, both isolated and stacked low-amplitude, lens-shaped deposits with a height of ~1.5 ms and a diameter of 30-40 m occur at the fjord bottom (Fig. 5.6 and 5.13).

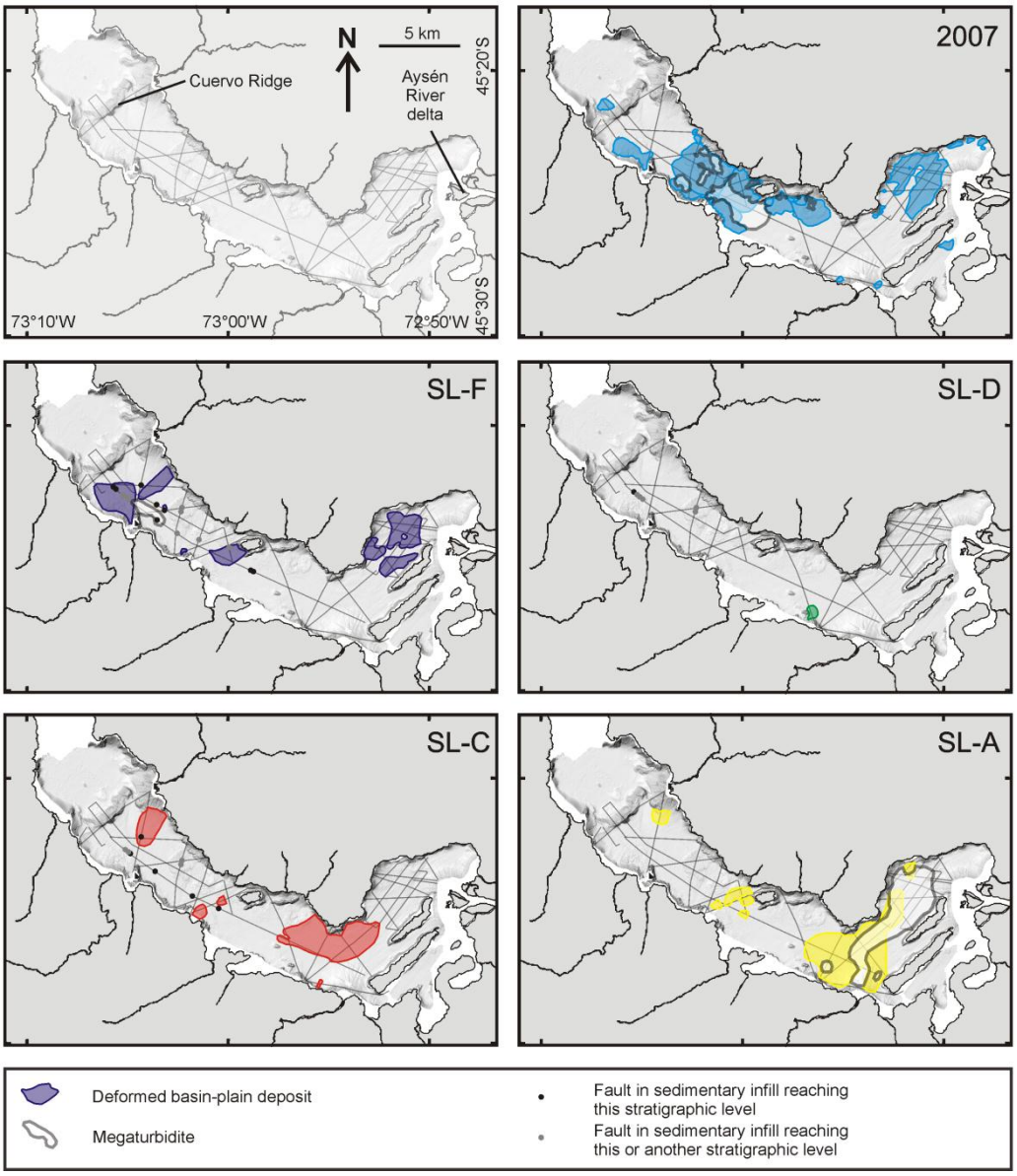

Fig. 5.13 *Maps of the DBPDs and their associated megaturbidites of the 2007 event and the four prehistoric events. Stratigraphic levels SL-A, SL-C and SL-F show similar basin-wide DBPDs as the 2007 DBPDs. The lower density of DBPDs at these levels can be attributed to incomplete coverage of the fjord by the seismic profiles (gray lines). Faults in the sedimentary infill that reach the specific stratigraphic level are also indicated (coordinates: Fig. 5.3).*

Furthermore, we point out that we expect an underrepresentation of buried DBPDs. Due to the incomplete coverage of the seismic-reflection grid and to blanking below younger DBPDs, it is likely that our data did not allow us to detect all buried deposits.

5.5 Discussion

5.5.1 2007 basin-plain deformation

The superficial DBPDs in Aysén fjord, mapped with seismic-reflection profiling and multibeam bathymetry, are assigned to the 2007 M_w 6.2 earthquake. The three short sediment cores (i.e. on top of one of the DBPDs, in the transparent unit and in a distal area) all show an evidently very recent event deposit with a maximum of 2 cm of draping sediment covering the top of the deposit (Fig. 5.12). Moreover, the largest of these superficial DBPDs can be spatially linked to subaerial debris flows and rock avalanches that entered the fjord after the 2007 M_w 6.2 earthquake. These large deposits form a jigsaw puzzle with the smaller deposits rather than covering them (Fig. 5.10), indicating that all the superficial deposits mapped using the seismic-reflection data and the multibeam bathymetry are triggered by a single event: the 2007 M_w 6.2 earthquake. The transparent ponding units that fill the depressions created by the DBPDs, are interpreted as megaturbidites (Bouma, 1987). The transparent, lens-shaped deposits connected by acoustic wipe-out to the SL-F megaturbidite, are interpreted as liquefaction structures or sediment volcanoes, similar to what has been described by Moernaut et al. (2009), and are tentatively attributed to the same earthquake.

All the DBPDs along the northwestern shores of Acantilada Bay occur where onshore debris flows, rock slides and avalanches entered the fjord. In the east, where the basin slopes are very steep (i.e. 15-35°), the deposits are likely mainly composed of material from these onshore mass movements, as suggested by the hummocky morphology. In the west of Acantilade Bay, where the slopes are less steep (i.e. 3-20°) and therefore possibly sediment-bearing, the onshore mass movements likely triggered offshore DBPDs, which have a higher mobility. The DBPDs at the base of the west-facing delta slopes and the absence of large channels on these slopes, suggest that these slopes have indeed failed during the 2007 earthquake.

We interpret that both the Type 2 basin-plain deformation along the northwestern shores of Acantilada Bay and the ones on the delta slopes triggered the Type 1 basin-plain deformation, the deposits of which cover a major part of Acantilada Bay (Fig. 5.7). In the east, this basin-plain deformation developed adjacent to a preexisting channel, which channelized density flows that originated at the delta and the northeastern shores of Acantilada Bay. In the west, a channel incises the Type 1 DBPD and continues to Mano Point, where it merges with the eastern channel (Fig. 5.7). This channel was most likely formed by density flows postdating the DBPD, indicating that the DBPD propagated faster than the density flows.

All the large DBPDs (i.e. Type 3 and 4) occur at locations where large subaerial debris-flows and rock slides/avalanches entered the fjord, and vice versa (Fig. 5.10). Only the Type 3 DBPD at Cola Point is caused by a mass flow of slope sediments, in turn triggered by an onshore rock avalanche that entered the fjord. For all the large and most of the Type 2 DBPDs, the model proposed by Schnellmann et al. (2005), with some minor adaptations, can be used to explain their formation and geometry. This model assumes that the increasing load at the slope break marking the transition between the fjord slope and basin floor induces gravity spreading of the basin-plain sediment leading to propagating overthrusting and sediment deformation, with the latter causing a completely transparent seismic facies. The proximal mass-flow wedge (i.e. the load) was recognized in some of our DBPDs.

The structure of the Type 3 DBPD at Cola Point can be explained by this model. However, the proximal depression that is characteristic for the Cola Point DBPD does not occur in the deposits studied by Schnellmann et al. (2005). A possible explanation for this difference is the larger height drop of the mass flow in Aysén fjord (>150 m versus ~100 m). This difference can cause higher impact velocities, resulting in a higher energy transfer and hence, a larger momentum of the basin-plain deformation.

In the Type 4 DBPDs, not only the central depression is deeper, but also proximal deformation penetrates deeper in the fjord sediments (Fig. 5.11). A succession of step-ups and a distal unconfined part is typical for these deposits. This enhanced mobility is probably caused by a larger height drop and steeper slopes (Moernaut and De Batist, 2011). All the Type 4 DBPDs occur where onshore rock avalanches and debris flows entered the fjord, resulting in an offshore height drop of >195 m. Moreover, the higher density of the rocks compared to the slope sediments will increase the inertia and energy transferred during impact with the basin-plain sediments. Types 3 and 4 of basin-plain deformation in Aysén fjord can be considered to be the two next steps in the model of Schnellmann et al. (2005).

The large height difference between the inner depressions and the thrust belts (up to 20 m) suggests that this strong basin-plain deformation (i.e. Type 3 and 4) could also be tsunamogenic. Similarly as in Lituya Bay (Alaska), such a tsunami sensu stricto can be potentially further reaching than an impact wave produced by onshore mass movements impacting on the fjord water (Ward and Day, 2010). However, both types of waves should be modeled to confirm this.

Another difference with the Schnellmann et al. (2005) model is the relative timing between basin-plain deformation and the overriding density flow. In the model, these two processes are suggested to occur synchronously, but the structure of the southeastern Cola Point frontally emergent DBPD suggests that the basin-plain deformation occurs first. The channel incising the inner thrust belt, is aligned with the on- and offshore mass-flow pathways (Fig. 5.10). Hence, we hypothesize that the density flow broke through the freshly deformed and up-thrusted basin-plain sediments. This delay can be explained by the higher viscosity of the sediment compared to water, causing the basin-plain deformation to propagate faster than the density flow. On top of the deformed basin-plain sediments, these density flows only leave a thin (i.e. a few centimeters) normally graded gravel to silt layer. However, distally, these density flows are preserved as ~10 cm thick sandy deposits (core AY20; Fig. 5.12), corresponding to what can be expected for a density-flow deposit (Mulder and Alexander, 2001).

5.5.2 Prehistoric events and chronology

Also the older DBPDs coincide with a distal density-flow deposit. The older DBPDs distally correspond to basin-wide high-amplitude reflections in the case of multiple DBPDs on one stratigraphic level, originating from different slope segments of the fjord (i.e. SL-A, SL-C and SL-F), or to local high amplitudes in the case of a single DBPD on one stratigraphic level (i.e. SL-D). Some of these stratigraphic levels can be tied to the MD-07 3117 core, a Calypso core which was taken from the RV Marion Dufresne 2 months before the M_w 6.2 earthquake. In this ~21 m long core, sandy (tephra) layers occur at depths of ~5 m, ~17 m and ~20 m, and at ~10 m a 50 cm thick tephra and pumice layer occurs (Kissel et al., 2007). The tephras at ~5 m and ~20 m depth correlate with SL-F and SL-D, respectively (Fig. 5.6). Based on our seismic-stratigraphic mapping and interpretation of the DBPDs in

the fjord, we suggest that these high-amplitude reflections represent distal density-flow deposits, similar to the 2007 density-flow deposit (i.e. ~10 cm thick sandy layers in AY20, at approximately the same location; Fig. 5.10A), rather than tephras. The pumice-tephra layer correlates with SL-E (Fig. 6). The older density-flow deposits (i.e. SL-A and SL-C; Fig. 5.6 and 5.12) are also used as BSSs by the 2007 basin-plain deformation.

On stratigraphic levels SL-A, SL-C and SL-F, basin-wide mass-movements occurred on a scale comparable to that of the 2007 event. During all these events, faults affecting the sedimentary infill of the fjord were formed or re-activated (Fig. 5.6 and 5.13), suggesting movement along bedrock faults that cross the fjord. We infer that these faulting and mass-movement events were triggered by 2007-like earthquakes along the LOFZ, with epicenters very close to Aysén fjord. The SL-D DBPD and the single synchronous fault were probably formed during a smaller earthquake in the fjord or a similar earthquake, but with an epicenter further away from the fjord.

The DBPD at the northwestern side of the Cuervo Ridge described by Araya Vergara (2011) is also evident on the bathymetry (Fig. 5.4), but could not be linked to any of the described events. The seismic reflection data of the two basins (i.e. north and south of the Cuervo Ridge) cannot be unambiguously correlated.

Based on its intercalated, local nature, we interpret the Condor River fan and its coeval ponding unit to be deposited in a relatively short time period (Fig. 5.6), and tentatively attribute it to the ~8260 cal yrs BP H_1 Hudson eruption. The dimensions at sea level of the Condor River fan (i.e. ~1.1 km²) are of the same magnitude as the fan deposited in Chaitén Bay (Fig. 5.1C) after the 2008 Chaitén eruption (i.e. ~1.3 km²) presented by Lara (2009) (Fig. 5.4), indicating that it is possible for such a fan to be deposited during a single event. The H_1 eruption was the largest Holocene eruption of the Hudson Volcano, and the characteristics of the related tephras are consistent with a caldera being formed during this eruption (Naranjo and Stern, 1998). The Condor River is draining some of the southern slopes of the Hudson Caldera (Fig. 5.1), hence, caldera formation could produce pyroclastic flows potentially reaching the fjord, and/or provide the Condor River with large amounts of volcanoclastic sediment. The thickening of the ponding unit towards the Aysén River delta is consistent with the fact that also the Aysén River drains a part of the Hudson Volcano (Fig. 5.1). However, studying volcanic outcrops in the Condor River valley is necessary to confirm this hypothesis.

Correlating the Condor River fan with the ~8260 cal yrs BP H_1 Hudson eruption, results in an average sedimentation rate of about 0.3 cm/yr at the location of the MD-07 3117 Calypso core. This sedimentation rate is very similar to the sedimentation rates of 0.19-0.30 cm/yr that Salamanca and Jara (2003) determined in the upper 25 cm of sediment on two locations in the inner Aysén fjord. Hence, these sedimentation rates support our correlation and by assuming a constant sedimentation (in TWT ms) –and in the absence of any direct age control on these deposits–, we can make an informal assessment of the ages of the prehistoric eruptions and earthquakes. The resulting age for SL-E would be ~3170 yrs BP. Hence, this pumice-tephra layer –which is best developed close to the Condor River fan– can be tentatively attributed to the 3600 14C yrs BP H_2 Hudson eruption. This H_2 pumice-tephra layer was deposited in large areas to the south of Aysén fjord (Naranjo and Stern, 1998), and is the only known pumice deposit that close south of the fjord (Naranjo and Stern, 1998 and 2004; Stern, 2008; Fig. 5.1B). The ages of SL-A, SL-C, SL-D and SL-F would be ~9160 yrs BP, ~7160 yrs BP, ~5830 yrs BP and ~1500 yrs BP, respectively. Hence, three to four catastrophic events

comparable in effect to the 2007 earthquake and tsunami have struck Aysén fjord during the Holocene. Following this age model, the transition between the ponding and the draping stratified units would occur around 10 ka BP, making the draping unit roughly correspond to the Holocene. This correlation is in agreement to other fjords and lakes where similar seismic units represent the postglacial infill (Eyles and Mullins, 1997; Lysså et al., 2004; Hjelstuen et al., 2009; Heirman et al., 2011).

In the studied inner part of the fjord we do not see signs of major DBPDs that could be attributed to the 1927 seismic swarm and associated M 7.1 earthquake. The estimated epicenter of this major earthquake is located about 100 km to the north of the fjord, probably along one of the northernmost en echelon faults connecting the two overlapping master faults of the LOFZ. By using the formulas of Keefer (1984) and Rodriguez et al. (1999) to extrapolate the maximum epicentral distances for onshore disrupted landslides and flows obtained by Sepúlveda et al. (2010) for the 2007 earthquake, we find maximum epicentral distances of ~90 km and ~50-70 km for disrupted landslides and flows, respectively. Hence, it could be expected that no major subaerial landsliding affected Aysén fjord.

5.5.3 Activity along the Liquiñe-Ofqui Fault Zone (LOFZ)

Activated faults

The faults that were activated during the 2007 seismic swarm can be tracked in the bedrock below the fjord sediments. We created a new fault map for Aysén fjord, based on submarine bedrock morphologies and onshore faults (Fig. 5.14). Aligned bedrock irregularities, submarine ridges, mounds and basin-wall irregularities were used as tie points. Subsequently the inferred fault traces were combined with previously mapped onshore faults (Mora et al., 2010; Knight Piéshold Consulting, 2009), and based on submarine faults, geomorphology and the 2007 seismic swarm epicenters (Mora et al., 2010; Legrand et al., 2011), some additional onshore fault traces have been added (Fig. 5.14).

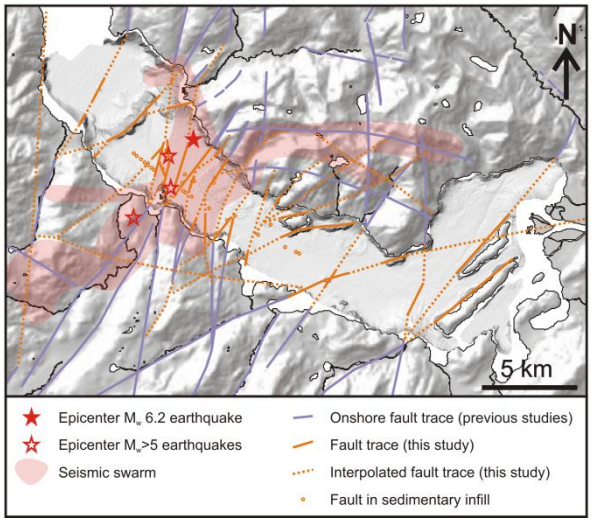

Fig. 5.14 *Fault map of the inner Aysén fjord area with faults mapped in previous studies (Mora et al., 2010; Knight Piéshold Consulting, 2009) and in this study (bedrock irregularities and highs). The area of the 2007 seismic swarm, epicenters of the main shocks (Mora et al., 2010; Legrand et al., 2011) and seafloor-reaching faults in the sedimentary infill provide an indication of the faults that were activated during the 2007 seismic swarm (coordinates: Fig. 5.3).*

The pre-21 April epicenters of the 2007 seismic swarm (Mora et al., 2010; Legrand et al., 2011) in the fjord concentrate clearly around the faults occurring between Playa Blanca and the Cuervo River delta. The epicenter of the M_w 6.2 event (Legrand et al., 2011) lies on one of the fault traces that we detected in the fjord. The epicenters of the 2nd and 3rd largest earthquakes of the 2007 seismic

swarm (i.e. M_w 6.1, 02/04/2007 and M_w 5.7, 23/02/2007) plot on the same fault trace and a fault trace to the west. These faults connect the Quitralco Fault in the south and the faults along the Cuervo River valley in the north, indicating that this is the main strand of the LOFZ that was activated during the 2007 seismic swarm. After the 21 April earthquake, the earthquakes (or aftershocks) in the seismic swarm were spread over more faults, both on- and offshore (Legrand et al., 2011; Fig. 5.14).

Activity along the LOFZ

2007-like events can occur regularly in the Patagonian fjordland. Scarce historical and instrumental records indicate that seismic swarms, both with and without a large main shock, are common along the southern part of the LOFZ (i.e. south of Puerto Montt). The 1927, 2005, 2007 and 2008 seismic swarms in the Patagonian fjordlands (Lange et al., 2008, Naranjo et al., 2009, Servicio Sismológico, 2012) demonstrate that these swarms, which are often accompanied by large main shocks, are common along the LOFZ. The low recurrence rate of on average 2500-3000 years in Aysén fjord shows that at a specific location along the LOFZ, these catastrophic events are scarce. We expect, however, that similar events occur relatively frequently along the LOFZ in the Patagonian fjords between Reloncaví fjord in the north (41.50° S) and San Rafael Lake in the south (46.75° S), and should be taken in into account for hazard assessments. North of Reloncaví fjord, the nature of the LOFZ becomes more segmented and displacement decreases (especially north of 40° S, dying out at 38° S) (Roseneau et al., 2006), reducing the risk of large earthquakes in this area.

LOFZ versus megathrust

No effects of megathrust earthquakes were detected in Aysén fjord. The youngest megathrust earthquake affecting the fjord was the 1960 Great Chilean Earthquake, but in the cores, until a depth of 50 cm in draping sediment, no evidence was detected for earthquake-related deposits prior to those of the 2007 event. This is in agreement with a Macroseismic Intensity of IV during the 1960 earthquake in Puerto Aysén (Lazo Hinrichs, 2008), which is likely too low to cause significant seismically-induced event-deposits. In Reloncaví fjord, mass-wasting deposits and related turbidites have been attributed to the 1960- and older megathrust earthquakes (St-Onge et al., 2012), but in this area the correlation with the 1960 earthquake is in agreement with reported Intensities in Puerto Montt –~50 km NW of Reloncaví fjord– of VII-IX (Lazo Hinrichs, 2008). However, it must be noted that similar Intensities of VII-IX throughout Reloncaví fjord may also be caused by a local, 2007 Aysén-type event (e.g., along the LOFZ). Hence, $M_w > 6$ earthquakes, with a recurrence rate of a few thousand years, triggering offshore basin-plain deformation or mass movements and megaturbidites, cannot be excluded in Reloncaví fjord, nor in other Patagonian fjords.

5.5.4 Volcano or moraine?

Lara (2008) argued that the summits of the Cuervo Ridge are formed by monogenetic volcanic cones; however, based on our new data, the Cuervo Ridge is identified as a moraine (Fig. 5.15). The two summits of the Cuervo Ridge were identified as submarine volcanoes based on morphology and a grab sample containing vesicular basalt. Our new bathymetric and seismic data provide new evidence regarding the nature of the ridge: i) elongated morphology, ii) steeper southeastern slopes, iii) onlapping fjord sediments (indicating a glacial age) and iv) poor seismic penetration with some isolated reflection hyperboles (Fig. 5.4, 5.5A and 5.15). These are consistent with a moraine formed

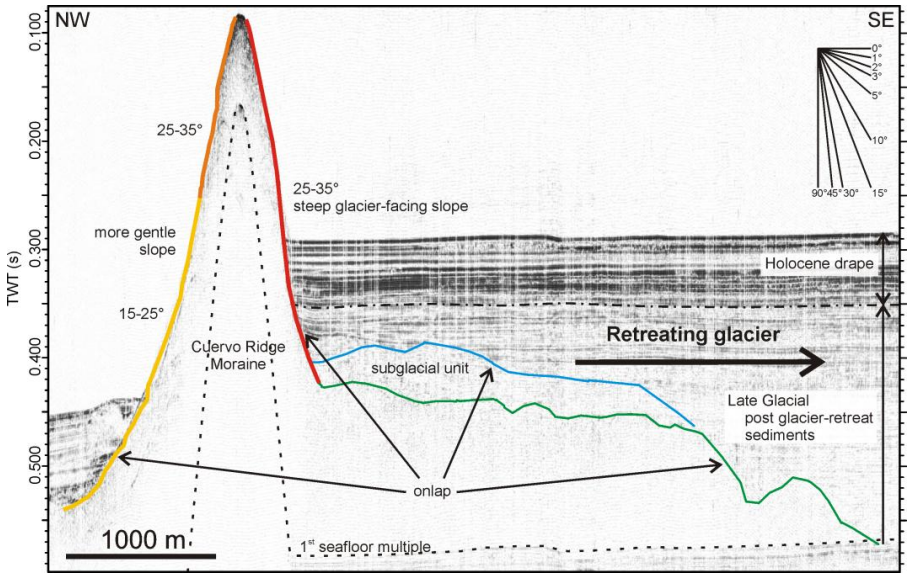

Fig. 5.15 *Sparker profile presented in Fig. 5.5, with interpretation of the different seismic facies. The different slope gradients on the southeastern and northwestern side of the Cuervo Ridge, and the subglacial unit on its southeastern side, show that the ridge is a moraine and that the glacier retreated towards the southeast.*

by a glacier from the southeast (i.e. where the ice divide of the former Patagonian Ice Cap was situated; Glasser et al., 2008). The vesicular basalt on top of the ridge can be explained by outlet glaciers transporting these (possibly sub-glacially) erupted basalts from its original location to the moraine. This original location could be the Macá or Cay volcanoes, or one of their satellite cones, located to the north of the fjord. The plateau could have been covered with a late-glacial ice-field with an outlet glacier to the fjord via the present Cuervo River valley. This outlet glacier is also a candidate for causing the bend in the northeastern part of the Cuervo Moraine (Glasser, N., pers.comm.). The weakly stratified unit at the southeastern side (i.e. the glacier-facing side) of the Cuervo Ridge (i.e. the oldest unit that onlaps the Cuervo Ridge) can be interpreted as a subglacial unit (Fig. 5.15). In lakes, similar units have been interpreted as a till deposit (Eyles and Mullins, 1997; Heirman et al., 2011).

The subvertical acoustic wipe-outs above the bedrock irregularities, buried ridges and mounds (Fig. 5.5B) are interpreted as fluid escape with a possible volcanic or geothermal origin. The occurrence of the subvertical acoustic wipe-outs is clearly linked to tectonic structures crossing the fjord. The two zones of seafloor-reaching wipe-outs are located within the area of the 2007 seismic swarm (Barrientos, 2007; Legrand et al., 2011). The occurrence of low-amplitude, lens-shaped deposits at the seafloor above this wipe-out suggests that the wipe-out is caused by fluid flow able to mobilize sediments. Whether this fluid flow is linked to the 2007 seismic swarm and/or still ongoing, can, however, not be derived from the data.

5.6 Conclusions

This study gives an overview of the impact of the 2007 seismic swarm and M_w 6.2 main shock on the sedimentary record of the fjord, and provides a hypothesis on the recurrence of such events. The main conclusions are:

1) The onshore mass movements –triggered by the 2007 M_w 6.2 earthquake– that entered the fjord, all triggered deformation of basin-plain sediments, which may have been more important for tsunami generation than the impact of the onshore mass movements themselves. Multiple small offshore mass movements and sediment volcanoes have been triggered directly by the earthquake.

2) The largest offshore deformed basin-plain deposits were produced by the impact and load of the onshore mass movements, resulting in unique morphologies of the basin-plain deformation, characterized by proximal depressions and high inner and outer thrust belts.

3) Density flows originating from the Acantilada Bay and Cola Point mass flows, formed or enlarged channels, occasionally cutting through the deformed basin plain, indicating that the latter propagate faster.

4) We hypothesize that three to four similar events have struck the fjord during the Holocene. A similar hazard should be taken into account for the other fjords between 41.5° and 46.5° S.

5) The Cuervo Ridge is identified as a moraine, and the interpretation as two monogenetic volcanic cones can be ruled out. However, there are indications for fluid flow from tectonic structures below the fjord to the seafloor, which could be related to volcanic and tectonic activity, such as the 2007 seismic swarm.

Acknowledgements

This research was funded mainly by the Fund for Scientific Research Flanders (FWO-Vlaanderen) and by the Special Research Fund of Ghent University (BOF). We are grateful to Litoral Austral and the RV Don Este crew (especially captain J. Matamala Nuñez) to make the 2009 survey possible and successful. We thank K. De Rycker for the technical support during the survey in 2009. Dr. J. Greinert is acknowledged for the substantial help in processing of the multibeam data. We are grateful to C. Leal for the use of the CTD. B. Beuselinck and Prof. Dr. M. Vincx are acknowledged for the use of the Malvern Mastersizer 2000. We thank Ph. De Smedt for sharing the Bartington MSE2 point sensor. M. Cuylaerts is acknowledged for her work in the sedimentary lab. Finally we thank Dr. K. Heirman, Dr. I. Meyer, Dr. J. Moernaut and W. Vandoorne for the fruitful discussions. M. Van Daele is currently funded by the Fund for Scientific Research Flanders (FWO-Vlaanderen).

References

Araya Vergara, J.F. (2011) Submarine failures in the bottom of the Aysén fjord, Northern Patagonia, Chile. *Investigaciones Geográficas,* Santiago, Chile, **43,** 17-34.

Barrientos, S. (2007) *Informe del Servicio Sismológico sobre actividades realizadas entre 3 – 8 Marzo 2007 y Evolución de la Sismicidad,* Servicio Sismológico, Santiago, 5 pp. Available at http://www.sismologia.cl/informes/inf_aysen/Segundo_Informe_Aysen.pdf, accessed on May 2012.

Bouma, A.H. (1987) Megaturbidite - an acceptable term. *Geo-Marine Letters*, **7,** 63-67.

Bozzano, F., Mazzanti, P., Anzidei, M., Esposito, C., Floris, M., Fasani, G.B. and Esposito, A. (2009) Slope dynamics of Lake Albano (Rome, Italy): insights from high resolution bathymetry. *Earth Surface Processes and Landforms*, **34,** 1469-1486.

Bøe, R., Hovland, M., Instanes, A., Rise, L. and Vasshus, S. (2000) Submarine slide scars an mass movements in Karmsundet and Skudenesfjorden, southwestern Norway: morphology and evolution. *Marine Geology*, **167,** 147-165.

Cembrano, J. and Lara, L. (2009) The link between volcanism and tectonics in the southern volcanic zone of the Chilean Andes: A review. *Tectonophysics*, **471,** 96-113.

Cembrano, J., Schermer, E., Lavenu, A. and Sanhueza, A. (2000) Contrasting nature of deformation along an intra-arc shear zone, the Liquine-Ofqui fault zone, southern Chilean Andes. *Tectonophysics*, **319,** 129-149.

Dawson, A.G. (1999) Linking tsunami deposits, submarine slides and offshore earthquakes. *Quaternary International*, **60,** 119-126.

Eyles, N. and Mullins, H.T. (1997) Seismic-stratigraphy of Shuswap Lake, British Columbia, Canada. *Sedimentary Geology*, **109,** 283-303.

Glasser, N.F., Jansson, K.N., Harrison, S. and Kleman, J. (2008) The glacial geomorphology and Pleistocene history of South America between 38[degree sign]S and 56[degree sign]S. *Quaternary Science Reviews*, **27,** 365-390.

Heirman, K., De Batist, M., Charlet, F., Moernaut, J., Chapron, E., Brümmer, R., Pino, M. and Urrutia, R. (2011) Detailed seismic stratigraphy of Lago Puyehue: implications for the mode and timing of glacier retreat in the Chilean Lake District. *Journal of Quaternary Science*.

Hjelstuen, B.O., Haflidason, H., Sejrup, H.P. and Lyså, A. (2009) Sedimentary processes and depositional environments in glaciated fjord systems - Evidence from Nordfjord, Norway. *Marine Geology*, **258,** 88-99.

Jibson, R.W. (1996) Use of landslides for paleoseismic analysis. *Engineering Geology*, **43,** 291-323.

Keefer, D.K. (1984) Landslides caused by earthquakes. *Bulletin of the Geological Society of America*, **95,** 406-421.

Knight Piéshold Consulting (2009) *Energía Austral Ltda., Proyecto Central Hidroeléctrica Cuervo, Estudio de Impacto Ambiental (Ref. No. SA203-00047/3-1)*. Santiago, 7907 pp.

Kissel, C., The shipboard scientific party (2007) *MD159 - PACHIDEME IMAGES XV,* cruise report, Institut polaire français Paul-Emile Victor, Plouzané, France, 84 pp.

Lange, D., Cembrano, J., Rietbrock, A., Haberland, C., Dahm, T. and Bataille, K. (2008) First seismic record for intra-arc strike-slip tectonics along the Liquiñe-Ofqui fault zone at the obliquely convergent plate margin of the southern Andes. *Tectonophysics*, **455,** 14-24.

Lara, A. (2008) Holocene submarine volcanoes in the Aysén fjord, Patagonian Andes (44ºS): Relations with the Liquiñe-Ofqui Fault Zone. *7th International Symposium on Andean Geodynamics (ISAG 2008, Nice), Extended abstracts***,** 285-288.

Lara, L.E. (2009) The 2008 eruption of the Chaiten Volcano, Chile: a preliminary report. *Andean Geology*, **36,** 125-129.

Lazo, R.G. (2008) *Estudio de los daños de los terremotos del 21 y 22 de mayo de 1960*, Universidad de Chile, Santiago, 427 pp.

Legrand, D., Barrientos, S., Bataille, K., Cembrano, J. and Pavez, A. (2011) The fluid-driven tectonic swarm of Aysen Fjord, Chile (2007) associated with two earthquakes (M_w =6.1 and M_w =6.2) within the Liquiñe-Ofqui Fault Zone. *Continental Shelf Research*, **31,** 154-161.

L'Heureux, J.S., Glimsdal, S., Longva, O., Hansen, L. and Harbitz, C. (2011) The 1888 shoreline landslide and tsunami in Trondheimsfjorden, central Norway. *Marine Geophysical Research*, **32,** 313-329.

Lyså, A., Sejrup, H.P. and Aarseth, I. (2004) The late glacial-Holocene seismic stratigraphy and sedimentary environment in Ranafjorden, northern Norway. *Marine Geology*, **211,** 45-78.

Masson, D.G., Arzola, R.G., Wynn, R.B., Hunt, J.E. and Weaver, P.P.E. (2011) Seismic triggering of landslides and turbidity currents offshore Portugal. *Geochem. Geophys. Geosyst.*, **12,** Q12011, 11 pp.

Melnick, D., Bookhagen, B., Strecker, M.R. and Echtler, H.P. (2009) Segmentation of megathrust rupture zones from fore-arc deformation patterns over hundreds to millions of years, Arauco peninsula, Chile. *Journal of Geophysical Research-Solid Earth*, **114,** 23 pp.

Moernaut, J., De Batist, M., Charlet, F., Heirman, K., Chapron, E., Pino, M., Brummer, R. and Urrutia, R. (2007) Giant earthquakes in South-Central Chile revealed by Holocene mass-wasting events in Lake Puyehue. *Sedimentary Geology*, **195,** 239-256.

Moernaut, J., De Batist, M., Heirman, K., Van Daele, M., Pino, M., Brümmer, R. and Urrutia, R. (2009) Fluidization of burried mass-wasting deposits in lake sediments and its relevance for paleoseismology: Results from a reflection seismic study of lakes Villarrica and Calafquén (South-Central Chile). *Sedimentary Geology*, **213,** 121-135.

Moernaut, J. and De Batist, M. (2011) Frontal emplacement and mobility of sublacustrine landslides: Results from morphometric and seismostratigraphic analysis. *Marine Geology*, **285,** 29-45.

Mora, C., Comte, D., Russo, R., Gallego, A. and Mocanu, V. (2010) Aysen seismic swarm (January 2007) in southern Chile: analysis using Joint Hypocenter Determination. *Journal of Seismology*, **14,** 683-691.

Mulder, T. and Alexander, J. (2001) The physical character of subaqueous sedimentary density flows and their deposits. *Sedimentology*, **48,** 269-299.

Naranjo, J.A. and Stern, C.R. (1998) Holocene explosive activity of Hudson Volcano, southern Andes. *Bulletin of Volcanology*, **59,** 291-306.

Naranjo, J.A. and Stern, C. (2004) Holocene tephrochronology of the southernmost part (42°30'-45°S) of the Andean Southern Volcanic Zone. *Revista Geológica de Chile*, **31,** 225-240.

Naranjo, J.A., Arenas, M., Clavero, J. and Munoz, O. (2009) Mass movement-induced tsunamis: main effects during the Patagonian Fjordland seismic crisis in Aisen (45 degrees 25'S), Chile. *Andean Geology*, **36,** 137-145.

Rodriguez, C.E., Bommer, J.J. and Chandler, R.J. (1999) Earthquake-induced landslides: 1980-1997. *Soil Dynamics and Earthquake Engineering*, **18,** 325-346.

Rosenau, M., Melnick, D. and Echtler, H. (2006) Kinematic constraints on intra-arc shear and strain partitioning in the southern Andes between 38 degrees S and 42 degrees S latitude. *Tectonics*, **25**.

Salamanca, M.A. and Jara, B. (2003) Distribución y acumulación de plomo (Pb y 210Pb) en sedimentos de los fiordos de la XI región, Chile. *Cienc. Tecnal. Mar*, **26,** 61-71.

Schnellmann, M., Anselmetti, F.S., Giardini, D. and McKenzie, J.A. (2005) Mass movement-induced fold-and-thrust belt structures in unconsolidated sediments in Lake Lucerne (Switzerland). *Sedimentology*, **52,** 271-289.

Sepulveda, S.A. and Serey, A. (2009) Tsunamigenic, earthquake-triggered rock slope failures during the April 21, 2007 Aisen earthquake, southern Chile (45.5 degrees S). *Andean Geology*, **36,** 131-136.

Sepúlveda, S., Serey, A., Lara, M., Pavez, A. and Rebolledo, S. (2010) Landslides induced by the April 2007 Aysén Fjord earthquake, Chilean Patagonia. *Landslides*, **7,** 483-492.

Sernageomin (Servicio Nacional de Geología y Minería) (2003) *Mapa Geológico de Chile: versión digital,* Scale 1:1,000,000, Santiago, Chile, 25 pp.

Servicio Sismológico (2012) *Todos los sismos en Chile (2000-Presente).* Servicio Sismológico, Depto. de Geovísica, Universidad de Chile, Santiago. Available at: http://www.sismologia.cl/seismo.html, accessed on May 2012.

St-Onge, G., Chapron, E., Mulsow, S., Salas, M., Viel, M., Debret, M., Foucher, A., Mulder, T., Winiarski, T., Desmet, M., Costa, P.J.M., Ghaleb, B., Jaouen, A. and Locat, J. (2012) Comparison of earthquake-triggered turbidites from the Saguenay (Eastern Canada) and Reloncavi (Chilean margin) Fjords: Implications for paleoseismicity and sedimentology. *Sedimentary Geology*.

Stern, C. (2008) Holocene tephrochronology record of large explosive eruptions in the southernmost Patagonian Andes. *Bulletin of Volcanology*, **70,** 435-454.

Stern, C. and Weller, D. (2012) A Revised Age of 7430 ± 250 14C yrs BP for the Very Large mid-Holocene Explosive H_1 Eruption of the Hudson Volcano, Southern Chile. In: *13th Chilean Geologic Congress*, pp. 2, Antofagasta, Chile.

Strasser, M., Anselmetti, F.S., Fah, D., Giardini, D. and Schnellmann, M. (2006) Magnitudes and source areas of large prehistoric northern Alpine earthquakes revealed by slope failures in lakes. *Geology*, **34,** 1005-1008.

Suleimani, E., Nicolsky, D., Haeussler, P. and Hansen, R. (2011) Combined Effects of Tectonic and Landslide-Generated Tsunami Runup at Seward, Alaska During the M_w 9.2 1964 Earthquake. *Pure and Applied Geophysics*, **168,** 1053-1074.

Syvitski, J.P.M. and Schafer, C.T. (1996) Evidence for an earthquake-triggered basin collapse in Saguenay Fjord, Canada. *Sedimentary Geology*, **104,** 127-153.

Tocher, D. and Miller, D.J. (1959) Field observations on effects of Alaska earthquake of 10 July 1958. *Science*, **129,** 394-395.

Tripsanas, E.K., Piper, D.J.W. and Campbell, D.C. (2008) Evolution and depositional structure of

earthquake-induced mass movements and gravity flows: Southwest Orphan Basin, Labrador Sea. *Marine and Petroleum Geology*, **25,** 645-662.

Urgeles, R., Locat, J., Lee, H.J. and Martin, F. (2002) The Saguenay Fjord, Quebec, Canada: integrating marine geotechnical and geophysical data for spatial seismic slope stability and hazard assessment. *Marine Geology*, **185,** 319-340.

Wang, K., Hu, Y., Bevis, M., Kendrick, E., Smalley, R. and Lauria, E. (2007) Crustal motion in the zone of the 1960 Chile earthquake: Detangling earthquake-cycle deformation and forearc-sliver translation. *Geochemistry Geophysics Geosystems*, **8,** 14 pp.

Ward, S.N. (2001) Landslide tsunami. *Journal of Geophysical Research-Solid Earth*, **106,** 11201-11215.

Ward, S.N. and Day, S. (2010) The 1958 Lituya Bay landslides and tsunami - A tsunami ball approach. *Journal of Earthquake and Tsunami*, **4,** 285-319.

Watt, S.F.L., Talling, P.J., Vardy, M.E., Heller, V., Hühnerbach, V., Urlaub, M., Sarkar, S., Masson, D.G., Henstock, T.J., Minshull, T.A., Paulatto, M., Le Friant, A., Lebas, E., Berndt, C., Crutchley, G.J., Karstens, J., Stinton, A.J. and Maeno, F. (2012) Combinations of volcanic-flank and seafloor-sediment failure offshore Montserrat, and their implications for tsunami generation. *Earth and Planetary Science Letters*, **319-320,** 228-240.

“Fue como en la Biblia, cuando Moises abre el agua”

“It was like in the Bible, when Moses opens the water”

Local inhabitant living at Lake Aculeo, talking about standing waves –triggered by the shaking of the 2010 earthquake– at the lake shore.

Chapter 6

Multidirectional, amalgamated density-flow deposits revealed by X-ray computed tomography (CT)

Modified version submitted for publication as:

Van Daele, M., Cnudde, V., Duyck, P., Pino, M., Urrutia, R. and De Batist, M. Multidirectional, amalgamated density-flow deposits revealed by X-ray computed tomography (CT). *Sedimentology*.

Abstract

On April 21, 2007, an M_w 6.2 earthquake struck Aysén fjord (Chilean Patagonia) and caused on- and offshore mass movements which triggered tsunamis and density flows in the fjord. To better understand the sedimentary-facies successions in and intercalation of the density-flow deposits, we studied the 2007 deposits in 22 short sediment cores taken in the inner Aysén fjord. By combining grain-size analysis with X-ray computed tomography (CT) scanning, we were able to demonstrate that the encountered facies correspond to classical divisions of density-flow deposits and turbidites. The deposits consist of a succession of several sub-deposits with different paleoflow directions and can be interpreted as amalgamated density-flow deposits. We used orientations of i) folds, ii) imbricated mud clasts, iii) back- and foresets of climbing ripples and iv) asymmetric convolute lamination, to determine relative paleoflow directions at the location of the cores. By assigning the basal flow of the amalgamated density-flow deposits to the closest principal mass-flow, the absolute flow directions of the sub-deposits were determined, which, in combination with multibeam basin-floor morphology, allowed reconstruction of the 2007 density-flow successions in Aysén fjord. Furthermore, alternating flow directions provide evidence for a seiche induced by the density flows. Traction carpets, in which rip-up mud clasts correspond to the floating, coarsest grains, occur at the base of the density-flow deposits. We conclude that X-ray CT scans provide crucial information for reconstructing paleoflows and can be a useful tool in marine and lacustrine sedimentology and paleoseismology. Multidirectional, amalgamated density-flow deposits and turbidites are an indication for simultaneous triggering of density flows and can therefore in most cases be attributed to earthquakes, ruling out other triggers, such as floods.

6.1 Introduction

Turbidite deposits, or, in the broader sense density-flow deposits, are increasingly being used in paleoseismological research, both in marine (e.g., Goldfinger, 2011) and lacustrine environments (e.g., Beck, 2009; Strasser et al., accepted). In order for density-flow deposits to be suitable as a paleoseismological proxy, it is important that they can unambiguously be assigned an earthquake origin and distinguished from other types of density-flow deposits (e.g., generated by floods or by non-seismically-triggered delta- or slope collapses). Density-flow deposits resulting from simultaneous failing of different slope segments are usually considered as good candidates to be earthquake-triggered, although establishing this is far from straightforward. A detailed analysis of sedimentary-facies successions and oriented internal sedimentary structures within these deposits can be of help in achieving this (Nakajima and Kanai, 2000; Goldfinger et al., 2012).

The different types of density-flow deposits and turbidites were initially described and defined by Bouma (1962) and Lowe (1982), based on the detailed study of outcrops. These authors produced their own classification of respectively classic and coarse-grained turbidites by studying outcrops of ancient sediments. Divisions for fine-grained turbidites were developed by Stow and Shanmugam (1980), who compared outcropping sediments with continental-margin sediment cores.

Several authors have successfully determined paleoflow directions in mass-movement deposits. Alsop and Marco (2011) clearly showed and summarized how folds and faults in slumps can be used to infer paleoflow direction. They also illustrated how paleoflow directions of seismically triggered tsunami and seiche waves can be recorded in these slumps (Alsop and Marco, 2012). McClelland et al. (2011) linked eye- and sheath-fold orientation in turbidite convolute lamination with paleoflow directions determined by sole structures and ripple cross lamination. Mulder et al. (2009) reconstructed the seiche movement within a megaturbidite by analyzing grain orientation. Above-mentioned studies illustrate that it is possible to reconstruct paleoflow direction based on the detailed study of outcrops. In recent years, an increasing number of sediment cores have been taken in oceans and lakes. However, the limited diameter of marine and lacustrine sediment cores and the punctual sampling locations sometimes cause difficulties in determining the sedimentary facies and sedimentary structures and in performing paleoflow reconstructions.

In this study, we use a recent, well described density-flow event in Aysén fjord, Chilean Patagonia, to show that X-ray computed tomography (CT) –already proven to be a useful tool in geosciences (Cnudde et al., 2006)– offers new applications in marine and lacustrine sedimentology. In combination with grain-size analysis it provides a complete 3D image of the deposit. In this way, sedimentary facies can be better determined and therefore also possible inverse facies successions, e.g. indicating a waxing flow or a succession of different flows, can be recognized. Moreover, the relative orientation of sedimentary structures can give indications of relative paleoflow directions, which –after overcoming the problems of core orientation– allows reconstructing absolute paleoflow directions.

6.2 Setting

6.2.1 Geographical, geomorphological and geological setting

Aysén fjord (45.5°S) is one of the many fjords in the Chilean fjordland, which extends between Puerto Montt in the north and Cape Horn in the south. It is carved in the Andean Cordillera, which reaches altitudes of approximately 2000 m asl in this region.

The northern Patagonian fjordland is a tectonically active region. Not only is it located along the subduction zone that produced the largest earthquake ever instrumentally recorded (i.e. the 1960 Great Chilean earthquake), but it is also crossed from north to south by the Liquiñe-Ofqui Fault Zone (LOFZ). The LOFZ is a 1000 km long dextral strike-slip lineament, which has been accommodating the oblique subduction of the Nazca Plate underneath the South-American Plate since the mid-Miocene. The fault zone separates the north-moving (6.5 mm/y) Chiloé sliver (in the west) from the rest of the South-American Plate (in the east) (Cembrano et al., 2000; Wang et al., 2007; Melnick et al., 2009). In the study area, the LOFZ consists of two overlapping, NNE-striking, master faults, connected by a series of NE-striking, right lateral en echelon faults (Legrand et al., 2011).

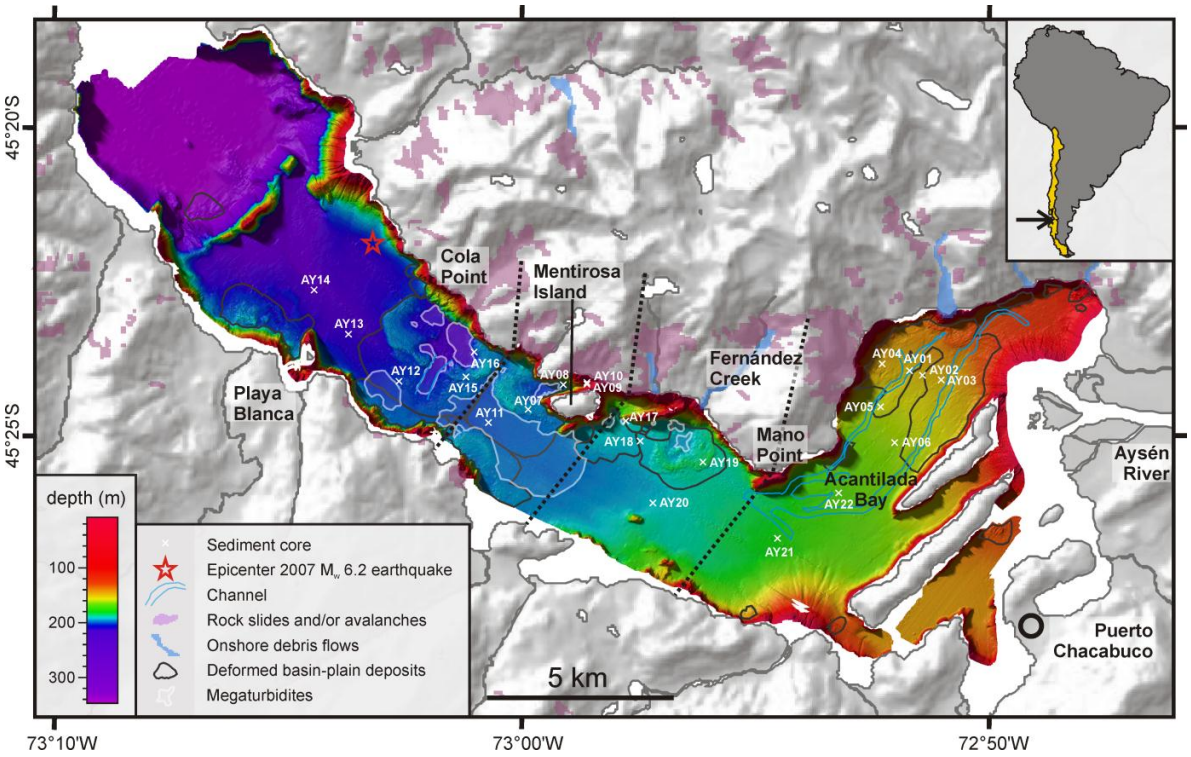

Fig. 6.1 *Setting of Aysén fjord with location in South America (Chile in yellow). Shaded relief map of the fjord surroundings with onshore debris flows, rock slides and avalanches (Sepúlveda et al., 2010) and used locations. Multibeam bathymetry map of the inner Aysén fjord with indication the 2007 epicenter, short sediment cores, channels, deformed basin-plain deposits and megaturbidites (Chapter 5).*

6.2.2 The 2007 earthquake, onshore landslides and offshore mass movements

During the first months of 2007 a seismic swarm with more than 7000 registered earthquakes affected the region around Aysén fjord. The series of seismic movements started on 22 January 2007 and reached a maximum on 21 April 2007 with an M_w 6.2 earthquake. The earthquake occurred at a depth of <9 km and had its epicenter in the fjord (Fig. 6.1). Intensities as high as VIII to IX on the Modified Mercalli scale were reported around the epicenter. In Puerto Chacabuco (at the eastern end of the fjord; Fig. 6.1) Modified Mercalli Intensities still reached VII (Naranjo et al., 2009; Sepulveda and Serey, 2009; Sepúlveda et al, 2010). Multiple debris flows, rock slides and avalanches were triggered along the fjord's flanks and coastline (Fig. 6.1), several of them causing tsunamis with wave heights of up to 6 m that inundated the fjord's shores and resulted in 7 casualties and 7 missing persons (Naranjo et al., 2009).

In Chapter 5 we showed how these onshore debris flows, rock slides and avalanches triggered submarine basin-plain deformation. The distribution and structure of these deformed basin-plain deposits are shown in Fig. 6.1 and 6.2, respectively. Characteristic for this basin-plain deformation is the presence of an inner depression, proximal to where the mass flows impacted on the basin plain, and more distal thrust belts, with a higher topography and an almost radial distribution. This basin-plain deformation, which affects large parts of the fjord's bottom, might have been even more important for tsunami generation than the impact of the onshore landslides itself. In Chapter 5, we also discussed how density flows developed when the mass flows reached the basin plain. These density flows travelled more distally than the basin-plain deformation and resulted in the deposition of sandy density-flow deposits beyond the thrust belts, as well as in megaturbidites in the proximal depressions (Fig. 6.1 and 6.2).

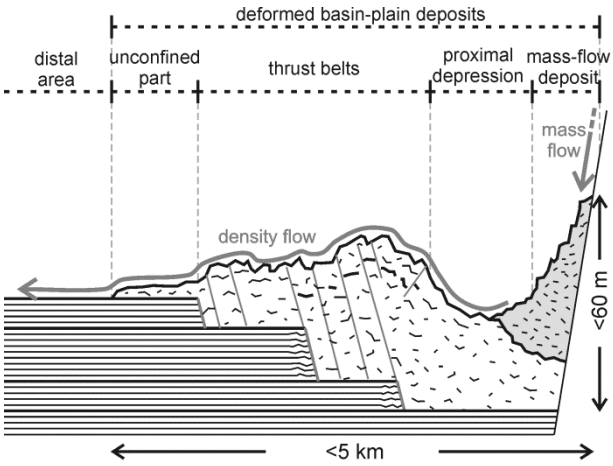

Fig. 6.2 *Schematic illustration of the structure of the mass-flow (gray) and deformed basin-plain (white) deposits triggered by the 2007 M_w 6.2 earthquake in Aysén fjord (after Van Daele et al., submitted). The flow path of the density flows originating from the mass flow during and after the basin-plain deformation is indicated with a gray arrow.*

6.3 Materials and methods

6.3.1 Multibeam bathymetry

The bathymetry of the inner fjord was mapped using a ELAC 'SeaBeam 1050' Multibeam sonar. More information about the data acquisition and processing is presented in Chapter 5.

6.3.2 Sediment cores

In order to ground-truth the sedimentary signature of the 2007 event, 22 short gravity cores were taken throughout the inner fjord region (Fig. 6.1). The cores were taken with a Swiss gravity corer and have a length ranging between 7 and 130 cm (Fig. 6.3). Photographs of the cores were processed by applying the Histogram equalization in the Corel PHOTO-PAINT software. This processing method allows visualizing minimal color changes, which facilitates core description and interpretation, but produces slightly unnatural colors.

On eight cores (i.e. AY07, AY11, AY13, AY14, AY16, AY18, AY19 and AY20) grain sizes were measured with a Malvern Mastersizer 2000 at a sampling interval of 1-5 mm, without pretreatment. Measuring time was 15 s after 60 s of 10 % sonification and re-measurements have been performed for quality control.

The medical X-ray CT scanner at the Ghent University Hospital (Siemens, SOMATOM Definition Flash) was used to scan ten of the sediment cores (i.e. AY01, AY06, AY07, AY11, AY13, AY14, AY16, AY18, AY19 and AY20). This technique allows discriminating between sediment volumes with a different X-ray attenuation, which is a function of the material composition (effective atomic number) and density (Cnudde et al., 2004). One half of each core was scanned, allowing us to examine the 3D structures in the sedimentary deposit. The scanner has been employed at 100 kV, with an effective mAs of 100 and a pitch of 0.55. The reconstructed images have a voxel size of 0.5 mm and a down-core step size of 0.3 mm. It is therefore possible to distinguish individual particles and aggregates of very coarse sand and gravel size. The data was visualized and analyzed with the VGStudio Max 2.0 software.

6.4 Results

6.4.1 Sedimentary facies

Nine clearly distinguishable sedimentary facies are present in the upper sedimentary infill of the inner Aysén fjord and compiled in Fig. 6.3. Above the bioturbated hemipelagic mud, which is present in the lower part of some cores and represents the normal (i.e. non-event) background sedimentation in the fjord, we observed i) slumped sediment, ii) mud-clast conglomerate, iii) sand to mud-clast layers, iv) massive sand, v) parallel lamination, vi) cross lamination, vii) convolute lamination and viii) homogenous mud. Several sedimentary facies are restricted to certain grain-size classes.

-Slumped sediment is characterized by a folded, faulted and/or mottled appearance; however, packages of undisturbed strata are common. Frequently, the original stratigraphy observed in the undisturbed cores can still be recognized in the slumps (Fig. 6.3).

-The mud-clast conglomerate consists of well-packed granular-gravel to pebble-size mud clasts in a medium to coarse sand matrix. The volumetric importance of the sandy matrix is not constant and sometimes very limited. The mud clasts at the top of these units sometimes show imbrication. The maximum total thickness that was encountered in the Aysén cores is 12 cm (Fig. 6.3 and 6.4).

-Sand to mud-clast layers are inversely graded layers with a thickness of 0.5-3 cm. The base consists of medium to coarse sand and the top of inversely graded mud clasts with a sandy matrix. The boundary between both sub-layers is usually sharp. Shell fragments and mud clasts are sometimes imbricated in these layers. The imbricated mud clasts occur throughout the mud-clast layers, but rows of imbricated mud clasts occur at the base of the sublayers (Fig. 6.3, 6.4, 6.5, 6.6 and 6.7).

-Massive sand consists of graded coarse to medium sand with no or very few internal structures. Only on the CT-scans some very faint parallel layering can be discerned (Fig. 6.3).

-Parallel lamination occurs in a wide range of grains-size classes: from coarse silt to medium sand. These millimeter-scale laminae are frequently very well observed with the CT-scans, but not, or to a very limited extent, visible to the naked eye or on the pictures (Fig. 6.3, 6.4, 6.5, 6.6, 6.7 and 6.8).

-Cross lamination in the Aysén-fjord sediment cores is only recognized in very fine to medium sands. The laminae within this cross lamination are also of millimeter scale. Occasionally fore- and backsets of climbing ripples were identified. Again, these structures can be better discerned on the CT-scan images (Fig. 6.3, 6.4, 6.5, 6.6, 6.7 and 6.8).

-Convolute lamination occurs in laminae with grain-size modes of very coarse silt to fine sand. The thickness of the laminae in which the convolution occurs, ranges from ~1 mm to almost 1 cm, and frequently, the laminae show a clear asymmetry in one direction. Convolute lamination is predominantly observed in packages of several laminae, but can also occur as a single lamina intercalated in a parallel- or cross-laminated bed. The laminae always consist of couplets with fine and/or light material (i.e. with low X-ray attenuation) at the base and coarse and/or heavy material (i.e. with high X-ray attenuation) above (Fig. 6.3, 6.4, 6.6 and 6.8).

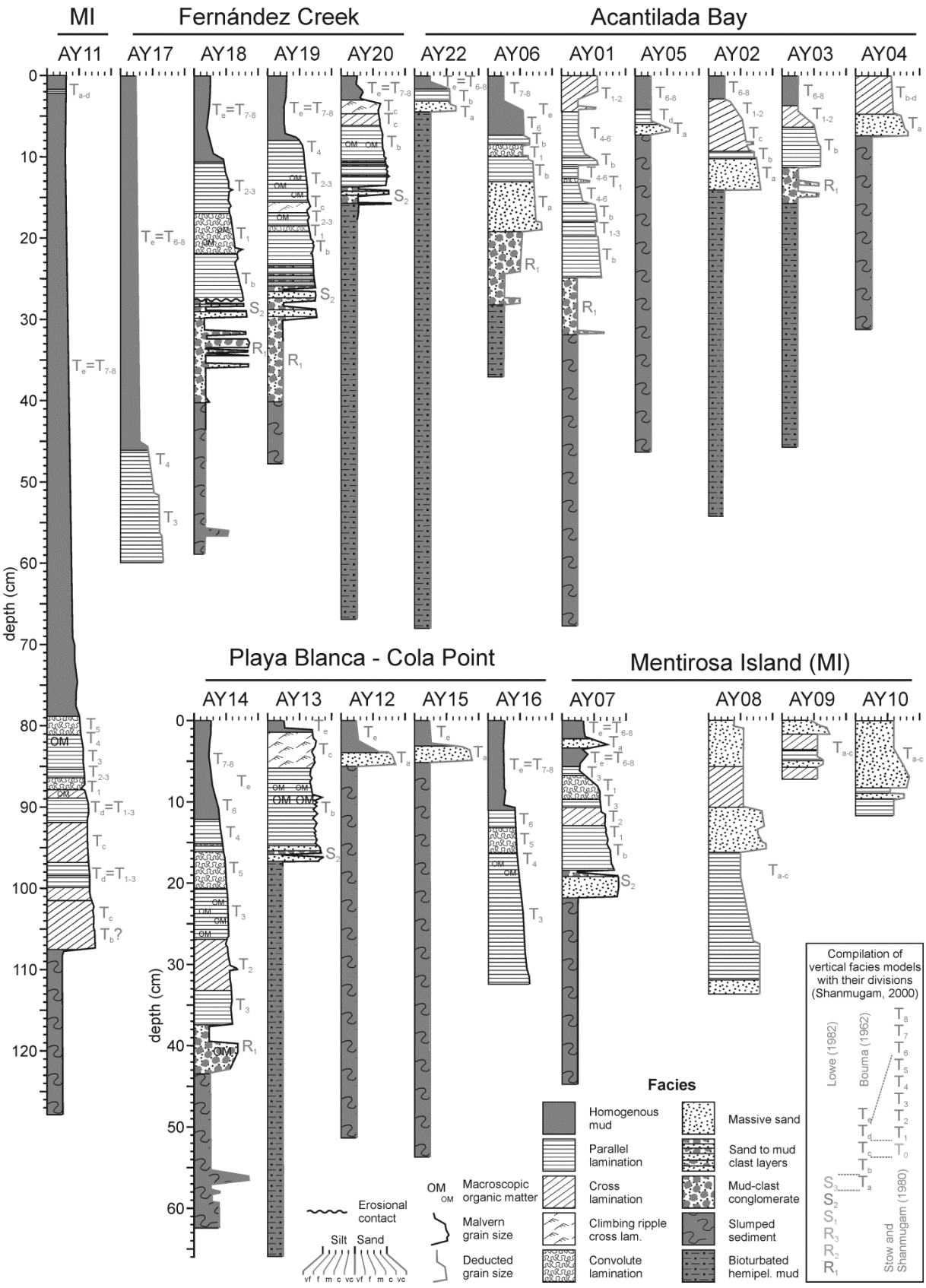

Fig. 6.3 *Lithologs of short sediment cores. Different sedimentary facies encountered in Aysén fjord and the assigned facies-model divisions (Bouma, 1962; Stow and Shanmugam, 1980; Lowe, 1982). Horizontal scale: grain size from silt to sand (vf = very fine, f = fine, m = medium, c = coarse and vc = very coarse).*

-Homogenous mud occurs at the top of almost every sediment core and has a composition which is very similar to the bioturbated hemipelagic mud. It consists of poorly sorted silts (>90 %) with minor amounts of clay and very fine sand (Fig. 6.3, 6.4, 6.5, 6.6, 6.7 and 6.8).

6.4.2 Core descriptions and sedimentary-facies successions

In the sediment cores, the above-defined sedimentary facies occur in different successions. The cores will be discussed below in four groups, depending on their location in the fjord: i) Acantilada Bay, ii) Fernández Creek, iii) Mentirosa Island and iv) Cola Point-Playa Blanca (Fig. 6.1).

The basal sedimentary facies of the cores are determined by their location in the fjord. Almost every core has bioturbated hemipelagic mud or slumped sediment at its base (except for AY08, AY09, AY10, AY16 and AY17; Fig. 6.3). The latter are mostly taken on top of the deformed basin-plain sediments mapped in Chapter 5, while the cores with hemipelagic mud at their base are taken on more distal locations (Fig. 6.1, 6.2 and 6.3). The top of the cores is mostly composed of a homogenous mud layer with a thickness that generally varies between 2 and 10 cm. Only the most proximal cores (i.e. AY04, AY08, AY09 and AY10) are not capped by this homogenous mud layer (Fig. 6.3). In between the basal slump or bioturbated hemipelagic sediments and the homogenous mud on top, all cores present a succession of the above described silty to sandy facies (Fig. 6.3).

Acantilada Bay

In Acantilada Bay, seven cores (AY01 to 06 and AY21 to 22) were taken in a range from proximal to more distal locations (Fig. 6.1). The most proximal core, AY04, was taken close to where onshore landslides propagated into the fjord and presents graded massive and laminated sands (Fig. 6.3). Cores AY02, AY03 and AY05 were taken on or adjacent to the deformed basin-plain deposits that cover a large part of Acantilada Bay (Fig. 6.1). They contain a succession of massive sand or mud-clast conglomerate, parallel- and cross-laminated sands and coarse silts (Fig. 6.3). In AY05, the most distal of these cores, this unit is clearly thinnest (7 cm) and mostly fine grained. Core AY01 was taken at the junction of 2 channels and contains a slumped deposit, in which an s-fold was observed. It is capped by a mud-clast conglomerate, overlain by mainly parallel laminated sands and silts. The latter can be subdivided in four graded sub-units, of which the lower two are both coarsest and thickest; and the third from below is erosional. AY06, taken more distally, comprises a succession of mud-clast conglomerate, massive coarse sand, massive to laminated sands, asymmetrically convoluted coarse silt laminae and more laminated sand. The even more distally located AY22 is thinner (5 cm) and presents massive and laminated sands (Fig. 6.3). AY21 is taken south of where the Acantilada Bay channels merge at Mano Point (Fig. 6.1). This core has a layer with macroscopic organic material covered by a thin (2 cm) disturbed sand layer on one side of the core.

Fernández Creek

Four cores were taken in the area where the Fernández-Creek onshore debris flow propagated into the fjord and deformed the basin plain (Fig. 6.1). AY18 and AY19 were both taken on the thrust belt of the deformed basin plain (Fig. 6.2) and have a similar succession of sedimentary facies: mud-clast conglomerate, sand to mud-clast layers with imbricated mud clasts, parallel laminated medium to fine sands, locally asymmetric convolute lamination and parallel laminated fine sands to very coarse silts (Fig. 6.4). In general AY19 is coarser grained than AY18 and in the upper laminated part, AY19

has an intercalated layer of climbing ripples, composed of fine sands with a high X-ray attenuation. In AY18, the lower parallel laminated part is erosional and the sediments above are strongly deformed in one side of the core (Fig. 6.3 and 6.4).

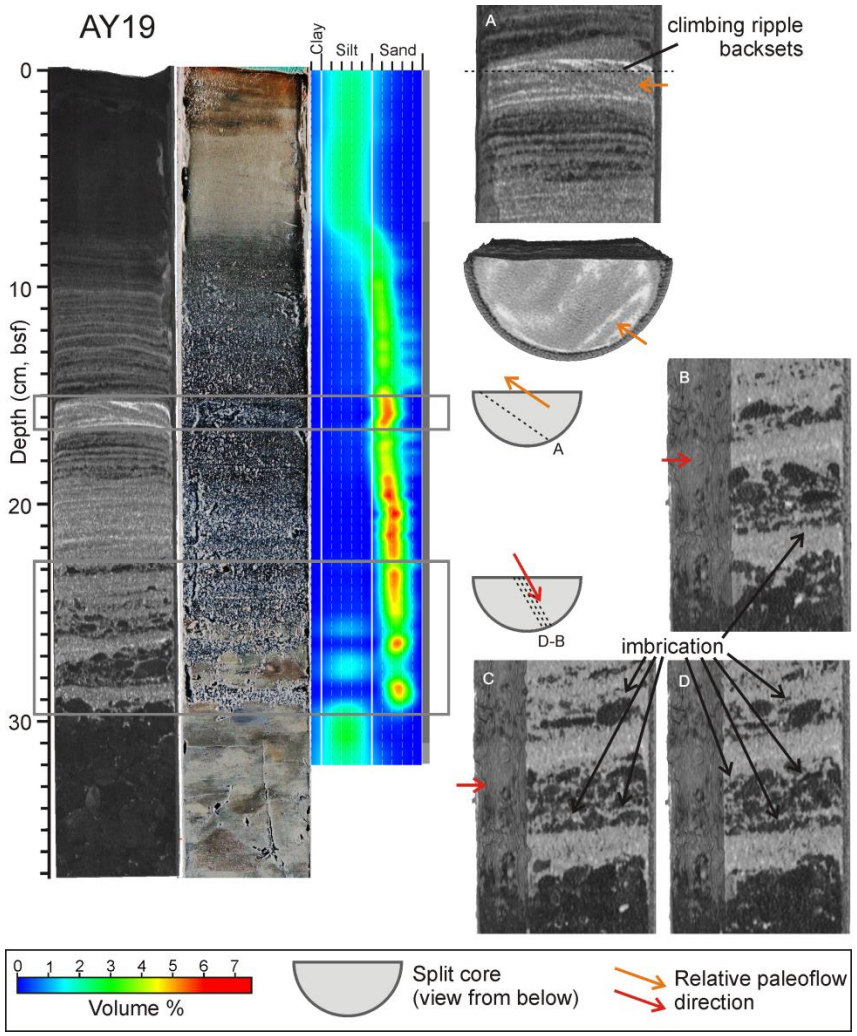

Fig. 6.4 *Top of sediment core AY19. Basal flow direction (from Fernández Creek) is determined by the imbrication of mud clasts in sand-mud clast layers (traction carpets). In a layer with high X-ray attenuation, the backsets of climbing ripples indicate a nearly opposite flow direction (from Acantilada Bay). Frontal X-ray CT view and processed photographs (histogram equalization). Grain-size distributions (silt and sand subdivisions: see Fig. 5.3; sampling resolution: dark-gray bar: 2 mm, medium-gray bar: 5 mm). A-D: schematic and CT split-core cross-sections with indication of climbing ripples, imbrication and derived relative paleoflow direction (arrow).*

The distally taken core AY20 (Fig. 6.5) is composed of mud-clast conglomerate with imbricated mud clasts, sand to mud-clast layers and parallel- covered by wavy cross-laminated fine sands. The upper part of the cross laminae is composed of fine to very fine sands with a high X-ray attenuation and forming climbing ripples (Fig. 6.2 and 6.5).

AY17 was taken in a small depression delimited by a submarine ridge and several deformed basin-plain deposits (Fig. 6.1). This core consists of graded, parallel laminated sands to coarse silts with 45 cm of homogenous mud on top (Fig. 6.3).

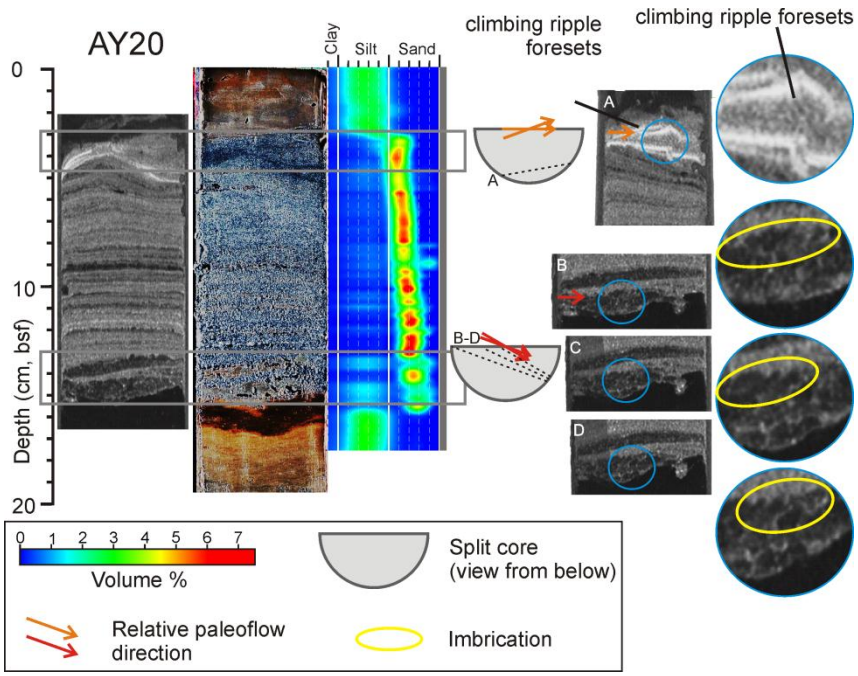

Fig. 6.5 *Top of sediment core AY20. Basal flow direction (from Fernández Creek) is determined by the imbrication of mud clasts in a mud-clast conglomerate. In a layer with high X-ray attenuation (similar to the one in AY19; Fig. 5.4) near the top of the deposit, the foresets of climbing ripples indicate a different flow direction (from Acantilada Bay). Frontal X-ray CT view and processed photographs (histogram equalization). Grain-size distributions (silt and sand subdivisions: see Fig. 5.3; sampling resolution: dark-gray bar: 2 mm). A-D: schematic and CT split-core cross-sections with indication of climbing ripples, imbrication and derived relative paleoflow direction (arrow).*

Mentirosa Island

North and west of Mentirosa Island, five cores were taken on the mass-flow deposit and deformed basin-plain deposit north and west of Mentirosa Island (Fig. 6.1 and 6.2). Three cores were taken on a proximal location (i.e. AY08, AY09 and AY10), on or adjacent to the basin slope, and consist of pure sandy facies, with successions of massive, parallel laminated and cross laminated sands (Fig. 6.3). The base of the core liner of core AY09 was damaged, probably due to impact with gravel during coring.

AY07 was taken on the thrust belt of the deformed basin-plain deposit (Fig. 6.1 and 6.2) and presents a succession of one shell-rich sand to mud-clast layer, followed by a succession of medium to very fine sandy parallel, cross, parallel and convolute lamination (Fig. 6.6). The convolute lamination consists of three laminae of which the first is thickest and the second clearly erosional. Moreover, the asymmetry in the middle lamina is opposite compared to the lower and the upper one and perpendicular to the dip of the imbricated mud clasts in the mud-clast layer (Fig. 6.3 and 6.6).

AY11 is the longest core (130 cm) and was taken in a depression delimited by several deformed basin-plain deposits and is located on top of the most distal unconfined part of the deformed basin-plain deposit west of Mentirosa Island (Fig. 6.1 and 6.2). This core consists of graded sands to coarse silts, with several successions of cross, parallel and/or convolute lamination, and finally ~80 cm of homogenous mud (Fig. 6.3). In the upper part of the homogenous mud, a 9 cm thick, mainly at the base sharply delimited, darker sub-unit can be distinguished, and 2 cm below the top a sand lamina is intercalated (Fig. 6.3).

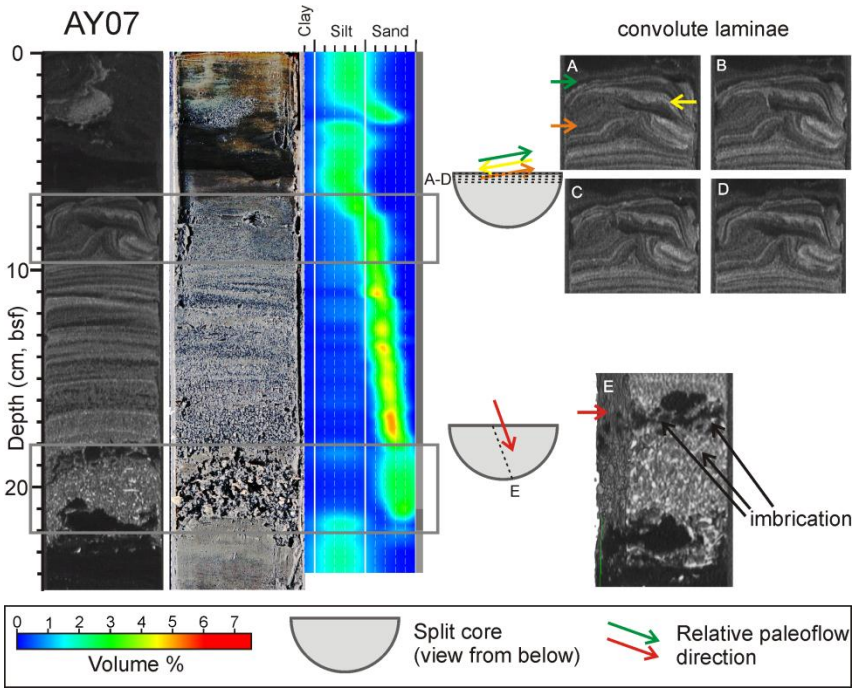

Fig. 6.6 *Top of sediment core AY07. Basal flow direction (from north of Mentirosa Island) is determined by the imbrication of mud clasts in sand-mud clast layers (traction carpets). Three laminae with asymmetric convolutions towards the top of the deposit indicate fluctuating flow directions perpendicular to the basal flow direction (from outer, inner and outer fjord) and suggest a seiche movement. Frontal X-ray CT view and processed photographs (histogram equalization). Grain-size distributions (silt and sand subdivisions: see Fig. 5.3; sampling resolution: dark-gray bar: 2 mm, medium-gray bar: 5 mm). A-D: schematic and CT split-core cross-sections with indication of asymmetric convolute lamination, imbrication and derived relative paleoflow direction (arrow).*

Cola Point – Playa Blanca

Five cores were retrieved south and west of Cola Point, three on the deformed basin plain and two on a more distal, western location (Fig. 6.1 and 6.2). AY16 was taken on the edge between the inner depression and the thrust belts (Fig. 6.2). The core consists of parallel laminated, graded fine sands to coarse silts with some asymmetric convolute laminae (Fig. 6.3).

Cores AY12 and AY15 were taken in the thrust belts of the deformed basin-plain deposits. These cores both consist almost entirely of slumped sediment covered by a graded massive-sand layer and a homogenous-mud layer (Fig. 6.2 and 6.3).

AY13 was taken on a distal location, west of where most basin-main deformation occurs. It comprises a succession of one sand to mud-clast layer and parallel to cross-laminated coarse to fine sands (Fig. 6.7). In the parallel laminated part, some small grain-size fluctuations occur, among which one layer of mud and macroscopic organic matter and one inversely graded layer. In the cross-laminated part, at least three cycles of climbing ripples with clear foresets and fluctuating grain-size mode occur (Fig. 6.3 and 6.7).

AY14, located north of Playa Blanca, is composed of a mud-clast conglomerate and parallel to cross laminated very fine sands (Fig. 6.8). Within the parallel lamination, two laminae with asymmetric convolute lamination occur; within the cross laminae, one lamina with medium sand is intercalated. Above this, parallel laminated very fine sand to very coarse silt is present. These are covered by graded, asymmetrically convolute and parallel laminated, very coarse silts (Fig. 6.3 and 6.8).

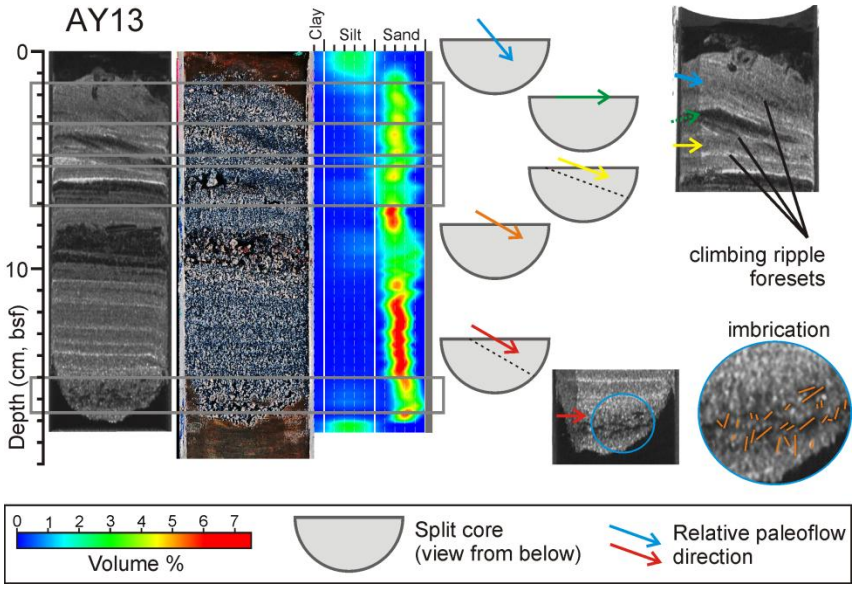

Fig. 6.7 *Top of sediment core AY13. Reconstructed paleoflows (reconstructed with imbricated mud clasts and climbing ripple foresets) have a similar direction throughout the deposit, indicating that separate paleoflows were merging in this part of the fjord. Frontal X-ray CT view and processed photographs (histogram equalization). Grain-size distributions (silt and sand subdivisions: see Fig. 5.3; sampling resolution: dark-gray bar: 2 mm). Schematic and CT split-core cross-sections with indication of climbing ripples, imbrication and derived relative paleoflow direction (arrow).*

6.5 Discussion

6.5.1 Density-flow deposits

Apart from the bioturbated hemipelagic mud, all the observed sedimentary facies are related to the deposits affected by the basin-plain deformation or to density flows. Since no cores have bioturbated hemipelagic mud at their top, we interpret all other sedimentary facies to have been deposited during events that were triggered by the 2007 M_w 6.2 earthquake. The slumped sediments correspond to the upper part of the deformed basin-plain deposits. The other sedimentary facies are deposited by density flows and can –based on the criteria of Mulder and Alexander (2001)– be subdivided into hyperconcentrated and concentrated density-flow deposits, and turbidites. We link the observed sedimentary facies to facies and divisions recognized by Bouma (1962), Stow and Shanmugam (1980) and Lowe (1982), which are based on changes in both grain size and internal structures. These divisions were compiled by Shanmugam (2000) into a classification model with 16 subdivisions (Fig. 6.3). We use nomenclature proposed by Mulder and Alexander (2001) for different types of density flows and their deposits: i) hyperconcentrated density flows, ii) concentrated density flows and iii) turbidity flows.

The mud-clast conglomerates that constitute the basal part of many density-flow deposits were deposited under conditions of a hyperconcentrated density flow (i.e. in which matrix support is the dominant particle support mechanism; Mulder and Alexander, 2001). The mud-clast conglomerates correspond to the basal R1 division of Lowe (1982) (Fig. 6.3).

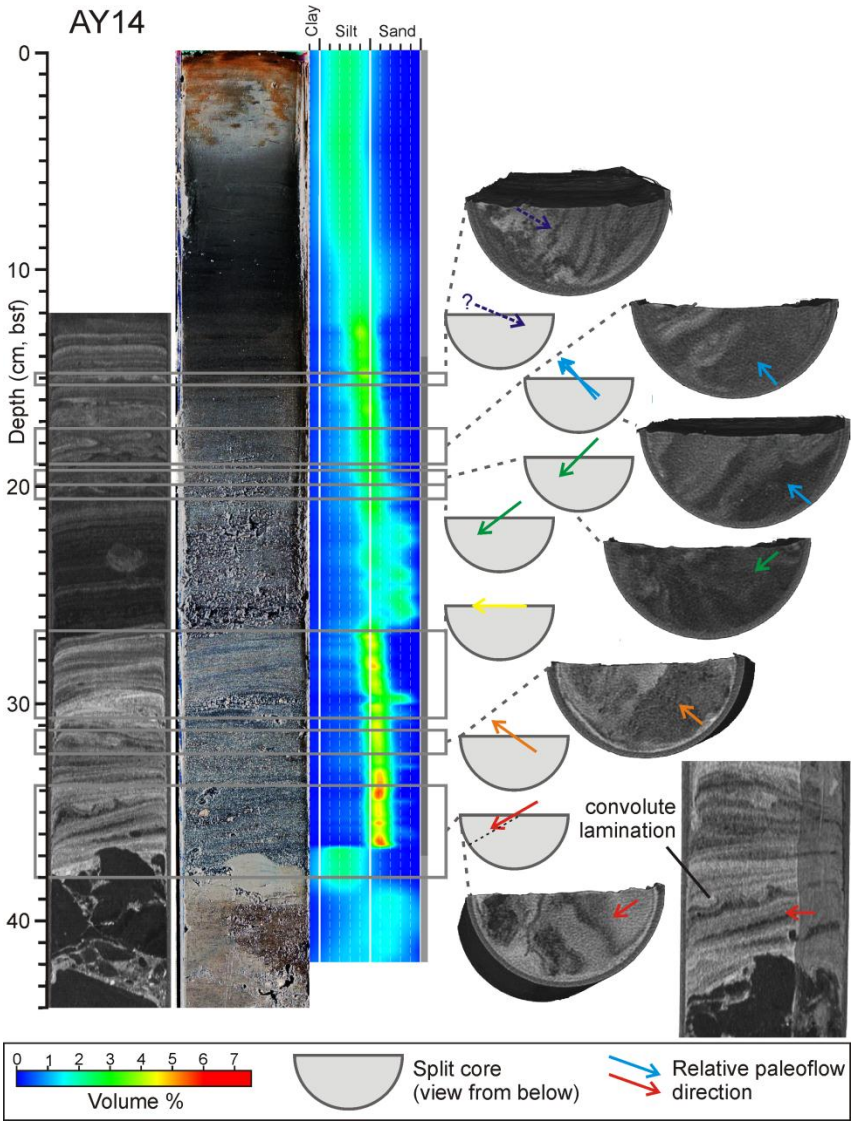

Fig. 6.8 *Top of sediment core AY14. Basal flow direction (from off Playa Blanca) is determined by the mud-clasts morphology basal asymmetric convolutions. Subsequent paleoflow directions (reconstructed with cross laminations and asymmetric convolutions) are fluctuating between Playa Blanca and the inner fjord, and finally the outer fjord, indicating a possible seiche effect. Frontal X-ray CT view and processed photographs (histogram equalization). Grain-size distributions (silt and sand subdivisions: see Fig. 5.3; sampling resolution: dark-gray bar: 2 mm, medium-gray bar: 5 mm). Schematic and CT split-core cross-sections with indication of climbing ripples, imbrication and derived relative paleoflow direction (arrow).*

The sand to mud-clast layers and massive sands are concentrated density-flow deposits (Mulder and Alexander, 2001). The sand to mud-clast layers are interpreted as traction carpets such as the S2 facies of Lowe (1982). The formation of these traction carpets is facilitated by the low density of the rip-up mud clasts, which makes floating easier. The imbricated mud clasts at the base of the mud-clast laminae are aligned in similar fashion as the outsized floating clasts of Postma et al. (1988). The massive graded sands correspond to the Ta division of Bouma (1962) (Fig. 6.3).

Parallel lamination, cross lamination, convolute lamination and homogenous mud are deposited by turbidity currents. Pure sandy parallel and cross lamination is interpreted as the Tb and Tc Bouma divisions. Very coarse silty to very fine sandy parallel, cross and convolute lamination is assigned to the T1-T5 divisions of Stow and Shanmugam (1980). The homogenous mud corresponds to their T6-T8 divisions, or the homogenous part of the Bouma Te division (Fig. 6.3).

In the Aysén cores, different sedimentary facies successions occur, some of them inverse with respect to the typical succession depicted in the classification model compiled by Shanmugam (2000). These inversions can either indicate intensification or waxing of the flow, or the arrival of a second flow at the same location. In the latter case, these deposits can be regarded as amalgamated density-flow deposits, similar to the amalgamated turbidites with several stacked pulses described by Nakajima and Kanai (2000) and Goldfinger et al. (2007). However, when the density flows originate from different sources, than the relative paleoflow directions stored in the deposits are very likely to be different for the sub-deposits. Hence, determining flow directions can help to differentiate between waxing-density-flow and amalgamated density-flow deposits.

6.5.2 Flow-direction indicators

Several sedimentary structures within the different sedimentary facies can provide an indication of the relative flow orientation (e.g., left to right = right to left) or direction (e.g., left to right) under which this structure was formed. The four structures we used to estimate orientation or direction of flow are i) folds (in slumps), ii) imbricated grains or clasts, iii) cross-laminae (strike, back- or foresets), and iv) convolution asymmetry (Fig. 6.9).

-Vergence of folds in slumped sediment is used to determine paleoflow direction and hence, the origin of the slump. Alsop and Marco (2011) show that folds in slumps verge in the direction of flow. Only in AY01 an s-fold could be used to determine the relative paleoflow direction (Fig. 6.9).

-Imbricated clasts can be used to determine paleoflow direction during deposition (Krumbein, 1939; Rust, 1972; Postma et al., 1988). The mud-clasts dip towards the stoss side (Fig. 6.9).

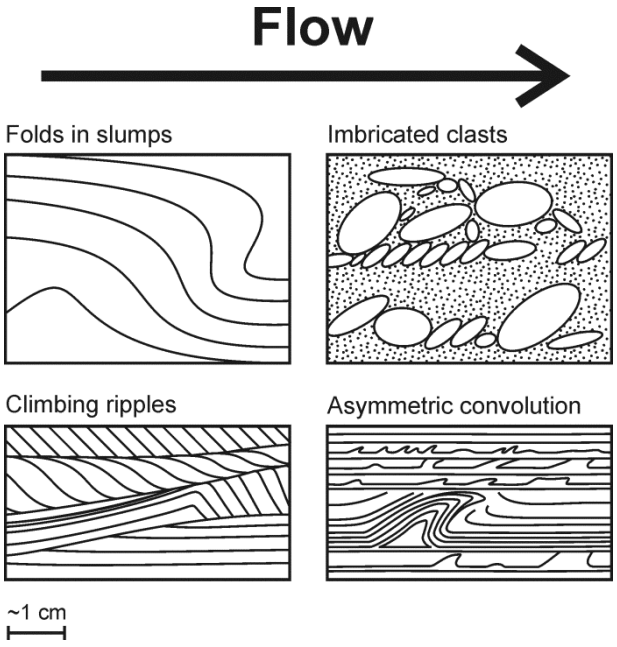

Fig. 6.9 *Schematic illustration of flow direction indicators: folds in slumps, imbricated clasts, climbing ripples and asymmetric convolution.*

-Cross lamination can be used to determine flow orientation and occasionally also direction. Due to the mostly low angles and the small diameter of the cores, it is not always possible to determine the type of ripple forming the cross laminae. The dominant strike of the laminae, however, gives an indication of the flow orientation. In some cores, fore- and backsets of climbing ripples were recognized, which allows identifying flow direction during deposition (Fig. 6.9).

-Many of the convolute laminae show a clear asymmetry in one direction. McClelland et al. (2011) found similar asymmetric convolution and show that due to current shear, the overturned side of the fold corresponds to the lee side of the paleoflow (Fig. 6.9). Hence, we can use the asymmetry of the convolution to determine paleoflow direction.

6.5.3 Core orientation

Eight sediment cores were oriented relative to the location of the nearest mass-movement (originating on- or offshore) using the relative flow direction reconstructed for the basal part of the density-flow deposit (or relative basal flow direction). For cores that are located on top of a deformed basin-plain deposit, the primary paleoflow direction (i.e. the flow direction of the density flow that arrives first on this location) is assumed to be parallel to the propagation of the basin-plain deformation. Likewise, for the more distal cores, the primary paleoflow direction is assumed to be the distal continuation of the deformed basin-plain deposit's propagation. The cores were oriented by aligning the relative basal flow directions in the core with the assumed primary paleoflow directions. The relative basal flow direction has been determined using flow-direction indicators in hyperconcentrated and concentrated density-flow deposits (i.e. folds in slumps and imbrication in mud-clast conglomerates or traction carpets; Fig. 6.4, 6.5, 6.6, 6.7 and 6.8). Only in AY14 the relative basal flow direction is determined by a combination of mud-clast morphology (forming a kind of sole structure) and asymmetry in convolute lamination in the basal part of the turbidite (Fig. 6.8). In two cores (i.e. AY06 and AY16) an orientation was hypothesized based on the most basally determined relative flow direction, which does not necessarily correspond to the basal flow direction.

6.5.4 Flow successions

Stacked and intercalated density-flow deposits

In oriented cores, the relative changes in paleoflow direction between different facies units can give an indication of the source area. In certain locations in the fjord density flows will merge, but each individual flow may still leave a distinct sedimentary imprint, resulting in amalgamated density-flow deposits.

At the junction of two channels in the north of Acantilada Bay (AY01), at least four inverse flow successions occur, showing that density flows originating at different locations in the bay flowed through these channels (Fig. 6.10). However, distally (in AY22) only one flow sequence is preserved, suggesting that the different flows homogenized into a single flow, similar to the merging coarse pulses offshore the Northern San Andreas Fault (Goldfinger et al., 2007; Fig. 6.10). The absence of a clear density-flow deposit in AY21 indicates that the density flow is indeed channelized and passes just south of Mano Point. A deposit of this density flow is also preserved in cores AY19 and AY20. A layer with climbing ripples and a high X-ray attenuation appears to be deposited by a flow coming from Mano Point (Fig. 6.4, 6.6 and 6.10), while the basal flows originate at Fernández Creek (Fig. 6.1 and 6.10). Finally, we hypothesize that the layer with a similar dark gray color in the upper part of the homogenous facies of AY11 is a distal deposit of the Acantilada Bay density flows (Fig. 6.3).

On the location of AY13, imbricated mud clasts and climbing ripples show that all flows are coming from a similar direction: i.e. the inner fjord (Fig. 6.7 and 6.10). More towards the northwest (AY14), the deposits of these flows (containing ripples and asymmetric convolutions in the T3 facies) overlay

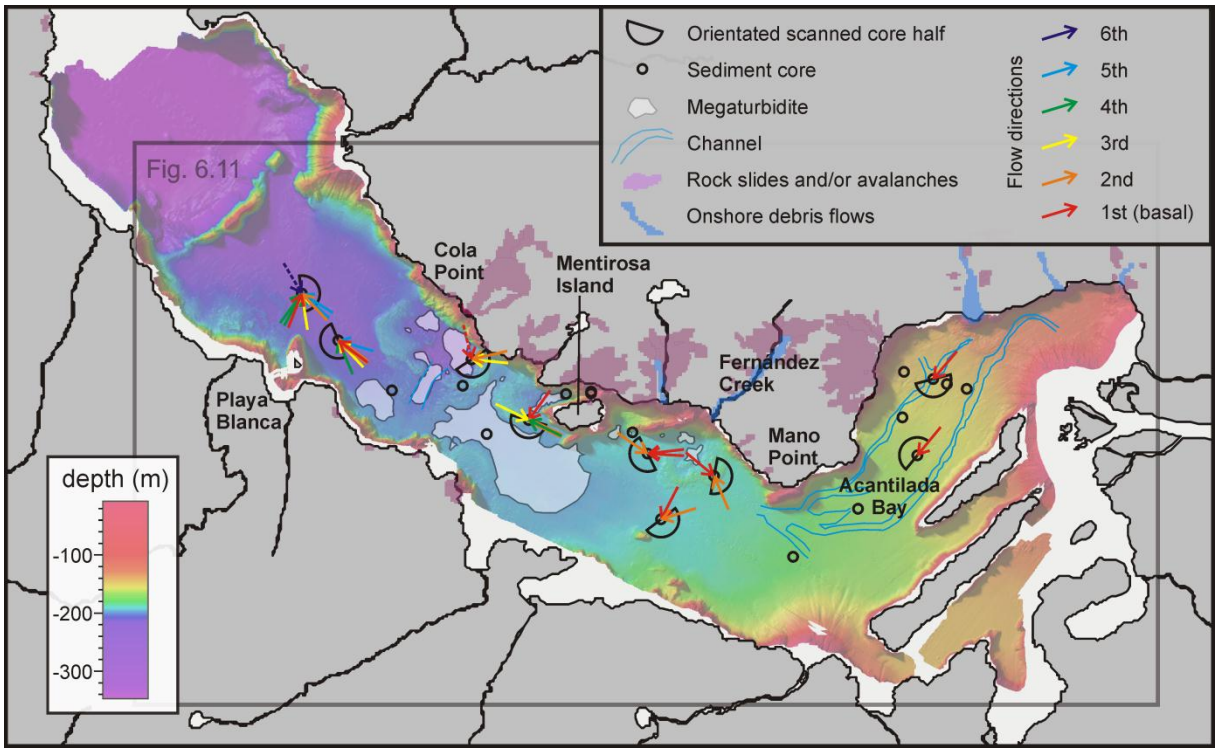

Fig. 6.10 *Multibeam bathymetry map of the inner Aysén fjord with oriented cores and paleoflow directions (red to blue arrow = basal to upper flow direction; same colors as in Fig. 5.4 to 5.8; a dashed red arrow indicates that, in absence of the base of the deposit, this is the assumed basal flow direction). Onshore debris flows, rock slides and avalanches propagating into the fjord (Sepúlveda et al., 2010). Megaturbidites and submarine channels were mapped in Chapter 5. Location = Fig. 5.1.*

a mud-clast conglomerate that is deposited by a hyperconcentrated density-flow originating offshore Playa Blanca (Fig. 6.7 and 6.10).

Travel paths and width of density flows are strongly influenced by the topography of the seafloor in the fjord. The density-flow deposits on top of the Cola Point deformed basin-plain deposits (AY12 and AY15) are thinner compared to the better developed density-flow sequences on top of the deformed basin-plain deposits west of Mentirosa Island and southwest of Fernández Creek (AY07, AY18 and AY19; Fig. 6.1 and 6.3). This discrepancy can be explained by two reasons: i) the larger height difference between the inner depression and the thrust belt, and ii) the breakthrough channelizing the density flow at Cola Point. These two features, however, can be attributed to one cause, namely the higher energy of the mass-flow traveling down the fjord slopes.

-The impact of the mass flow with the basin-plain sediments will result in a higher energy transfer, creating the larger vertical offsets within the basin-plain deformation (Chapter 5).

-The energetic mass flow will transform in a powerful, directional density-flow that is able to incise the thrust belts. This is consistent with the results of Alexander et al. (2008), who found that a higher slope gradient results in an increased forward momentum of the basin-plain flow. Indeed, the gradients of the slope along which the Cola Point mass flows travelled down are steeper (18-20°) than for all the other mass flows (10-16°) resulting from onshore landslides. Moreover, they are channelized in a straight channel, without any interruptions, which is not the case for any of the other mass-flows.

Also in Acantilada Bay, where the density flows are channelized, there is a clear difference in thickness of the deposit between on top of the deformed basin-plain deposits or in the channels.

Megaturbidites

Megaturbidites fill the depressions created by the deformed basin-plain deposits. AY11, AY16 and AY17 clearly show that both proximal inner depressions and more distal depressions delimited by deformed basin-plain deposits are all partly filled with ponding megaturbidites, which are characterized by a very thick upper division of the sequence: the homogenous mud (T_e or T_{7-8}) (Bouma, 1987; Fig. 6.1 and 6.3).

Seiche

In at least two cores, evidence for a seiche was found. The imbrication in the basal sand to mud-clast layer in AY07 allows orientating this core (Fig. 6.6), based on a basal flow originating where the Mentirosa Island onshore rock avalanche entered the fjord (Fig. 6.10). The resulting flow directions during deposition of the convolute laminae are parallel to the fjord's elongation and correspond to alternating flows coming from the inner and outer fjord. The occurrence of this alternating flow direction near the top of the turbidite is interpreted as the result of a seiche. Also in AY14, the upper unclear asymmetric convolute lamina appears to indicate a flow coming from the outer fjord (Fig. 6.8 and 6.10), suggesting a possible seiche effect.

6.5.5 Reconstruction of the 2007 density flows

The identification of different density-flow successions with changing paleoflow directions allowed reconstructing the 2007 density-flow pathways (Fig. 6.11). Flows originating at the 12 principal on- or offshore originating mass-movements were reconstructed based on paleoflow evidence from the sediment cores and basin-floor morphology. Relative flow velocities were tentatively adapted depending on the basin floor slopes (i.e. 0.2-1.0° in Acantilada Bay, 0.01-0.3° on the basin plain towards the west and up to 12° on the deformed basin-plain deposits), with higher relative flow velocities on the faster descending slopes (Keevil et al., 2007, Migeon et al., 2010). Fig. 6.11C and D show how the Acantilada-Bay flows are channelized south of Mano Point, to then travel further downslope until the depression between Aguas Calientes and Mentirosa Island (Fig. 6.11F), where the main megaturbidite deposited after many density flows reached this depression (Fig. 6.11A to E). Fig. 6.11C and D depict how several density flows merge around AY13, from where they propagate towards the northwest. Also the seiche effect, resulting from the first flows that reach the Cuervo Ridge, is illustrated in Fig. 6.11E and F.

6.5.6 CT-scanning in sedimentology

Our data illustrate that the use of X-ray computed tomography can be a very powerful tool in marine and lacustrine sedimentology. Due to the punctual sampling in coring or drilling, it is –compared to onshore sedimentary outcrops– often complicated to describe and interpret sedimentary structures in sediment cores. By using the CT-scans we were able to determine the sedimentary facies very accurately and to determine direction or orientation of sedimentary structures in a 3D space. The combination of these two advantages led to a detailed deciphering of the complex density-flow deposits and a reconstruction of the 2007 density flows. Hereafter we summarize the advantages of the use of CT-scanning in marine and lacustrine sedimentology.

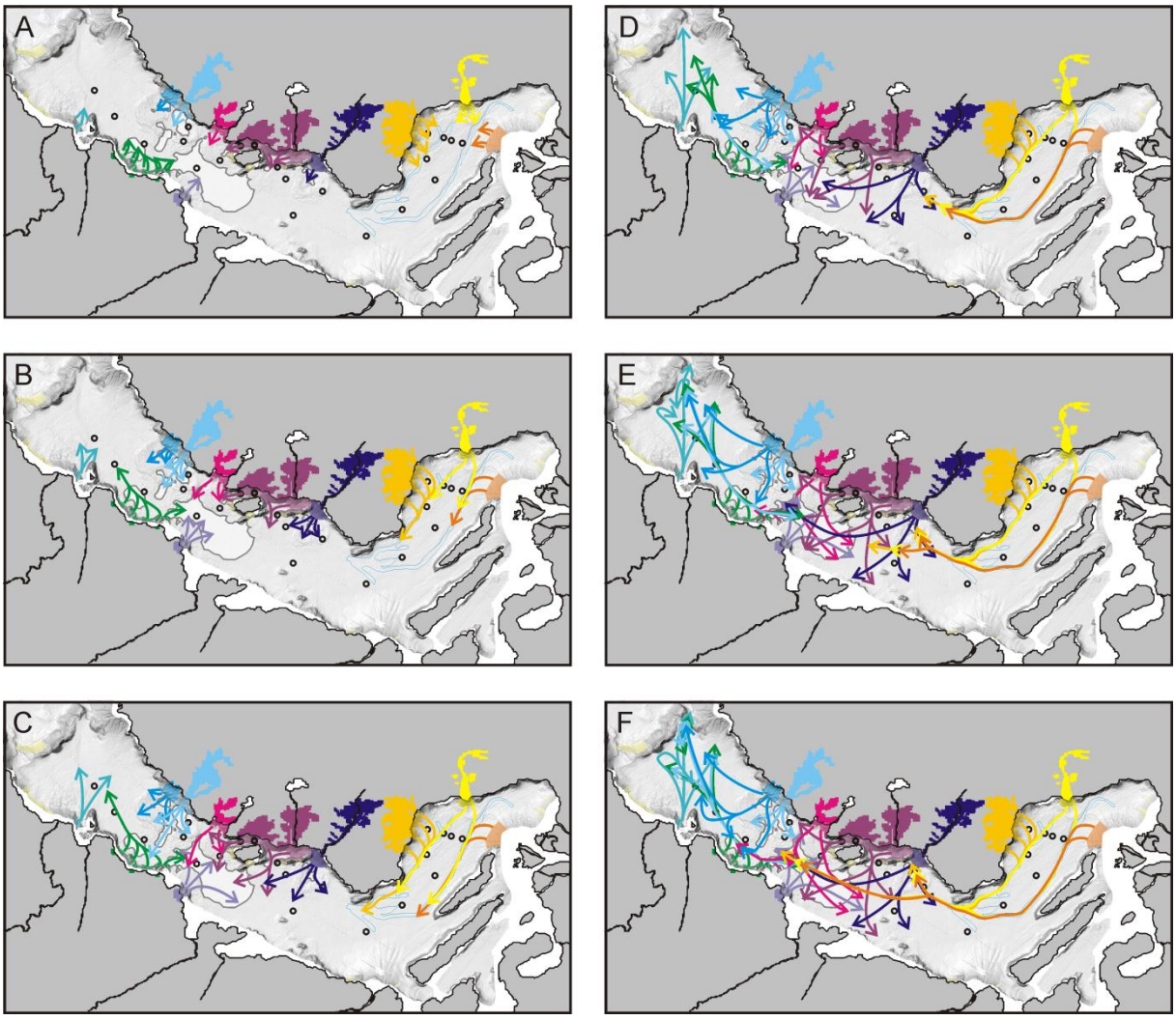

Fig. 6.11 *Conceptual reconstruction of the 2007 density flows in Aysén fjord. Figures A to F represent arbitrary time slices after the 2007 earthquake and the triggered on- or offshore landslides. Color-coded lines with arrow represent the principal density-flow pathways originating from the respective landslides (in the same color). Location: see Fig. 5.10.*

X-ray attenuation and 3D visualization

The changes in X-ray attenuation proved to be the best way to visualize changes in the sediment composition in all the Aysén cores. X-ray attenuation can also be visualized with radiographs. However, small millimeter-scale structures, such as very thin convolute laminae are perfectly visualized by X-ray CT scans, while these are not easily recognizable on radiographs, as also admitted by Stow and Shanmugam (1980). The convolute-like structures of Migeon et al. (2010) are clear on the radiographs and seem to be occurring –similarly as in Aysén fjord– in one direction and even appear to be asymmetric. On perpendicularly taken radiographs, however, it would be much harder to identify these structures. X-ray CT scans allow deciphering the sedimentary structures in a 3D space. This not only facilitates recognizing structures such as convolute lamination, erosional features, back-and foresets of climbing ripples, but also allows determining dips and relative strike of sedimentary structures.

The grain size of mud clasts

Our data show the presence of mud clasts in some of the identified sedimentary facies. Grain-size analyses using conventional methods (i.e., based on laser diffraction, the Coulter Principle (Coulter counter) or Stokes' Law (SediGraph) would classify these sedimentary facies as consisting of very fine-grained sediment, while the size of clasts themselves would not be revealed. Shanmugam and Moiola (1995) and Migeon et al. (2001), among others, already recognized mud clasts in density-flow deposits and Mulder et al. (2001) acknowledged that care should be taken when interpreting results of conventional grain-sizing methods. Indeed, mud clasts should be regarded as very coarse grains, rather than fine or clay-size particles. This mistake can easily lead to wrong observation of the grading within laminae or layers, causing flawed interpretations. The interpretation of grading in density-flow deposits has led to discussion in the past (Mulder et al., 2001, 2002; Shanmugam, 2002), showing that a correct observation is crucial for a correct interpretation of the depositional conditions of these laminae. For example, mud clasts will float easily in the traction carpets, making their identification crucial for the correct interpretation.

Implications for subaquatic paleoseismology

Nakajima and Kanai (2000) inferred that amalgamated turbidites (here discussed as amalgamated density-flow deposits) result from multiple or line sources and thereby conclude that they have a seismic origin. Studying such amalgamated density-flow deposits using X-ray CT-scans has three major advantages:

i) it becomes possible to differentiate between the sudden arrival of a second flow (typical for seismic triggering) and a gradually waxing flow (typical for flood turbidites; Goldfinger et al., 2012);

ii) it is possible to more accurately detect inverse successions and therefore differentiate between sub-deposits even when these have similar grain-size characteristics; and

iii) by determining paleoflow direction, it is possible to show that there are different source areas, even when these have a similar mineralogy or geochemistry, such as in Aysén fjord.

The multidirectional, amalgamated density-flow deposits that we analyzed in this study are therefore not just formed by pulses of a flow, but rather by the merging of several density flows from a different source. Such multidirectional deposits can only be recognized by using X-ray CT-scans and might be more common than generally assumed.

Multidirectional, amalgamated density-flow deposits are mainly expected to occur in enclosed basins such as fjords and lakes. However, also along continental margins, at the confluence of submarine channels, X-ray CT-scans could potentially support the 'confluence test' for simultaneous triggering, developed by Adams (1990) and successfully applied by e.g. Goldfinger et al. (2007; 2012). On a strategic location at the confluence of two channels, the determination of flow directions could help to unravel the order of density-flow arrival from the different channels. A more accurate determination of these flow successions could also shed light on the controversial interpretation of turbidites as paleoseismograms by Goldfinger et al. (2012). Finally, if an oriented core can be sampled, or the core can be oriented subsequently by paleomagnetic properties, the absolute flow direction can be determined. This information can then be used to determine source areas or channels, and, when combined with recurrence information, improve hazard assessments.

6.6 Conclusions

This study provides new insights in the formation of multidirectional, amalgamated density-flow deposits and demonstrates that X-ray CT scans can be crucial for a correct interpretation of sedimentary structures:

-Traction carpets are identified at the base of several density-flow deposits. Mud clasts are regarded as the coarsest grains and can float easier towards the top of the traction carpets due to their lower density than the sand grains.

-Folds, imbrication of clasts, ripples and convolute lamination can be used to determine relative flow directions and changes herein during deposition of the density-flow deposits. X-ray CT scans are essential for identifying these sedimentary structures and their orientation in full 3D space.

-Simultaneously triggered density flows with different source areas can produce deposits that are stacked or intercalated between each other, forming amalgamated density-flow deposits.

-It is possible to differentiate between a waxing flow (typical for flood turbidites) and a succession of multiple flows (typical for seismoturbidites).

Multidirectional, amalgamated density-flow deposits and turbidites can in most cases be attributed to earthquakes and represent therefore a solid paleoseismological proxy in marine and lacustrine environments.

Acknowledgements

This research was funded mainly by the Special Research Fund of Ghent University (BOF) and by the Fund for Scientific Research Flanders (FWO-Vlaanderen). We are grateful to Litoral Austral and the RV Don Este crew (especially captain J. Matamala Nuñez) to make the 2009 survey possible and successful. We thank W. Versteeg and K. De Rycker for the technical support during the survey in 2009. M. Vincx is acknowledged for the use of the Malvern Mastersizer 2000. M. Cuylaerts is acknowledged for her work in the sedimentology lab. Finally we thank K. Heirman and J. Moernaut for fruitful discussions and S. Bertrand and I. Meyer for proofreading an earlier version of the manuscript. M. Van Daele is currently funded by FWO-Vlaanderen (Research Foundation Flanders).

References

Adams, J. (1990) Paleoseismicity of the Cascadia subduction zone – evidence from turbidites off the Oregon-Washington margin. *Tectonics*, **9,** 569-583.

Alexander, J.A.N., McLelland, S.J., Gray, T.E., Vincent, C.E., Leeder, M.R. and Ellett, S. (2008) Laboratory sustained turbidity currents form elongate ridges at channel mouths. *Sedimentology*, **55,** 845-868.

Alsop, G.I. and Marco, S. (2011) Soft-sediment deformation within seismogenic slumps of the Dead Sea Basin. *Journal of Structural Geology*, **33,** 433-457.

Alsop, G.I. and Marco, S. (2012) Tsunami and seiche-triggered deformation within offshore sediments. *Sedimentary Geology*, **261-262,** 90-107.

Beck, C. (2009) Late Quaternary lacustrine paleo-seismic archives in north-western Alps: Examples of earthquake-origin assessment of sedimentary disturbances. *Earth-Science Reviews*, **96,** 327-344.

Bouma, A.H. (1962) *Sedimentology of Some Flysch Deposits: a Graphic Approach to Facies Interpretation*. Elsevier, Amsterdam, 168 pp.

Bouma, A.H. (1987) Megaturbidite - An Acceptable Term. *Geo-Marine Letters*, **7,** 63-67.

Cembrano, J., Schermer, E., Lavenu, A. and Sanhueza, A. (2000) Contrasting nature of deformation along an intra-arc shear zone, the Liquine-Ofqui fault zone, southern Chilean Andes. *Tectonophysics*, **319,** 129-149.

Cnudde, V., Cnudde, J.P., Dupuis, C. and Jacobs P.J.S. (2004) X-ray micro tomography used for the localisation of water repellents & consolidants inside natural building stones. *Materials Characterization,* **53,** 259-271.

Cnudde, V., Masschaele, B., Dierick, M., Vlassenbroeck, J., Van Hoorebeke, L. and Jacobs, P. (2006) Recent progress in X-ray CT as a Geosciences Tool. *Applied Geochemistry,* **21,** 826-832.

Goldfinger, C. (2011) Submarine Paleoseismology Based on Turbidite Records. In: *Annual Review of Marine Science, Vol 3*, *Annual Review of Marine Science*, **3**, pp. 35-66. Annual Reviews, Palo Alto.

Goldfinger, C., Morey, A.E., Nelson, C.H., Gutiérrez-Pastor, J., Johnson, J.E., Karabanov, E., Chaytor, J. and Eriksson, A. (2007) Rupture lengths and temporal history of significant earthquakes on the offshore and north coast segments of the Northern San Andreas Fault based on turbidite stratigraphy. *Earth and Planetary Science Letters*, **254,** 9-27.

Goldfinger, C., Nelson, C.H., Morey, A.E., Johnson, J.R., Patton, J., Karabanov, E., Gutierrez-Pastor, J., Eriksson, A.T., Gracia, E., Dunhill, G., Enkin, R.J., Dallimore, A. and Vallier, T. (2012) Turbidite event history—Methods and implications for Holocene paleoseismicity of the Cascadia subduction zone. *U.S. Geological Survey Professional Paper,* **1661–F,** 170 pp, available at http://pubs.usgs.gov/pp/pp1661/f

Keevil, G.M., Peakall, J. and Best, J.L. (2007) The influence of scale, slope and channel geometry on the flow dynamics of submarine channels. *Marine and Petroleum Geology*, **24,** 487-503.

Krumbein, W.C. (1939) Preferred orientation of pebbles in sedimentary deposits. *Journal of Geology*, **47,** 673-706.

Legrand, D., Barrientos, S., Bataille, K., Cembrano, J. and Pavez, A. (2011) The fluid-driven tectonic swarm of Aysen Fjord, Chile (2007) associated with two earthquakes (M_w=6.1 and M_w=6.2) within the Liquiñe-Ofqui Fault Zone. *Continental Shelf Research*, **31,** 154-161.

Lowe, D.R. (1982) Sediment gravity flows .2. Depositional models with special reference to the deposits of high-density turbidity currents. *Journal of Sedimentary Petrology*, **52,** 279-298.

McClelland, H.L.O., Woodcock, N.H. and Gladstone, C. (2011) Eye and sheath folds in turbidite convolute lamination: Aberystwyth Grits Group, Wales. *Journal of Structural Geology*, **33,** 1140-1147.

Melnick, D., Bookhagen, B., Strecker, M.R. and Echtler, H.P. (2009) Segmentation of megathrust

rupture zones from fore-arc deformation patterns over hundreds to millions of years, Arauco peninsula, Chile. *Journal of Geophysical Research-Solid Earth*, **114**.

Migeon, S., Savoye, B., Zanella, E., Mulder, T., Faugeres, J.C. and Weber, O. (2001) Detailed seismic-reflection and sedimentary study of turbidite sediment waves on the Var Sedimentary Ridge (SE France): significance for sediment transport and deposition and for the mechanisms of sediment-wave construction. *Marine and Petroleum Geology*, **18,** 179-208.

Migeon, S., Ducassou, E., Le Gonidec, Y., Rouillard, P., Mascle, J. and Revel-Rolland, M. (2010) Lobe construction and sand/mud segregation by turbidity currents and debris flows on the western Nile deep-sea fan (Eastern Mediterranean). *Sedimentary Geology*, **229,** 124-143.

Mulder, T. and Alexander, J. (2001) The physical character of subaqueous sedimentary density flows and their deposits. *Sedimentology*, **48,** 269-299.

Mulder, T., Migeon, S., Savoye, B. and Faugeres, J.C. (2001) Inversely graded turbidite sequences in the deep Mediterranean: a record of deposits from flood-generated turbidity currents? *Geo-Marine Letters*, **21,** 86-93.

Mulder, T., Migeon, S., Savoye, B. and Faugeres, J.C. (2002) Reply to discussion by Shanmugam on Mulder et al. (2001, Geo-Marine Letters 21 : 86-93) Inversely graded turbidite sequences in the deep Mediterranean. A record of deposits from flood-generated turbidity currents? *Geo-Marine Letters*, **22,** 112-120.

Mulder, T., Zaragosi, S., Razin, P., Grelaud, C., Lanfumey, V. and Bavoil, F. (2009) A new conceptual model for the deposition process of homogenite: Application to a cretaceous megaturbidite of the western Pyrenees (Basque region, SW France). *Sedimentary Geology*, **222,** 263-273.

Nakajima, T. and Kanai, Y. (2000) Sedimentary features of seismoturbidites triggered by the 1983 and older historical earthquakes in the eastern margin of the Japan Sea. *Sedimentary Geology*, **135,** 1-19.

Naranjo, J.A., Arenas, M., Clavero, J. and Munoz, O. (2009) Mass movement-induced tsunamis: main effects during the Patagonian Fjordland seismic crisis in Aisen (45 degrees 25'S), Chile. *Andean Geology*, **36,** 137-145.

Postma, G., Nemec, W. and Kleinspehn, K.L. (1988) Large floating clasts in turbidites – a mechanism for their emplacement. *Sedimentary Geology*, **58,** 47-61.

Rust, B.R. (1972) Pebble orientation in fluvial sediments. *Journal of Sedimentary Petrology*, **42,** 384-388.

Sepulveda, S.A. and Serey, A. (2009) Tsunamigenic, earthquake-triggered rock slope failures during the April 21, 2007 Aisen earthquake, southern Chile (45.5 degrees S). *Andean Geology*, **36,** 131-136.

Sepúlveda, S., Serey, A., Lara, M., Pavez, A. and Rebolledo, S. (2010) Landslides induced by the April 2007 Aysén Fjord earthquake, Chilean Patagonia. *Landslides*, **7,** 483-492.

Shanmugam, G. and Moiola, R.J. (1995) Reinterpretation of depositional processes in a classic flysch sequence (Pennsylvanian Jackfork Group), Ouachita Mountains, Arkansas and Oklahoma. *AAPG*

Bulletin-American Association of Petroleum Geologists, **79,** 672-695.

Shanmugam, G. (2000) 50 years of the turbidite paradigm (1950s-1990s): deep-water processes and facies models - a critical perspective. *Marine and Petroleum Geology*, **17,** 285-342.

Shanmugam, G. (2002) Ten turbidite myths. *Earth-Science Reviews*, **58,** 311-341.

Stow, D.A.V. and Shanmugam, G. (1980) Sequence of structures in fine-grained turbidites: Comparison of recent deep-sea and ancient flysch sediments. *Sedimentary Geology*, **25,** 23-42.

Strasser, M., Monecke, K., Schnellmann, M. and Anselmetti, F.S. (Accepted) Lake sediments as natural seismographs: A compiled record of Late Quaternary earthquakes in Central Switzerland and its implication for Alpine deformation. *Sedimentology***,** n/a-n/a.

Wang, K., Hu, Y., Bevis, M., Kendrick, E., Smalley, R. and Lauria, E. (2007) Crustal motion in the zone of the 1960 Chile earthquake: Detangling earthquake-cycle deformation and forearc-sliver translation. *Geochemistry Geophysics Geosystems*, **8,** 14.

“La ola llegó acá por la peninsula, fue más grande que la del ’60”

“The wave came this way along the peninsula, it was larger than the one of 1960”

Old fisherman on the beach of Pucón at Lake Villarrica talking about the lake tsunami in 2010, comparing it with the one of 1960.

Chapter 7

Conclusions and outlook

7.1 Conclusions

The main goal of this PhD research was to characterize deposits of recent natural catastrophic events (earthquakes and volcanic activity) in such a way that the results could be used to reconstruct the occurrence and magnitude of similar events in the past. The main conclusion is that lakes and fjords are excellent repositories of the sedimentary record of natural events, since the encountered deposits in all the study areas correlate well with (historical) reports, shaking intensities and catchment characterisitcs.

The most frequently encountered type of deposit linked to catastrophic events are density-flow deposits (which include turbidites). It was possible to differentiate between turbidites triggered directly by earthquakes and turbidites triggered by onshore debris or mud flows, lahars, or floods reaching the lake shore. One of the main breakthroughs of this study is the identification and high-resolution characterization of amalgamated turbidites or density-flow deposits. These amalgamated density-flow deposits were studied in high detail in Aysén fjord, where it was even possible to reconstruct the different paleoflow directions encrypted in individual sub-deposits. Such amalgamated density-flow deposits imply synchronous triggering (and hence, earthquake triggering) of mass-wasting events in one basin (lake or fjord sub-basin) and are therefore an excellent proxy for paleoseismological applications. Similar amalgamated deposits, with sub-deposits coming from different types of source areas, were found in lakes Negra, Llanquihue, Calafquén and Riñihue.

Another breakthrough of this study is the identification and fingerprinting of lacustrine volcanic event deposits that were not transported into the lake as direct fallout, but as precipitation-driven runoff of the fine-fallout ashes from the catchment. In lakes Villarrica and Calafquén, it was thus possible to match each of such event deposits to an eruption of Villarrica Volcano with a VEI ≥ 2, and vice versa. Also, deposits of lahars in lakes were described for the first time and an enormous fan and basin-focused deposit related to the caldera-forming eruption of Hudson Volcano was encountered in Aysén fjord.

In the following paragraphs the main conclusions of the four research chapters are briefly recapitulated.

Chapter 3: historical record of Villarrica Volcano

- A new, more detailed and reliable 500-year-long eruption record was constructed for Villarrica and surrounding volcanoes in the Chilean Lake District between 39° and 40° S.
- A combination of standard sedimentological techniques and µXRF scanning allowed the systematic detection of very thin event deposits in an objective and efficient manner down to a thickness of 100 µm. Three types of volcanic event deposits were detected and classified in this way:
  - *tephra fall-out layers:* characterized by drapes of coarse ash with very high Fe/Si and high Al/Si ratios;
  - *Fe-rich clay to fine silt laminae (FeLs):* clays and fine silts with a high Fe/Si ratio, that record fluvial erosion and transport of cryptotephra into the lake;

    - *lahar deposits:* fining-upwards event deposits with coarse basal deposits close to the inflow (high Fe/Si) and a fine silt to clay with the same composition as the detrital component of the background sediment (high Al/Si and Fe/Si).
- The eruption record of Villarrica Volcano has been significantly improved, with the identification of 88 VEI ≥ 2 eruptions between 1523 and 1991. Villarrica Volcano has experienced nearly constant eruptive activity during this period with an average and median of one eruption (VEI ≥ 2) every 5.32 and 4.5 years, respectively. The last VEI ≥ 2 eruption occurred in 1991 and the probability of a 21-year repose period (anno 2012) is ≤ 1.9 %. Based on the last 600 years, it was concluded that there is a high probability of a VEI ≥ 2 eruption in the near future. However, the possibility of cluster occurrence and hence, a temporarily decreasing activity, cannot be excluded.
- Tephra-fall deposits could not only be geochemically and mineralogically linked to Villarrica Volcano, but also to the Carrán-Los Nevados Volcanic Complex, El Mocho, Quetrupillán and Huanquihue or Lanín volcanoes. El Mocho Volcano has possibly experienced a decrease in activity frequency during the last centuries.

Chapter 4: sedimentary imprint of the 1960 and 2010 earthquakes

- Five distinct types of event deposits, all attributed to the 1960 and 2010 earthquakes (i.e. seismites), were identified during a regional exploration of 19 different Chilean lakes:
    - mass-transport deposits (MTDs);
    - in-situ deformation;
    - lacustrine turbidites with a similar composition as the background sediments (LT1s);
    - lacustrine turbidites with a different composition as the background sediments (more terrestrial; LT2s);
    - homogenites.
- The event deposits correspond very well to accounts and reports from local inhabitants and to observations that were made around the lake after the earthquake. For example, homogenites consistently occur where lake seiches were reported. LT2s can be a result of local near-shore mass wasting, a delta collapse or onshore landslides surging into the lake (direct imprint), but they can also result from debris or mud flows entering the lake, or fluvial remobilization of landslide debris in the catchment (indirect imprint). The distribution in the lake, composition and relation to other event deposits can help clarifying the origin of the deposits.
- Distinguishing between LT1s and LT2s is very important, since LT2s can have several origins, while LT1s can only be formed by mass-wasting within the lake, which excludes most triggers other than earthquakes. Synchronous LT1s in different lakes and/or different sub-basins within a single lake are therefore a very good indicator for earthquake triggering. Moreover, they most sensitively record different seismic intensities. The thickness and distribution of LT1s in a lake strongly depends on the local seismic intensity, while for the other seismites there only appears to be a minimum intensity threshold for each lake or sub-basin.
- In general the minimum encountered intensity threshold for most seismites is VI, but this can differ (i.e. be higher) between the lakes and/or sub-basins.
- Coastal lakes that barely contain slope sediments, on the border between Valdivia rupture zone and Concepción-Valparaíso rupture zone (i.e. lakes Lanalhue and Butaco), where seismic shaking

is frequent, record lake-level rise due to the co-seismic coastal tilting rather than the seismic shaking itself.
- Apart from the very shallow (6 m) Lake Aculeo, all lakes consistently recorded the megathrust earthquake that ruptured the thrust segment along which they are located. When the other earthquake was also recorded, the deposits where thinner and/or less widespread.

Chapter 5: basin-plain deformation in Aysén fjord

- The onshore landslides –triggered by the 2007 M_w 6.2 earthquake– that entered the fjord, all triggered deformation of basin-plain sediments, which might have been more important for tsunami generation than the impact of the onshore landslides themselves. Multiple small offshore mass movements and sediment volcanoes were also directly triggered by the earthquake.
- The largest offshore deformed basin-plain deposits were produced by the impact and load of the mass flows originating from the onshore landslides. This resulted in unique morphologies of the basin-plain deformation, characterized by proximal depressions and high inner and outer thrust belts.
- Some density flows (originating from the mass flows) created or enlarged channels, occasionally cutting through the thrust belts of the deformed basin-plain deposits, indicating that the latter formed more rapidly.
- Probably three to four similar events have struck the fjord during the Holocene. A similar hazard should be taken into account for the other fjords between 41.5° and 46.5° S.
- The Cuervo Ridge is identified as a moraine. The interpretation as two monogenetic volcanic cones, as proposed during previous studies, can be ruled out. However, there are indications for fluid flow from tectonic structures below the fjord to the seafloor, which could be related to volcanic and tectonic activity.

Chapter 6: amalgamated density-flow deposits in Aysén fjord

- Simultaneously triggered density flows originating from different source areas can produce deposits that are stacked or intercalated between each other, forming amalgamated density-flow deposits.
- Multidirectional, amalgamated density-flow deposits and turbidites can in most cases be attributed to earthquakes and represent therefore a solid paleoseismological proxy in marine and lacustrine environments.
- X-ray CT scans can offer key information for a correct interpretation of sedimentary structures and are the only method to reconstruct paleoflow directions based on these structures. Flow-direction indicators such as folds, imbrication of clasts, ripples and convolute lamination can all be used to determine relative flow directions and changes herein during deposition of the density-flow deposits.
- The latter results also make it possible to differentiate between a waxing flow (typical for flood turbidites) and a succession of multiple flows (typical for seismoturbidites).

7.2 Outlook

This study also raises more research questions and in this section strategies to solve some of these questions are proposed. For every research chapter these consist of two parts: i) how to improve the characterization of the deposits and ii) how to use the results in future research into event history. Some of the results are already being used to better understand and reconstruct older events, these studies are also mentioned here.

Chapter 3: historical record of Villarrica Volcano

- To better understand their formation, Fe-rich clay to fine silt laminae (FeLs) should be better characterized by attempting to subsample these laminae and further investigate them with SEM, EDS, XRD etc.
- Frustules of diatoms at the stratigraphic levels of the FeLs and other volcanic event deposits appear to be thicker and darker in color; this observation should be further investigated to determine the possible impact of these events on diatom communities.
- The lateral distribution and thickness of the fine-grained top of the lahar deposits should be compared with their proximal grain size and thickness, the reported impact of the lahars and the season in which they occurred. The latter influences the stratification of the lake waters, which can potentially affect the distribution of the fine-grained fraction within the lake (e.g., by interflows). This information is therefore crucial to accurately reconstruct lahars in prehistoric times.
- In long cores (on distal locations) of both lakes Villarrica and Calafquén, more lahar deposits were observed (Heirman et al., submitted; Moernaut, 2010) and should be used to construct a longer lahar record of Villarrica Volcano, possibly encompassing the (nearly) entire Holocene. The possible link of lahar formation with climate variablility has been made in this PhD study and is already used as a proxy for El Niño variability in the Holocene by Heirman et al. (submitted).
- Lahar deposits can be used to reconstruct lahars of volcanoes bordering other lakes in South-Central Chile. Lahar deposits were encountered in lakes Laja, Ranco and Llanquihue.
- Probability estimates should be used to improve existing hazard assessments for Villarrica Volcano region.

Chapter 4: sedimentary imprint of the 1960 and 2010 earthquakes

- To better characterize some of the deposits, X-ray CT scans could be used. Potentially, some of the turbidites could in fact be amalgamated turbidites, a result that would be extremely useful for future lacustrine paleoseismology.
- Intensity thresholds for lakes and sub-basins that were obtained in this study can be used to detect historical and prehistoric earthquakes and better constrain the associated rupture zones.
- The new knowledge on the imprint of the 1960 and 2010 earthquakes is already being used to determine historical and prehistoric events in some of these lakes. They are the subject of several studies: i) Lake Encañado, an ongoing Master thesis (T. Pille); ii) Lake Laja, a bachelor internship (E. Boes; Boes, 2011); iii) lakes Villarrica, Calafquén and Riñihue, Moernaut et al. (in prep); and iv) lakes Ranco and Puyehue, Master thesis (L. Doom; Doom, 2012). Especially close to Santiago, the

densely populated capital of Chile, there is an urgent need for reliable paleoseismological records (e.g., from lakes Negra and Encañado).

Chapter 5: basin-plain deformation in Aysén fjord

- Extracting the backscatter information from the multibeam data could further improve our understanding of the interaction between the mass-flow deposits and the deformed basin-plain deposits, since it should be possible to differentiate between both.
- A denser grid of seismic-reflection profiles would allow improved mapping of deposits, especially the features in the subsurface, such as the basal shear surfaces.
- To find out which process has the strongest influence on tsunami height and run-up, a tsunami triggered by both the onshore landslides and the basin-plain deformation should be modeled and compared to reported tsunami heights and run-up in 2007. Results from this study will help to better assess the tsunami hazard not only in Aysén fjord, but also in other fjords close to active faults, since not all onshore landslides will cause basin-plain deformation and the different waves will propagate in a different way through the fjords.
- Surveys similar to the one that was carried out in the inner Aysén fjord should be carried out in the outer fjord and in other fjords in the region. By detecting and dating similar events in other fjords, a regional hazard assessment for earthquake recurrence and tsunami impact can be developed. A first step in this process is already planned; in March 2013, a cruise with the *RV Hespérides* plans to visit the outer Aysén fjord and more northerly fjords.

Chapter 6: amalgamated density-flow deposits in Aysén fjord

- µCT-scanning with a resolution high enough to distinguish very fine sand grains can be used to detect imbrication in these sand grains, therefore allowing to study changes in paleoflow direction in even greater detail. This will also make us understand the interaction between these different flows better than we do thus far.
- Prehistoric events are already detected on reflection-seismic profiles. By studying the density-flow deposits that are present in the existing 22 m long core, these older events can be better characterized and an average recurrence rate could be established. Moreover, this core is oriented (K. Kissel, pers. comm.), which will allow reconstructing paleoflow directions and compare these to the landslides detected on the seismic profiles.
- X-ray CT scanning should be used more frequently in studies where turbidites are used for paleoseismology, for example in submarine channels, since it will help to detect synchronous triggering and hence, the earthquake origin.

References

Boes, E. (2011) *Karakterisatie van historische aardbevingen in Centraal Chili aan de hand van meersedimenten in Lago Laja.* Stageverslag 3de Bachelor Geologie, Ghent University, Ghent, 35 pp.

Doom, L. (2012) *Paleoseismiciteit in Zuid-Centraal Chili tijdens de laatste 500 jaar: het sedimentologische archief van Lago Ranco en Lago Puyehue.* Scriptie voorgelegd tot het behalen van de graad Van Master in de Geologie, Ghent University, Ghent, 91 pp.

Heirman, K., Van de Vyver, E., Abarzúa, A.M., Roberts, S., Van Daele, M., Moernaut, J., Eekhaut, M., Keppens, E., Hebbeln, D., Tjallingii, R., Kilian, R., Verleyen, E., Pino, M., Brümmer, R., Urrutia, R., De Batist, M. (submitted) A Holocene record of Southern Westerlies and ENSO variability from Lago Villarrica (39°S). *Palaeogeography, Palaeoclimatology, Palaeoecology.*

Moernaut, J. (2010) *Sublacustrine landslide processes and their paleoseismological significance: Revealing the recurrence rate of giant earthquakes in South-Central Chile.* PhD thesis, Ghent University, Ghent, 274 pp.

Moernaut, J., Van Daele, M., Heirman, K., Vandoorne, W., Strasser, M., Pino, M, Urrutia, R., Brümmer, R., De Batist, M. (in prep) Lacustrine turbidites in South-Central Chile as a tool for quantitative earthquake reconstruction. *Geochemistry, Geophysics, Geosystems.*